Antal Kerpely Doctoral School of Materials Science and Technology

Development of Innovative Thermal Insulation Building Materials Based on Zeolite-Poor Rock and Solid Wastes

A Dissertation Submitted in Partial Fulfillment of the Requirements for the Degree of Doctor of Philosophy in Ceramics Engineering as a Part of Stipendium Hungaricum Scholarship in Material Science and Technology

By

Jamal Eldin Fadoul Mohammed Ibrahim

Supervisors:

Prof. Dr. László A. Gömze †, Professor

Dr. István Kocserha, Associate Professor

Head of the Doctoral School

Prof. Dr. Valéria Mertinger

Institute of Ceramic and Polymer Engineering
Faculty of Materials and Chemical Engineering
University of Miskolc
Miskolc, Hungary
2022

“When modern man builds large load-bearing structures, he uses dense solids; steel, concrete, glass.

When nature does the same, she generally uses cellular materials; wood, bone, coral. There must be good reasons for it.”

M. F. Ashby

ACKNOWLEDGEMENT

My success in this Ph.D. program could not have been achieved without the deep cooperation, invaluable assistance, and ongoing support I was fortunate to have from many people. Through these few sentences, I would like to express my thanks to them.

First and foremost, I would like to express my massive appreciation to my previous supervisor *Prof. László A. Gömze*, for his overwhelming support, advice, encouragement, commitment, and supervision right from the start till the midway of my Ph.D. candidature at University of Miskolc. Prof. László A. Gömze passed away in January 2022. He was a very dedicated and supportive person with a huge passion for research. My deepest appreciation goes to my current supervisor, *Dr. Kocserha István*, who has always been actively engaged in my Ph.D. project by guiding, inspiring, and supporting me; this includes correcting my thesis and giving me meaningful advice. There is no way I could have completed this research work without his extensive support.

I would like to thank all the respected professors at the University of Miskolc who taught me various subjects over the first two years of the Ph.D. program.

I also like to express my gratitude to the reviewer, *Prof. Dr. Péter Baumli*, for his insightful comments and suggestions on several aspects of my study; his constant support and positive opinions about my work during this whole Ph.D. course helped me to achieve the desired outcomes.

I would also like to extend my thanks to the reviewers, *Dr. Katalin Kopecskó* and *Dr. Péter Telek*, for their valuable questions, feedback, and comments on my dissertation. I am very grateful for their careful review and constructive suggestions, which have helped me to highly improve this dissertation.

I would also like to thank *Dr. Emese Kurovics* and *Mr. Gál Károly* for their unlimited support in the experimental work. My thanks extend to *Dr. Daniel Koncz-Horvath* for his assistance in conducting the investigation related to scanning electron microscopy and energy dispersive spectroscopy. I would also like to warmly thank *Dr. Róbert Géber* for his assistance in conducting the particle size distribution analysis. I owe thanks to *Dr. Andrea Simon* for her assistance in carrying out the thermal conductivity test. Many thanks to *Dr. Tamás Szabó* and *Ms. Ildikó Tasnádi* for their help with conducting FT-IR analysis. I would also like to express my deepest appreciation to all the staff members in the Antal Kerpely Doctoral School of Materials Science and Technology, University of Miskolc, for their advice, technical support, continual assistance, and cooperation during the implementation of the experimental work throughout the past years.

I would like to express my sincere gratitude to *Ms. Agnes Solczi* not only for being our faculty coordinator facilitating all the administrative work but also for her encouragement, support, and generous invitations to join her hiking trips.

I also express my thankful feelings to my colleagues. I am thankful to all of them for the many hours of useful and enjoyable study, experimentation, and collaboration, as well as for sharing their extensive and valuable practical skills and knowledge with me.

I would like to acknowledge Hungarian government for providing me full scholarship during the period of my Ph.D. study. I am very much thankful to Ministry of Higher Education, Sudan and University of Bahri for their financial support.
I would like to thank my close colleagues, *Ms. Ei Ei Khine* and *Mr. Mohammed Tihtih,* for their encouragement, understanding, and support throughout my Ph.D. journey.
Finally, my love and deep gratitude go to all my family members, who have always provided me with their unconditional love, encouragement, and deep support throughout my Ph.D. program and my academic career.

Jamal Eldin F. M. Ibrahim
November 2022

CONTENTS

LIST OF FIGURES

LIST OF TABLES

LIST OF ABBREVIATIONS

ZR	**Z**eolite-poor **r**ocks
SD	**S**aw**d**ust
ESP	**Eggshell p**owder
XRD	**X**-**R**ay **D**iffraction
XRF	**X**-**R**ay **F**luorescence
SEM	**S**canning **E**lectron **M**icroscope
EDS	**E**nergy **D**ispersive **S**pectroscopy
CT	X-ray micro-**c**omputed **t**omography
BET	**B**runauer, **E**mmett and **T**eller
TGA	**T**hermal **G**ravimetric **A**nalysis
DTA	**D**ifferential **T**hermal **A**nalysis
PBU	**P**rimary **b**uilding **u**nits
SBU	**S**econdary **b**uilding **u**nits
BC	**B**efore **C**hrist
SSA	**S**pecific **S**urface **A**reas
P	**P**ressure
P_o	**S**aturation **P**ressure
2θ	Diffraction Angles
λ	Wavelength
PDF	**P**owder **D**iffraction **F**ile
ICDD	**I**nternational **C**enter for **D**iffraction **D**ata
PDF	**P**owder **D**iffraction **F**ile
rpm	**r**evolutions **p**er **m**inute
ASTM	**A**merican **S**ociety for **T**esting and **M**aterials
MTPS	**M**odified **T**ransient **P**lane **S**ource
LOI	**l**oss **o**n **i**gnition
FWHM	**F**ull **W**idth at the **H**alf **M**aximum

1. Introduction

Energy consumption recently became a global concern due to its environmental and economic impact [1-4]. It has been reported that an expected 50% increase in overall energy consumption will take place worldwide until the year 2050. The most energy demand (80%) of this increase is likely to be in developing countries [5], while the buildings sector is anticipated to dissipate 40% of the total global energy consumption (Fig. 1) [6-8]. Therefore, energy efficiency is becoming a top priority for eco-friendly construction since the building sector is the biggest energy consumer. In the hot climate area and especially during the summer, a considerable amount of energy is used for cooling the building, while in the cold climate area, almost the same amount is used to worm the building to achieve internal comfort [9] (Fig. 2).

Future high-energy-saving buildings can play a crucial role in facing sustainable energy challenges by reducing the contribution of building to climate change, reducing global greenhouse gas emissions, and enhancing energy security and sovereignty [10]. Therefore minimizing energy usage in buildings by using passive techniques such as thermal insulation is of increasing popularity [11]. The use of ceramic specimens with enhanced thermal insulation aids in the mitigation of heat losses. The walls are the main areas via which significant quantities of heat interchange between the building and the surrounding environment. It is worth mentioning that a large amount of energy consumption in the building is due to heat loss and gain throughout the wall [12,13]. The U-value, also known as thermal transmittance, is the rate of transfer of heat through a structure (which can be a single material or a composite) divided by the difference in temperature across that structure. The wall's optimal U-value based on the European standard EN832 is considered to be in the range of 0.4–0.7 W/m^{2}K [14]; the lower the U-value, the better the performance. To achieve this objective, a big effort has been dedicated lately to preparing ceramic specimens (porous bricks and glass-ceramic foams) with superior properties such as lightweight, good mechanical properties, and lower thermal conductivity [15-18]. Producing ceramic bricks and foams from relatively cheap raw materials (waste and natural materials) while enhancing the properties to achieve the optimum cost-benefit relationship is of great interest.

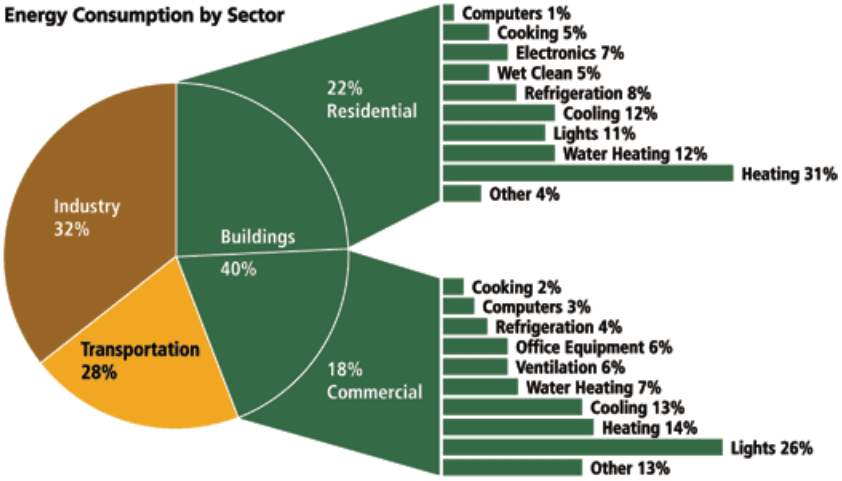

Figure 1. Global energy consumption by sector [19].
(Taken from: D. Simone, *et al*. (2018): Occupant Behavior: A "New" Factor in Energy Performance of Buildings - Methods for Its Detection in Houses and in Offices)

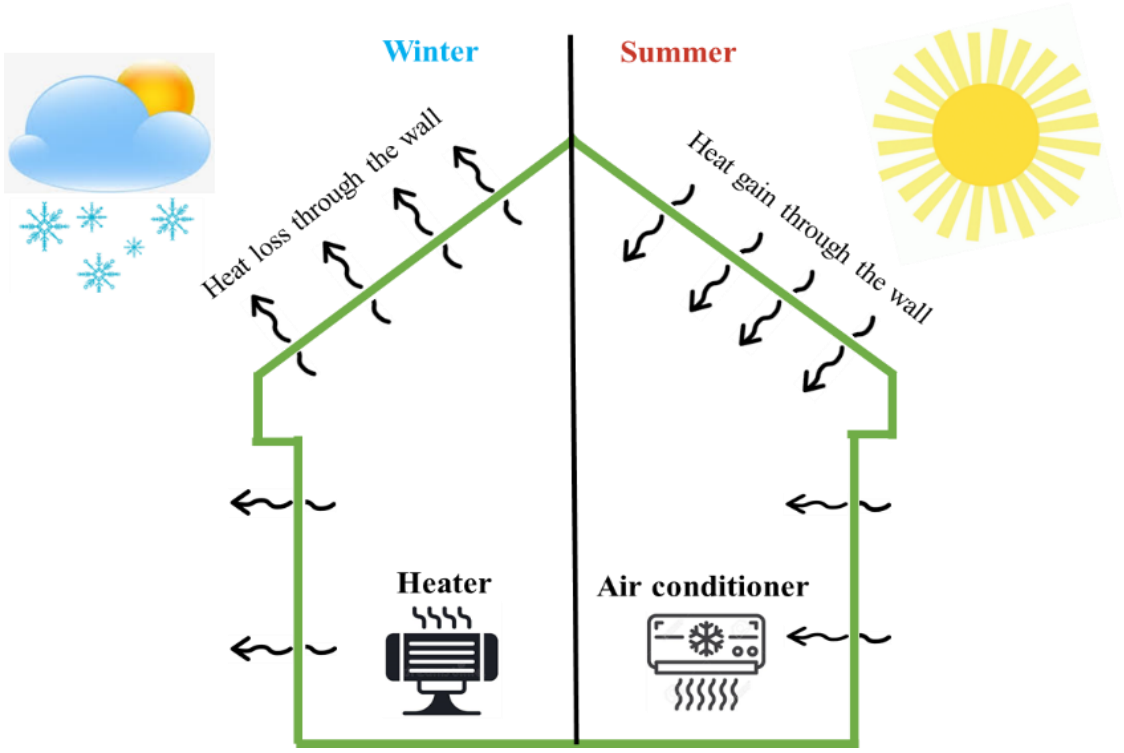

Figure 2. Heat loss and gain through the wall

The fast population growth (Fig. 3), urbanization, industrialization, and various other human activities lead to a huge release of waste and a great demand for construction materials [20]. It has been noted that the global amount of solid waste produced will increase 3 times by the year 2100, rising from 4 million tons to 12 million tons per day (Fig. 4) [21]. The dramatic growth in waste materials has resulted in serious environmental issues in all communities [22]. Therefore, waste management has become a worldwide concern. Several countries have implemented strong environmental protection laws and developed waste management technologies to reduce pollution and damage to the environment [23,24]. Another problem is the fast depletion of natural resources, resulting in scarcity and concerns about the availability of raw materials [25,26]. Sintered ceramic materials such as bricks and glass-ceramic foams have emerged as a highly promising technical option for recycling solid wastes lately [27], [28]. Waste reuse is attainable if it is technologically, environmentally, and economically feasible [29-31]. In this sense, waste recycling is considered an ecologically excellent approach to more eco-efficient buildings [32,33]. This alternative not only reduces the cost of waste disposal but also conserves natural resources by reducing the use of nonrenewable raw materials in manufacturing ceramic bricks and glass-ceramic foams, decreasing the harmful environmental impact, for instance, pollution and top-soil loss [34,35]. Although recycling waste materials is an old and common practice, new waste is continuously used to avoid the depletion of natural resources and promote public health [36]. This approach appears to be promising in terms of drastically lowering energy usage in the hopes of fulfilling the concept of a future nearly zero-energy building [37,38]. As a result, lowering heat energy requirements is a vital contribution to eco-friendly buildings.

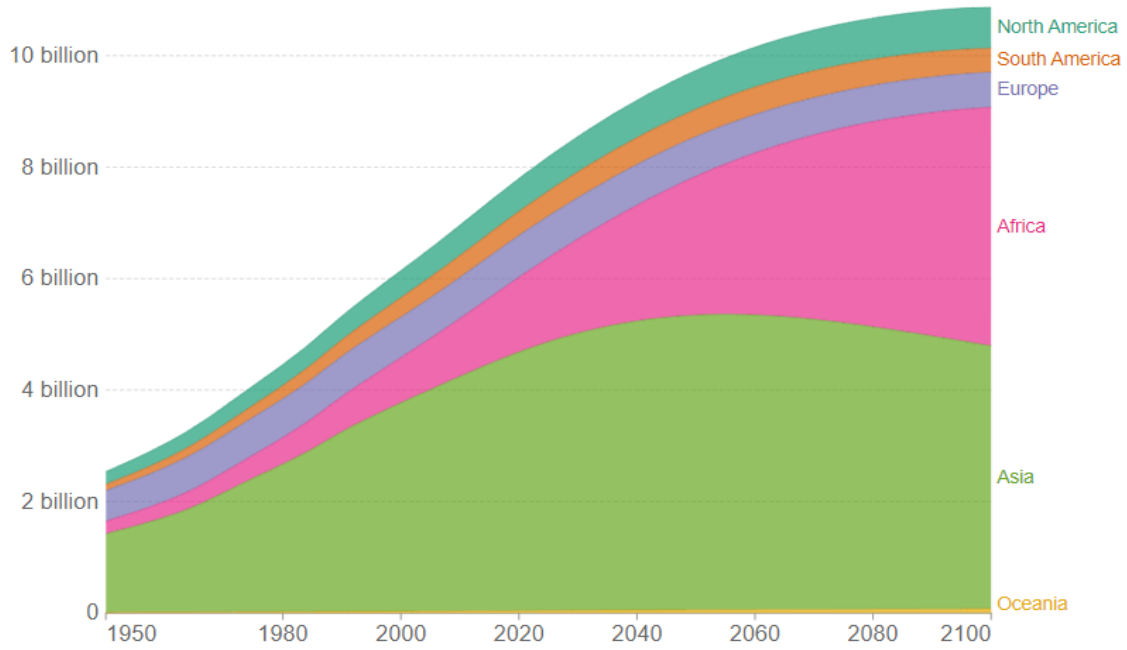

Figure 3. The expected increase in world population by region [39].
(Taken from: Roser Max (2013): "Future population growth")

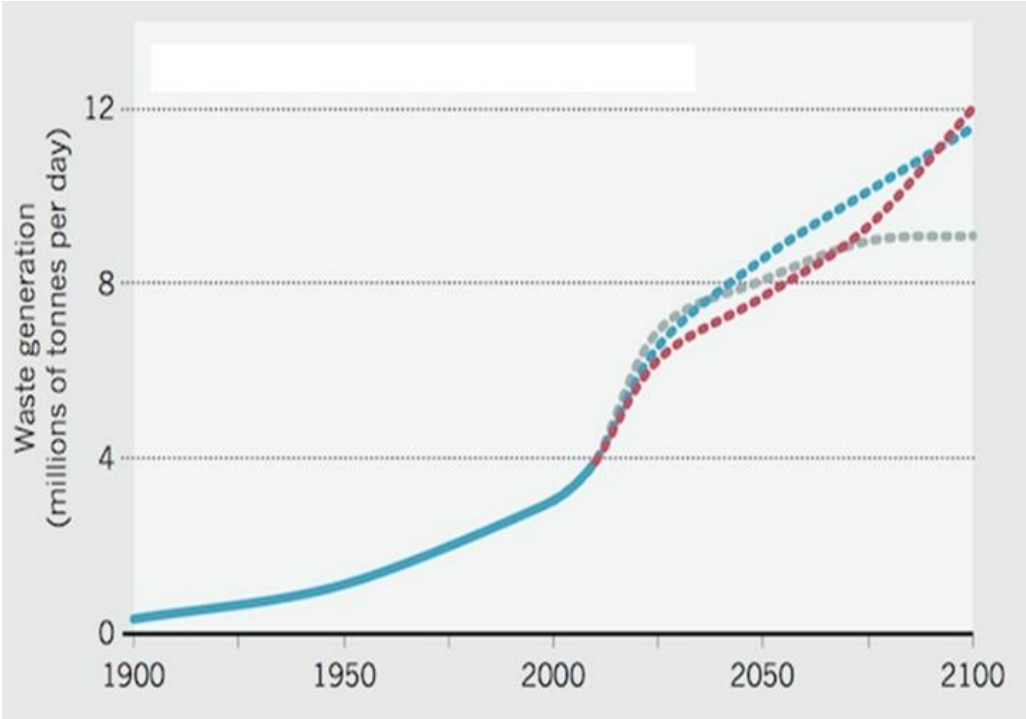

Figure 4. Global waste generation in the past and in the future [21]. The prediction if the global population is a) 7 billion, 90% are urbanized and environmentally conscious (grey line), b) 9.5 billion and 80% are urbanized and environmentally unconscious (blue line), c) 13.5 billion and 70% are urbanized and environmentally unconscious (red line).
(Taken from: D. Hoornweg, *et al*. (2013): Environment: Waste production must peak this century)

The growing demand for building materials prompted an urgent search for sustainable alternatives, including natural and waste materials that can be used to synthesize construction materials with superior thermal insulation characteristics.

Among natural materials, zeolite-poor rocks and solid waste could be excellent candidates for synthesizing construction materials with better thermal insulation [40]. Zeolite-poor rocks are naturally occurring tuffs. They usually contain a low percentage of zeolite, besides other minerals [41]. Their low amount of zeolite restricted their advanced applications. But due to their superior mechanical characteristic, porous structure, and lightweight, zeolite-poor rocks are excellent building materials that can be used to manufacture porous structural materials with enhanced thermal insulation properties [42]. Various scientific studies have been performed on using zeolite-poor rocks in construction as an additive to cement or masonry blocks [43,44]. Despite many studies on this topic, no research has been conducted to evaluate zeolite-poor rocks together with sawdust and eggshell as primary raw materials for bricks and glass-ceramic foams production.

The development of novel composite bricks and glass-ceramic foams utilizing easily obtainable, low-price raw materials at an economical cost is particularly appealing. This may significantly decrease production costs, increase competitiveness, and minimize environmental concerns by conserving energy, decreasing pollution, and lowering waste disposal expenses.

1.1. Knowledge gap and objectives of the research

To the best of our knowledge, no research has been conducted to investigate zeolite-poor rock incorporated solid waste usage as primary raw materials for preparing porous bricks and glass-ceramic foams. Based on the literature, The possibility of using solid waste (sawdust and eggshell) as pore-forming agents in zeolite-poor rock samples needs to be examined. Furthermore, mechanical milling and the optimal condition for the compaction process of zeolite-poor rocks containing sawdust and eggshell need to be investigated. In addition, the effect of alkali activation, composition and sintering temperature on the technical properties of the produced new porous bricks and glass-ceramic foams are worth studying.

The main objective of this study is to examine the potential usage of zeolite-poor rock as an alternative and eco-friendly construction material for preparing ceramic bricks and glass-ceramic foams with outstanding thermal insulation properties. Furthermore, to assess the use of sawdust and eggshell as pore-forming agents and their function in improving the thermal insulation and technical aspects of the composite ceramic specimens (porous bricks and glass-ceramic foams).

Sawdust (SD) and eggshell powder (ESP) were used to partially substitute zeolite-poor rock. This study's goals were achieved by doing comprehensive research at various stages and major testing on the produced new ceramic bricks and foams samples. The major goal was realized by the following objectives:

- **Objectives for the development of new ceramic bricks**

1. **To systematically investigate the raw materials (zeolite-poor rock from Tokaj region), sawdust and eggshell based on their mineralogical composition, phase identification, microstructural feature, chemical constituents, thermal analysis, particle size distribution, and specific surface area.**
2. **To evaluate different types of local solid wastes, including sawdust and eggshell, for integration into the ceramic specimens. Furthermore, to estimate the proper mixing proportions, then to prepare various mixtures of zeolite-poor rock and wastes through mechanical activation using a ball mill operating at optimal conditions.**
3. **To experimentally prepare green ceramic specimens using uniaxial dry pressing and investigate their characteristics.**
4. **To suggest appropriate, cost-effective sintering conditions (heating rate, sintering temperature, and residence time) for the preparation of zeolite-poor rock-incorporated sawdust and eggshell ceramic samples.**
5. **To assess the influence of sawdust and eggshell inclusion on the technical characteristics of the produced ceramic bricks and foams, such as bulk density, shrinkage, apparent porosity, water absorption, thermal conductivity, and compressive strength based on international standards.**
6. **To compare the results of the technical properties of the prepared specimens to that of the current literature in the field of burned ceramic bricks.**

- **Objectives for the development of innovative glass-ceramic foams**

1. **To investigate the effect of alkali activation on the prepared ceramic powders based on zeolite-poor rock and solid waste (sawdust and eggshell).**
2. **To evaluate the effect of the sawdust and eggshell incorporation on the foamability of the alkali-activated mixture.**
3. **To evaluate the impact of sawdust and eggshell incorporation on the technical properties of the developed glass-ceramic foams, such as bulk density, shrinkage, apparent porosity, water absorption, thermal conductivity, and compressive strength**.
4. **To compare the results of the technical properties of the produced samples to that of the current literature in the field of glass-ceramic foams.**

Finding answers to these objectives was the aim of the research. The answers to the objectives can be found in the „Discussion" sub-chapters (4.2, 4.4, 4.6, 4.8., 4.10).

2. Literature review and background of the research

Theoretical background and literature are addressed based on the lightweight fired clay bricks and glass-ceramic foams utilized for the building's thermal insulation. This chapter also discusses the prospective use of zeolite-poor rock as promising building materials, as well as the inclusion of various waste materials as pore-forming agents and their influence on the technical qualities of the generated ceramic specimens.

2.1. Thermal insulation in buildings

Insulation standards for new construction have grown over time in response to rising concerns about indoor air quality, human comfort, and environmental impact. For this reason, there is a great potential for energy savings and for policies to impose energy-efficiency improvements for both new and existing buildings. HVAC (heating, ventilation, and air conditioning) often uses the most energy in residential and non-residential buildings. It is widely accepted that increasing a building's thermal insulation is a great way to cut down on HVAC costs [45]. Insulation materials are low-thermal-conductivity materials used in building components to limit heat transfer between the indoor and outdoor spaces, lower the building U-value, and keep the inside of the building at a constant temperature regardless of changes in the surrounding environment. For that reason, it diminishes the demand for fossil fuels used in power plants to create electricity by decreasing the need for heating and cooling [46]. There are various types of materials that are used for insulation nowadays. These materials can be categorized into four groups: organic materials, inorganic materials, combined materials, and new technology materials [47]. Among the building materials that offer thermal insulation, porous bricks and glass-ceramic foams are reliable sustainable materials. Lowering the thermal conductivity of building materials is a crucial step in improving thermal insulation in buildings. One way to do this is by incorporating appropriate additives into the raw materials and/or using new materials. Huge interest has been devoted lately to the development of new thermal insulation materials [48,49]. Zeolite-poor rock is a potential candidate for the synthesis of porous bricks and glass-ceramic foams with outstanding properties.

2.2. Zeolites

2.2.1. Definition and historical background

Zeolites are a large group of naturally occurring minerals, normally consisting of crystalline hydrated aluminosilicates of group I or II elements (sodium, potassium, calcium, and barium) formed from largely extending three-dimensional frameworks of $[SiO_4]^{4-}$ and $[AlO_4]^{5-}$ tetrahedra bonded from their corners with shared oxygen atoms (Fig 5) [50]. Zeolite is characterized by its uniform porous structures with large interconnected cavities which accommodate cations such as Na^+, K^+, Ca^{2+} and Mg^{2+} that neutralize the negatively charged framework [51,52]. They have a large interior surface area of up to 800–1000 m^2/g [53].
Natural zeolites were first discovered in 1756 by a Swedish mineralogist, Cronsted. The name zeolites come from a combination of two Greek words. ("zeo", to boil) and ("lithos", stone) meaning "boiling stone", as these minerals seem to boil when heated over a certain temperature

because of the boiling water inside their structures [54]. Their useful microporous properties and their applications in the adsorption and ion exchange process were not recognized until the 19th century; then, in the 1940s, synthetic zeolites with low Si/Al ratios were successfully produced. The successful preparation of synthetic zeolites opens a wide gate for fast research growth in zeolite development and applications in the different fields of industry in the 20th and 21st centuries [55]. Various structures (more than 200) are introduced for zeolites, of which 20% are considered natural minerals and the remainder are synthetic materials. Zeolite, which can be prepared in a high amount at relatively moderate temperatures, is popular for large-scale applications. Therefore, the most highly used are high-alumina zeolites with large pore systems, such as zeolites Linde type A and zeolites Linde type X [50].

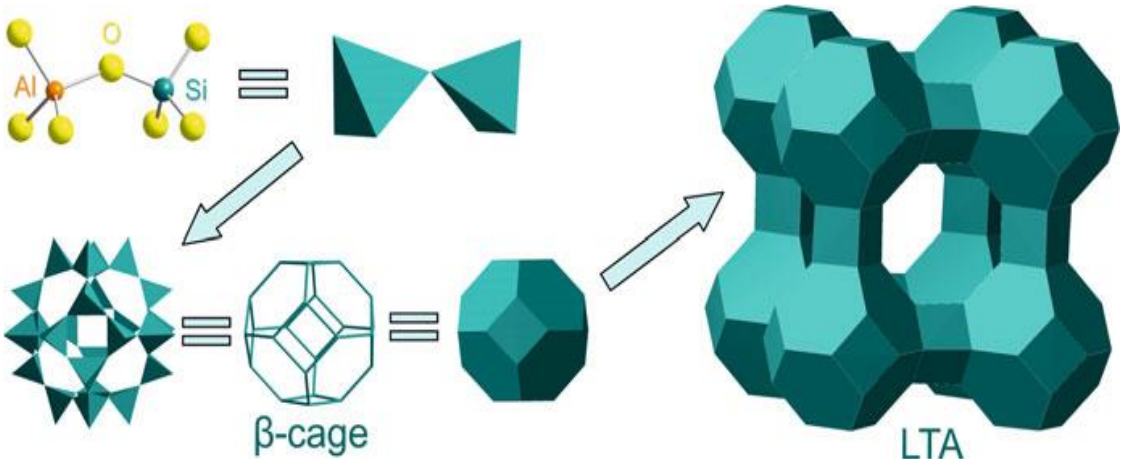

Figure 5. Schematic construction of zeolites from SiO_4 and AlO_4 tetrahedra and simplified polyhedra representation of a zeolite structure [50].
(Taken from: Inamuddin and M. Luqman (2012): Ion exchange technology I: Theory and materials)

2.2.2. Structure and classification

2.2.2.1. Primary building units

As previously mentioned, zeolites are crystalline hydrated aluminosilicates consisting of corner-sharing of TO_4 (T=Si or Al) tetrahedra that form a three-dimensional four-connected framework with uniformly sized pores of molecular dimensions [56]. These [SiO_4] or [AlO_4] tetrahedra are the primary structural building units (PBU) of a zeolite framework. Extra cations compensate for the overall negative charge in the framework (Fig. 6). Moreover, a large amount of combined water exists in the zeolite cages [57]. The chemical formula of zeolite can be expressed as:

$$M^{x+}{}_{n/x}[Si_{n-1}Al_nO_2].nH_2O$$

Where *M* is the replaceable cation of valence *x*. *M* is normally a cation of Group I or II, *n* is the number of Al [58].

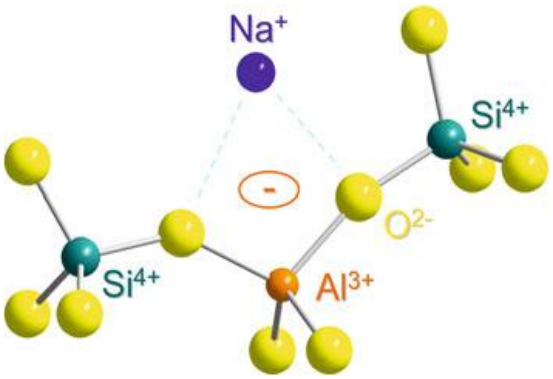

Figure 6. Compensation of negative zeolite framework charge by sodium cation [50].
(Taken from: Inamuddin and M. Luqman (2012): Ion exchange technology I: Theory and materials)

As seen in Fig. 7, the tetrahedra's centre atom, T (Al or Si), is joined in the corner with four oxygen atoms. To represent the tetrahedron, the phrase TO_4 is commonly used. In contrast to the flexible T-O-T connection, the O-T-O angle for a structurally ideal tetrahedron is rigid and usually has a value of about 109.28' and rarely changes. The flexibility of the T-O-T angle, which is the degree of freedom that allows acceptable thermodynamic creation of diverse frameworks, is critical for producing many distinct zeolite frameworks. The bond length of [AlO_4] tetrahedra d(Al-O) and [SiO_4] tetrahedra d(Si-O) are ~ 1.73 Å and ~ 1.59–1.64 Å, respectively [58].

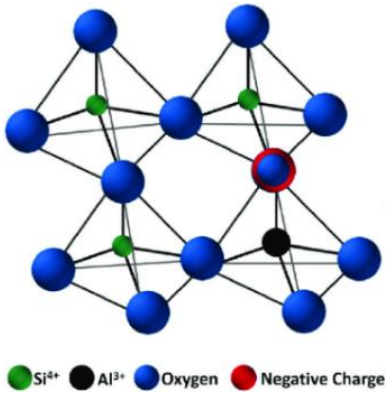

Figure 7. The structure of the zeolite framework consists of tetrahedrals with a Si/Al substitution linked by corner shard oxygens [59].
(Taken from: Sudarsanam, Putla, et al. (2019): Advances in porous and nanoscale catalysts for viable biomass conversion)

2.2.2.2. Secondary building units

The polyhedral loops that are produced by sharing O atoms and joined in a variety of ways are called secondary building units (SBU). These SBUs are connected to form various zeolite skeletal structures through further connections. Fig. 8 depicts a number of common SBUs. Loops constructed from 6, 8, 10, 12, and 14 oxygen atoms are joined to produce cavities and pores with diameters ranging from 3 to 10 Å in the zeolite structure [60]. The extra-framework cations' location, size, and coordination influence the size of the channels. The structural features of natural zeolites are summarized in Table 1, and the structures of commonly utilized kinds of natural zeolites are depicted in Fig. 9.

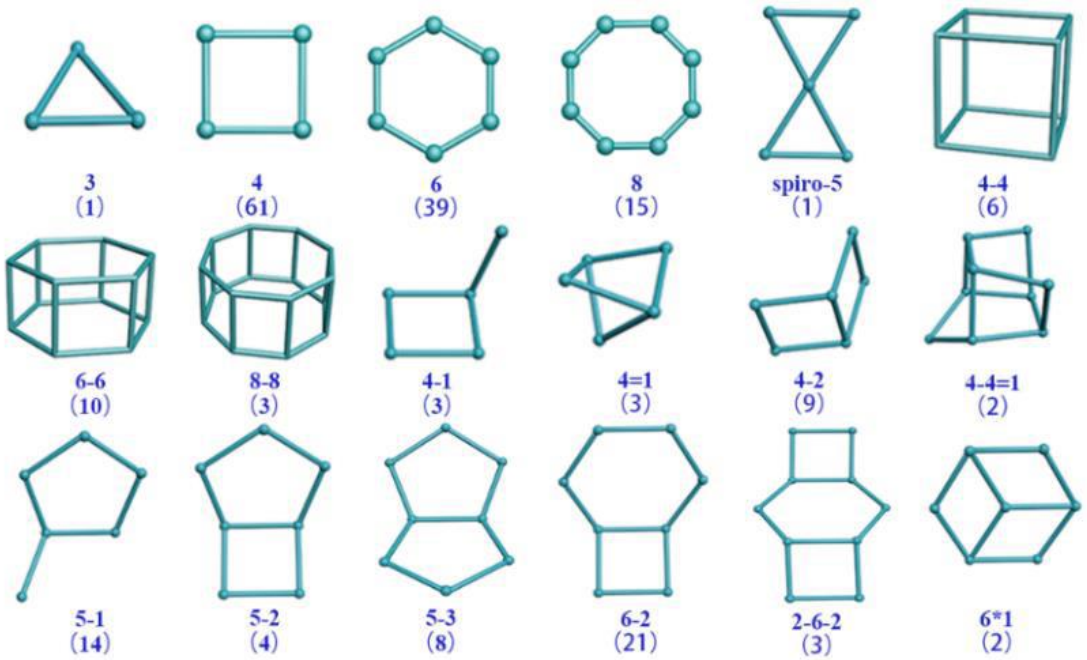

Figure 8. Secondary building units (SBU) in zeolites (the balls indicate T atoms of TO_4 tetrahedra; the oxygen atoms have been hidden for clarity; the numbers in parenthesis show the frequency of occurrence) [61].

(Taken from: Ren, Xiaoyu, et al. (2020): Synthesis of zeolites from coal fly ash for the removal of harmful gaseous pollutants: A review)

Table 1. The structural features of typical natural zeolite types [62].

Types of natural zeolite	Chemical formula	SBU	Channels (Å)	Si/Al ratio
Clinoptilolite	$(Na,K,Ca)_6(Si,Al)_{36}O_{72}\cdot 20H_2O$	4-4-1	3.6×4.6 3.1×7.5	6
Heulandite	$(Ca,Na)_{2\text{-}3}\ Al_3(Al,Si)_2Si_{13}O_{36}\cdot 12H_2O$	4-4=1	2.6 x 4.7	6.4
Mordenite	$(Ca,Na_2,K_2)Al_2Si_{10}O_{24}\cdot 7H_2O$	5-1	6.5×7 2.6×5.7	5.5
Chabazite	$CaAl_2Si_4O_{12}\cdot 6H_2O$	6-6 or 6 or 4-2 or 4	3.8×3.8	1.0-4

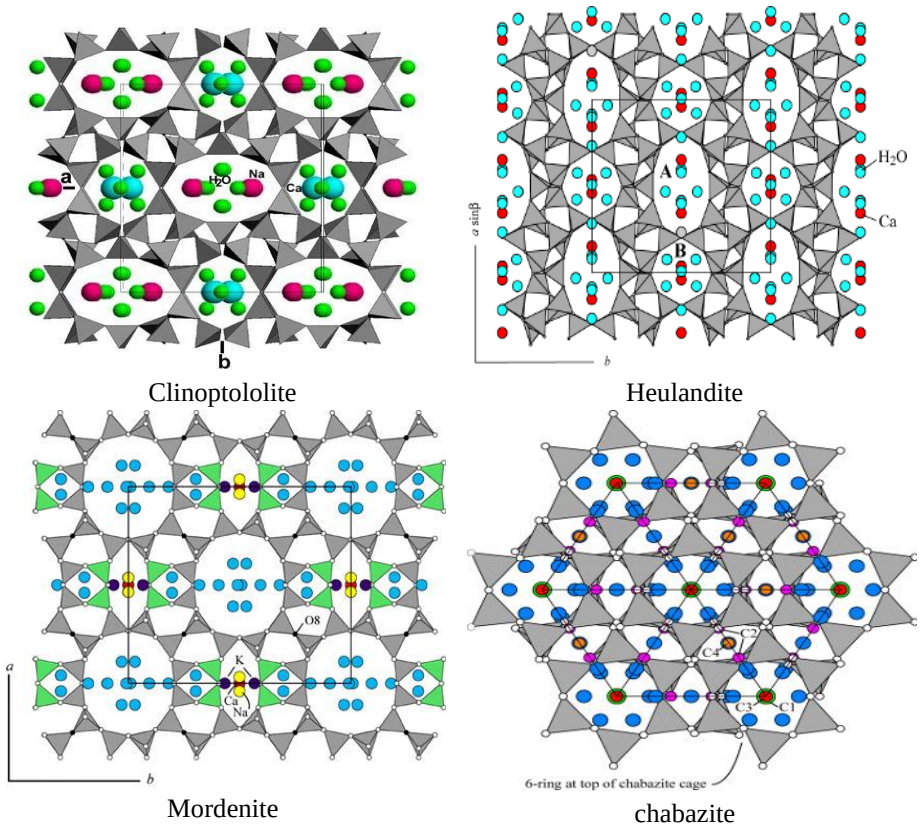

Figure 9. Structures of the most abundant natural zeolites [62].
(Taken from: Tran, Yen Thi, et al. (2019): Natural zeolite and its application in concrete composite production)

The existence of pores, cages, and cavities within a molecular dimension is a unique structural property of zeolite; hence it is critical to define these concepts. The quantity of T-atoms per 1000 $Å^3$ is known as framework density, and zeolites have the highest framework density of 19–21 (T-atoms per 1000^3) [63]. Cages are formed when the SBU apertures are less than six rings and are connected by pore openings; cages are small to pass molecules bigger than H_2O. Cavities are polyhedra with at least one side greater than a six-ring. When pores are bigger than six rings, channels are created, which are expanded and wide enough to allow access to the guest molecules [64].

2.2.3. Zeolites' physical and chemical characteristics

The Si/Al ratio is an important characteristic of zeolites. The charge imbalance due to the presence of aluminium in the zeolite framework determines the ion-exchange characteristics of zeolites and is expected to induce potential acidic sites. The cation concentration is inversely related to the Si/Al ratio, while thermal stability is directly proportional. When the ratio rises, the surface selectivity shifts from hydrophilic to hydrophobic. Silicalite molecular sieves possess a neutral structure with hydrophobic nature and lack ion-exchange or catalytic characteristics [65]. The hydrophobic characteristic of high silica zeolites is caused by the existence of ≡Si−O−Si≡ linkages, which lower the zeolitic surface's attraction to water.
Based on Si to Al atoms' ratio, zeolites can be categorized into four different types, as shown in Table 2. [65]. Many kinds of zeolites have various heat stability; strongly siliceous zeolites possess excellent thermal stability and are resistant to decomposition at temperatures of

approximately 1300 °C, whereas low Si/Al ratio zeolites melt at temperatures around 700 °C. High Si/Al zeolites have good stability in heated acidic solutions but poor stability in alkaline solutions, whereas low Si/Al zeolites have poor stability in low pH solutions. Due to the fact that aluminium is leached from tetrahedral frameworks, zeolite structures disintegrate at low pH [66].

Table 2. Types of zeolite [64].

Composition	Example
"Low" Si/Al zeolites (1-1.5)	Zeolites A and X.
"Intermediate" Si/Al zeolites (~2-5)	A) Natural zeolites: Mordenite, Clinoptilolite, Erionite. B) Synthetic zeolites: L, Y, Omega, large pore Mordenite.
"High" Si/Al (~10-100)	A) By thermochemical framework modification. B) By direct synthesis: beta.
Silica molecular sieves (=100)	Silicalite.

Zeolites are among the most powerful cation exchangers, with a cation interchange capability of two to three times that of other soil minerals. Because of their microporous structures' capacity to adsorb molecules at low pressure, zeolites are promising adsorbents [67]. Because of the different nature of diverse zeolite cage architectures, inherent structural flaws, bound ions, and their related minerals, zeolites have a broad range of cation-exchange capabilities. In summary, due to fixed pore widths and active sites in the crystalline structure, zeolites are natural materials that may exchange ions, capture gases and vapours, operate as molecular sieves, and catalyze processes [65].

2.2.4. Classification of natural zeolites

Natural zeolites are well-known microporous materials of volcanic origin. They form under variable geochemical conditions by the alternation of volcanic glass. They can be found in crystalline states in igneous and metamorphic rocks and sedimentary rock grains of lower dimensions [68]. The annual global production of natural zeolite is estimated to be around 3 million metric tons, and the reserves are anticipated to be significant [69]. Natural zeolite can be classified into two categories: (2.2.4.1 and 2.2.4.2.).

2.2.4.1. Zeolite-rich rocks

In nature, porous pyroclastic rocks with high amounts of volcanic glass frequently convert into zeolite-rich rocks. The type and amount of the zeolite-rich rocks produced depend upon many factors, including pH, temperature, pressure cation concentrations, hydrological system, and geological environment [70]. Zeolite-rich rocks normally contain a large percentage of zeolite together with quartz and feldspar. They have many exciting properties like high ion exchange capacity, large specific surface area, and porous structure. These make them popular candidates for different applications such as ion exchangers, sorbents, and catalysts [71-73]. Tuffs rich in heulandite/clinoptilolite are economically appealing due to their low prices and wide range of applications in agriculture, commerce, and the environment [74].

2.2.4.2. Zeolite-poor rocks

Zeolite-poor rocks are naturally-occurring rocks. They generally have a low zeolite content (less than 10%), besides other minerals like calcite, cristobalite, quartz, montmorillonite, and sometimes feldspar [75]. Their low amount of zeolite limited their advanced capabilities. However, zeolite-poor rocks are good construction materials because of their good mechanical behaviour, excellent porosity, and lightweight. They could be utilized to make porous structural materials with improved thermal insulation characteristics [76,77].

2.2.5. The constituents of zeolite-poor rocks (Tokaj)

Zeolite-poor rocks (Tokaj) contain many minerals, including clinoptilolite, silica and montmorillonite.

2.2.5.1. Clinoptilolite

Clinoptilolite minerals are considered the most abundant zeolites in nature. They have been found in many areas worldwide, for example, Hungary, Italy, Romania, Slovakia, Slovenia, Turkey, and many other countries around the world; clinoptilolite is a silica-rich mineral that belongs to the heulandite zeolite family. The empirical formula of clinoptilolite is $(K,Na)_6[(AlO_2)6(SiO_2)_{30}].24H_2O$. Clinoptilolite structure contains eight-membered rings channels and ten-membered rings channels pore system. They have four cation positions in their hydrated structure; two are found in the main channels (Fig. 10). Clinoptilolite unit cells are monoclinic and have pore diameters varied between 4.5 and 6 Å. The Si/Al ratio of clinoptilolite may vary from 4.0 to 5.3. The characteristic of clinoptilolites differs according to the environment and the place of the deposits.

Clinoptilolite offers a unique structure and fascinating properties. These outstanding characteristics make clinoptilolite a potential candidate for many applications, such as water purification, cleaning of radioactive wastes, biomedical applications, catalysis for many reactions, and building materials.

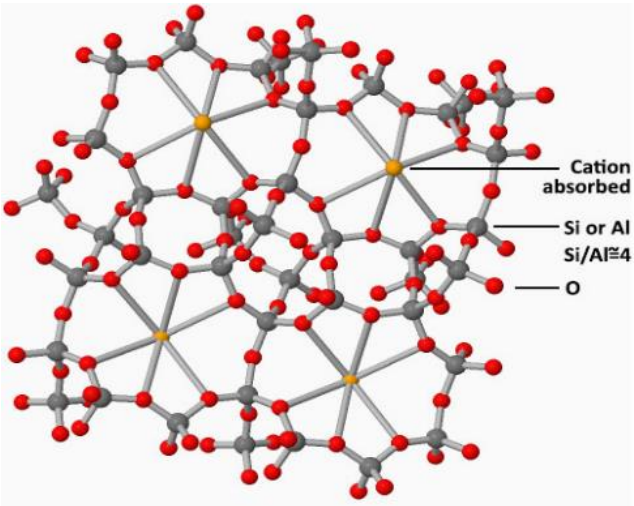

Figure 10. The framework of the natural clinoptilolite [78].
(Taken from: Raja, VK Bupesh, et al. (2021): Geopolymer green technology)

2.2.5.2. Silica

Crystalline silica is a tectosilicate mineral with a highly ordered framework pattern; the crystalline structure of silicon dioxide is formed by the arrangement of oxygen and silicon atoms in a pattern that is repeated infinitely in three dimensions. The most abundant polymorph of silica found in nature is quartz. There are two types of quartz: alpha (low temperature) and beta (high temperature). The most common type of quartz is alpha quartz, which may be found in numerous rocks and soils worldwide. The fact that quartz is one of the most abundant minerals in soils reflects its chemical stability and weathering resilience. Tridymite and cristobalite are two further crystalline silica types commonly associated with high-temperature rocks, such as volcanic rocks (Fig. 11) [79]. Upon heating, silica undergoes several phase transformations accompanied by volume change, as shown below [80].

$$\alpha\text{-quartz} \xrightarrow{573\ ^\circ C} \beta\text{-quartz} \xrightarrow{870\ ^\circ C} \beta\text{-tridymite} \xrightarrow{1470\ ^\circ C} \beta\text{-cristobalite} \xrightarrow{1710\ ^\circ C} \text{liquid}$$

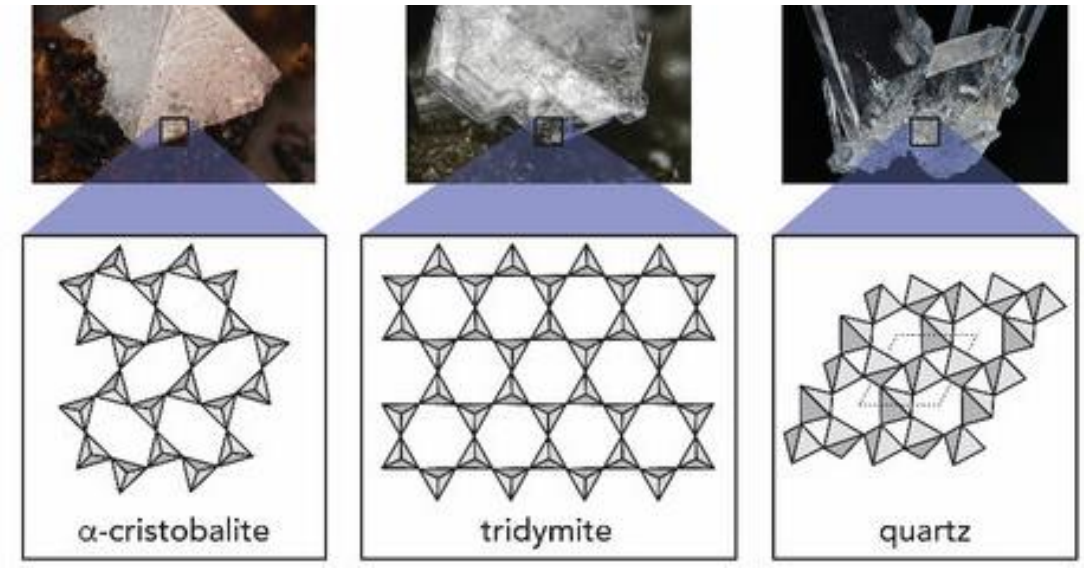

Figure 11. Illustrations of various polymorphs of crystalline SiO_2 (cristobalite, tridymite, and quartz) [81].

(Taken from: Moura, Hipassia M., and Miriam M. Unterlass: (2020): Biogenic Metal Oxides)

2.2.5.3. Montmorillonite

The structure of montmorillonite particles is composed of sheets and layers (Fig. 12). There are two types kinds of sheets in every layer: octahedral and tetrahedral. The sheet is made up of silicon-oxygen tetrahedra that are joined together by three shared corners, forming a hexagonal network. Each tetrahedron's remaining fourth corner connects to a neighbouring octahedral sheet. Aluminium or magnesium, in 6-fold coordination with oxygen from the tetrahedral layer and with hydroxyl, make up the octahedral sheet. Together, the two sheets create a layer. Interlayer cations, electrostatic force, hydrogen bonding, and Van der Waals force can all be used to link layers in a clay crystallite [82]. Montmorillonite has the chemical formula of $(Na,Ca)_{0.33}(Al,Mg)_2(Si_4O_{10})(OH)_2 \cdot nH_2O$.

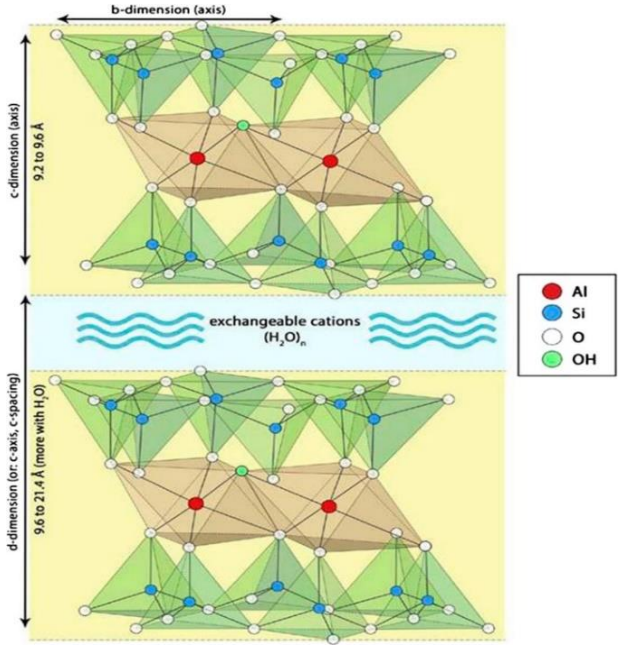

Figure 12. Crystal structure of montmorillonite
(Taken from: Sachs-Barrable, K., Darlington, J. W., & Wasan, K. M. (2014). The effect of two novel cholesterol-lowering agents)

2.2.6. Use of zeolitic tuff in the building industry

Despite several research investigations on zeolite-poor rocks, very little research has been done to assess zeolite-poor rocks as raw materials for construction applications. Samardzioska et al. studied the stability of natural zeolite bricks under different laboratory conditions. Kazantseva et al. [42] investigated the usage of zeolite-poor rocks as primary raw materials to prepare porous ceramics. Tanijaya et al. [83] also examined the potential application of natural zeolite as an additive for concrete production. It's worth noting that zeolite-poor rocks are very cheap and are widely distributed. It can also be a waste product from the separation during screening procedures for manufacturing granulated zeolite-rich rock in quarries. Zeolite-poor rocks can be used together with organic wastes to produce new porous ceramic materials.

2.3. Organic wastes

Waste materials are widely used as additives in bricks and glass-ceramic foam manufacturers to generate a product with adequate physicomechanical characteristics. The additives are chosen based on the required properties. It is preferable to use lightweight ceramics specimens with acceptable compressive strength and minimal water absorption. Incorporating organic or inorganic pore-forming agents into these materials is one technique to boost capacity [84-86]. Organic pore-forming agents are often less expensive than inorganic ones.
Moreover, they also provide a heat contribution to the sintering and reduce the amount of fuel required for firing. Therefore, they are more favourable than inorganic pore formers. A broad range of waste materials has been investigated for use in the preparation of both clay bricks and foams, including fly ash, rice husk waste, agricultural wastes, eggshell, and sawdust [40],

etc. In this research work, sawdust and eggshell are used as pore-forming agents in the development of new porous bricks and foams based on zeolite-poor rocks.

2.3.1. Sawdust

Sawdust is one of the common organic wastes consisting of tiny pieces of discontinuous chips of wood. It is produced when the wood is chopped, sawed, ground, drilled, sanded, or otherwise pulverized. Noting how many trees are cut down annually (in European Union alone, more than 400 million m^3 since 2000), which are used for sawn wood, fuel, veneers, pulp, and paper, it's easy to imagine the enormous amounts of sawdust produced during cutting. Based on the species of wood being cut, the grain size, colour, and texture of the sawdust might vary widely [87].

Sawdust usually consists of cellulose (48%), hemicel1ulose (19%), lignin (24%), extractive (7.5%), ash (1.6%) and moisture (33%). The amount of these constituents vary from one plant species to another [88]. The cellulose consists of straight-chain macromolecules; it is crystalline and normally incorporated in a matrix of hemicellulose and lignin [89]. Cellulose is the major constituent of biomass. In contrast, hemicellulose has an amorphous structure with a low degree of polymerization. Lignin is a phenolic compound consisting of a randomly connected amorphous structure that has high molecular weight. Therefore, the firing of these constituents takes place through a series of complex processes [90]. This process can be observed in the thermogravimetry of biomass.

Sawdust can contaminate both soil and water. It generally keeps a high moisture content enabling the growth of several kinds of fungus, which subsequently spread to neighbouring plants causing them to decompose [91]. Therefore, recycling sawdust could be the best alternative to avoid this environmental problem. Only a limited proportion of sawdust is reused in the fabrication of the cleaning of wet floors, chipboard panels, and, lately, in the creation of fuel pellets. The usage of sawdust as a pore-forming agent is a promising and cost-effective alternative for sustainable development while saving energy and reducing pollution and deterioration of the environment.

2.3.2. Eggshell

Many eggshells are dumped as waste from the food industries, causing environmental issues that lead to health risks, pollution, and environmental harm due to incorrect disposal. On average, a chicken eggshell weighs 5–6 g and involves 85–95% calcium carbonate ($CaCO_3$), which makes up the majority of eggshells together with 1.4% magnesium, carbon, and other elements in trace amounts [92]. Eggshell wastes are composed of two basic components: calcified eggshell and protein-rich shell membrane [93]. Calcite ($CaCO_3$) which is the main component in eggshells, can be employed in a variety of applications, including pharmaceuticals, paints, plastics, fertilizers, and construction applications [94,95]. However, the inappropriate disposal of eggshell wastes has become a source of worry for food industries [96]. Despite the promising application of eggshell in building materials, very few studies have been reported on the use of eggshell in ceramic bricks and foams making [97]. Incorporating eggshell into the fired-brick and ceramic foams-making process will help conserve clay resources while also ensuring the proper disposal of these wastes.

2.4. Fired-clay bricks

2.4.1. History and development of brick manufacturing

For thousands of years, man has utilized brick for construction. Fired bricks are one of the earliest known building materials; they are one of the most durable and long-lasting construction materials [98]. The oldest bricks discovered date back to about 7000 BC. They were discovered near the ancient city of Jericho (Fig. 13), in the southern part of present Turkey [99]. Mud bricks hardened by sun-drying in the open air were the earliest bricks created by mankind.

Archaeological excavations in the Middle East and the Persian Gulf have found bricks dating back to 7000 and 3500 BC. In Pakistan and other parts of South Asia, homes made from air-dried adobe bricks have also been discovered [100].

Clay and straw were used to make ancient Egyptian bricks, making them the first known example of lightweight brick. Today, the remains of Harappa Buhen and Mohenjo-daro bear witness to this. Egyptians are seen mixing, firing, and hauling clay for the sun-dried bricks in paintings on the tomb walls of Thebes [101].

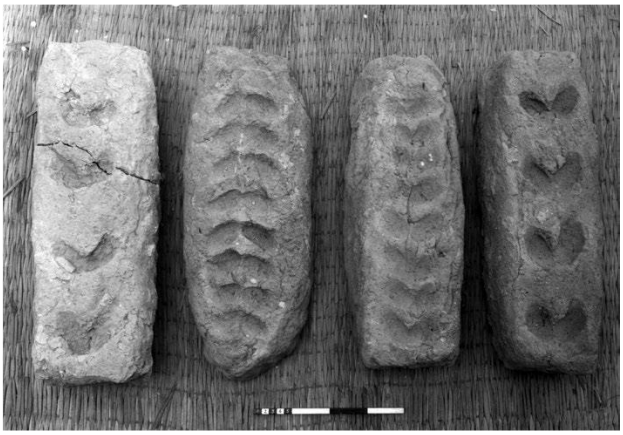

Figure 13. Mud brick from Jericho [102].
(Taken from: Ripepi, Gaia, (2020): Mudbricks and Modular Architecture at Tell es-Sultan from the Neolithic to the Bronze Age." Digging Up Jericho: Past, Present and Future)

The creation of burned brick around 3,500 B.C. was the most significant breakthrough. Bricks could now be manufactured without the use of sunlight, and they quickly became popular in colder climes. Bricks were exclusively made out of red clay. Thanks to the development of mobile kilns, the Romans were able to expand brick manufacture across the nation and later throughout the empire [103]. Roman bricks were more typically circular, rectangular, triangular, and oblong in shape and size than other previous bricks. The Romans were responsible for many of Europe's earliest brick structures, including the Herculaneum gate at Pompeii and Caracalla's baths in Rome [104,105]. The Romans extended the skill production of brick across the Roman Empire, and it was completely favoured during the medieval and Renaissance periods. Brick manufacture declined along with the Roman Empire. It mostly returned to Italy and the Byzantine empire and then moved from these areas to France in the 11th century. Bricks were imported to northern Germany from northern parts of Italy in the 12th

century. The brick Gothic style arose in Germany and various Scandinavian and Baltic regions, with structures made primarily of burned red clay bricks.
Until around 1885, bricks were produced manually. The introduction of brickmaking machines coincided with the beginning of the Industrial Era. As a result, the number of clays that might be used to make bricks grew dramatically, affecting manufacturing capacity [106]. By 1925, brick-making machines could produce up to 12,000 bricks a day, compared to 36,000 bricks per week by hand. Apart from wood, bricks currently appear to be the most often utilized construction material. As a result, brick and terracotta architecture dominates its sector, with the brick industry growing rapidly. Moreover, the development of energy-saving kilns greatly contributes to brick production advancement [107].
Although the 19th century saw significant advancements in the manufacturing of bricks, there was still a big production problem that lasted for a long time and hindered even more productivity. This question was about how to speed up the drying process of bricks so that they could be made and fired at the same rate. Pre-firing operations had previously depended on the bricks being dried outside, which was susceptible to the changeable weather of the brickyards. Later, many dryer types were invented and introduced to overcome this problem [108].

2.4.2. Composition of clay

Clay is the most common raw material used for brick making. Long-term chemical weathering of silicate-rich rocks is the most predominant process for the formation of clays [109]. Clays are chemically stable materials because of the long-term effects of erosion, rock decomposition, and alluvial deposition. Clays are made up of aluminosilicate, free silica, and a low fraction of the initial rock that has been decomposed. These rock particles make the clay burn into bricks of different colours and looks. The most significant features of clays are that they become plastic when combined with water and harden when heat-treated, which removes the water. This makes them ideal for making bricks [110]. Clays normally consist of silica as a major constituent together with alumina and some other oxide as minor components, such as iron oxide, magnesium oxide, calcium oxide, etc. Common clays are made up of different clay minerals (kaolinite, montmorillonite, illite, and chlorite).

2.4.3. Types of bricks

In addition to construction, bricks may be used for a variety of applications, such as facing, floors and pavement. Depending on their appearance and qualities, bricks may be categorized into different grades, as shown in Fig. 14 [111].

- Common bricks
- Facing bricks
- Engineering bricks

The name "common bricks" comes from the fact that they are manufactured all over the globe. Common bricks were simply composed of clay and were not created to a precise level; many of those from the same furnace may have a variety of colours and textures. Burning certain clays results in a reddish colour, while others burn to a variety of colours and shades, making brick matching a bit more challenging. However, now ordinary bricks are manufactured to

fulfil precise size, compressive strength, thermal conductivity, and cold weather resistance criteria. But, since the 1970s, the rising need and popularity of lightweight bricks have had an impact on the market for conventional bricks [112].

Facing bricks are meant to be seen from the outside, carefully designed to give a beautiful look without the need for plaster or other surface treatments on the wall. The bricks are often utilized for their aesthetic value, as well as their strength and resistance to environmental conditions. In addition, they must also be weather-resistant since they are typically utilized on the building's outside walls. The sand facing and/or pigments used in the burning process give this kind of brick a smooth surface that is free of surface fractures.

Engineering bricks can survive harsher environments, like being wet or frozen all the time. Engineering bricks are often designated as Class A or Class B based on the required strength and water absorption of the brick. They have a smooth finish and holes that go from the top to the bottom. These holes can be used to pour in a mortar or to add more steel bars for extra strength. Engineering bricks got their name because they were used in different engineering projects like building bridges, tunnels, and accessways.

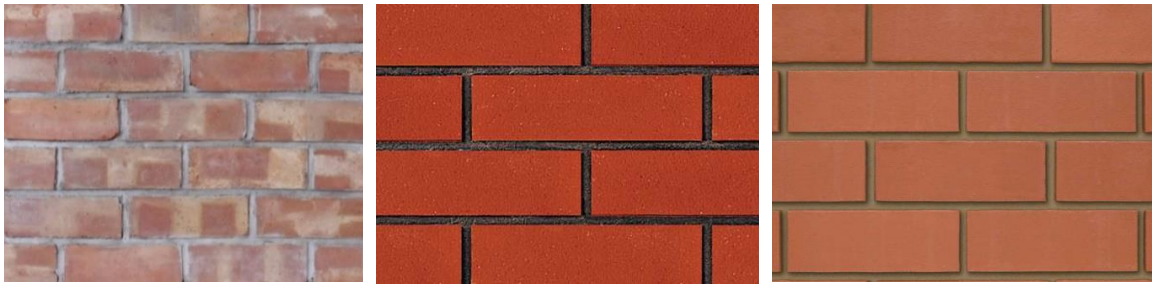

Common brick | Facing bricks | Engineering bricks

Figure 14. Types of bricks

2.4.4. Manufacturing of fired-clay bricks

It's worth looking at the stages that bricks go through before they become a final product (Fig. 15). The production of building bricks normally requires appropriate control of the processing steps, which include firstly, preparation of the raw materials; in this process, extraction of clay is the initial step, followed by crushing, mixing, and proportioning. Usually, there are many storages from different clay sources. The clays can be mixed together to produce more homogeneous mixtures. This can help in controlling colour, texture, and other technical properties.

Secondly: shaping begins with the preparation of uniform plastic material that is capable of moulding. Plastic clay is formed by adding water and chemicals at this stage in a chamber that has one or more rotating shafts with blades. Based on the shaping procedure, moulded green brick may include anywhere from 5–30% moisture. Several fabrication methods could be utilized to produce ceramics materials, for example, mechanical compaction (dry and semi-dry pressing), extrusion, injection moulding, and various other forming processes [113]. Clay is extruded by being forced through a mould. Once the column has passed through the automatic cutter, the formed brick is ready to be assembled. The distance between cutter wires and the size of the moulds must be precisely calculated to account for shrinkage during the wet stages

of drying and firing. The dry pressing process is especially adaptable for clays with extremely low plasticity. Among these forming techniques, extrusion is a highly used method. However, powder compaction could be a cost-effective method due to its higher production output of ceramic specimens in a relatively short time [114].

The next step is drying, which is done prior to sintering; it provides the required strength for the brick to be handled and stacked for firing without distortion. Drying takes place in chambers using hot flue gas from a neighbouring kiln. The fast dryers can dry a formed brick in only three hours. Based on the dryer's configuration and the kind of brick to be dried, chamber dryers may take about 18 to 45 hours to dry. As the brick is extruded, the moisture content reduces to a value between 1–5%. Using furnace cars, modern factories place the dried bricks back into a fire set before transferring them to the kiln for firing. If furnaces are utilized on a regular basis, the drying unit may need a manual transfer [108]. Heat treatment and cooling are important processes in making bricks. At the end of drying, the sintering process starts. The firing process involves three steps, around 100 °C, free water could evaporate, then at 400 °C, the crystalline water and organic materials are burned out; then sintering, accompanied by volume shrinkage of the samples, occurs in the last step of burning, between 900 °C and 1200 °C [115]. Throughout the last stage of sintering, many phase transformations and physicochemical reactions will take place, which to a large extent, govern the final properties of the produced samples by forming new compounds that will affect the stability of the final ceramic products due to the volume change. The durability and strength of the products are highly connected to the microstructure and composition. Tite and Maniatis [116] have demonstrated that vitrification of ceramic specimens during high-temperature sintering plays a crucial role in the quality and the final characteristics of the produced ceramic products, for instance, porosity, density, shrinkage, strength, and thermal conductivity.

Finally, all of the bricks are sorted and classified at the completion of the firing step, unloaded, packed, and sent to storage for further processing before being shipped out to customers. The removal of bricks from the furnace is normally done by hand, although packing is mostly done by machines.

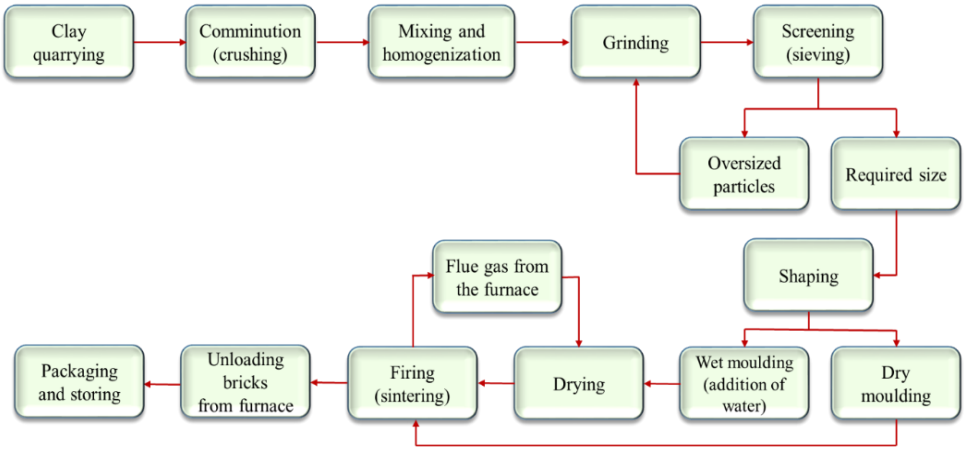

Figure 15. Primary steps in brick making

2.4.5. Production of bricks

Bricks are a key building material that is widely utilized all over the world. With anticipated annual manufacturing of 1500 billion bricks across the world, Asia alone produces over 87%; China ranked the first in global brick making with more than two-thirds of world brick manufacturing. With over 144,000 brick kilns running in the country, India is the world's second-largest brick manufacturer (Fig. 16), with an expected annual production of 250 billion bricks [117]. The demand for building bricks is expected to increase highly due to the expected increase in population and urbanization; therefore, the production of innovative building bricks from new materials (basic raw materials and additives) has drawn a huge interest lately, focusing on issues of sustainability.

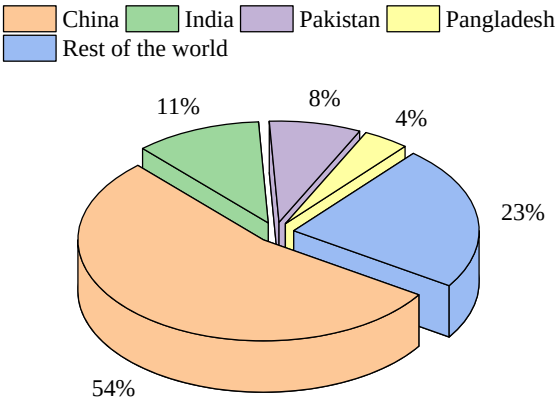

Figure 16. Global brick making [118].
(Taken from: Jain SA. (2016): Development of unfired bricks using industrial waste)

2.4.6. Additive to clay bricks

Additives are highly used by researchers or engineers in brick manufacture to generate a product with desired properties and can be classified into two

2.4.6.1. Inert materials

Upon mixing with water, clay normally has high plasticity, which presents several industrial challenges, including a slow drying rate and higher volume shrinkage after drying. To overcome these problems, an inert (non-plastic) material could be used. Inert materials could also prevent the occurrence of the 'black heart' phenomenon inside the burnt clay bricks since they remain inert even at high temperatures. Normally sand and chamotte are used as inert materials [119].

2.4.6.2. Pore-forming agents

Pore-forming compounds can be added to clay bricks in order to increase their capability. Moreover, they help to speed up the sintering process and save on the quantity of fuel used in the furnace. Micropores are formed during the sintering process, while residues from the pore-forming compounds are mixed with the glassy phase. The formation of micropores could reduce thermal conductivity and enhance thermal insulation of the produced bricks. Recycling

waste is strongly recommended to save resources and minimize emissions in light of environmental concerns and the need for environmental sustainability [120]. The utilization of a wide variety of waste materials in the production of clay bricks is a well-known process.

2.4.7. Composition of burnt clay bricks

Upon the firing of the clay green bodies, many complex processes occur, such as fusion accompanied by vitrification which normally occurs above 900 °C and leads to the formation of an amorphous glassy phase. The creation of the glassy phase is crucial for the technical characteristics of the produced bricks; moreover, some chemical reactions could take place and lead to the formation of new aluminosilicate phases, and some unfired components (silica, other residues) may also exist depending on the firing temperature. Fig 17 is an SEM picture of the solid phase of burnt clay bricks, which clearly shows the glassy nature of fired clay [99].

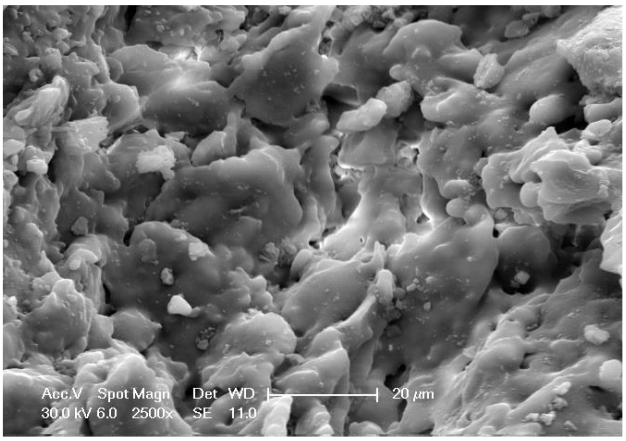

Figure 17. SEM photograph of clay-incorporated treated wastewater sludge [99].
(Taken from: Mohajerani, Abbas, et al. (2019): A proposal for recycling the world's unused stockpiles of treated wastewater sludge (biosolids) in fired-clay bricks)

The mineralogical composition of the burned clay brick done using XRD is shown in Fig. 18. The XRD diffractogram of the fired clay incorporated glass waste composite brick is depicted in Fig. 19. According to both figures, fired clay brick is mostly made up of quartz feldspar, a considerable amount of amorphous glassy phase, and a small number of other minerals, despite that their source components are derived from many types of clay minerals. This amorphous glassy phase makes up the bulk of the fired bricks. At an elevated firing temperature, the amount of the amorphous phase can rise. Even after the incorporation of the different additives, the basic constituents of the hybrid clay bricks are still quartz with some other phases (hematite, anorthite).

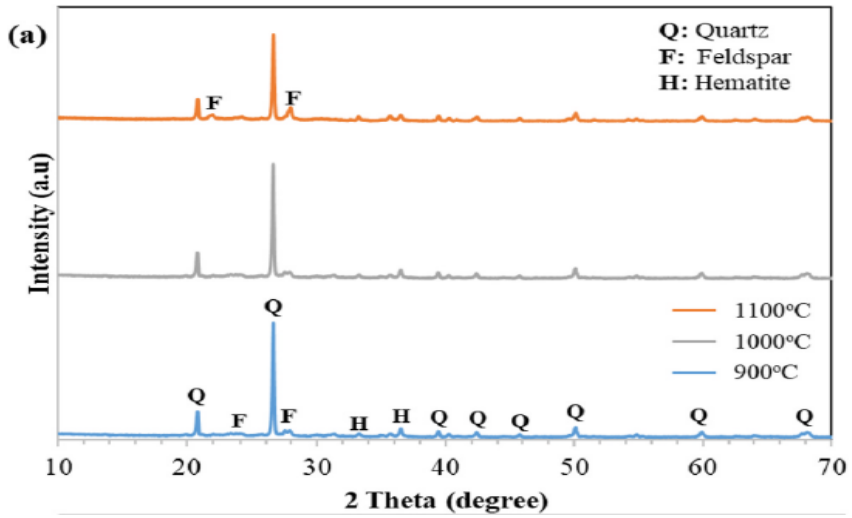

Figure 18. XRD diffractogram of fired clay brick [121].
(Taken from: Yaras, Ali, et al. (2021): Recycling and immobilization of zinc extraction residue in clay-based brick manufacturing)

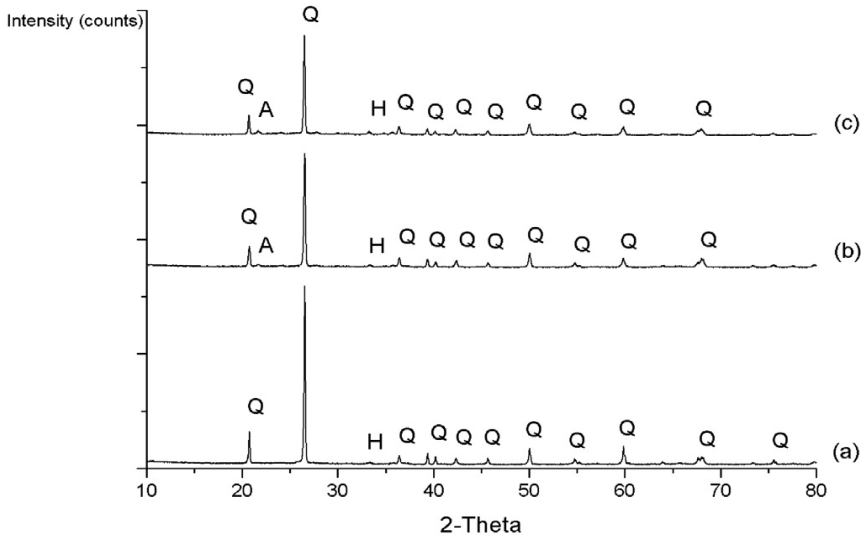

Figure 19. XRD spectra of clay brick burnt at 1000 °C (a) 0% waste glass, (b) 5% waste glass, and (c) 10% waste glass (Q = Quartz, A= Anorthite, H = Hematite) [122].
(Taken from: Phonphuak, Nonthaphong, et al., (2016): Utilization of waste glass to enhance physico–mechanical properties of fired clay brick)

2.4.8. The topographical and microstructural features of burned clay bricks

The structure of the clay bricks normally consists of different grains of glassy phase, some crystalline phases, and micropores; the pore size and distribution could highly depend on the types of raw materials and additives, forming technique, and sintering temperature. Krakowiak et al. [123] studied the microstructure configuration of the clay bricks produced by extrusion, the microstructural properties of the samples are shown in Fig. 20. In this image, the micropores are clearly oriented in the same direction as the extrusion. They are roughly ellipsoid in shape, and the principal axis of the pores is aligned with the extruded path.

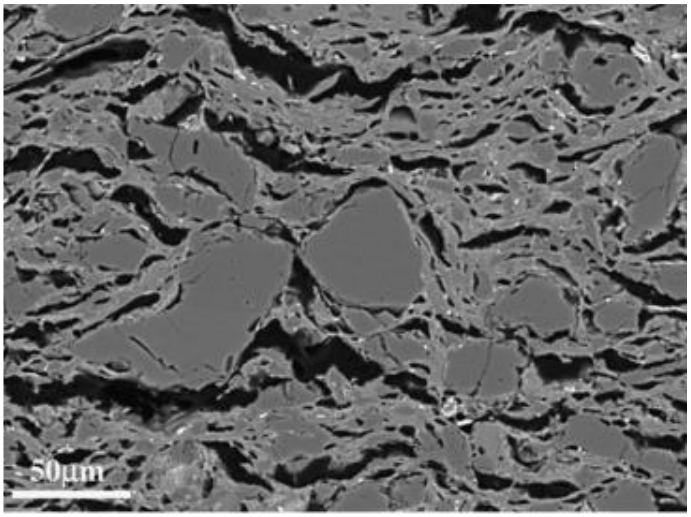

Figure 20. The morphology of burnt bricks created by extrusion [123].
(Taken from: Krakowiak, Konrad J., et al. (2011): Multitechnique investigation of extruded clay brick microstructure)

Yaras [124] studied the influence of paper mill sludge addition to the clay brick on the microstructural feature of the produced bricks; the SEM results (Fig.21) revealed the formation of an amorphous phase with many micropores distributed all along with the structure. The most important notice is that the addition of paper mill sludge resulted in the formation of a larger number of micropores since it burned out during the sintering. The formation of these pores could have a crucial effect on the produced bricks' technical properties.

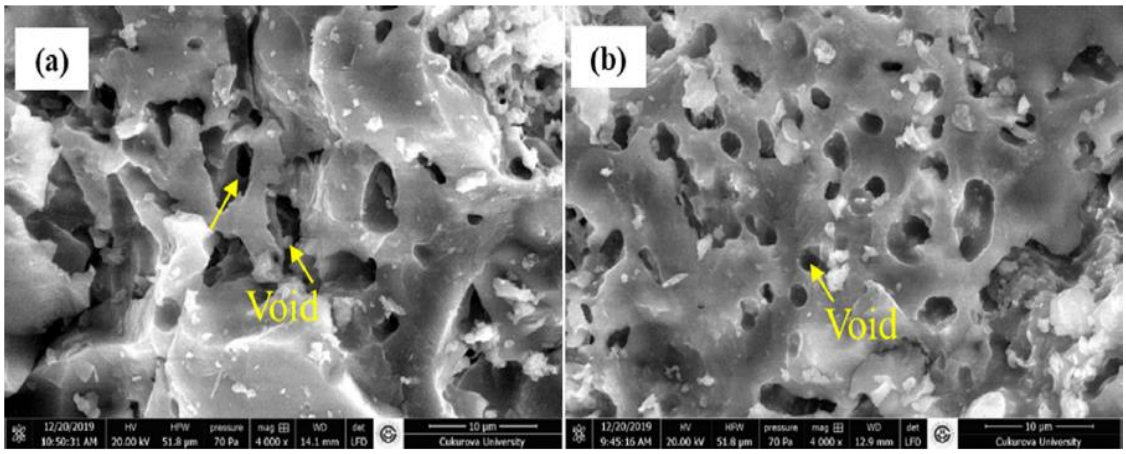

Figure 21. SEM micrograph of the fracture surface of the bricks fired at 1100 °C; a) reference brick, b) clay + 15% paper mill sludge brick [124].
(Taken from: Yaras, Ali (2020): Combined effects of paper mill sludge and carbonation sludge on characteristics of fired clay bricks)

2.4.9. The mechanical characteristics of fired clay bricks

Clay bricks' uniaxial compressive characteristic serves as the basis for understanding the bricks' strength, deformation and fracture. A ceramic's mechanical behaviour may be described using the notions of stress and strain (such as maximum strength and terminal deformation). Usually, ceramic microstructures aren't uniform, and the total mechanical behaviour is the product of

atomic-scale processes. When a solid is under stress, it will bend and if the stress exceeds its strength, it will fail [125].
Chen, et al. [126] conducted uniaxial compressive tests on burnt bricks and obtained the load-unload charts depicted in Fig. 22. The fired clay bricks are clearly brittle. The maximum peaks represent the fracture strength beyond which the failure takes place. Using the stress-strain curve, the mechanical characteristics such as deformation and fracture strength could be determined.

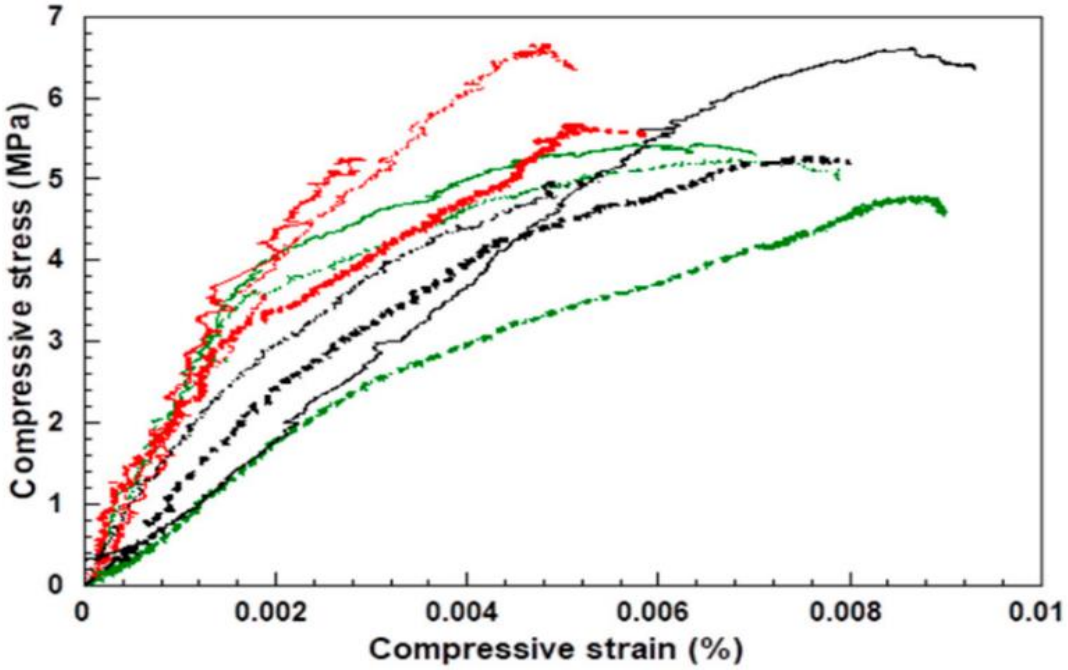

Figure 22. Compressive stress-strain curves [126].
(Taken from: Chen, Zhouyi, et al. (2021): Experimental study on the compressive behaviors of brick masonry strengthened with modified oyster shell ash mortar)

2.4.10. Previous studies on recycling waste materials in fired-clay bricks

Waste management is becoming an issue in many countries since untreated waste materials create critical environmental problems. Thus, the inclusion of waste materials in the brick preparation will reduce the massive use of clay resources and contribute to these wastes' safe disposal. Several research works have been reported regarding the inclusion of many waste materials into the clay to produce eco-friendly building bricks (Table. 3). A detailed review of the literature on the utilization of waste materials in the manufacturing of fired-clay bricks compared to this research work will be reported in this section. When comparing the findings of this study to those in Table. 3, it is worth noting that zeolite-poor rock incorporated sawdust and eggshell are promising materials for brick making, as their produced bricks have higher compressive strengths and better insulation properties than many of the studies listed in the literature.

Table 3. Previous studies on bricks incorporated waste materials

Main raw materials	Added waste	Replacement ratio (%)	Shaping method	Sintering temperature (°C)	Main technical properties					Ref.
					Density (g/cm^3)	Apparent porosity (%)	Water absorption (%)	Compressive strength (MPa)	Thermal conductivity (W/mK)	
Zeolite-poor rock	Sawdust	0, 2, 6, 4, 8, 10	Dry-pressing	950–1250	1.4–1.88	15.7–39.6	9.02–27.2	4.1–36.63	0.13–0.7	This work
Zeolite-poor rock	Eggshell	0, 5, 10, 15, 20	Dry-pressing	950–1150	1.45–1.76	26.7–42.0	13.12–28.8	10.3–25.3	0.2–0.68	This work
Clay	Sawdust	0, 2.5, 5, 10	Extrusion	900	1.56–1.8	30–33.4	16.65–21.4	13.60–15.5	–	[120]
Clay	Sawdust	0, 4, 8	Hand Molding	700, 850	1.4–2.1	–	7–23	5–11	–	[127]
Clay	Eggshell	0, 5, 10, 15, 20	Extrusion	800, 900, 1000, 1100	1.63–1.8	–	14.36–16.7	7.05–8.28	–	[97]
Clay	Eggshell	0, 5, 10, 15	Hand Molding	800, 900, 1000	1.5–2.1	14–22.5	11–16	1.2–4.8	–	[128]
Iron ore tailings, coal gangue, shale	Sewage sludge	0, 3, 6, 9, 12	Plastic Molding	950–1150	1.62–1.74	–	17.1–19.8	8.2–19.8	–	[84]
Earth material	Construction and demolition waste	0, 30, 50, 70, 100	Extrusion	800 and 1000	1.4–1.7	–	–	4.4–16.8	–	[129]
Reservoir sediments	Glass waste	0, 10, 20, 30	Semi-dry pressing	900–1050	2.21–2.24	–	12.9–14.5	35.2–48.2	–	[130]
Soil (laterite and alluvial)	Paper mill sludge	0, 5, 10, 15, 20	Hand Molding	850–900	–	–	13–31	1.5–33	–	[131]
Diatomite	Sugar filter mud	0, 10, 20, 30	Semi-dry pressing	700–900	1.02–1.37	45–50.4	48.82–58.7	10.05	–	[132]
Waste diatomite	Water purification sludge	0, 5, 10, 15, 20	Dry pressing	1000–1270	0.74–0.97	50–67	51–91	3–18	–	[133]
Diatomaceous earth	Nutshell ash	10, 20, 30	Dry pressing	–	0.85–1.85	5–61	–	3–23	0.22–0.75	[134]
Yellow river silt	Red mud	0, 10, 20, 30, 40, 50, 60, 70, 80, 90	Semi-dry pressing	1000–1100	–	–	15.1–28	36.7–41.4	–	[135]
Iron tailings	Fly ash	0, 5, 10, 15, 20	Dry pressing	900–1000	1.85–2.07	28–32.5	15.2–17.5	16–26	–	[136]
Clay	Municipal sewage sludge	35, 40, 45, 50	Semi-dry pressing	1050	0.22–0.29	–	6–13.8	8.5–12.5	0.25–0.23	[137]
Clay	Ferrochromium slag, Zeolite	0, 10, 20, 30	Semi-dry pressing	900	0.88–1.13	32.1–41.2	13.12–28.8	14.9–35.1	1.25–0.7	[23]
Clay	waste glass	0, 5, 10	Hand Molding	900, 950, 1000	1.65–1.76	29.7–35.1	16.1–25.9	–	–	[122]
Clay	Red mud	0, 10, 20, 30, 40, 50	Extrusion	860	1.81–2.04	14.2–22.5	–	0.5–22	–	[138]
Clay	Waste marble sludge	0, 10, 20, 30, 40	Hand Molding	1000, 1100	1.28–1.55	13–31.5	19–43	23.8–42.1	0.4–0.56	[139]
Soil	Water hyacinth	0, 5, 10, 15, 20	Hand Molding	850, 900	1.07–1.56	13–28	12.1–21.9	12.1–30	–	[140]
Clay	Bentonite	0, 5, 10, 15, 20	Semi-dry pressing	800, 1000	0.92–1.5	–	13.1–29.9	3.2–33	0.38–0.51	[141]
Clay	Paper pulp residues	0, 5, 10, 15, 20	Extrusion	900	1.22–1.72	27–34	18.1–24.9	4.65–10.4	0.65–0.78	[24]
Clay	Rice husk ash	0, 5, 10, 15	Semi-dry pressing	1050, 1075, 1100	1.21–1.52	36–44	20–39	2.7–7.6	0.18–0.247	[142]

2.5. Glass-ceramic foams

Compared to the other construction materials that provide thermal insulation, glass-ceramic foams are considered the most dependable eco-friendly materials. They compose of a widespread array of pores and is made up of vitreous (amorphous) phase together with crystalline phases [143]. Glass-ceramic foam is a heterogeneous system containing a mixture of gaseous and solid constituents; the solid phase is a glassy phase with micrometre-thick single-cell walls, while the gaseous phase fills the cells [144].

2.5.1. Historical background of glass-ceramic foams

Glass-ceramic foams manufacturing began in the 1930s when considerable research was performed worldwide. Due to the large number of patents issued within the same time period, it is unclear who pioneered the invention of glass foams. Kern [145] reported the development of glass-ceramic foam from the combination of finely powdered amorphous silica with a gasifier (wood and coal) through the chemical activation using NaOH solution or hydrochloric acid and firing at 1500 °C. In 1932, Kitaigorodski started mass-producing glass-ceramic foam using the technology developed at Mendeleev Institute of technology, in which glass powder and $CaCO_3$ as a foaming agent were heated in steel moulds to about 850 °C [146]. Saint-Gobain in France, Pittsburgh Plate Glass, and Corning Glass Works in the United States were among the first to do extensive studies on direct gas injection into molten glass. Using a combination of silica, borax, and zinc oxide, Long proved in 1934 that a cellular-like glass could be made by producing a glass containing a significant quantity of dissolved gases from the blend [147]. Glass foam was first documented in 1940 by Lytle [148], who detailed the process of making it in a column kiln by introducing carbon dioxide, steam, or air, either slowly or rapidly, into the glass melts. The foamed glass was put into moulds while still molten and transported by belt. In the years that followed, other patents were awarded for variations on the same basic idea [149], [150]. A study by Peyches [151] found that the heating of glass on the electrodes of Joule-heated glass melters led to the generation of gases, which could be further accelerated by the injection of gas straight through that surface. Because it was widely employed as flame retardant thermal insulation in the interior walls and roofs of ships and submarines during World War II, the creation, research, and manufacture of glass foam in the United States were highly accelerated [146].
Ford [152] describes the use of carbon black as a blowing agent for borosilicate glass; in the same patent, special attention was paid to the existence of oxygen-emitting agents like SO_3 in the glass composition or Fe_2O_3 and Sb_2O_3 as additives to the combination of glass powders and foaming agents.

2.5.2. Production of glass-ceramic foams

Glass-ceramic foams are normally produced by sintering a mixture of fine ceramic powder and gas-forming compounds in a temperature range of 800–1000 °C [153], after which the generated porous structure is cooled and annealed [154,155]. To obtain a sufficiently expanded material, three requirements must be met. Firstly, the raw materials must include compounds that decompose at high temperatures and generate gas. Secondly, the heat-treated raw materials

must create gas and a very viscous liquid phase capable of entrapping the gases. The emission of the gas increases the internal pressure, causing viscoelastic materials to foam [156]. Finally, upon cooling, the samples must form an outer glassy layer that is impermeable to water, resulting in a porous structure with excellent thermo-physical properties. The gas emission generated from the additives should be properly coordinated with viscous flow sintering and crystallization [157].

2.5.3. Properties and applications of glass-ceramic foams

In comparison to organic insulation materials like polymer foams which have short lives and are flammable, glass-ceramic foams have unique features, including lightweight, high thermal stability, excellent thermal and electrical insulation, fireproof, good corrosion resistance sound, and shock wave absorption [158,159]. Bioactivity and microbial resistivity are also features of certain glass-ceramic foams [160]. All these properties make them a material of choice for thermal and sound insulation of buildings (Table. 4). Catalytic supports, filters, and structural materials are among the other potential applications [161]. Porosity in these materials is generally greater than 60%, including open and closed pores. The pores morphology, pores size and pores distribution play a crucial role in determining the properties of the produced foam, such as thermal conductivity, density, water permeability, and compressive strength [162]. It is possible to manipulate the pore size and morphology by varying the heat treatment process (namely, the sintering temperature and residence time) and the amount of foaming agent used [163]. Open-pore structures and big pores have been found to reduce mechanical characteristics while increasing thermal conductivity owing to the convective heat transfer [156]. It's worth noting that foamed glass ceramic's thermal and mechanical characteristics are highly dependent on its density. The coefficient of thermal conductivity of the glass-ceramic foams varies from 0.06–0.2 W/mK.

Table 4. Properties of common glass-ceramic foams [166].

Density	0.1–0.3 g cm^{-3}
Porosity	85–95%
Crushing strength	0.4–6 MPa
Flexural strength	0.3–1 MPa
Flexural modulus of elasticity	0.6–1.5 GPa
Coefficient of thermal expansion	8.9 x 10^{-6} K^{-1}
Thermal conductivity	0.04–0.08 W m^{-1} K^{-1}
Specific heat	0.84 kJ kg^{-1} K^{-1}
Thermal diffusivity at 0 °C	(3.5–4.9) x 10^{-7} m^2 s^{-1}
Sound transmission loss at normal frequency	28 dB/100 mm

2.5.4. The main factors affecting the properties of glass-ceramic foams

2.5.4.1. The particle size of the ceramic material-foaming agent mixture

The particle size of the ceramic powder plays a crucial role in the pore size and distribution of the produced glass-ceramic foams. Normally, the fine powder results in glass-ceramic foam with smaller pores and homogeneous pore distribution. Generally speaking, the bigger pore sizes lead to lower thermal conductivity (better thermal insulation). On the other side, smaller pore sizes lead to a greater compressive strength of the glass-ceramic foam [164].

2.5.4.2. Heating parameters (heating rate, sintering temperature, and residence time)

Accurate control of the heating rate is essential for enhancing the quality of the glass-ceramic foam. Normally, large samples require a slow heating rate to ensure a consistent temperature distribution throughout the sample. In the case of fast heating, normally, large cracks can be obtained in the produced glass-ceramic foam. In most cases, heating rates of 5–10 °C min^{-1} are not a concern. A very weak heating rate, on the other hand, might result in unfavorable early gas formation before the sintering of the ceramic powder.

When it comes to the foaming process, the optimal sintering temperature is a critical factor. The mixture viscosity is a temperature-dependent factor; therefore, selecting the heating temperature must be based on the stability of foam, which is governed by viscosity, and the internal pores structure, which is defined by the consistent form and size of the cells as well as the smallest possible thickness of the dividing walls [165]. At high foaming temperatures, the molten powder's viscosity decreases. Therefore, the bubbles migrate to the top of the samples, making it harder to regulate the structure since the bubble dispersion is not homogeneous. In contrast, using a low heating temperature results in a high viscosity of the powder melt. This process hinders the gas expansion and leads to small volume growth; in this scenario, incomplete development of the dividing walls will take place, leading to high open porosity [166].

The residence time in the maximum heating temperature is crucial for the preparation of good quality glass-ceramic foam. At the optimal temperature and throughout the gas emission, the density gradually drops to a minimum. After this period, the foam gradually breaks and collapses due to pore agglomeration. The driving force for this process is to reduce the surface energy by reducing the specific surface area of the cell walls. Hence the density increase [167].

2.5.4.3. Foaming agent

During the foaming process, the foaming agents break down or react and generate gaseous products at temperatures above the glass softening temperature. There are two kinds of foaming agents: redox and neutralization agents. Carbon-containing materials are often used as redox foaming agents, such as sawdust, coffee waste, and silicon carbide. The oxidation reaction of the foaming component by gases dissolved in the glass melt causes a gas release in these materials. The second group often comprises alkali-carbonates, which break down when heated, releasing CO_2 gas [168]. The rapid gas emission during the pore formation breaches the walls of individual pores forming a maze-like structure of voids. This foam possesses superior sound-proof characteristics [169]. If the gas emission takes place at a temperature

below the glass softening temperature. The produced gases cannot be maintained by the mass since the glass particles are not yet sintered. On the other hand, if the gas creation occurs when the glass melt is overheated, in this case, the glass viscosity decreases, and the gas discharged from the melt leads to the collapse of the foams.
The viscosity and the optimal foaming temperature are very closely linked. When the chemical composition of the raw materials, notably the kind and quantity of foaming agent, is changed, the viscosity and foaming temperature are directly affected. In addition, the finely scattered ash left by the breakdown of many foaming agents might affect the glass's viscosity and crystallization propensity. The size of the final pores is greatly influenced by the foaming agent's fineness and amount [170]; as a result, care must be taken while selecting the foaming agent's kind, size, and optimal concentration.

2.5.5. Thermal conductivity of glass-ceramic foams

The thermal conductivity of glass-ceramic foams is critical for insulating applications. For porous materials, the thermal conductivity decreases linearly with decreasing density (and hence increasing porosity). The thermal conductivity value is a summation of the radiation, convection and the solid phase. The contribution of the heat transfer by radiation in the glass-ceramic foam is rather complex since it depends on many factors such as the composition of solid and gas phases, porosity, pores shape, and thickness of cell walls [171]. The light normally consists of IR, visible, and UV radiation. When it is directed to a sample, it is either absorbed, reflected, or transmitted. Due to its low values, solids and liquids transmittance is usually ignored. The total porosity of the glass-ceramic foam is significant for heat radiation since it decreases with decreasing porosity. Glass-ceramic foams often have a radiation contribution to the thermal conductivity of 5–20% [172]. The contribution of convection in the foams is shown to be insignificant and can be neglected, especially for the foams with small pores [173]. On the contrary, the solid phase has the highest contribution to thermal conductivity. Crystalline materials normally have better heat conductivity than amorphous materials [174]. Therefore, the amorphous nature of the glass-ceramic foam minimizes thermal conductivity. Moreover, the formation of the crystalline phase in the solid matrix could lead to phonon scattering when heat is transported through a material. This process reduces the total thermal conductivity [175].

2.5.6. The uses of alternative raw materials for producing glass-ceramic foam

Glass is highly used for the production of foams. However, the production of glass-ceramic foam is an energy-consuming process if they made from mixes based on prepared powdered glass or cullet obtained straight from the manufacturing process due to a twofold heating process: initially, the manufacture of raw glass requires a firing temperature between 1450–1500 °C, secondly, sintering the raw glass mixture at 800–900 °C [76]. Therefore, the topic of employing less expensive raw materials in foams manufacturing has long been raised. Using natural materials and recycling waste glass that is both highly efficient and cost-effective is one of the techniques for resolving this challenge. When natural raw materials are used, the production comprises three processing stages, including milling of the raw materials, combining with fluxes (KOH or NaOH) and heat treatment. Recently, various solid wastes,

including fly ash [176], tailings wastes [177], incineration ashes [178], red mud, and coal bottom ash waste [179], have been studied as potential materials for the production of glass-ceramic foam. Nevertheless, very limited attention has been given to the utilization of zeolite-poor rock to manufacture glass-ceramic foams.

2.5.7. Previous studies on the preparation of glass-ceramic foam

Table 5 summarizes the results of multiple research published on using various materials to create glass-ceramic foams. When comparing the results of this study to the results in the literature, it is important to note that zeolite-poor rock containing solid waste (sawdust and eggshell) are appealing materials for glass-ceramic foams manufacturing since they have low production cost and excellent properties.

Table 5. Previous studies on the preparation of glass-ceramic foam

Main raw materials	Foaming agent	Replacement Ratio (%)	Sintering Temperature (°C)	Heating rate (°C/min)	Holding time (min)	Main technical properties			Ref.
						Density (g/cm^3)	Compressive strength (MPa)	Thermal conductivity (W/mK)	
Zeolite-poor rock	**Sawdust**	**0, 2, 6, 4, 8, 10, 20**	**850, 900, 950**	**10**	**10**	**0.3–0.7**	**0.3–4.5**	**0.04–0.17**	**This work**
Zeolite-poor rock	**Eggshell**	**0, 2, 6, 4, 8, 10, 20**	**850, 900, 950**	**10**	**10**	**0.54–1.07**	**1.01–6.7**	**0.06–0.3**	**This work**
Ceramic tile polishing waste	**SiC**	**0, 0.5, 1, 1.5, 2**	**1100, 1150, 1200, 1250, 1300**	**10**	**120**	**0.3–2.35**	–	–	[180]
Glass powder	**Oyster shells**	**0, 3**	**800, 850, 900, 950**	**10**	**30–120**	–	**1.00–2.33**	**0.057–0.077**	[181]
Coal bottom ash	**MgO**	**0, 2, 4, 6, 8**	**1180, 1200, 1220**	**5**	**60**	**0.15–0.99**	**0.3–5.25**	–	[179]
CRT panel glass	**MnO_2**	**0, 1.8, 3.6, 5.4, 7.2, 9**	**800, 820, 840**	**10**	**5–60**	**0.14–0.32**	–	**0.038–0.056**	[182]
Fly ash	**Na_2SiO_3**	**0, 10, 20, 30**	**1000, 1050, 1100, 1150, 1200**	**5**	**60**	**0.55–1.6**	**3.2–5.35**	–	[183]
Sand sludge	**Carbon black**	**0, 0.4**	**825, 850, 875, 900**	–	**60**	**0.17–0.39**	**0.29–3.46**	–	[184]
Porcelain waste	**Carbon ash waste**	**0, 1, 2, 3, 4**	**1030–1080**	**10**	**10–50**	**0.29– 0.37**	**1.32–2.88**	–	[185]
Coal fly ash + waste glass	**$CaCO_3$**	**0.5**	**600, 650, 700, 750, 800, 850, 900**	**20**	**45**	**0.46–0.72**	**4.2–10.5**	**0.36-1.3**	[186]
Glass waste + titanium tailing	**Na_2CO_3**	**2**	**760, 770, 780, 790**	**5**	**10–40**	**0.30–0.61**	**1.0–5.1**	**0.060-0.150**	[187]
CRT glass + germanium tailings	**SiC**	**0.5, 1, 1.5, 2**	**880**	–	**30**	**0.22–0.47**	**3.32**	**0.68-1.53**	[188]
Glass waste + mineral wool waste	**$CaCO_3$**	**1**	**700, 800, 1000**	**20**	**20**	**0.45–2.2**	–	–	[189]
Waste glass	**Eggshell**	**1, 3, 6, 9**	**800**	**10**	**60**	**0.32–1.22**	**0.04–0.81**	–	[190]

3. Materials and Methods

This chapter addresses the raw materials used in this research work as well as the techniques used to characterize them. It also describes the method used to prepare ceramic specimens. The primary purpose of employing natural and waste materials is to generate cost-effective ceramic materials with enhanced properties.

3.1. Raw materials used in the research work

3.1.1. Main raw material (zeolite-poor rock)

Zeolite-poor rock was utilized as the primary raw material in this investigation. It was obtained from mining in Mád (Tokaj region) which is placed on the coordinates (48.1907° N, 21.2802° E) in Northeastern Hungary, as shown in Fig 23. Tokaj area is famous for its large deposition of natural zeolite, which is widely spread in the region. Zeolite-poor rock was collected as granules after quarrying and pre-crushing. The material under consideration was oven-dried at 110 °C and ball-milled to a powder using a planetary ball mill (Retsch PM-100) (Fig 24).

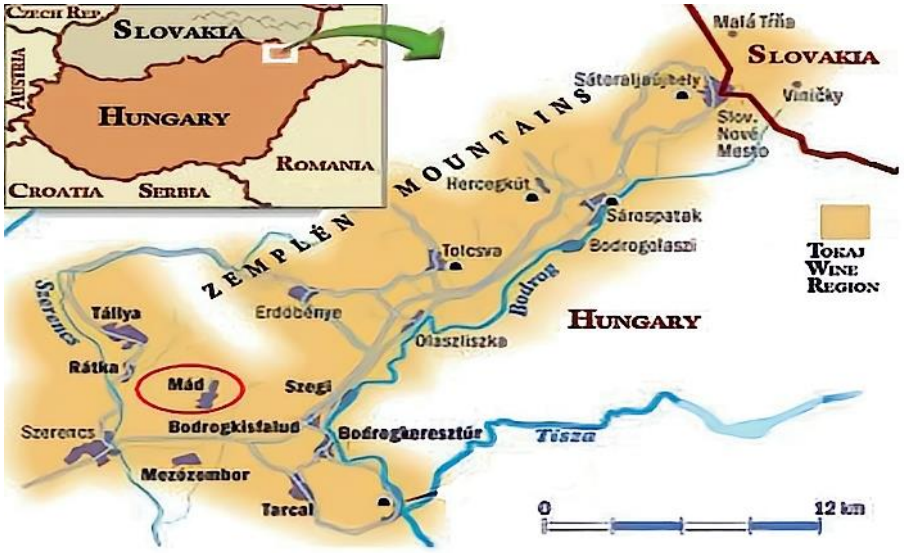

Figure 23. Location of zeolite-poor rock in Mad (Tokaj region, Hungary)

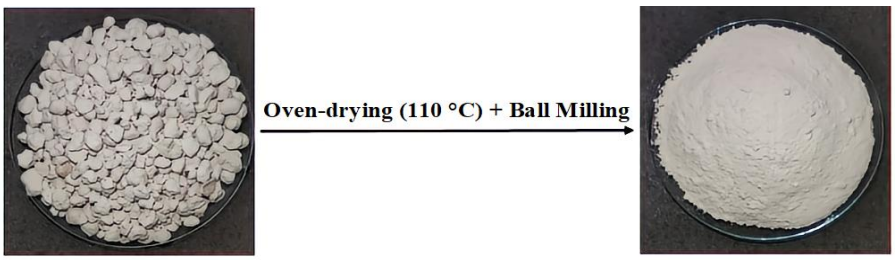

Figure 24. Pretreatment of zeolite-poor rock raw material

3.1.2. Sawdust

Sawdust was collected as waste material from local areas, oven-dried at 110 °C and sieved to pass a 200 µm gyratory sieve (Fig 25), then blended and packed in plastic bags for future analysis and use.

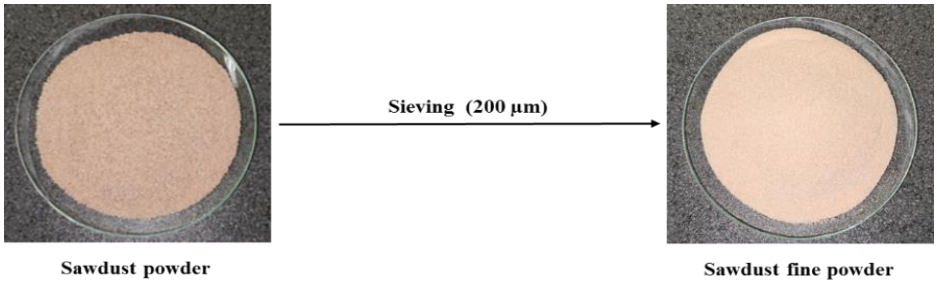

Figure 25. Sawdust powder before and after sieving

3.1.3. Hen's eggshell

Hen's eggshell was obtained as waste, washed with tap water, and dried in the air at room temperature. Using the ball-milling, the cleaned hen's eggshell was then ground to powder (Fig. 26).

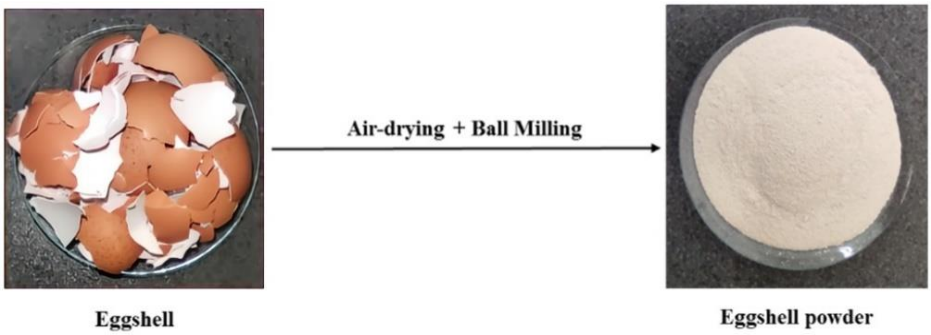

Figure 26. Pretreatment of eggshell

3.1.4. Sodium hydroxide

Sodium hydroxide was purchased from Donauchem GmbH (Hungary) in the form of a granule. The granules were dissolved in water and then added to the powder mixtures (Fig 27). Based on the supplier's data sheet, the purity is 85%.

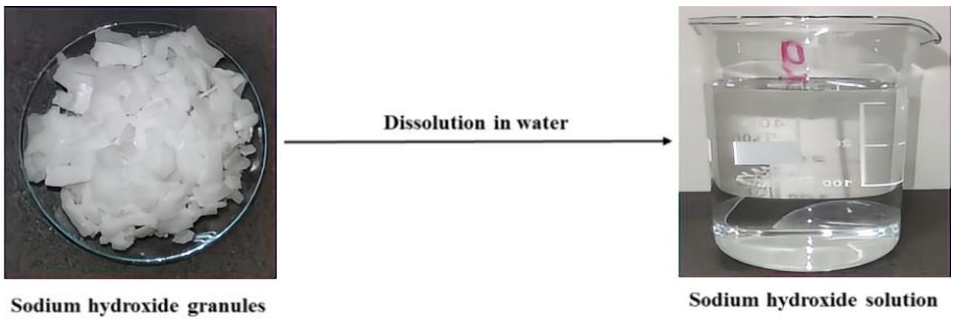

Figure 27. Dissolution of sodium hydroxide granules in water

3.2. Characterization methods of the raw materials

3.2.1. Determination of particle size distribution

It is essential to determine the particle size distribution and specific surface area of the ceramic raw materials since these factors affect the compaction and product qualities. The particle-size distributions of the raw materials powders were performed on a laser particle size analyzer (QUANTACHROME, model CILAS715) (Fig 28). Distilled water was utilized as the dispersion medium for all samples. A few grams of the powder to be measured are injected into the liquid medium to create a suspension that is continually cycled throughout the system. A laser is used to measure the size distribution based on the diameter of the solid particles. The particle size is estimated when the suspension is passed through two parallel glass plates. The measurement in each case was repeated three times, and the average values for the particle sizes were obtained.

Figure 28. Particle size distribution analyzer (CILAS 715)

3.2.2. BET Specific surface area analysis

The sample's specific surface areas (SSA) were determined based on the Brunauer-Emmett-Teller technique [191] using a Micromeritics Tristar 3000 instrument (Fig 29). A sample's surface area and porosity are determined using physical adsorption and capillary condensation techniques. After being cooled to extremely low temperatures, a sample is placed in a vacuum sample tube and subjected to a series of carefully regulated pressures with the analytical gas (nitrogen). The quantity of gas molecules absorbed on the surface rises with increasing pressure. To determine the relative pressure ratio (P/P_o), the equilibrated pressure (P) is compared to the saturation pressure (P_o), and the amount of gas adsorbed by the material at each equilibrated pressure is measured. At liquid nitrogen temperatures and relative pressures (P/P_o) ranging from 0.01 to 1.0, data were collected using nitrogen adsorption-desorption isotherms.

Figure 29. Micromeritics Tristar 3000 instrument

3.2.3. XRD investigations of raw materials

The identification of mineral phases of the raw materials in dried powder form was conducted via the XRD technique. The used X-ray equipment was Miniflex II, Rigaku X-ray diffractometer equipped with a monochromator and operated in Bragg-Brentano geometry as shown in Fig 30. The samples were scanned in a broad range of diffraction angles (2θ) intervals (5-90 °) using CuKα radiation with a wavelength (λ = 1.54184 Å) at operating voltage and current of 40 kV and 25 mA, respectively. The scan rate was maintained at 1°/min with a step size of 0.0101 °. The existence of different phases in the tested samples was determined by comparing their XRD patterns to the PDF (Powder Diffraction File) Database of the International Center for Diffraction Data (ICDD) using X'Pert HighScore Plus software.

Figure 30. A Rigaku Miniflex II X-ray diffractometer setup in ceramic's laboratory at the University of Miskolc

3.2.4. XRF investigations

The oxide compositions of the starting raw materials were investigated using an X-ray fluorescence spectrometer. The samples under investigation are bombarded with high-intensity x-rays; every element existing in a sample creates a unique set of unique fluorescence x-rays, which is why XRF spectroscopy is very effective for elemental investigation. In the spectrum, XRF peaks of varying intensities are formed and shown. The peak energy identifies the element, while the peak intensity indicates its concentration

3.2.5. Thermal analysis of raw materials using thermal analyzer

The thermal characteristics, including simultaneous differential and thermogravimetric analysis, were evaluated using 1750 SETARAM, Setsys evolution thermal analyzer (Fig 31) at a heating rate of 10 °C min^{-1} in a static oxygen atmosphere in a temperature interval of 40-1200 °C. In this test, the sample and the reference holders are located on a common rod in a small-size tube furnace. This rod is connected to a four-decimal precision micro-balance. 15 mg of the samples were loaded in platinum crucibles. The data collection mechanism of the test identifies temperature and mass changes in the sample compared to annealed alumina (reference material).

Figure 31. 1750 SETARAM, Setsys evolution thermal analyzer

3.2.6. SEM and EDS investigations of the raw materials

The microstructural features and the morphology of the raw materials were examined via Carl Zeiss EVO MA10 scanning electron microscopy and Helios G4 PFIB CXe DualBeam SEM (Fig 32) equipped with Bruker microprobe, run at an operating voltage of 20 kV. The samples were coated with layers of gold using a sputter coater to create better conduction prior to SEM imaging. Secondary electron mode was used to capture the photos at various magnifications. Qualitative analysis of the elemental composition of the raw materials was obtained using an energy-dispersive X-ray spectrometer (EDAX Genesis). The combination of these analytical procedures supplies rapid and accurate interpretations for qualitative and quantitative investigation of the samples.

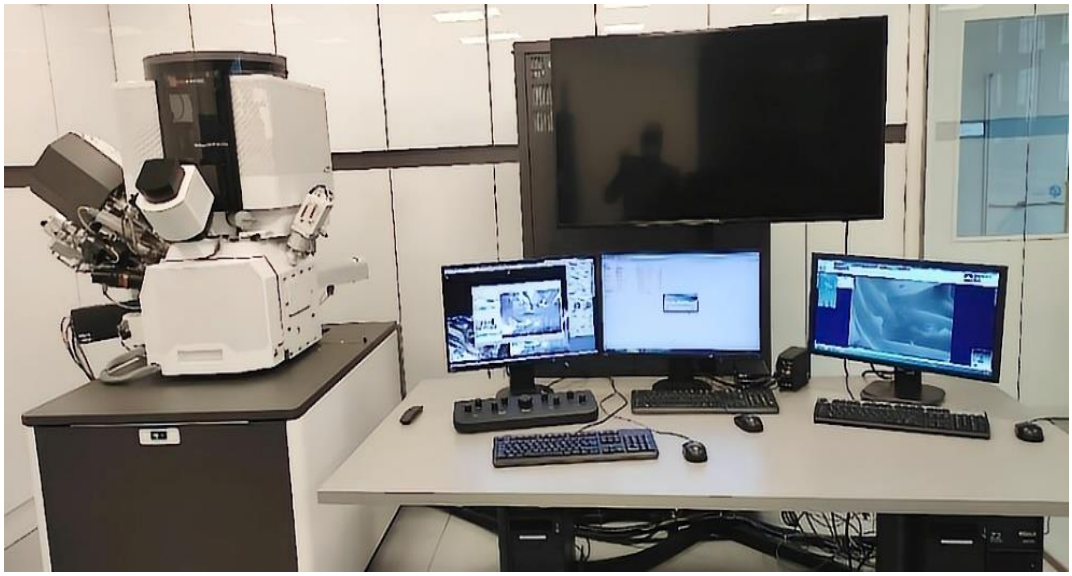

Figure 32. Helios G4 PFIB CXe DualBeam SEM setup in University of Miskolc

3.2.7. FTIR analysis

The samples' infrared (IR) spectra were captured via Bruker Tensor 27 FTIR (Fourier transform infrared spectroscopy) equipment (Fig. 33). An average resolution of 4 cm^{-1} was used to capture 400–4000 cm^{-1} spectra. Prior to IR inspection, the sample powders were mixed with a small amount of KBr powder and ground to produce a homogenous mixture. The functional group's analysis was performed on all samples using the transmittance technique.

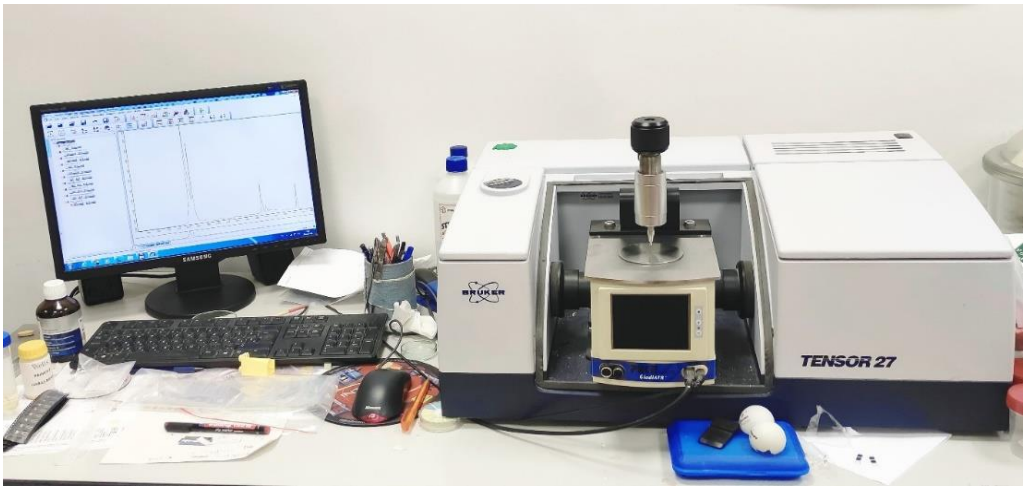

Figure 33. FTIR analysis device

3.2.8. Heating microscopy analysis

The geometrical deformation process of ceramics during sintering could be investigated using heating microscopy. The measurements were performed using a Camar Elettronica heating microscope (Fig 34). The tube furnace's temperature could be customized at a maximum value of 1600 ° C. The instrument employs a light source and a camera to produce binary pictures. The produced images could be used to track changes in the sample's height while it is heated in the tube furnace. The melting point and wetting characteristics of materials may be determined through heating microscopical measurements. There are five distinct states that may be seen as the material is heated: sintering, softening, sphere, half-sphere and melting. In this work, the purposes were to estimate the size change associated with the sintering temperature of the mixes for the brick-making and the maximum expansion (foamability) of the sample mixtures used for the foams making.

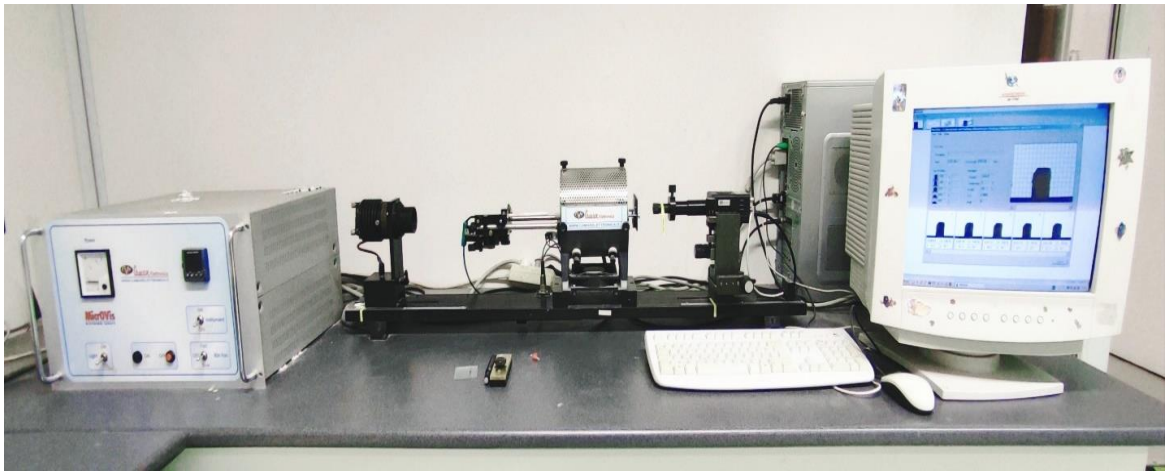

Figure 34. Camar Elettronica heating microscope

3.3. Development of thermal insulation ceramic specimens (bricks and foams)

3.3.1. Preparation of zeolite-poor rock incorporated sawdust composite bricks

The ceramic specimens were prepared based on zeolite-poor rock and sawdust as starting raw materials, as shown in Fig 35. Zeolite-poor rock powder was homogeneously milled and mixed with 2%, 4%, 6%, 8%, and 10% sawdust in Retsch PM 400 planetary ball mill for 15 minutes at 150 rpm using silica balls. The prepared mixtures (Table 6) were used to produce ceramic disc specimens with a thickness of about 10 mm and a diameter of 25 mm using hydraulic uniaxial compacting machines performed under 40 MPa. The produced green ceramic samples were then sintered at variable temperatures (950 °C, 1050 °C, 1150 °C, and 1250 °C) for 3 h using a programmable laboratory chamber furnace with a heating rate of 60 °C/h.

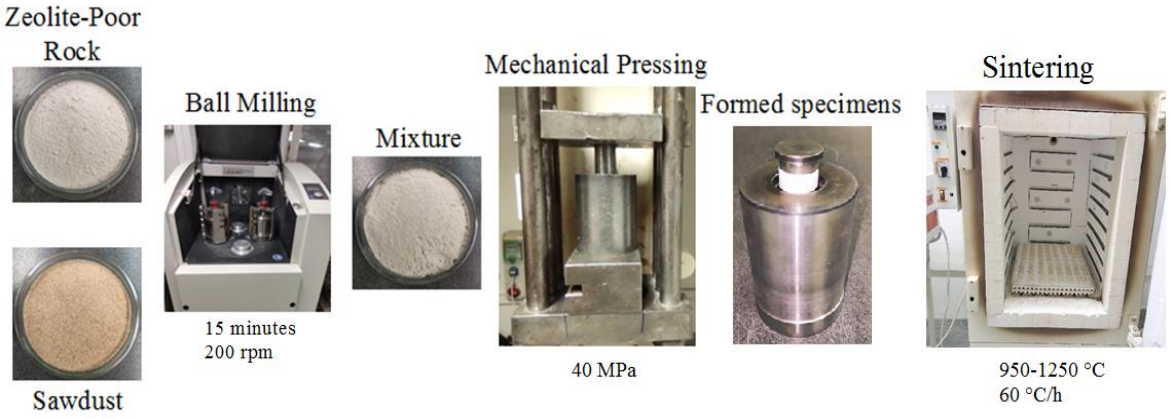

Figure 35. Preparation steps of the zeolite-poor rock/sawdust ceramic bricks

Table 6. Mixture proportions of the raw materials (%)

Mix code	Zeolite-poor rock (wt%)	Sawdust (wt%)
Z (Control brick)	100	0
ZS2	98	2
ZS4	96	4
ZS6	94	6
ZS8	92	8
ZS10	90	10

3.3.2. Preparation of zeolite-poor rock incorporated eggshell composite bricks

Fig 36 shows a manufacturing diagram with the essential steps involved in making burnt zeolite-poor rock incorporated eggshell composite bricks. Several proportions of eggshell (0%, 5%, 10%, 15%, and 20) have been selected and uniformly blended and milled with zeolite-poor rock using PM 400 Retsch planetary ball mill for 15 minutes run at 200 rpm to produce homogenous mixtures. Table 7 shows the proportions of the mixtures. The produced dry mixtures were then uniaxially compacted to form cylindrical composite bricks with a thickness of roughly 10 mm and a diameter of 25 mm using a pressure of 45 MPa. The compacted

samples were then sintered in a laboratory-scale electrical kiln at various temperature ranges (950, 1050, and 1150 °C) for 2 h at a rate of 60 °C/h to acquire the desired strength.

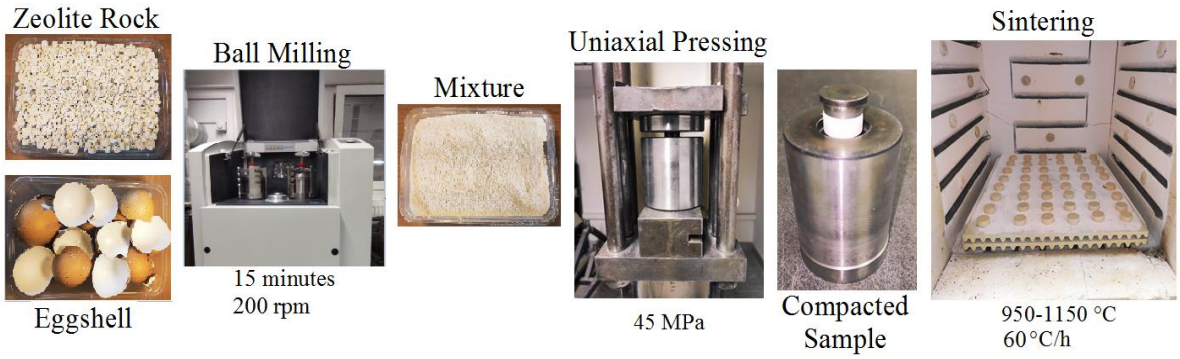

Figure 36. Processing steps of the zeolite-poor rock/eggshell composite ceramic bricks

Table 7. The composite ceramic bricks mixture ratios (wt%)

Mix code	Zeolite-poor rock (wt%)	Eggshell (wt%)
Z (Control brick)	100	0
ZE5	95	5
ZE10	90	10
ZE15	85	15
ZE20	80	20

3.3.3. Preparation of alkali-activated zeolite-poor rock incorporated sawdust ceramic foams

Sawdust incorporated zeolite-poor rock foams were fabricated using alkali activation and reactive sintering techniques (Fig. 37). Zeolite-poor rock powder (Tokaj, Hungary), sawdust, and sodium hydroxide were used as starting raw materials. Stoichiometric amounts of these powders were precisely weighed (Table. 8), mixed with 2M NaOH (produced by dissolving 15 wt% of NaOH granules in distilled) then dried in the oven at 200 °C for 2 days. The dried powders were ground in a planetary ball mill (Retsch PM 400) containing silica balls for 15 minutes at 150 rpm. Using uniaxial pressing machines at a pressure of 18 MPa, the milled powders were then compacted to form cylindrical pellets with a diameter of around 20 mm and a thickness of 10 mm. The green ceramic bodies were heat-treated at varied temperatures (850, 900, and 950 °C) in a high-temperature customizable kiln for 5 minutes of residence time, with 5 °C/min heating rate. Overall, 150 foam samples were produced after firing in a laboratory electric furnace.

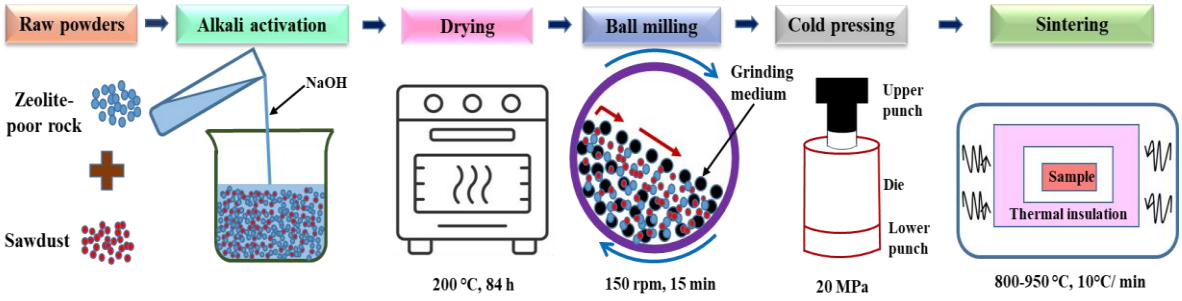

Figure 37. Flowchart for the preparation of zeolite-poor rock/sawdust ceramic foams

Table 8. Mix proportion in wt (%) of zeolite-poor rock-sawdust foams

S. No	Designation of the mixtures	Prepared mixture composition		
		Zeolite-poor rock (wt%)	Sawdust (wt%)	Sodium hydroxide (wt%)
1	ZS (Control)	100	0	15
2	Z2SS	98	2	15
3	Z4SS	96	4	15
4	Z6SS	94	6	15
5	Z8SS	92	8	15
6	Z10SS	90	10	15
7	Z20SS	80	20	15

3.3.4. Preparation of alkali-activated zeolite-poor rock incorporated eggshell ceramic foams

Zeolite-poor rock combined with eggshell foams were synthesized using the alkali activation and reactive sintering technique (Fig. 38). Crushed zeolite-poor rock powders were mixed with different proportions of eggshell (Table 9), 15 wt% of NaOH granules were dissolved in distilled water and added to the previously prepared zeolite poor rock with eggshell mixtures, an exothermic reaction took place associated with evolving of heat and bubbles. The mixtures were then dried in the oven for two days at 200 °C. The alkali-activated mixtures were ground in a planetary ball mill (Retsch) at 150 rpm for 15 minutes. Then, the produced powders were uniaxially compacted into pellets at 18 MPa with a height of 10 mm and a diameter of 20 mm. The green specimens were then sintered at 850-950 °C for 10 min using a laboratory electric kiln.

Figure 38. Preparation steps of alkali-activated zeolite-poor rock incorporated eggshell foams

Table 9. Mix proportion in wt (%) of zeolite-poor rock-eggshell foams

S. No	Designation of the mixtures	Prepared mixture composition		
		Zeolite-poor rock (wt%)	Eggshell (wt%)	Sodium hydroxide (wt%)
1	ZS	100	0	15
2	Z2ES	98	2	15
3	Z4ES	96	4	15
4	Z6ES	94	6	15
5	Z8ES	92	8	15
6	Z10ES	90	10	15
7	Z20ES	80	20	15

3.4. Characterization of the prepared thermal insulation ceramic specimens

3.4.1. Measurement of the physical properties

Various technical parameters of the fired ceramic bricks and foams, including apparent porosity, bulk density, and water absorption, were measured using the Archimedes approach according to ASTM C20 [192]. In this method, the fired composite bricks and foams were soaked for 2 hours in boiling water, and then the suspended and saturated weights of the specimens were recorded. The following equations were used to compute the bulk density, water absorption, and apparent porosity of the samples:

$$Bulk\ density\ \left(\frac{g}{cm^3}\right) = \frac{W_d}{W_s - W_{su}} \times 100 \quad (1)$$

$$Apparent\ porosity\ (\%) = \frac{W_s - W_d}{W_s - W_{su}} \times 100 \quad (2)$$

$$Water\ absorption\ (\%) = \frac{W_s - W_d}{W_d} \times 100 \quad (3)$$

Where W_d, Ws, and Wsu are dry weight, saturated weight, and suspended weight, respectively

The linear shrinkage was measured based on ASTM C326 by determining the volume of the samples before and after firing using a Vanier calliper, and the percentage of the linear shrinkage was calculated based on the following equation (ASTM C326, 1997):

$$Linear\ shrinkage\ (\%) = \frac{l_0 - l_1}{l_0} \times 100 \qquad (4)$$

Where l_0 and l_1 are the pre-sintered and post-sintering lengths of the sample

3.4.2. Thermal conductivity measurement

The default C-Therm TCi Thermal Conductivity Analyzer (Fig 39) employs the modified transient plane source (MTPS) technique used in characterizing the thermal conductivity and effusivity of materials. It employs a one-sided, interfacial heat reflectance sensor that applies a momentary constant heat source to the sample. Thermal conductivity and effusivity are measured directly at room temperature, providing a detailed overview of the heat transfer properties of the samples.

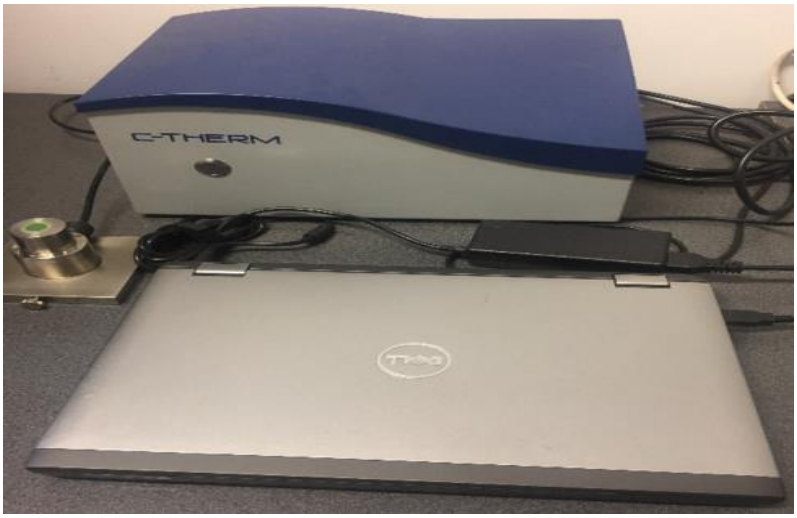

Figure 39. Thermal conductivity analyzer (TCi C-THERM)

3.4.3. Compressive strength test

The compressive strength was determined based on ASTM C67 using hydraulic universal testing equipment, as shown in Fig 40. The compressive strength test is performed on cylindrical samples. 5 compressive strength measurements are used to determine the average value of the compressive strength.

Figure 40. Hydraulic universal testing equipment

3.4.4. SEM, EDS, and XRD of the sintered samples

SEM, EDS, and XRD of the produced samples were used to investigate the microstructural features and phase identification.

3.4.5. CT scan

The detailed information about the pore size, structure, and distribution of the produced glass-ceramic foams was studied using YXLON FF35 Multi-application, high-resolution computed tomography (CT) inspection system (Geminy) (Fig. 41). The machine is equipped with water-cooled nano-focus transmission X-ray tubes providing detailed visibility of 150 nm with a stable focus part. Using reconstruction software algorithms, the machine achieves high-quality 3D CT images.

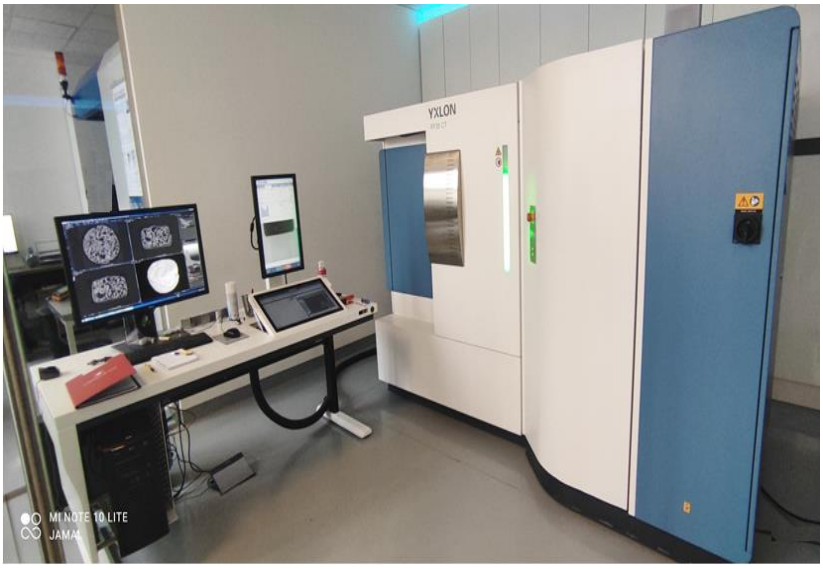

Figure 41. CT scan equipment

3.4.6. Determination of porosity using pycnometer

Firstly, the weight of the empty pycnometer and the weight of the pycnometer with the loaded material must be determined. The liquid is then introduced, and the solid weight is calculated as a portion of the overall determined weight. The volume of water added may then be calculated. The volume of the determined solid particle is the difference between the entire volume and the volume of water that occupies the empty pycnometer. The density of the powder is then calculated.

$$PD = \frac{m_s}{V_s} \quad (5)$$

Where: *PD*= Powder density, m_S= mass of the solid, V_S= volume of the solid

The porosity can be calculated from the powder density and solid density using the equation bellow

$$P = 1 - \frac{BD}{PD} \quad (6)$$

Where: *P*= Porosity, *BD*= Bulk density

4. Results and discussion

4.1. Raw materials analysis

4.1.1. Particle size distribution of the raw materials

The particle size distribution curves of zeolite-poor rock, sawdust, and eggshell are illustrated in Fig. 42. The analysis was carried out using distilled water as suspension fluid in a tri-laser QUANTACHROME analyzer, model CILAS715. The curves exhibit a broad range of particle sizes, most of which are less than 100 µm. The sawdust and eggshell contain some particles larger than 100 µm, as shown in Fig. 42. The particle size distribution curves demonstrate that zeolite-poor rock has a larger percentage of smaller particles, whereas sawdust has a high percentage of a coarser fraction. The average sizes for zeolite-poor rock, sawdust and eggshell (D50) were 16.61 µm, 71.2 µm, and 25.49 µm, respectively. Combining zeolite-poor rock with sawdust or eggshell might result in a tightly compact packing during the dry pressing process since the finer particles fill the pores and gaps between coarser particles. This process can result in a better reaction between the raw materials during the sintering due to good contact.

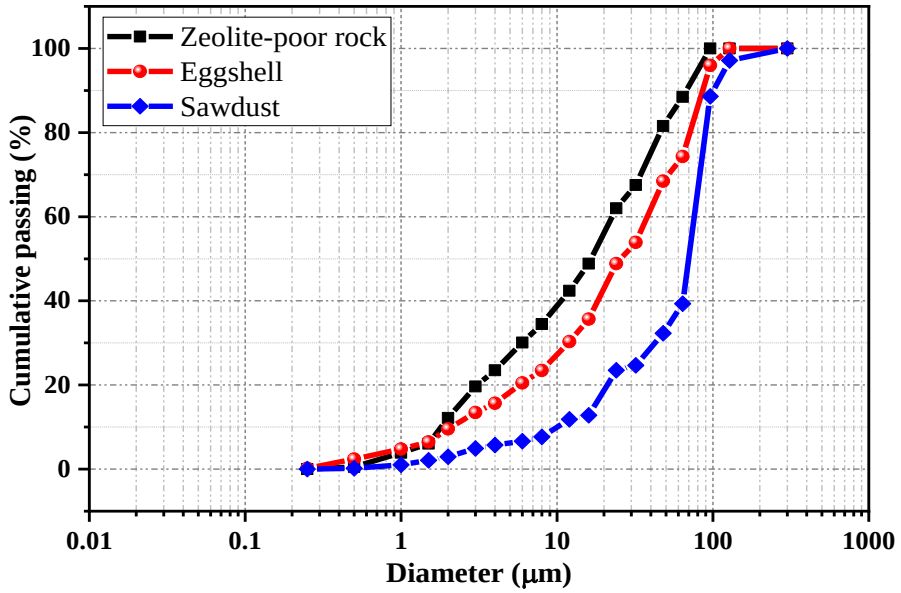

Figure 42. Particle-size distribution of the zeolite-poor rock, sawdust and eggshell

4.1.2. XRD and XRF examinations of the raw materials

Zeolite-poor rock from Tokaj region (Hungary) contains clinoptilolite together with other identified mineral phases, including montmorillonite, quartz, cristobalite, and calcite, as confirmed by XRD measurement (Fig. 43). The amount of zeolite (clinoptilolite) is 10%, while the major minerals phases are cristobalite 50% and montmorillonite 30%. The result of oxides composition, mineralogical constituents, and the loss on ignition (LOI) of the zeolite-poor rock obtained from XRD and XRF analysis are shown in Table 10; silica is the predominant oxide with a percentage of about 83%, followed by alumina, MgO and Na_2O as minor constituents. The loss on ignition obtained after sintering to 1000 °C was measured as 5.5%.

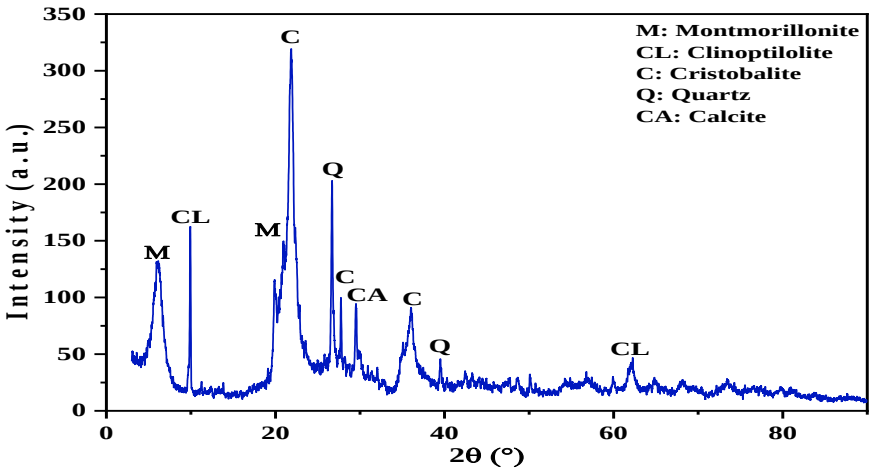

Figure 43. XRD patterns of zeolite-poor rock

Table 10. Chemical composition and mineralogical percentages of the zeolite-poor rock (Tokaj, Hungary) as determined by XRD and XRF

	wt%	CaO	SiO_2	Al_2O_3	MgO	Na_2O	CO_2	H_2O	Loss on ignition
Quartz	8	–	8.00	–	–	–	–	–	0.00
Cristobalite	50	–	50.00	–	–	–	–	–	0.00
Montmorillonite	30	–	19.13	4.06	3.21	0.74	–	2.87	2.87
Calcite	2	1.12	–	–	–	–	0. 88	–	0.88
Clinoptilolite	10	–	5.79	1.89	–	0.57	–	1.6	1.75
Total	100	1.12	82.92	5.95	3.21	1.31	0. 88	4.47	5.50

Fig 44 depicts the XRD diffractogram of sawdust. The result shows two diffraction peaks at corresponding 2θ values of 15.6 ° and 22.4 °, which are designated to the crystallographic planes of (101) and (002) of cellulose I [194,195]. Another small peak is detected at 2θ= 34.7 °, which is attributed to (400) lattice plane of crystalline cellulose I [196]. The sawdust is expected to have lignin and hemicellulose, which are amorphous, besides crystalline cellulose.

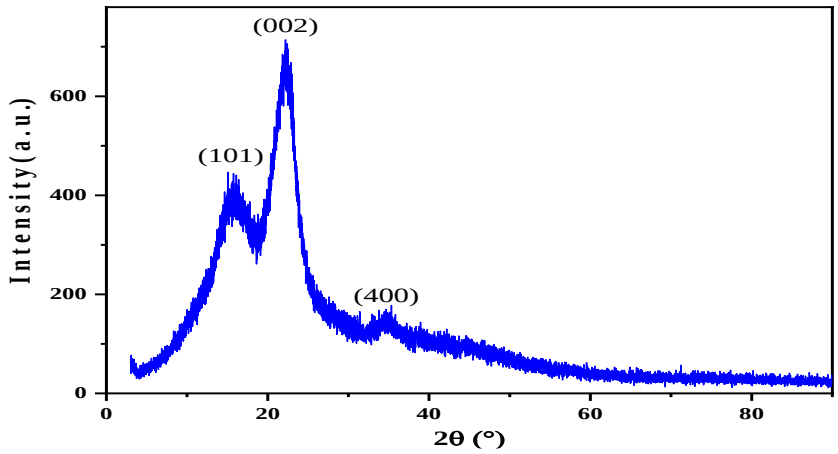

Figure 44. XRD diffractogram of sawdust

The XRD analysis of the eggshell is shown in Fig. 45. The occurrence of calcite with rhombohedral structure was confirmed as the fundamental component of the eggshell. This result is in line with prior research findings [197]. At high temperatures, high quantities of carbonates break down to generate CO_2. The release of CO_2 creates pores in the ceramic bricks and foams, which reduces density and improves thermal insulation.

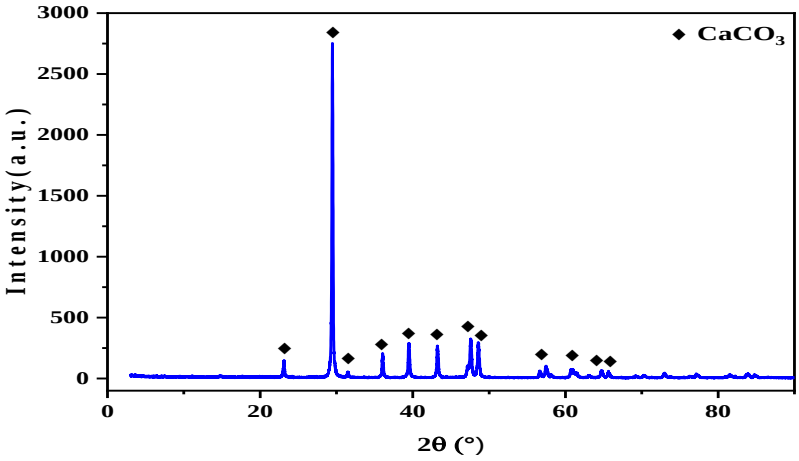

Figure 45. XRD patterns of eggshell

Table 11 shows the chemical compositions of the eggshell as determined by XRF. The obtained results confirm the existence of the CaO as the main component (51.4%) and a small amount of other oxides. These results are consistent with the XRD findings (Fig. 45).

Table 11. Chemical composition of eggshell as determined by XRF.

Component (wt%)	Hen eggshell
SiO_2	0.08
Al_2O_3	0.03
MgO	0.13
Na_2O	0.11
CaO	51.4
P_2O_5	0.28
Loss on ignition (%)	47.77

4.1.3. Thermal investigation of raw materials (TG/DTA)

TG/ DTA curves of zeolite-poor rock are illustrated in Fig. 46. An overall weight loss of 9.02% was obtained. Three step-like mass losses are distinguished in the TG graph. The initial weight loss (Δw = 2.95%) is due to the single-step evaporation of physically adsorbed water in microspores, surface and zeolite cavities. It correlates to the intense endothermic peak at 111.08 °C as observed on the DTA curve. The hydration energy of the additional framework cations has a big role in the overall quantity of water and the dehydration of zeolite. Zeolites with large-hydration-energy cations, such as Ca^{2+} hold much more water and keep it at a higher temperature compared to those with low-hydration-energy cations, such as K^+ [198]. The second weight loss is (Δw = 4.097%), which could be attributed to removing combined water

and the combustion of volatile organic materials. It correlates to the wide exothermic peak at the temperature range of 179–524 °C on the DTA curve. The final weight loss (Δw = 1.97%) could be assigned to the continuous burning of the organic matter and coincides with the broad exothermic peak at temperatures ranging from 524 to 693 °C on the DTA graph.

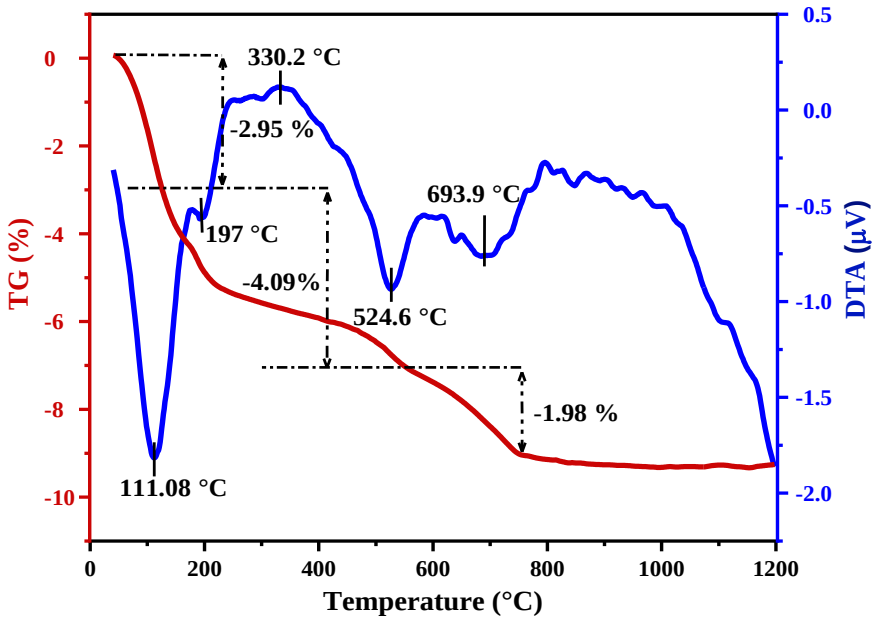

Figure 46. TG/DTA curves of zeolite-poor rock

TG/DTA curves of the sawdust are illustrated in Fig 47. TG curve indicates an overall weight loss of approximately 86.238%, divided into three stages of decomposition. Firstly, 4.7% weight loss is observed at a temperature range of 40–116 °C relating to the endothermic phase; this could be attributed to the evaporation of free water. Secondly, the highest weight loss (56.27%) was obtained at a temperature between 221 to 342 °C; the weight loss, in this case, may be attributed to the evaporation of the volatile organic content. The last weight loss was obtained between 342 °C and 646 °C, assigned to the continuous burning of organic matter. In the DTA curve, very broad exothermic peaks are obtained in the temperature range of 233–656.7 °C; these peaks could be ascribed to the decomposition of hemicellulose, cellulose, and lignin, respectively. Hemicellulose has a linear structure with a small chain; therefore, its decomposition normally takes place at lower temperatures to give a lower molecular weight compound, while cellulose and lignin decompose at relatively higher temperatures due to their complex structures to yield carbon dioxide, water, and ash [199]. These results confirm that, upon heating the green ceramic samples, the sawdust will gradually burn as the sintering temperature increases; this will reduce the possibility of crack formation in the produced ceramic materials and leads to the formation of the different pores in the samples.

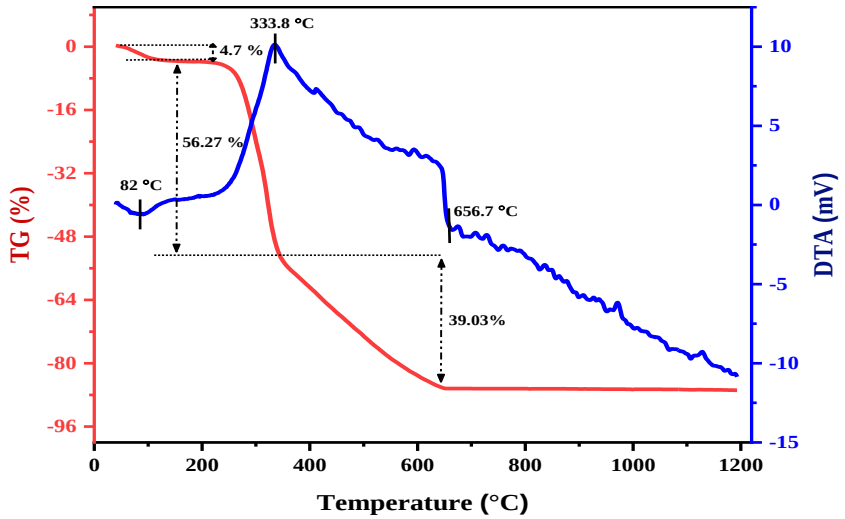

Figure 47. TG/DTA curves of sawdust

The thermal decomposition induced by the increased temperature of the eggshell powder, which is mostly comprised of $CaCO_3$, is shown in a typical TG/ DTA profile (Fig. 48). The quantity of CaO in the eggshell was found to be around 47% (w/w%). A very little weight loss in the range of ≈ 1% was observed in the TG curve, accompanied by small endothermic peaks in the DTA curve when the temperature was raised from room temperature to 200.9 °C, which can be attributed to the loss of volatile components and free water. The second breakdown stage in the TG curve, which results in a weight loss of 5.8%, occurs between 200 and 599 °C and is associated with an intense exothermic peak in the DTA curve at 352.7 °C and is caused by the degradation of organic content that makes up the outer eggshell membrane. The most substantial weight loss is detected between 680 and 930 °C, with a characteristic weight loss of 47%, accompanied by a large endothermic peak at 892.1 °C in the DTA pattern, which correlates to the complete breakdown of $CaCO_3$ to CaO and CO_2. The outcomes of the thermal investigations of eggshell powder are consistent with the previous literature on eggshell [200]. The emission of CO_2 resulted in the formation of many pores in the produced ceramic samples (bricks and foams).

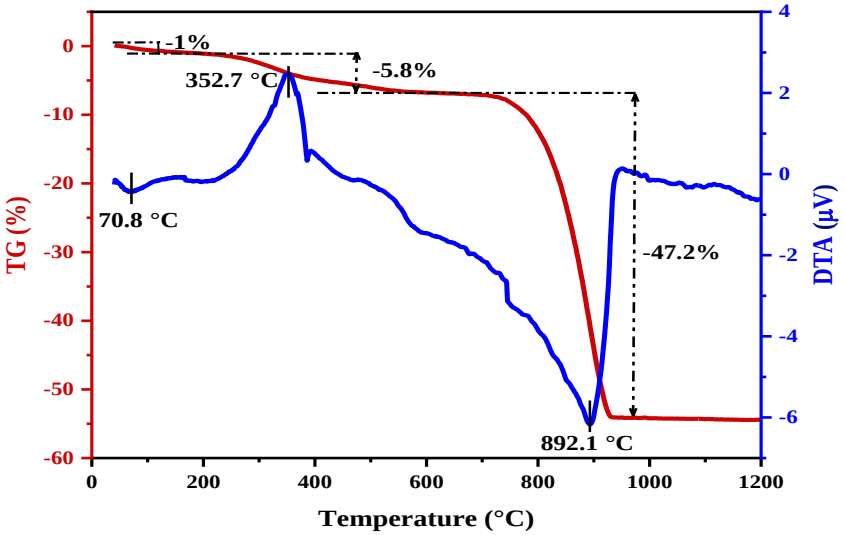

Figure 48. TG/DTA curves of eggshell powder

4.1.4. BET specific surface area analysis of raw materials

Table 12 displays various physical parameters of zeolite-poor rock, sawdust, and eggshell, depending on BET surface area and moisture percentages. The specific surface area of zeolite-poor rock is greater than sawdust and eggshell. This property may be explained by the fact that zeolite-poor rock contains a significant number of open pores. Furthermore, the quantity of moisture in zeolite-poor rock and sawdust is larger than that of the eggshell, as moisture can readily be sucked into the zeolite and sawdust micropores.

Table 12. BET surface area and moisture of prepared powders

Properties	Zeolite-poor rock	Sawdust	Eggshell
BET surface area (m^2/g)	16.8759	1.0899	4.06
Moisture (mass%)	5.32	6.51	1.20

4.1.5. SEM and EDS analysis of used raw materials

The morphology and the chemical composition of the raw materials powders were shown in the SEM and EDS images (Fig. 49). All the powders exhibit a wide range of irregular angular particles with different sizes, reflecting the particle size distribution depicted in Fig. 42. In zeolite-poor rock powder, SiO_2 is the predominant constituent beside other oxides (Al_2O_3, MgO, and CaO) that exist in minor quantities, as confirmed by EDS point investigation (Fig. 49.b). This result is consistent with the XRD result (Fig. 43). The SEM image and the EDS graph of the sawdust are exhibited in Fig. 49.c and d, which show irregular and plate-like particle shapes with relatively larger sizes and mainly consist of C and O. The SEM images and EDS spectra of the eggshell powder are depicted in Fig. (49e and f), which mainly confirms the existence of $CaCO_3$. This result is in very good agreement with the XRD result of eggshell (Fig. 45).

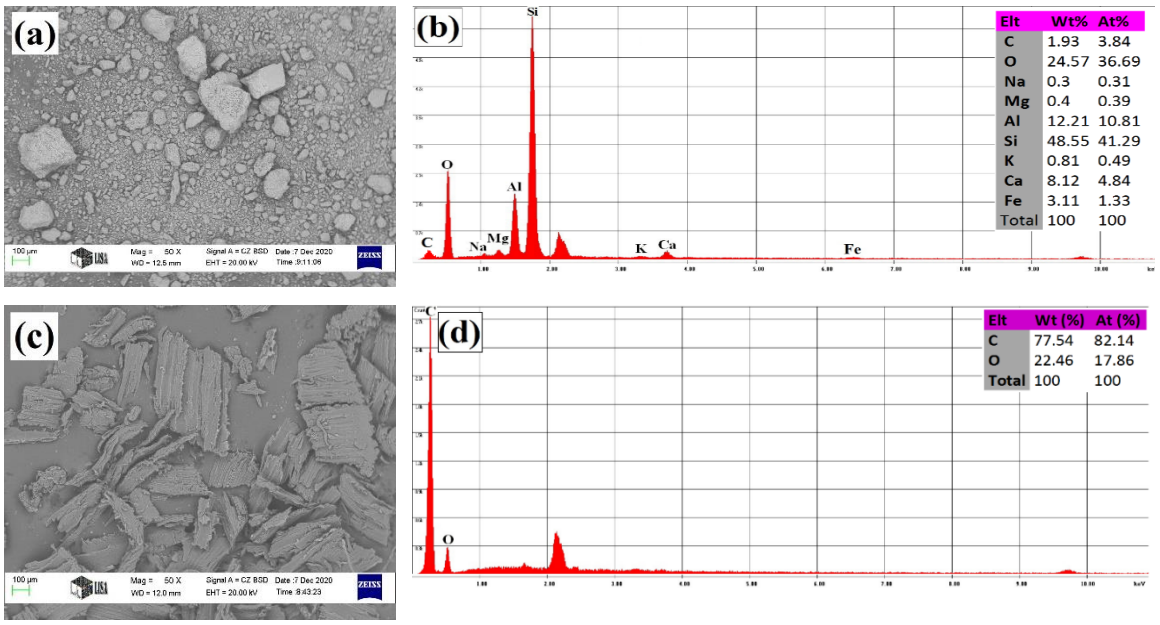

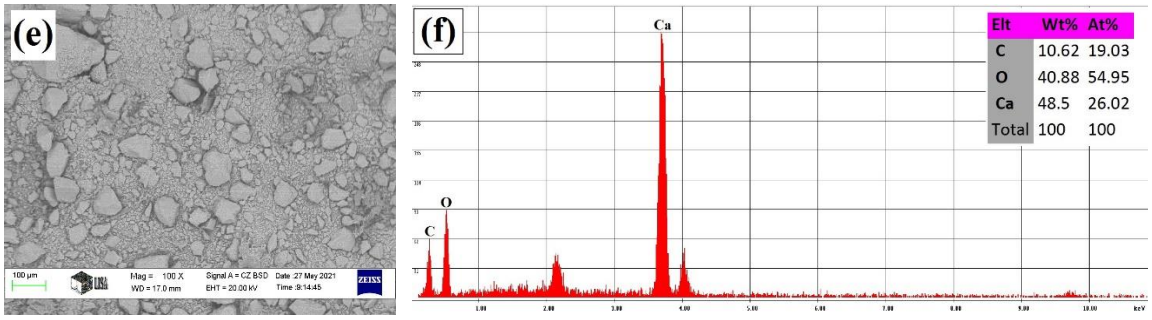

Figure 49. a) SEM image and (b) EDS spectrum of zeolite-poor rock. (c) SEM image and (d) EDS spectrum of sawdust (e) SEM image and (f) EDS spectrum of eggshell powder

4.2. Discussion and conclusions

Objective listed in Chapter 1.1 and the answers:

- **To systematically investigate the raw materials (zeolite-poor rock from Tokaj region) based on their mineralogical composition, phase identification, microstructural feature, chemical constituents, thermal analysis, particle size distribution, and specific surface area.**

A comprehensive analysis has been conducted for the detailed characterization of raw materials (zeolite-poor rock, sawdust and eggshell). These starting raw materials were investigated based on their particle size distribution, chemical constituents, BET (Brunauer, Emmett and Teller), X-ray diffraction (XRD), X-ray fluorescence (XRF), energy-dispersive X-ray spectroscopy (EDS), thermogravimetric (TG), differential thermal analysis (DTA) and scanning electron microscopy (SEM).

The particle size analysis confirms that the raw materials have a wide range of particle sizes which is good for better compaction during the forming process. The BET specific surface area analysis of the raw materials shows that zeolite-poor rock has a higher specific surface area. This feature is attributed to the large number of open pores in the zeolite-poor rock. Also, the amount of moisture in zeolite-poor rock is quite higher compared to sawdust and eggshell since moisture can easily be absorbed into the zeolite-poor rock micropores. The moisture in the mixture can also improve the compaction during the uniaxial dry-pressing process.

XRD investigation confirms that zeolite-poor rock includes clinoptilolite (10%) along with cristobalite (50%), montmorillonite (30%), quartz (8%), and calcite (2%), while XRF confirms the existence of high content of silica in zeolite-poor rock which is good for the preparation of porous bricks and glass-ceramic foams.

TG/DTA investigations reveal that the decomposition of zeolite-poor rock takes place around 900 °C suggesting the ideal sintering temperature. Furthermore. The TG/DTA analysis of sawdust and eggshell reveals the decomposition of these materials and formation of CO_2 gas, which is important for the creation of the porous structure, making them suitable pore-forming agents.

Conclusions

I have experimentally demonstrated that zeolite-poor rock is a very soft rock with complex composition, easy to crush and has high silica content. On the other hand, sawdust and eggshell could be suitable pore-forming agents. The good compatibility of these raw materials makes them a potential candidate for the preparation of new porous bricks and glass-ceramic foams.

4.3. Results of the new zeolite-poor rock incorporated sawdust composite bricks

4.3.1. Dimensional characteristic of zeolite-poor rock/sawdust bricks after firing

Cylindrical zeolite-poor rock bricks incorporated with different percentages of sawdust are manufactured using variable sintering temperatures (Fig. 50). It is worth mentioning that changing the bricks from cuboid to cylindrical shape could affect some properties of the samples, such as compressive strength [40]. The produced samples are fired into interesting white-like colours with noticeable volume shrinkage.

950 °C 1150 °C 1250 °C

Figure 50. Laboratory-scale zeolite-poor rock/sawdust ceramic bricks sintered at different temperatures

4.3.2. XRD investigations of the fired zeolite-poor rock/sawdust bricks

X-ray diffraction measurements, which demonstrate the crystallinity and phase composition of the sintered samples, are shown in Fig. 51. The XRD analysis confirms the presence of silica (cristobalite) as the major phase and other minor phases. Above 900 °C, decomposition of montmorillonite, clinoptilolite, and calcite has taken place and the formation of a small portion of anorthite. Upon increasing the temperature, the peak intensities increase, which indicates the increase in the crystallinity of the different phases. At 1050 °C, mullite, a new phase is formed. No carbon phase is detected, which confirms the burnout of all sawdust during the sintering process.

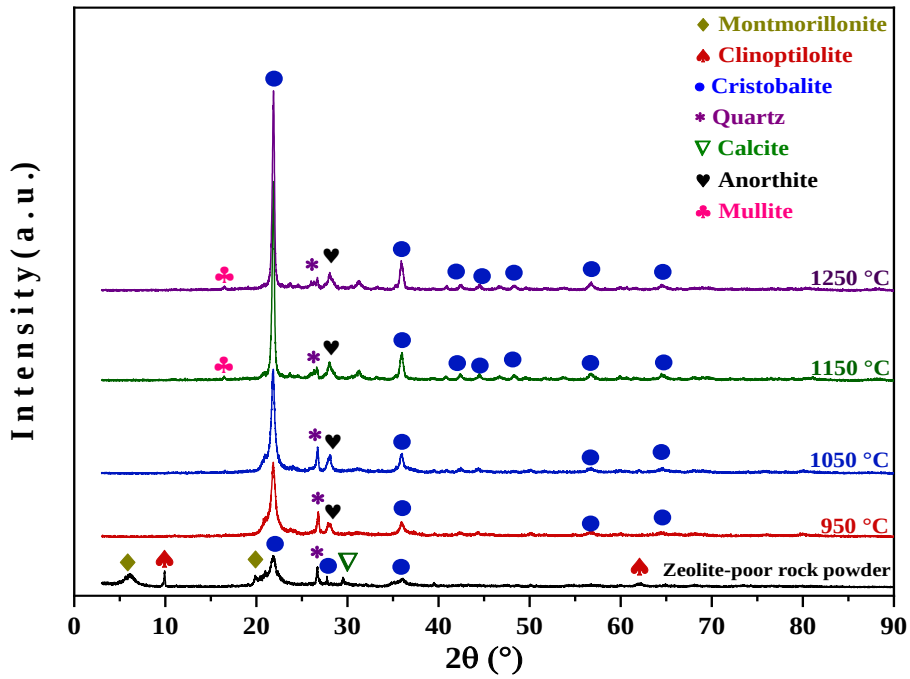

Figure 51. XRD results of zeolite-poor rock powder and fired specimens with 6% sawdust

4.3.3. SEM examination of the fired zeolite-poor rock/sawdust bricks

The morphological features and the microstructural characteristics of the fractured surface of the different ceramic bricks fired at a temperature of (950–1250 °C) have been studied via scanning electron micrographs. Fig. 52 shows different magnifications of the fracture surface of ceramic bricks containing 8% sawdust sintered at 1150 °C. The SEM images show different types of pores (open, closed, and capillaries) of different sizes. At high magnification, a whisker-like structure can be seen; EDS analysis of this sample (Fig. 53) reveals that the whisker-like structure (point 1) contains silicon, oxygen and a larger amount of aluminium compared to point 2. This could indicate the formation of whisker-like mullite, which can enhance the compressive strength through the crack deflection. Fig. 54 exhibits SEM images of ceramic bricks with different sawdust concentrations. It can be seen that increasing the sawdust concentration increases the pore size and porosity.

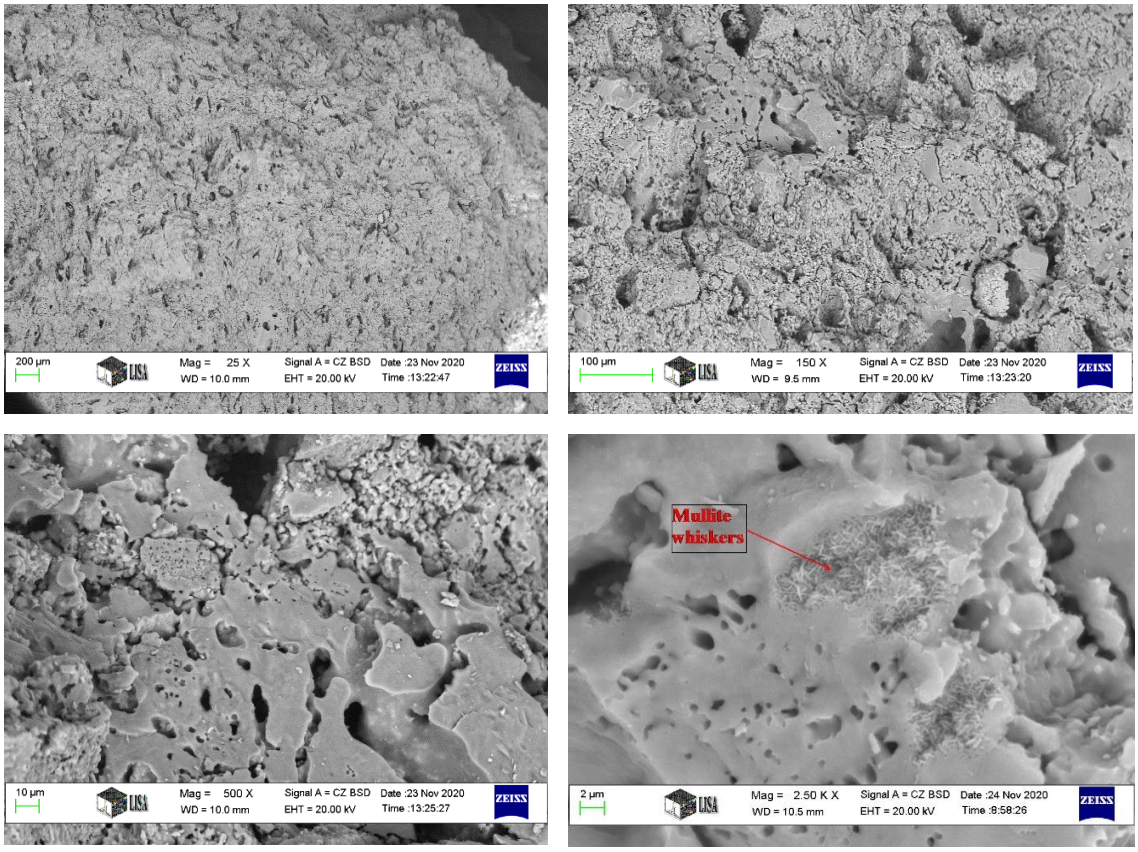

Figure 52. SEM images with different magnifications of the fracture surface of ZS8 sintered at 1150 °C

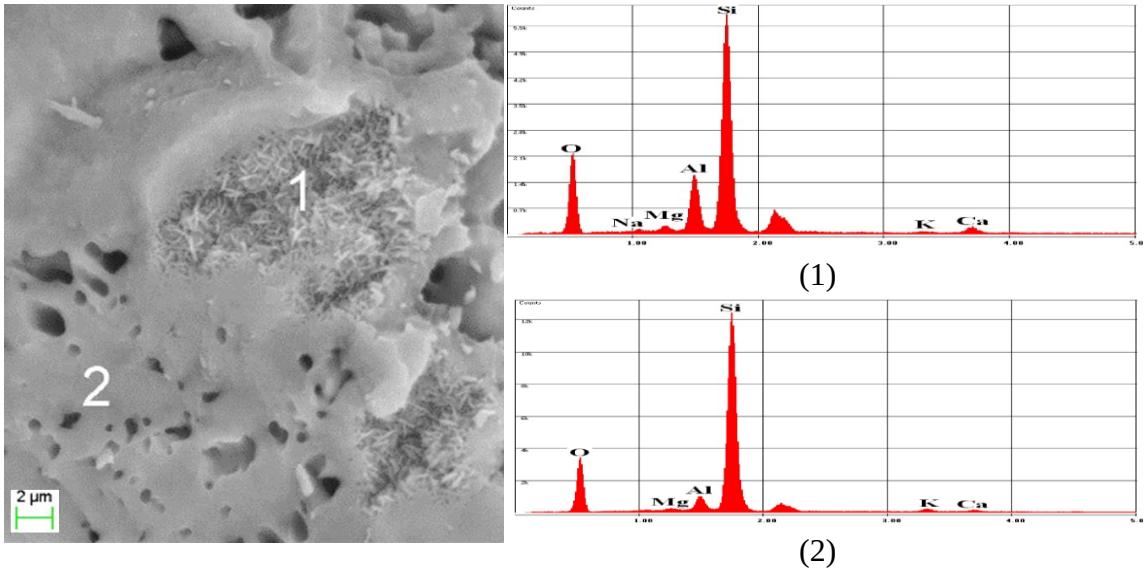

Figure 53. SEM and EDS micrograph of the fracture surface of ZS8 sintered at 1150 °C

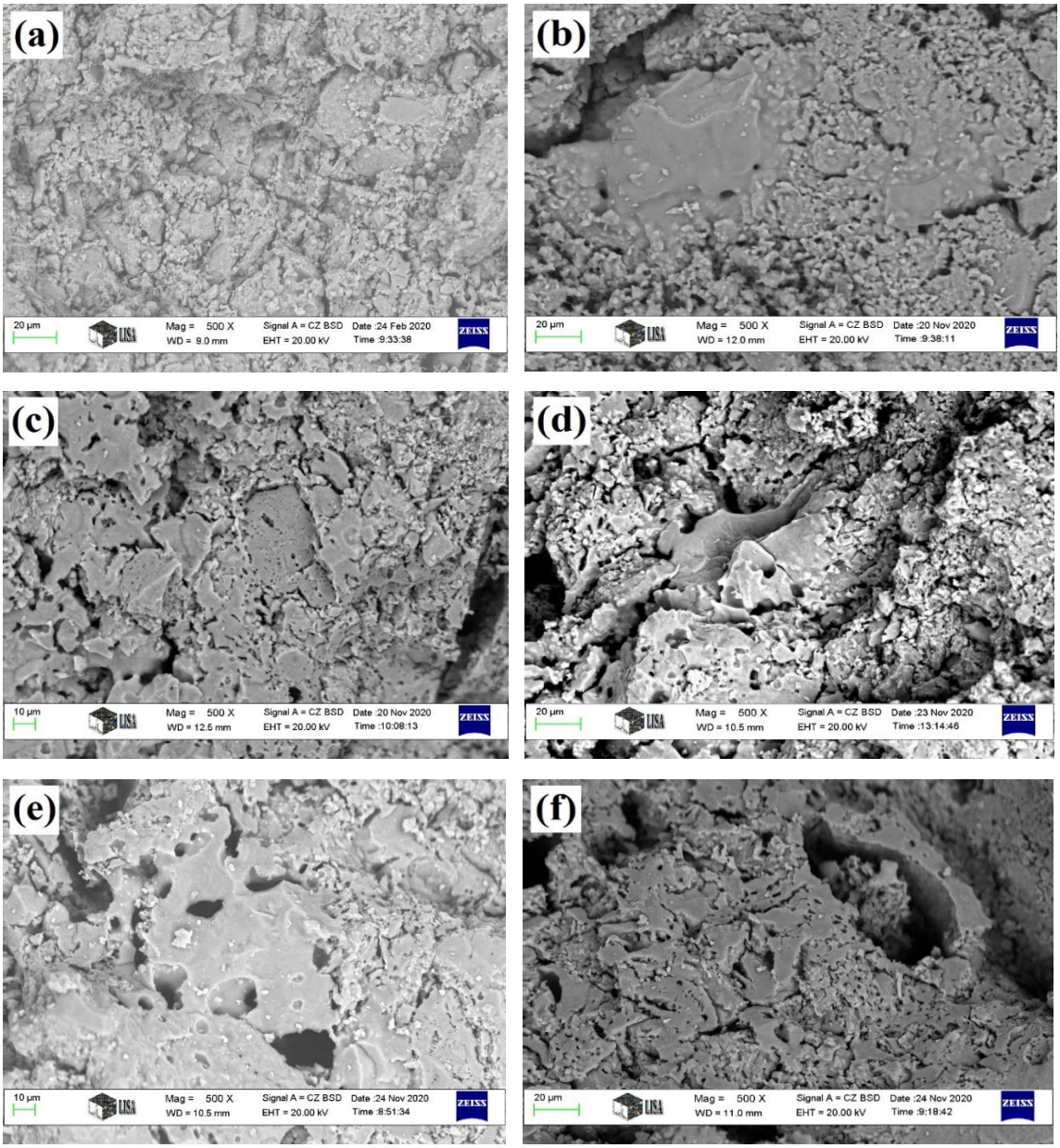

Figure 54. SEM images of the zeolite-poor rock ceramic bricks with different dosages of sawdust a) 0%, b) 2%, c) 4%, d) 6%, e) 8% and f) 10% sintered at 1150 °C

4.3.4. Bulk density of the fired zeolite-poor rock/sawdust bricks

The bulk densities of the zeolite-poor rock ceramic bricks with sawdust are illustrated in Fig. 55. The calculated densities values of the bricks are in the range of 1.4 to 1.88 g/cm^3. The blank samples have relatively higher bulk densities compared to the other samples. The bulk density tends to decrease with the increasing percentage of sawdust. This could be attributed to the burning of the sawdust during the sintering, forming several pores in the sample.

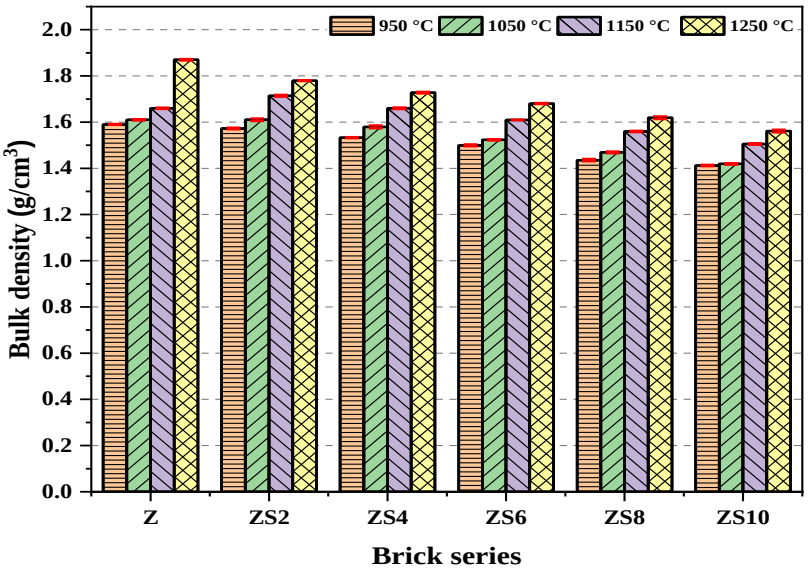

Figure 55. The bulk density of the zeolite-poor rock/sawdust ceramic bricks sintered at variable temperatures

4.3.5. Volume shrinkage of the fired zeolite-poor rock/sawdust bricks

The volume shrinkage of the sintered bricks is presented in Fig. 56; increasing the sintering temperature increases the brick's volume shrinkage. Similar findings were also obtained in other research works [15]. Upon raising the firing temperature, alkali oxides increase the amount of liquid-phase formation. This can increase vitrification, leading to a larger volume shrinkage. With increasing the sawdust content, the volume shrinkage is only slightly decreased in all sintering temperatures. This could be due to the lower melting amount from a relatively lower percentage of zeolite-poor rock used. The overall volume shrinkage of the sintered bricks lies in the range of 8–20%.

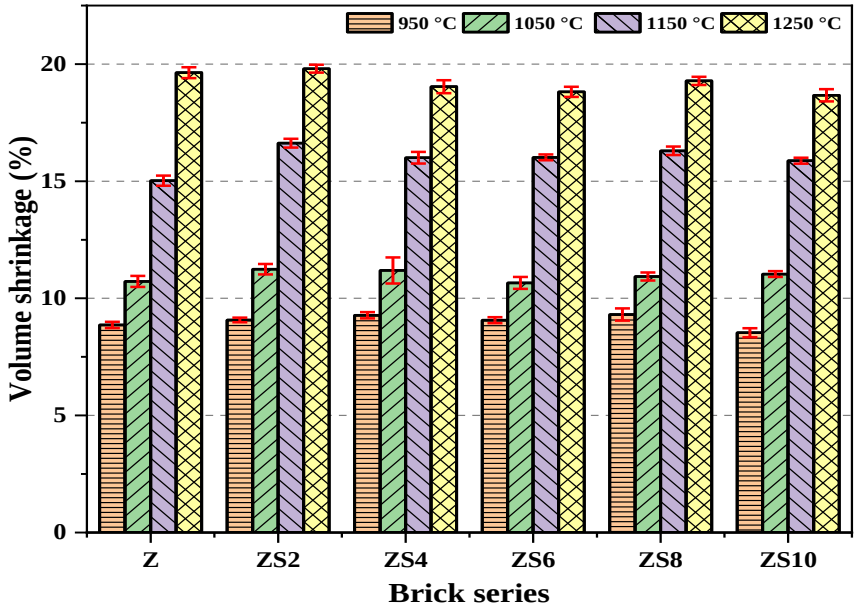

Figure 56. The volume shrinkage of the zeolite-poor rock/sawdust ceramic bricks sintered at variable temperatures

4.3.6. Apparent porosity and water absorption of the fired zeolite-poor rock/sawdust bricks

The average values of the ceramic bricks' apparent porosity and water absorption as a function of the amount of sawdust added and sintering temperature are determined according to ASTM C20 [201] (Figs 57 and 58). The apparent porosity tends to decrease with increasing the sintering temperature. This occurs due to the effect of sintering, shrinkage, and vitrification [84], which either fully or partially fill the pores through partial melting and atomic diffusion of the zeolite-poor rock materials into the pores. The existence of some fluxes (MgO, CaO, and Na_2O) in the zeolite-poor rock led to a low-temperature fusion followed by low-temperature vitrification. This can convert some of the open pores into closed pores. This phenomenon reduces water absorption as well (Fig 58).

The increase in the sawdust amount leads to an increase in the apparent porosity, therefore reducing the density [202]. During the bricks' firing, the sawdust components (hemicellulose, cellulose, and lignin) tend to gradually decompose and produce CO_2 gas and water vapour; these gases will move out, producing capillaries in the ceramic bricks. With increasing the sawdust, a viewer amount of zeolite-poor rock will be used; therefore, a relatively low amount of liquid phase will be produced during the fusion. Hence a relatively larger number of open pores will remain. This can explain the increase in porosity and water absorption. These results are in good agreement with the SEM micrograph of the bricks (Fig. 54) and are similar to some previous studies on clay bricks [203].

Water absorption is an essential factor that describes the durability of the bricks; lower water absorption bricks last long with a low tendency toward environmental damage [5]. The water absorption indicates the densification and its connection to the porosity in the materials [204]. In this work, the water absorption shows a minimum value for the blank bricks in all firing temperatures and a maximum value for the specimens containing 10% sawdust. Increasing the sawdust content increases the water absorption; this is coherent with the SEM investigation and porosity measurement. Despite the high differences in the samples' water absorption values, the result is still within the range of 10–30%. Previous studies in wastes incorporated clay bricks showed a water absorption of a similar value [5,205].

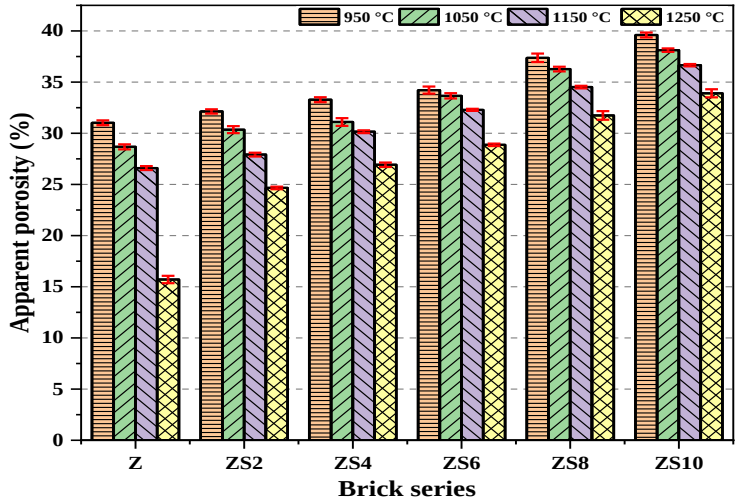

Figure 57. The open porosity of the zeolite-poor rock/sawdust ceramic bricks sintered at variable temperatures

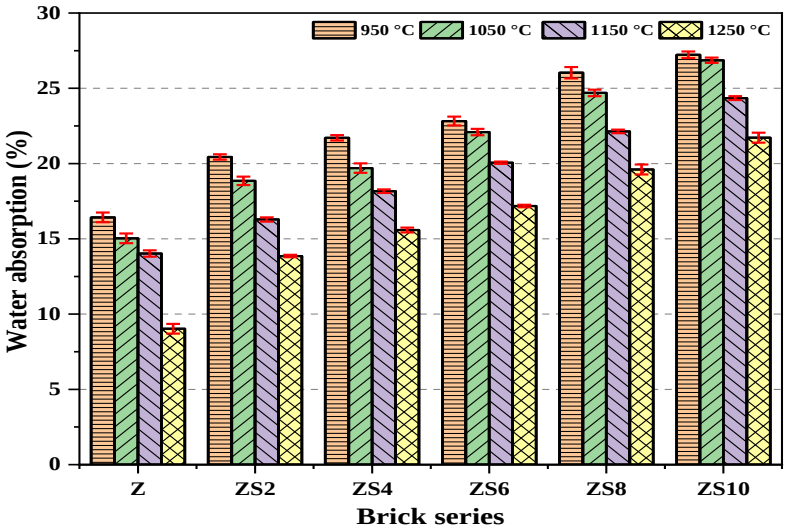

Figure 58. The water absorption of the zeolite-poor rock/sawdust ceramic bricks sintered at different temperatures

4.3.7. Thermal conductivity of the fired zeolite-poor rock/sawdust bricks

The thermal conductivity values of the different brick-containing sawdust samples as a function of firing temperatures are plotted in Fig. 59. The thermal conductivity of the ceramic samples increases with increasing the sintering temperature. The largest value of the thermal conductivity was 0.7 W/mK achieved when the reference sample was fired at 1250 °C, while the lowest value was 0.13 W/mK obtained from the samples containing 10% sawdust sintered at 950 °C. The thermal conductivity of the bricks containing sawdust is reduced by approximately 65% compared to that of the blank bricks. Thermal conductivity is well known to be connected to porosity since the open pores are usually filled with air, acting as an insulator and reducing thermal conductivity [206]. Increasing the sintering temperature produces a dense brick with lower porosity. This explains the increase in thermal conductivity. While incorporating sawdust creates a larger number of pores, which leads to a decrease in thermal conductivity.

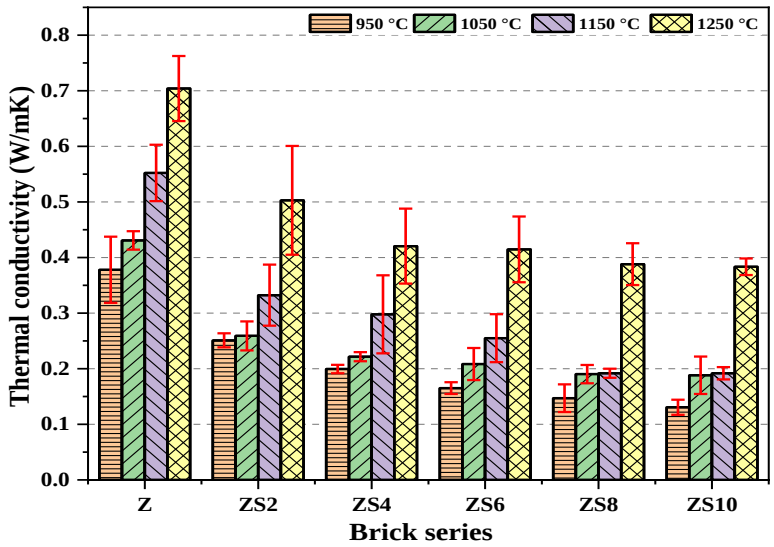

Figure 59. The thermal conductivity of the zeolite-poor rock/sawdust ceramic bricks sintered at variable temperatures

4.3.8. The compressive strength of the fired zeolite-poor rock/sawdust bricks

Compressive strength is a crucial factor that determines the quality and durability of the bricks. Fig. 60 illustrates the relationship between the average value of the compressive strength of the different zeolite-poor rock/sawdust samples and the sintering temperatures. The blank samples show higher strength compared to the hybrid bricks. The maximum compressive strength was 37 MPa obtained from the reference samples sintered at 1250 °C. The inclusion of sawdust in the zeolite-poor rock reduces the compressive strength in all sintering temperatures. The lowest strength value was obtained when the bricks containing 10% sawdust (ZS10) were sintered at 950 °C. Upon increasing the firing temperature, some minerals in zeolite-poor rock (montmorillonite, clinoptilolite, and calcite) decompose, followed by physicochemical reaction (formation of mullite and anorthite) as confirmed by the XRD test (Fig. 51). At high temperatures, zeolite starts to melt, and the liquid-phase sintering process densifies the samples and reduces the porosity. The increases in density can highly improve compressive strength. Another factor is the formation of the mullite whiskers, which start at a temperature above 1050 °C, as revealed in the XRD test (Fig. 51) and EDS analysis (Fig. 53). The mullite whiskers form an interlocked structure (Fig. 53) which may enhance the mechanical strength by crack deflection and whiskers pull out associated with energy absorbance [207-210]. In contrast, the addition of sawdust increases the porosity and reduces the density since the sawdust fired out, forming a large number of pores that can reduce the compressive strength. Based on the standard [211], the required compressive strength of the bricks is 5 MPa. The building bricks can be classified as first-class or second-class if their crushing strength is above 5 MPa and 7 MPa, respectively [212]. In this work, all the produced bricks show compressive strength above 7 MPa, except the samples that contain 10% sawdust fired at 950 °C, which offers a compressive strength of 4 MPa. Therefore, these bricks are suitable for construction applications.

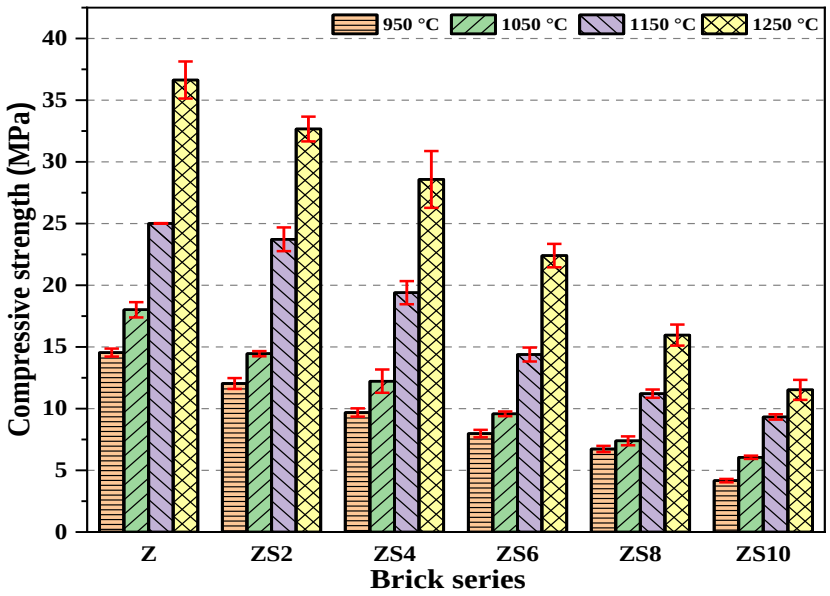

Figure 60. Compressive strength of the zeolite-poor rock/sawdust ceramic bricks sintered at variable temperatures

4.3.9. The correlation between density, thermal conductivity, and compressive strength of fired zeolite-poor rock/sawdust bricks

Fig. 61 depicts the connection between the developed specimens' density, thermal conductivity, and compressive strength. Densification causes a noticeable rise in both thermal conductivity and compressive strength because the densified structure has higher bonding and fewer pores.

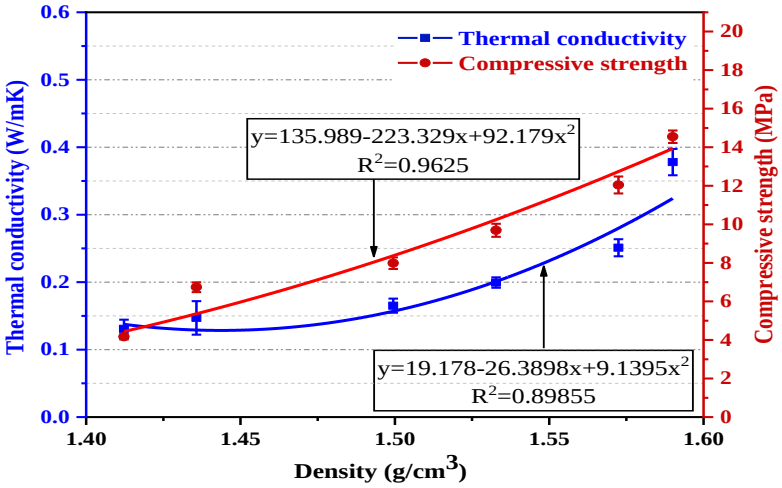

Figure 61. The correlation between thermal conductivity, density, and compressive strength of zeolite-poor rock/sawdust bricks with different compositions fired at 950 °C

4.3.10. The correlation between thermal conductivity, apparent porosity, and water absorption of fired zeolite-poor rock/eggshell bricks

Fig. 62 depicts the relationship between apparent porosity, thermal conductivity, and water absorption of produced bricks. Thermal conductivities tend to decrease as porosity increases. Normally, open holes are filled with air, which serves as an insulator and reduces heat conductivity, while porosity increases water absorption. This is due to the fact that normally open pores reflect water absorption capability since water can be easily leaked into the open pores.

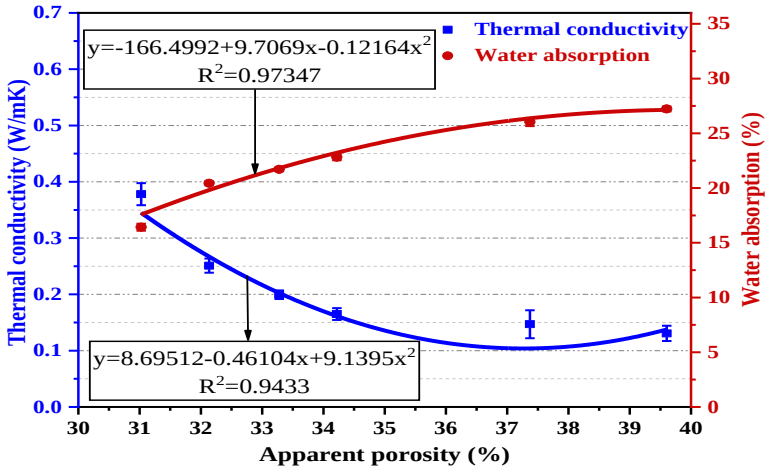

Figure 62. The correlation between apparent porosity, thermal conductivity, and water absorption of zeolite/sawdust composite bricks with different compositions sintered at 950 °C

4.4. Discussion and conclusions

Objective listed in Chapter 1.1 and the answers:

- **To evaluate different types of local solid wastes, including sawdust, for integration into ceramic specimens. Furthermore, to estimate the proper mixing proportions, then to prepare various mixtures of zeolite-poor rock and sawdust through mechanical activation using a ball mill operating at optimal conditions.**

Sawdust has been evaluated as a potential candidate for the preparation of porous bricks and glass-ceramic foams because it is an available waste material. Moreover, sawdust can cause some environmental problems by contaminating both soil and water. It generally keeps a high moisture content enabling the growth of several kinds of fungus, which subsequently spread to neighbouring plants causing them to decompose. Therefore, recycling sawdust could be the best alternative to avoid this environmental problem. During the heat treatment process, large amounts of sawdust decompose and produce gases that are responsible for the formation of the pores in the zeolite-poor rock bricks. In this work, sawdust was added as a partial replacement for zeolite-poor rock in the specimens. The replacement percentages were 0%, 2%, 4%, 6%, 8% and 10% by mass of zeolite-poor rock. The restrictions for the inclusion of the sawdust arise from the increase of water absorption value and the decrease of mechanical strength. Up to 10% sawdust was found to be suitable for inclusion into zeolite-poor rock. Milling at 200 rpm for 10 min was found to be a suitable condition for producing fine mixtures above which coarse particles have been produced.

- **To experimentally prepare green ceramic specimens using uniaxial dry pressing and investigate their characteristics**

Zeolite-poor rock and sawdust possess large numbers of open pores, which normally fill with moisture that helps in compaction during the dry forming process. Based on the experimental work, the uniaxial pressing at 40 MPa was found to be suitable for producing compacted green ceramic samples that can be easily handled and sintered to produce bricks with good compressive strength.

- **To suggest an appropriate, cost-effective sintering curve (sintering temperature and residence time) for the preparation of zeolite-poor rock incorporated sawdust ceramic samples.**

Sintering is considered one of the important processes in the production of bricks. In the mass production of bricks, reducing the sintering temperature and residence time are crucial for the preparation of a cost-effective product. TG/DTA and XRD investigations of the samples suggest that the suitable sintering temperature could be around 1000 °C, where the decomposition of raw materials and physicochemical reactions are taking place, resulting in bricks with good mechanical strength. The incorporation of sawdust can also contribute to the heating, reducing the sintering temperature and residence time. Furthermore, it induces the formation of a whiskers-like mullite structure. The experimental finding suggests that the optimal sintering temperature is in the range of 950-1000 °C and the suitable residence time is 3-4 hours.

- **To assess the influence of solid waste inclusion on the technical characteristics of the produced ceramic bricks and foams, such as bulk density, shrinkage, apparent porosity, water absorption, thermal conductivity, and compressive strength based on international standards**

The result of this research reveals that sawdust can effectively be used as a pore-forming agent in zeolite-poor rock bricks. The bulk density of the prepared samples decreased with the inclusion of sawdust from approximately 1.88 g/cm^3 of control bricks to about 1.4 g/cm^3 of the bricks with 10% sawdust. This can lead to the production of lightweight bricks due to the increased number of pores produced by the combustion of the organic content in sawdust, as shown in TG–DTA analysis. The heat generated during the combustion of sawdust can contribute to the heat requirements during the manufacturing process.
The inclusion of sawdust in the zeolite-poor rock body raised the number of open pores from 26% for the blank samples to about 36% for the bricks containing 10% sawdust, making a total increase of 38%, as confirmed by the SEM analysis and water absorption measurements, and therefore, decreases the compressive strength of the bricks while enhancing their thermal insulation characteristics. Most of the samples showed a compressive strength of more than 7 MPa, making them first-class bricks for construction applications. Zeolite-poor rock and sawdust are available materials that could prepare lightweight bricks with excellent thermal insulation properties, contributing to better sustainability and safe disposal of sawdust.

- **To compare the results of the technical properties of the prepared zeolite-poor rock/sawdust specimens to that of the current literature in the field of burned ceramic bricks.**

The quality and durability of the brick are determined by a number of factors, including the raw material composition, shaping techniques and sintering method. These variables can influence the brick's technical properties, such as density, compressive strength, thermal properties, and so on. The influence of various waste materials as an additive for fired brick production has been investigated by a number of researchers. Table 3 summarizes the findings of several experiments on the use of various waste materials to produce fired bricks that have been reported in the literature. In most of the studies, the inclusion of waste materials increases water absorption, porosity and decreases compressive strength. When comparing the findings of this study to those in Table 3, it is worth noting that zeolite-poor rock incorporated sawdust is a promising material for brick-making, as it has higher compressive strengths and better insulation properties than many of the studies listed in Table 3.

Conclusions

- **It was proved that it is possible to produce innovative building bricks with low density (1.4–1.88 g/cm^3) and low thermal conductivity (0.13–0.7 W/mk) based on zeolite-poor rock (D <100 µm) together with sawdust (D90<100 µm). Sawdust was added as a partial replacement for zeolite-poor rock in the specimens. The replacement percentages of sawdust were 0–10 wt% by mass of zeolite-poor rock. The mixed powders were milled for 15 min at 150 rpm to produce homogenous mixtures. The prepared mixtures were pressed at 40 MPa. The produced green**

ceramic samples were then sintered at variable temperatures (950, 1050, 1150, and 1250 °C) for 3 h holding time and a heating rate of 60 °C/h.

- **I established that the inclusion of 8 wt% sawdust (D90 <100 µm) into zeolite-poor rock powder (D <100 µm) followed by ball milling for 15 min at 150 rpm, dry pressing at 40 MPa and sintering at a temperature range of 950-1250 °C with a residence time of 3 h and a heating rate of 60 °C/h resulted in bricks with an irregular porous structure having large numbers of open pores (Fig. 52).**
- **I established that the inclusion of 8% sawdust into zeolite-poor rock (D <100 µm), followed by the ball milling for 15 min at 150 rpm, dry pressing at 45 MPa and sintering at a temperature range of 950-1250 °C with a residence time of 3 h contributes to the firing raising the temperature. As a result, a mullite phase in a whisker-like structure has been formed at a relatively lower temperature (1150 °C), as confirmed by SEM and EDS (Fig. 53).**

4.5. Result of innovative composite bricks based on zeolite-poor rock and hen's eggshell

4.5.1. Dimensional properties of fired zeolite-poor rock/eggshell bricks

The zeolite-poor rock bodies could sustain the addition of eggshell powder in different percentages, as can be seen in the produced composite bricks heat-treated at variable temperatures (Fig. 63). With increasing the firing temperature, variations in the colours of the sintered bricks were noticed. The key alterations that the samples underwent throughout the heat treatment process were decomposition and phase transformation accompanied by volume shrinkage. The produced zeolite-based composite bricks have excellent surface finishing, which can be used as facing bricks.

950 °C 1050 °C 1150 °C

Figure 63. Prototype zeolite-poor rock/eggshell ceramic bricks sintered at variable temperatures

4.5.2. XRD analysis of fired zeolite-poor rock/eggshell bricks

Fig. 64 shows the X-ray diffractogram that indicates the crystallinity and phase identification of the composite brick containing different amounts of eggshell fired at 1050 °C.

Upon increasing the firing temperature, the clay minerals (montmorillonite), zeolite (clinoptilolite), and silica (quartz, cristobalite) exist in zeolite-poor rock, react with calcite and other constituents in eggshell. This reaction led to the formation of new crystalline vitreous phases that influenced the physical and mechanical properties of the produced brick. It can be seen that all CaO, which results from the decomposition of calcite, exists in the eggshell react with the minerals in the zeolite-poor rock and form anorthite, bytownite, and wollastonite in the composite bricks structure. This could be the reason beyond the good compressive strength of the samples.

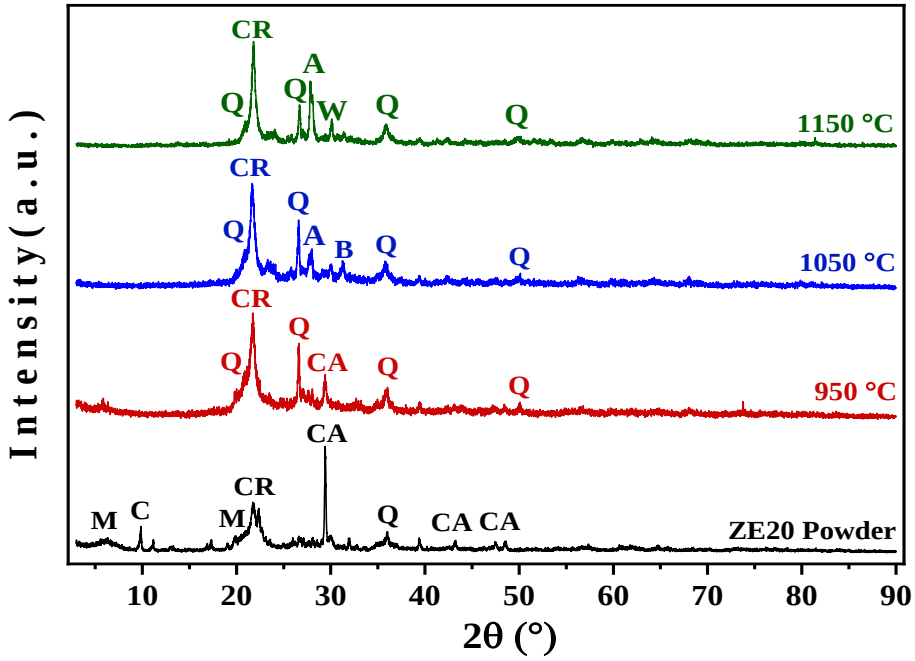

Figure 64. XRD analysis of zeolite-poor rock containing 20% eggshell (ZE20) fired at different temperatures, M= montmorillonite, C= clinoptilolite, CR= cristobalite, Q= quartz, CA= calcite, A= anorthite, W= wollastonite, B= bytownite

4.5.3. SEM examination of fired zeolite-poor rock/eggshell bricks

The fracture surface morphology of the produced composite (ZE20) with different magnifications (100X-2500X) is illustrated in Fig. 65. At 1000 magnification (Fig. 65.c), a large number of closed pores can be seen together with the open pores. This could be created due to the decomposition of the calcite in the eggshell associated with the emission of the CO_2, which could be trapped in the zeolite-poor rock body forming close pores. These pores can play a crucial role in enhancing thermal insulation of composite ceramic bricks. SEM images of the composite bricks with various eggshell concentrations are shown in Fig. 66. The porosity of the produced ceramic bricks increases as the concentration of eggshell rises.

Fig. 67 demonstrates the liquid-phase formation, which occurs at higher temperatures due to the existence of some fluxes (MgO, Na_2O, and CaO) that lead to lower-temperature vitrification. It is worth mentioning that the addition of eggshell induces the formation of a larger amount of liquid phase, as can be seen in Fig. 67.

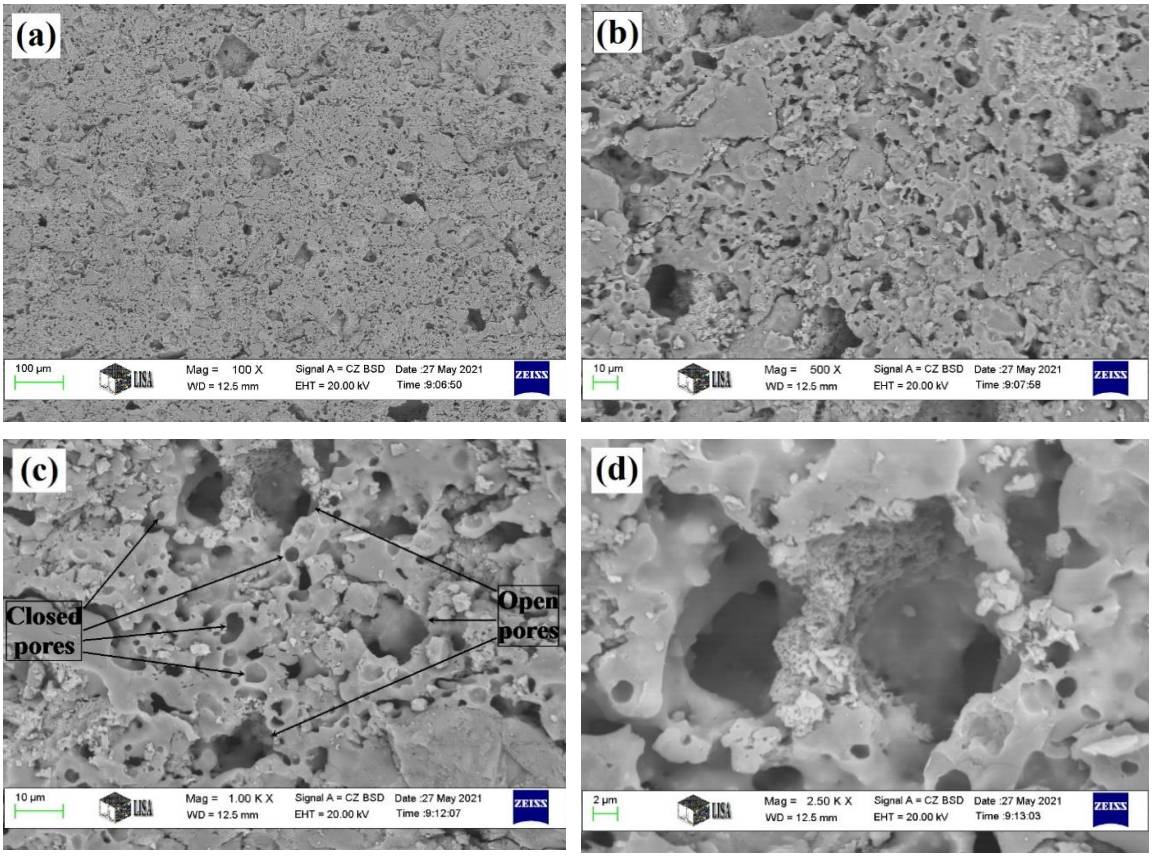

Figure 65. SEM micrograph of the fracture surface of ZE20 with different magnifications sintered at 1050 °C. a-100X; b-500X; c-1000X; d-2500X

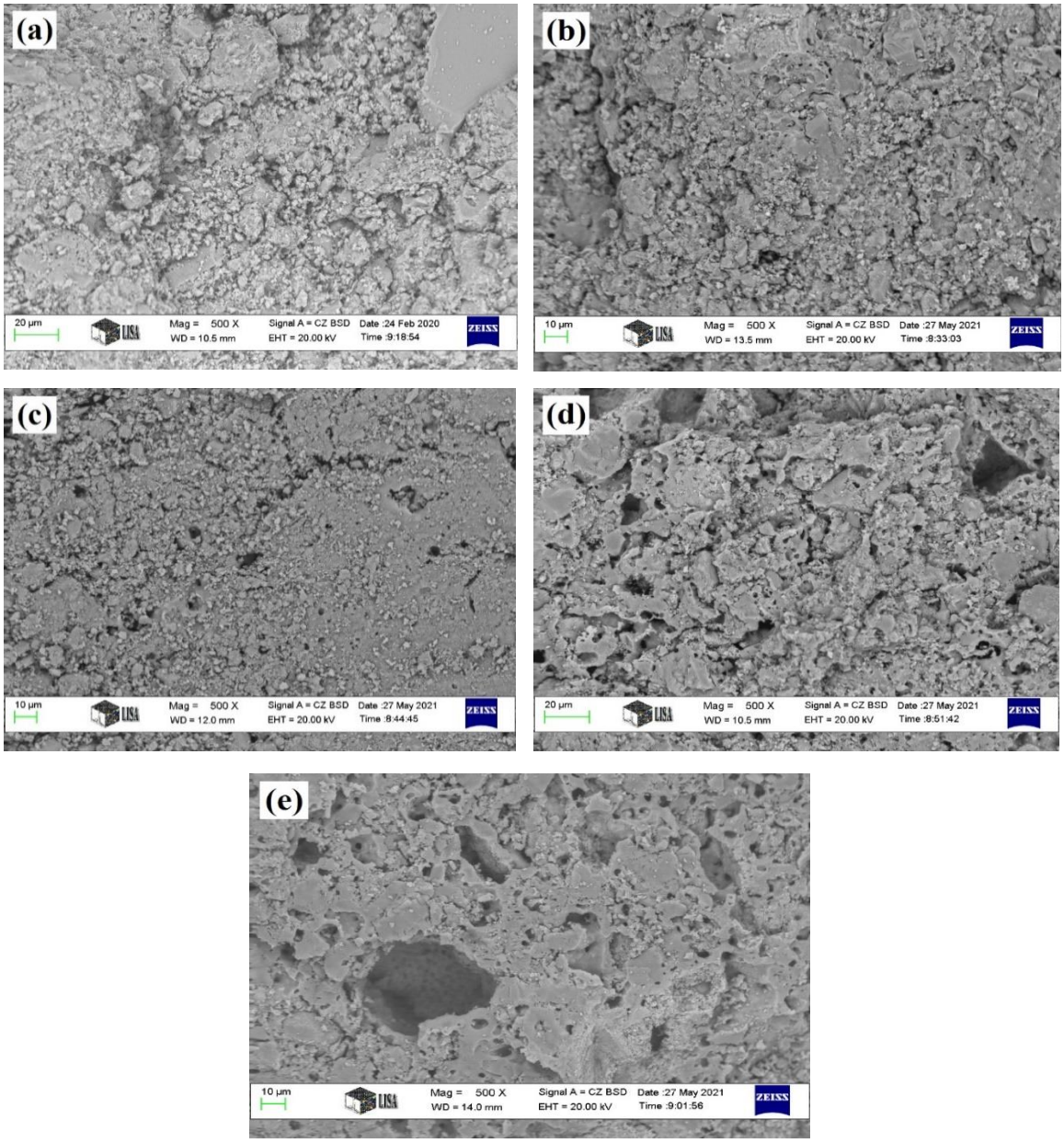

Figure 66. SEM micrographs of produced zeolite-poor rock containing eggshell composite ceramic bricks with (a) 0% (b) 5% (c) 10% (d) 15% and (e) 20% eggshell.

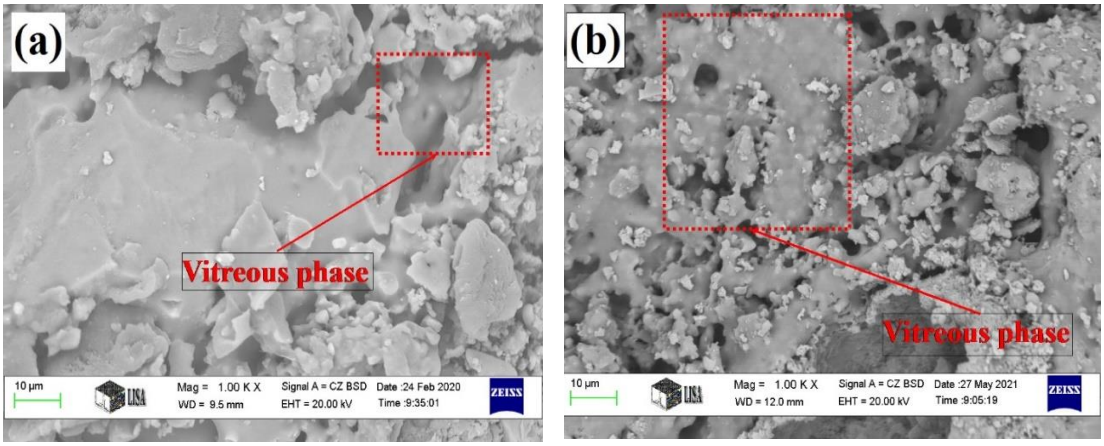

Figure 67. SEM images of (a) Z (blank) and (b) ZE10 samples sintered at 1050 °C

4.5.4. Bulk density of fired zeolite-poor rock/eggshell bricks

The bulk density of produced zeolite-poor rock/eggshell composite bricks as a function of eggshell fraction and sintering temperature is shown in Fig. 68. In general, the bulk density of the samples from all groups indicated a gradual decrease with increasing eggshell. This could be due to the fact that at 900 °C, vitrification will take place associated with CO_2 emission resulting from the decomposition of calcite contained in raw materials (zeolite-poor rock and eggshell), part of the gas will be released, making open pores and capillaries in the brick body while the viscous phase holds part of the gas inside making closed pores, the higher amount of eggshell release a larger amount of CO_2 which resulted in higher porosity and low density of the samples. The bulk density of the produced zeolite-poor rock/eggshell composite bricks dropped from 1.76 g/cm^3 for reference ceramic bricks to 1.45 g/cm^3 for ceramic bricks with 20% eggshell, making a decrease of 17.61% in density. The samples in all the batches showed an increasing value of density with increasing the firing temperature. This could be attributed to the improved sintering and densification induced by increasing the firing temperature. A similar fashion was observed in the previous works in clay bricks.

The bulk density indicates the degree of densification. Based on ASTM C90, the densities of burnt ceramic bricks are categorized as lightweight (less than 1.68 g/cm^3), medium weight (1.68–2 g/cm^3), and standard weight (greater than 2.00 g/cm^3). All the blank samples fired at variable temperatures are categorized as medium weight. In contrast, all the samples containing eggshell sintered at various temperatures possess lightweight.

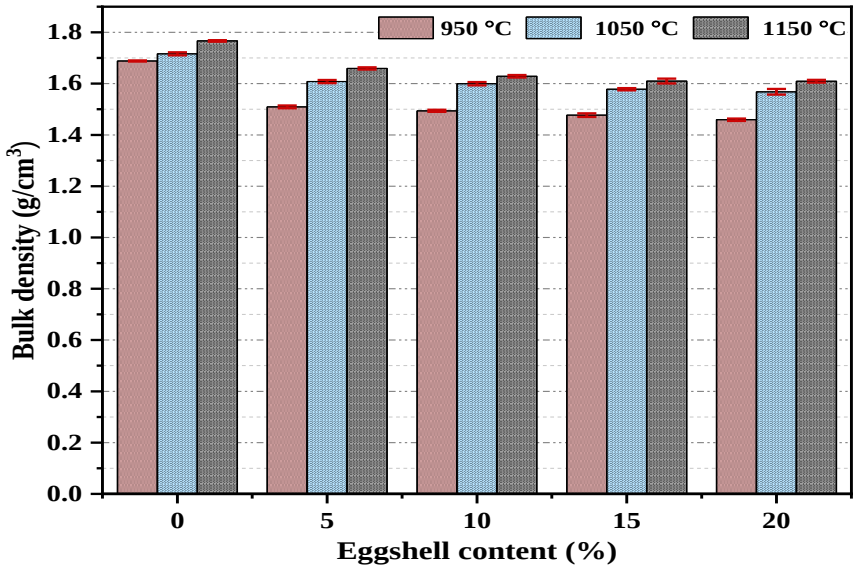

Figure 68. The effect of eggshell content on the bulk density of composite ceramic bricks sintered at different temperatures

4.5.5. Volume shrinkage of fired zeolite-poor rock/eggshell bricks

The volume shrinkage of the zeolite-poor rock/eggshell composite bricks fired at a temperature range of 950–1150 °C is depicted in Fig. 69. With a rise in sintering temperature, the volume shrinkage of the sample showed an increasing tendency. This could be attributed to the liquid-phase sintering induced by the increasing temperature. Furthermore, all the samples reveal an increase in volume shrinkage as the eggshell content increases. The highest volume shrinkage was 12.6%, obtained from ZE20 fired at 1150 °C, while the lowest linear shrinkage was around 3.01%, achieved from ZE0 sintered at 950 °C.

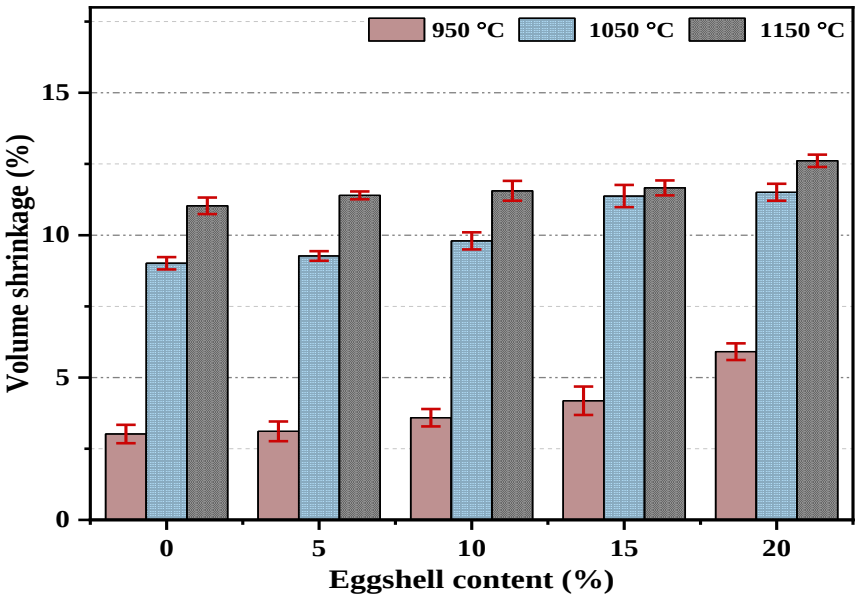

Figure 69. The effect of eggshell content on the volume shrinkage of composite bricks fired at different temperatures

4.5.6. Apparent porosity of fired zeolite-poor rock/eggshell bricks

The average values of the apparent porosity of zeolite-poor rock/eggshell composite bricks based on eggshell content and firing temperature are demonstrated in Fig. 70. The apparent porosity is gradually increased with increasing the eggshell content. This could be due to the fact that, upon sintering, the calcite in eggshell tends to progressively disintegrate and create CO_2 gas; the emission of CO_2 gas results in the formation of several types of pores (open, close, and capillaries), which increased the apparent porosity. All the samples showed decreasing trends in apparent porosity as the sintering temperature increased. This could be due to vitrification, which normally begins at around 900 °C. The existence of alkaline oxides (fluxing agents), primarily MgO, Na_2O, and CaO, cause lower temperature melting, which promotes the quantity of liquid phase generated. This process can lead to lower temperature vitrification, accompanied by the tendency of the particles to reduce their surface area during sintering. This can aid in inter-particle adhesion and densification of the ceramic framework. The most intensive decomposition of the calcite in the eggshell takes place around 892 °C, as revealed in TG/ DTA curve Fig. 48. The release of CO_2 gas in the liquid phase matrix leads to the creation of a large number of pores that grow rounder and narrower as sintering proceeds. Some pores are then totally separated from the surface and subsequently closed. Above 950 °C, sintering is intensified, forming a liquid phase. This phase enters the pores, seals them closed, and subsequently isolates them from neighbouring pores, hence reducing the pore's size. This explains the decrease in porosity with increasing temperature. This behaviour is in agreement with previous literature.

Table. 13 shows the closed porosity of the sample sintered at 1050 °C evaluated using ImageJ. It can be clearly seen that increasing the eggshell content promotes the formation of closed pores. This could be due to the larger amount of gas emission associated with an increasing amount of eggshell.

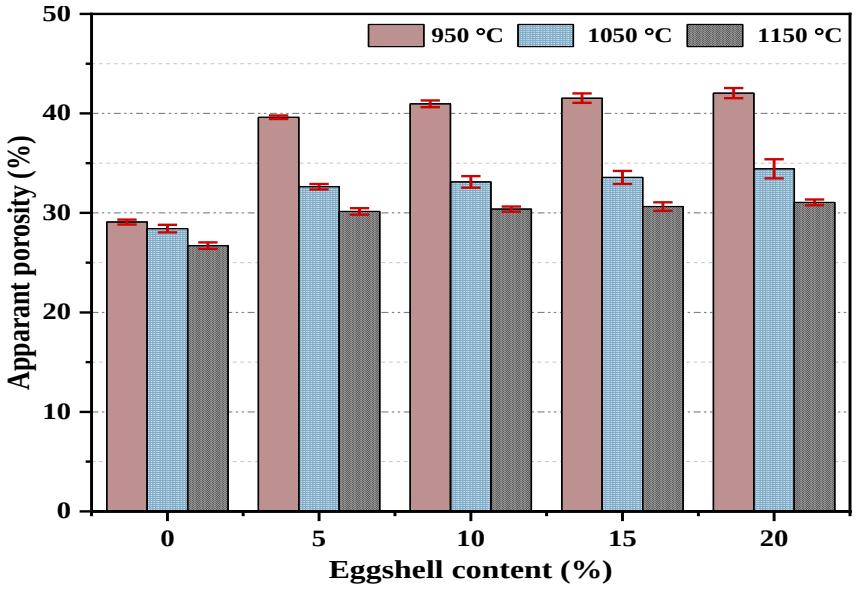

Figure 70. The effect of eggshell content on the apparent porosity of composite ceramic bricks fired at different temperatures

Table 13. Closed porosity of the samples sintered at 1050 °C as determined by ImageJ

Sample	Z	ZE5	ZE10	ZE15	ZE20
Closed porosity (%)	4.2	6.906	9.650	17.40	28.102

4.5.7. Water absorption of fired zeolite-poor rock/eggshell bricks

One of the most important behaviours of building materials is durability which is thought to be directly linked to the level of water absorption and compressive strength. Water absorption is a critical factor in determining its environmental resilience. The resistance to weathering of ceramic bricks increases as the water absorption of the ceramic bricks decreases. The fundamental deteriorating mechanisms that originate the destruction of building bricks due to high water absorption are freezing-thawing, wetting-drying, and soluble salt crystallization, which can initiate stress that forms microcracks followed by crack propagation. Water absorption is well known to be highly linked to porosity, especially the open pores, which are interconnected to the specimen's surface since the water normally goes to the pores of the specimens. Therefore, they both show similar trends. They rose approximately linearly with an increase in eggshell concentration. This connection is confirmed in previous research works. The highest value of water absorption was found to be 28.8%, obtained from the sample containing 20% eggshell. In contrast, the blank samples yielded the lowest water absorption value of 13.1% (Fig. 71).

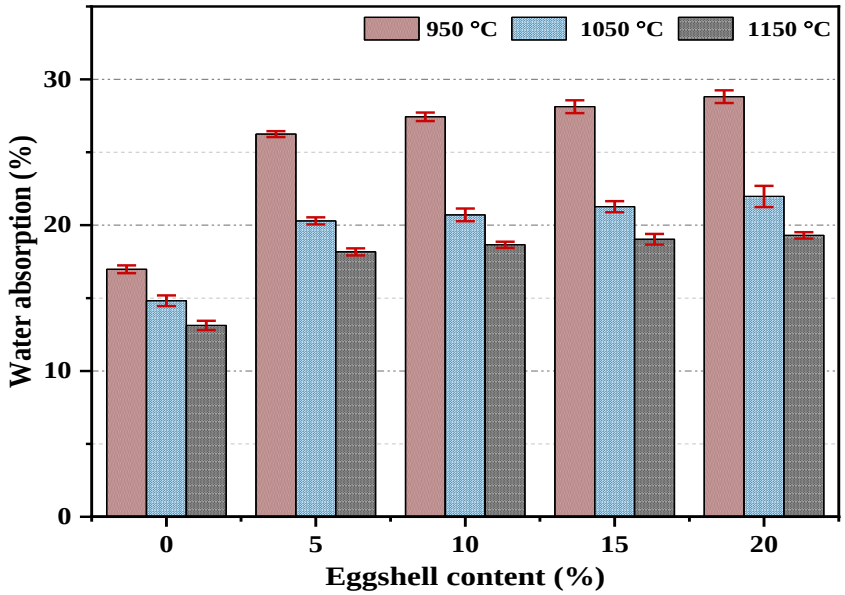

Figure 71. The effect of eggshell content on the water absorption of composite ceramic bricks fired at different temperatures

4.5.8. Efflorescence of fired zeolite-poor rock/eggshell bricks

The recrystallization of soluble salts that migrate from the bulk of the specimens to or near the surface is known as efflorescence which can be found in a variety of forms like calcium carbonates, calcium sulphates, alkaline sulphates, etc. This visual problem shows as a thin layer of white salt normally appears on the building ceramic bricks with porous structures. The

efflorescence test was carried out on the samples with different compositions. All the samples were half immersed in the distilled water for 7 days, followed by room temperature drying; then, the immersed areas of the samples were examined for the formation of white or grey layers and compared to the no-soaked areas. All the samples show no formation of any salts on the surfaces, indicating a "Nil" efflorescence (Fig. 72). The "Nil" efflorescence could be attributed to the complete reaction of CaO resulting from the decomposition of eggshell with other minerals that exist in the zeolite-poor rock during the sintering process and formation of new phases. This result is in good agreement with the XRD result (Fig. 64). The existence of free CaO in the brick is crucial because when exposed to moisture, CaO reacts quickly and transforms into portlandite ($Ca(OH)_2$). This is an exothermic process that results in a significant increase in volume. Furthermore, the portlandite interacts with CO_2 to create $CaCO_3$, causing a further increase in volume and greater fracture tendency. The efflorescence test was also carried out on commercial masonry bricks, which showed a considerable amount of white salt on the surface Fig 73.

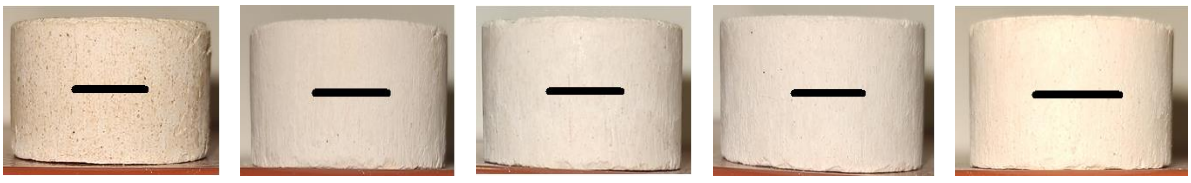

Figure 72. Zeolite-poor rock/eggshell ceramic bricks after the efflorescence test

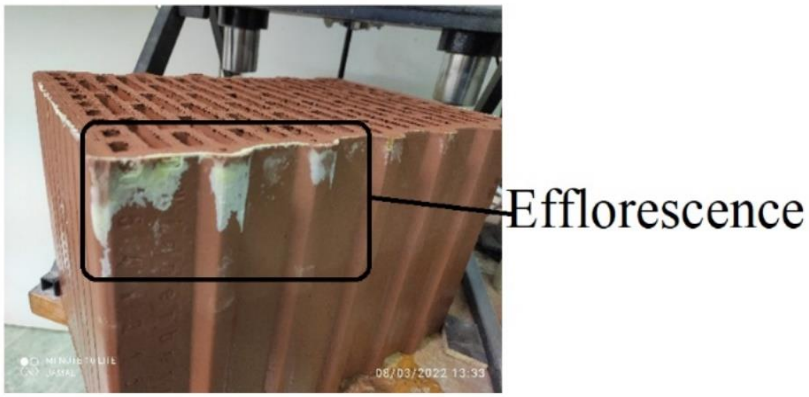

Figure 73. Efflorescence in masonry brick after immersing in water for a week followed by room temperature drying

After the efflorescence test, the remaining water was tested for the TDS (Fig. 74). The value of the TDS obtained from the remaining water of the zeolite-poor rock-based bricks was very low, between 13–27.5 ppm (TDS for drinking water is 50–150 ppm), confirming the "Nil" efflorescence in the bricks (Table. 14). While that of commercial bricks was in the range of 315–1740 ppm, indicating the possibility of efflorescence formation (Table. 15).

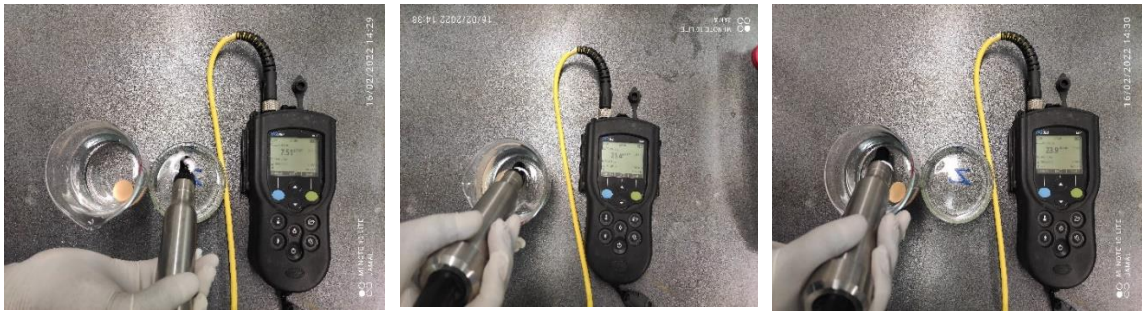

Figure 74. The TDS test for water after a week of immersing zeolite-poor rock-based bricks

Table 14. TDS test of water obtained from the immersion of different samples.

Samples	Deionized Water	Z bricks (blank)	Z+4% sawdust brick	Z+8% sawdust brick	Z+10% eggshell brick	Z+20% eggshell brick
TDS (ppm)	4.8	13.4	14.7	15.4	21.1	27.5

Z= Zeolite-poor rock, TDS= total dissolved solids

Table 15. TDS test of water obtained from the immersion of commercial bricks.

Samples	Red clay bricks	Red clay bricks	Masonry bricks
TDS (ppm)	1740	474	315

4.5.9. Thermal conductivity of fired zeolite-poor rock/eggshell bricks

Fig. 75 depicts the results of the thermal conductivity of the reference samples as well as the eggshell-containing ceramic bricks sintered at different temperatures. It can be observed that increasing the eggshell content reduces thermal conductivity due to the decomposition of calcite in the eggshell associated with pores formation. This is in line with earlier research on clay bricks that include waste marble sludge (carbonate) [213]. The pore-generating technique is a straightforward approach to reducing thermal conductivity, thanks to the combustion of the organic materials that occur during the sintering process, resulting in the formation of micro-pores in the brick body. As a consequence, lightweight ceramic bricks with improved thermal insulation are produced. Aside from the impact of the eggshell addition, firing temperature considerably impacts thermal conductivity. Increasing the firing temperatures promotes the creation of the liquid phase and densification of the samples, decreasing the pore volume and porosity and increasing the thermal conductivity. The ceramic bricks containing 20% eggshell sintered at 950 °C had the highest reduction in thermal conductivity, with a 40% drop. These findings are linked to the absorption and porosity investigation since mixes with a greater eggshell' concentration were shown to be more permeable and porous. Lower thermal conductivity is advantageous since it reduces the amount of energy required for heating and cooling buildings.

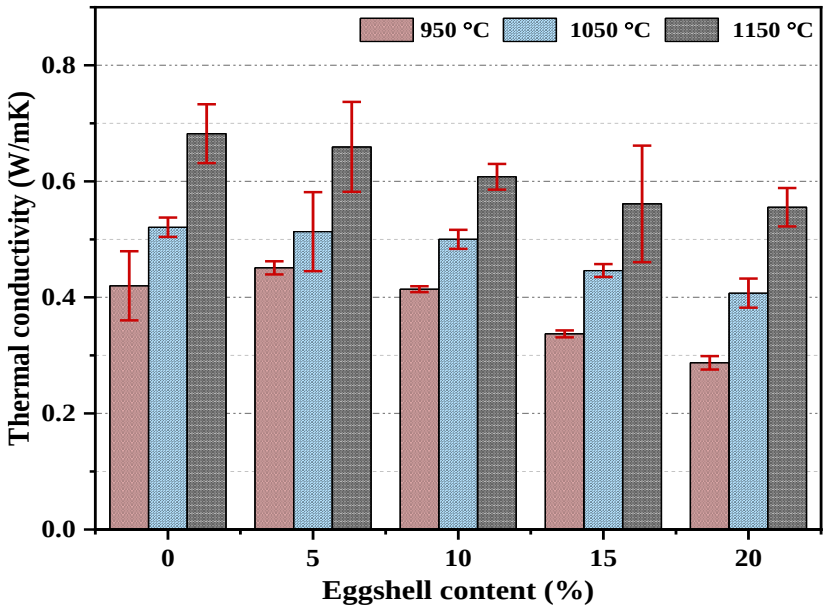

Figure 75. The effect of eggshell content on the thermal conductivity of composite ceramic bricks fired at different temperatures

4.5.10. The compressive strength of fired zeolite-poor rock/eggshell bricks

The compressive strength test is carried out in a cylindrical sample. Normally the cubic samples show higher compressive strength than the cylindrical ones. This could be due to the fact that normally lateral tensions in the cubic specimens are caused by frictional reactions between the specimen and machine platens. As a result, multiaxial specimens are produced. In a cone-shaped or pyramid-shaped area, lateral stresses impact the specimen stress state; therefore, cubes are predicted to have larger strength than cylinders. Normally the cube strength is approximately 1.15 times that of the cylinder.

The compressive strength of the examined ceramic bricks decreases with increasing eggshell content (Fig. 76). The inclusion of eggshell reduces the compressive strength due to the formation of a porous structure. On the other hand, increasing the sintering temperature improves the compressive strength due to the formation of a dense structure. Similar findings have been obtained with the inclusion of carbonate in clay bricks. The produced zeolite-poor rock/eggshell composite bricks have compressive strengths ranging from 10.3 to 25.3 MPa. The greatest compressive strengths were obtained in the blank samples sintered at 1150 °C, whereas the minimum compressive values were measured in 20% eggshell bricks sintered at 950 °C.

The minimum range of compressive strength of load-bearing building bricks required by the standards is 6–12 MPa. All the samples showed compressive strength values greater than the standard's minimal requirement for load-bearing building ceramic bricks.

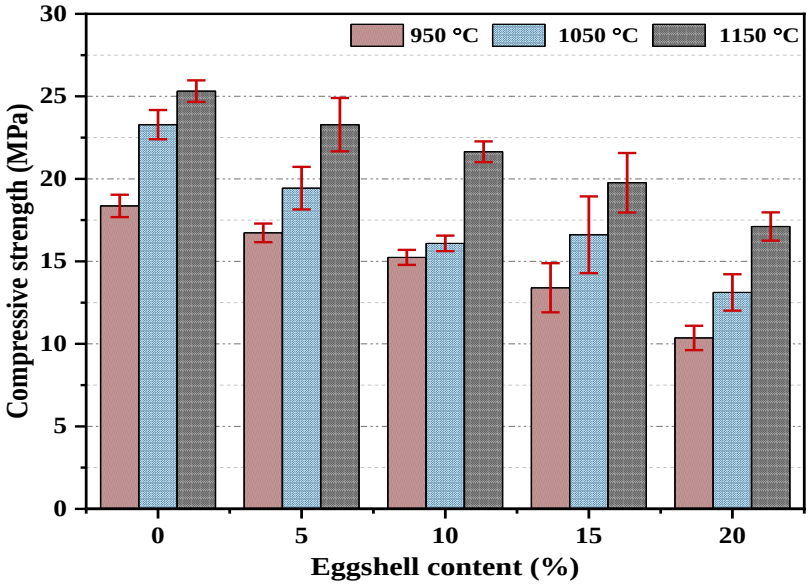

Figure 76. The effect of eggshell content on the compressive strength of composite ceramic bricks fired at different temperatures

4.5.11. The correlation between density, thermal conductivity, and compressive strength of fired zeolite-poor rock/eggshell bricks

Fig. 77 illustrates the relationship between density, thermal conductivity, and compressive strength of the produced specimens. Increasing the density leads to a linear-like increase in thermal conductivity and compressive strength because the densified structure normally has better adhesion and low pores.

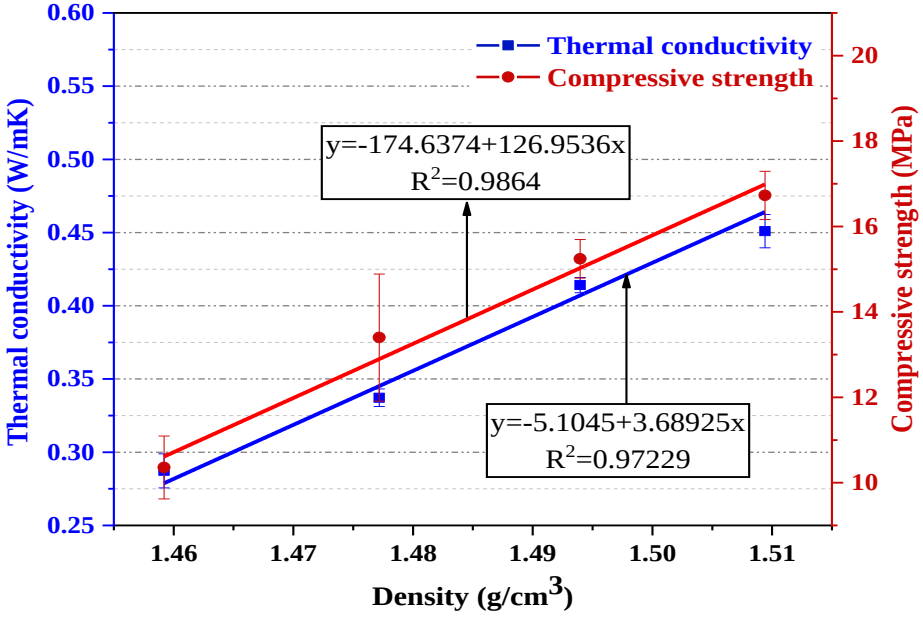

Figure 77. The correlation between thermal conductivity, density, and compressive strength of composite ceramic bricks with different compositions fired at 950 °C

4.5.12. The correlation between thermal conductivity, apparent porosity, and water absorption of fired zeolite-poor rock/eggshell bricks

The apparent porosity has generally been considered to be linked to thermal conductivity and water absorption. Nonetheless, even for ceramic materials with the same value of apparent porosity, thermal conductivity can vary significantly. The chemical composition, as well as the characteristics of the pore size and structure, may be accountable for these differences. The water absorption increases with increasing apparent porosity, as shown in Fig. 78. This could be due to the fact that normally open pores reflect the water absorption capacity. In contrast, the thermal conductivity decreases with increasing the apparent porosity. Normally the open pores are filled with air which acts as an insulator reducing thermal conductivity. M. J. Munir *et al.* reported similar findings when waste marble sludge was added to clay bricks [26].

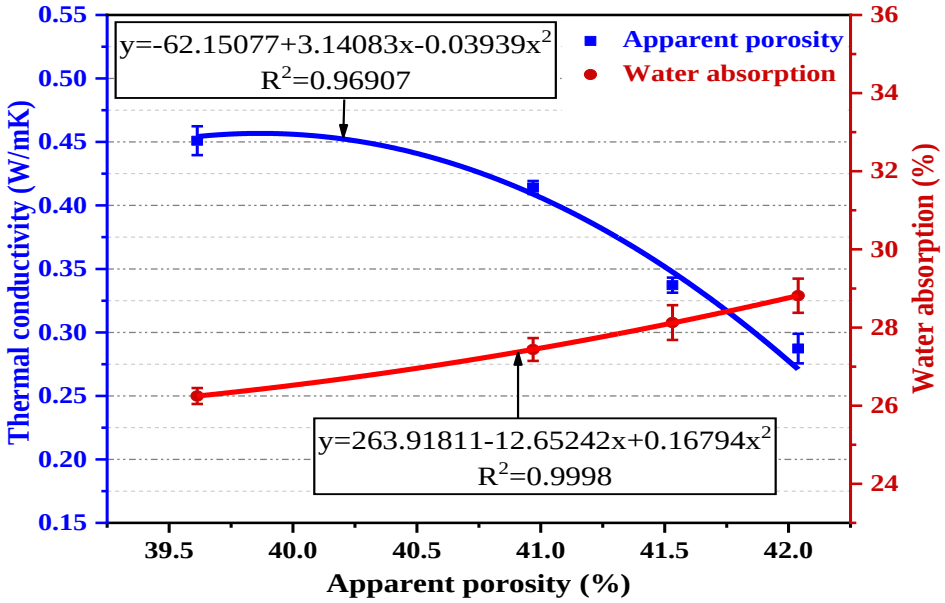

Figure 78. The correlation between apparent porosity, thermal conductivity, and water absorption of zeolite/eggshell composite bricks with different compositions sintered at 950 °C

4.6. Discussion and conclusions

Objective listed in Chapter 1.1 and the answers:

- **To evaluate different types of local solid wastes, including eggshell, for integration into ceramic specimens. Furthermore, to estimate the proper mixing proportions, then to prepare various mixtures of zeolite-poor rock and eggshell through mechanical activation using a ball mill operating at optimal conditions.**

Eggshell has been evaluated as a potential candidate for the preparation of porous bricks and glass-ceramic foams. High compatibility between zeolite-poor rock and eggshell has been achieved. Eggshell powder (ESP) was used to partially substitute zeolite-poor rock. The substitution percentages were 0%, 5%, 10%, 15% and 20% by wt% of zeolite-poor rock. The optimal milling conditions were (150-200 rpm for 15 min) in which fine homogenous powder

mixtures were produced. Increasing the milling time and rotation speed resulted in lager particle sizes.

- **To experimentally prepare green ceramic specimens using uniaxial dry pressing and investigate their characteristics**

The produced homogenous mixtures resulting from the ball milling of zeolite-poor rock and eggshell were compacted using uniaxial compaction machines. A series of compaction experiments have been done and the results show that dense ceramic samples can be produced using a pressure of 45 MPa. The compacted samples show good strength for handling and good compressive strength after sintering.

- **To suggest an appropriate, cost-effective sintering curve (sintering temperature, and residence time) for the preparation of zeolite-poor rock incorporated eggshell ceramic samples.**

TG/DTA and XRD analyses of the samples reveal that the optimal sintering temperature could be approximately 1000 °C, where the disintegration of raw materials and physicochemical reaction are taking place, resulting in bricks with high mechanical strength. The decomposition of the eggshell creates CaO, which acts as flux, decreasing the sintering temperature of the mixes. Therefore, the inclusion of eggshell has benefits in creating gases which are responsible for the development of the porous structure as well as decreasing the sintering temperature and residence time owing to the production of the fluxing agent (CaO). The ideal residence time was found to be 3-4 hours.

- **To assess the influence of solid waste inclusion on the technical characteristics of the produced ceramic bricks and foams, such as bulk density, shrinkage, apparent porosity, water absorption, thermal conductivity, and compressive strength based on international standards**

The experimental findings confirm that integrating up to 20 wt% eggshell into the composite bricks minimizes the sintered samples' bulk density, leading to lightweight ceramic bricks. This can lower the expenses associated with their handling and transportation. Moreover, in earthquake-susceptible locations, lightweight constructions are highly preferable. With eggshell dosage increased, the hybrid bricks demonstrated greater water absorption and apparent porosity. Brick specimens with 20% eggshell, on the other hand, met the absorption criteria for mild weathering. The fluxing behaviour and pore-forming capabilities of eggshell could enhance the compressive strength and thermal insulation characteristics of sintered ceramic bricks. The composite ceramic bricks have a mechanical strength higher than that required by standards. The lowest compressive strength was obtained for ZE20 samples burned at 950 °C. With the inclusion of eggshell, the compressive strength was decreased due to the formation of cellular structure. The thermal conductivity of burnt composite ceramic bricks was shown to decrease as the eggshell concentration was increased. Thermal conductivity in control brick specimens was 0.68 W/mK, which decreased to 0.25 W/mK after a 20 wt% addition of eggshell in brick samples. This indicates the superior thermal insulation of composite ceramic bricks.

The efflorescence test was performed on the samples with different compositions. All the samples exhibit no production of any salts on the surfaces, suggesting a “Nil” efflorescence

(Fig. 16). This reveals the complete reaction of CaO generated by the decomposition of eggshell with other minerals present in the zeolite-poor rock during the heat treatment process

- **To compare the results of the technical properties of the prepared zeolite-poor rock/eggshell specimens to that of the current literature in the field of burned ceramic bricks**

Table 5 outlines the findings of numerous studies on the usage of different wastes to make burnt ceramic bricks that have been published in the literature. When comparing the findings of this study to the results shown in Table 3, it's worth noting that zeolite-poor rock and eggshell are attractive materials for brick manufacturing since they have greater compressive strengths and better thermal insulation than most of the studies mentioned in Table 3.

Conclusions

- **It was proved that it is possible to produce innovative building bricks with low density (1.45–1.76 g/cm3) and low thermal conductivity (0.2–0.68 W/mk) based on zeolite-poor rock (D <100 µm) together with eggshell powder (D90<100 µm). Eggshell was added as a partial replacement for zeolite-poor rock in the specimens. The replacement percentages of eggshell were 0–20 wt% by mass of zeolite-poor rock. The mixed powders were milled for 15 min at 150 rpm to produce homogenous mixtures. The prepared mixtures were pressed at 45 MPa. The produced green ceramic samples were then sintered at variable temperatures (950, 1050 and 1150 °C) for 3 h holding time and a heating rate of 60 °C/h. Bricks produced by this technique using these raw materials show no efflorescence (no salt formation on the surfaces).**
- **I established that the inclusion of 20 wt% eggshell (D90 <100 µm) into zeolite-poor rock powder (D <100 µm) followed by ball milling for 15 min at 150 rpm, dry pressing at 45 MPa and sintering at a temperature range of 950-1250 °C with a residence time of 3 h and a heating rate of 60 °C/h led to the formation of a cellular structure with a relatively larger number of round-like closed pores (Fig. 65).**
- **I established that with the addition of 10 wt% eggshell powder (D90<100 µm) into zeolite-poor rock powder (D<100 µm), followed by the ball milling, dry pressing at 45 MPa and sintering at a temperature range of 950-1250 °C with a residence time of 3 h and a heating rate of 60 °C/h, bricks with higher compressive strength can be obtained. This could be explained by the fact that during the sintering, the eggshell decomposes and produce CaO, which acts as a flux that induces the liquid phase formation causing verification that binds the particles together and results in higher compressive strength of the produced eggshell containing bricks (Fig. 67)**

4.7. Result of alkali-activated zeolite-poor rock incorporated sawdust glass-ceramic foams

4.7.1. TG/DTA of the alkali-activated zeolite-poor rock/sawdust mixtures

Fig. 79.a depicts the TG/DTA profiles of the alkali-activated ZS sample. At 1200 °C, a total mass loss of around 15.2% was obtained. The TG curve indicates three significant mass losses. In the first stage, a mass loss of about 6.98% was achieved in a temperature range of 40–190.8 °C, correlating to the endothermic peak at 121.5 °C in the DTA graph. This is due to the removal of free water. The second mass loss was 5.12% between 190 and 383 °C, which might be attributed to the evaporation of combined water and the combustion of organic materials. In the last step, about 2.78% mass loss was observed between 383 and 802 °C. This might be linked to the continued firing of organic materials and decomposition of the alkali-activated zeolite-poor rock. In the DTA graph, a board exothermic peak is shown between 785–1154 °C, indicating the disintegration of alkali-activated material.

Fig. 79.b demonstrates the TG/DTA analysis of the alkali-activated Z6SS sample. The TG graph shows a total mass loss of 27.1%, separated into three parts. To begin, 9.3% mass loss is seen at temperatures ranging from 40 to 199 °C, corresponding to the endothermic peak at 117.3 °C in the DTA graph; this is due to evaporation of the moisture. In the second stage, a mass loss of 7.52% was recorded at temperatures ranging from 200 to 329.2 °C and related to the exothermic peak appearing at 268.6 °C in the DTA curve. This mass loss could be ascribed to the crystalline water's evaporation and the organic matter's burnout, including sawdust. Finally, a maximum mass loss of 8.91% was achieved between 330 °C and 802.2 °C, correspondence to exothermic peaks obtained at 437.9 °C in the DTA graph, indicating the continuous firing of the sawdust. A wide peak is shown at the temperature range of 803–1169 °C in the DTA curve. This could be assigned to the decomposition of the sodium aluminosilicate materials and the physicochemical reaction of the alkali-activated component.

The total mass loss in Z6SS is higher than in ZS; this is due to the addition of sawdust which burns out during the analysis. The addition of sawdust is useful in producing gases during heat treatment that will enhance foamability.

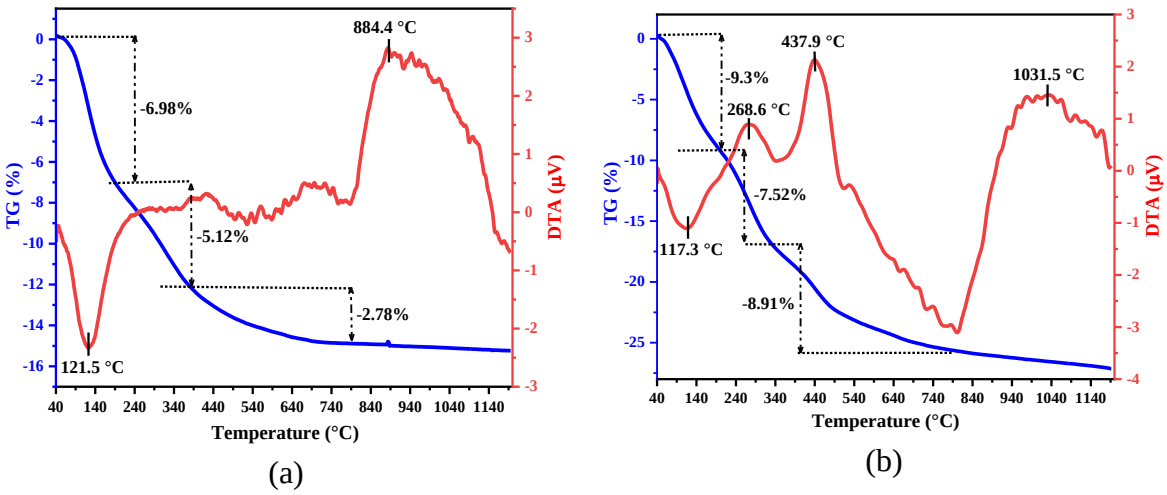

Figure 79. TG and DTA curves of alkali-activated (a) ZS and (b) Z6SS samples

4.7.2. Dimensional properties of the sintered zeolite-poor rock/sawdust foams

Fig. 80 depicts the produced glass-ceramic foams' macrostructures and morphology. It is worth mentioning that increasing the sawdust content and sintering temperature increases pore size, porosity, and overall volume expansion. Due to the fact that adding more sawdust produces more gas and raising the temperature produces viscous material coupled with greater internal gas pressure, the pores rapidly expanded owing to the coalescence of tiny pores. Moreover, the pores' shape is altered from a circular to an irregular maze-like structure. The most important point to emphasize is that a portion of the sawdust gets converted through the reduction sintering to carbon and deposited on the foam's inside surface, resulting in black colouration. When the alkali-activated mixture decomposes at elevated temperature, vitreous-like materials form on the bulk, trapping the sawdust. Therefore, the surface-located sawdust reacts with atmospheric oxygen and turns into CO_2, whereas bulk-located sawdust turns into carbon; this explains why the surface appears white and the bulk turns black. The formation of C is useful for thermal insulation since the carbon layer can reflect heat. The technique of adding carbon to the produced foams to reduce thermal conductivity is commonly used in industry, such as in the manufacturing of expanded polystyrene (EPS) foams. Samples with sawdust sintered at 950 °C appear shinier (have smooth and glazed surfaces) than the other samples, indicating more glassy phase formation. This is consistent with the XRD results (Fig. 81).

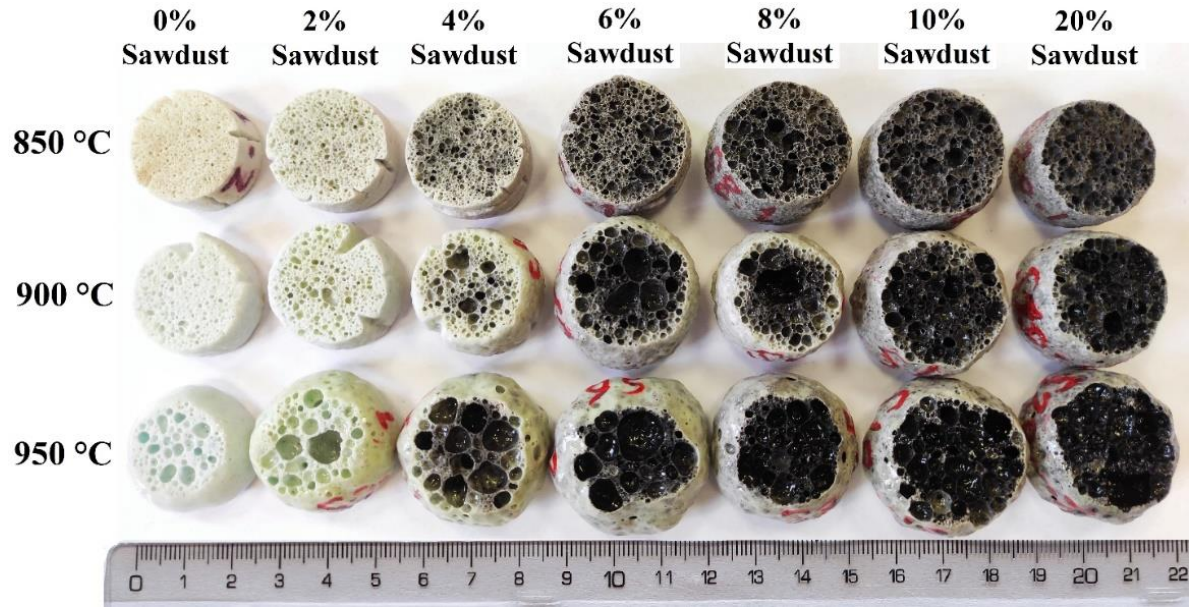

Figure 80. The produced foams with different sawdust contents sintered at different temperatures

4.7.3. XRD investigations of the sintered zeolite-poor rock/sawdust foams

Fig. 81 exhibits the XRD spectra of zeolite-poor rock powder, alkali-activated Z6SS mixture, and Z6SS glass-ceramic foams heat-treated under different sintering temperatures. The XRD of the alkali-activated sample confirms the chemical reaction of cristobalite, quartz, montmorillonite, clinoptilolite, and calcite with sodium hydroxide and the formation of

heulandite ($Na_{1.52}Al_{1.21}Si_{36}O_{97.84}$, PDF# 96-900-2185). The porous structure of clinoptilolite allows NaOH penetration and higher reactivity. The alkali-activation process is associated with a reduction in the crystallization tendency. Therefore, the peaks of the alkali-activated samples appear with very small intensities in the XRD graph. Upon the sintering and at 850 °C, the decomposition of heulandite has taken place, and formation of anorthite ($Na_{1.92}Ca_{2.08}Si_{10}Al_6O_{32}$, PDF# 96-100-8758) and amorphous phase. At a higher temperature of 950 °C, anorthite decomposes to form a completely amorphous glassy phase.

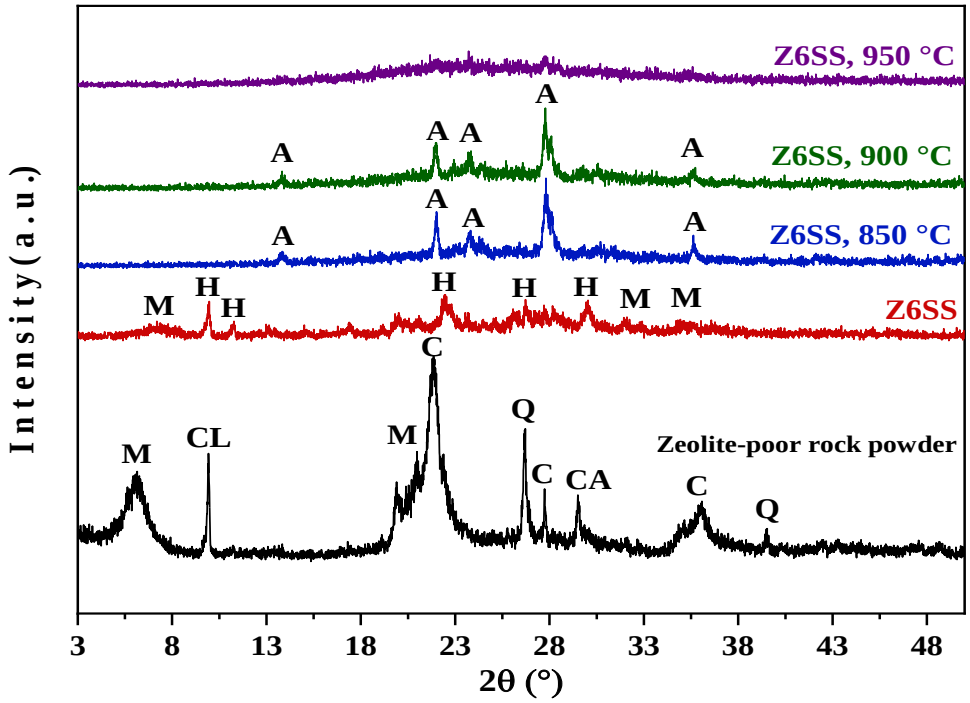

Figure 81. X-ray diffractogram of zeolite-poor rock, alkali-activated (ZS), and (Z6SS) foamed specimens fired at variable temperatures. M= montmorillonite, CL= clinoptilolite, C= cristobalite, Q= quartz, CA= calcite, H= heulandite, A= anorthite

4.7.4. FT-IR analysis of the alkali-activated and sintered zeolite-poor rock/sawdust samples

The infrared absorption spectra of alkali-activated samples (ZS and Z6SS) and their sintered products at various temperatures are determined and shown in Fig. 82. The bands of the low-frequency range regions between 1200 and 400 cm^{-1} are related to the material's aluminosilicate structure and generated by the Si–O–Si(Al) linkage' vibrations. The band at 453 cm^{-1} was for Si-O-Si bending vibrations, while the vibrations of the Al-O bond for aluminium in the octahedral configuration are responsible for the band at 748 cm^{-1}. A significant wide-stretching vibration signal at mid-region 1013 cm^{-1} is produced as a consequence of the production of asymmetric Si-O-T (T = tetrahedral Si or Al) absorption bands. Alkali-activated zeolite-poor rocks samples and their sintered foams have quite similar locations for the major band. This suggests the formation of the aluminosilicate phase after sintering. At roughly 1400-1600 cm^{-1}, a distinct band can be seen in alkali-activated samples, which is attributed to the C-O bond in carbonate ions and the O-H bond in water molecules. For alkali-activated samples (before

sintering), the OH stretching vibration of structural hydroxyl groups and water has a single band at about 3600 cm^{-1}. After heat treatment, the materials' spectra are noticeably modified. The dihydroxylation and decomposition processes eliminate the bands formed from water, OH groups, and C-O bond in carbonate ions. Furthermore, the full width at the half maximum (FWHM) of the sintered samples generated by vibrations of Si-O and Al-O bonds have widened compared to the FWHM of the initial materials, which indicated a lower degree of crystallization (the formation of amorphous phase) [214]. This finding agrees well with the XRD analysis (Fig.78). The addition of sawdust results in only a slight change in the main peak.

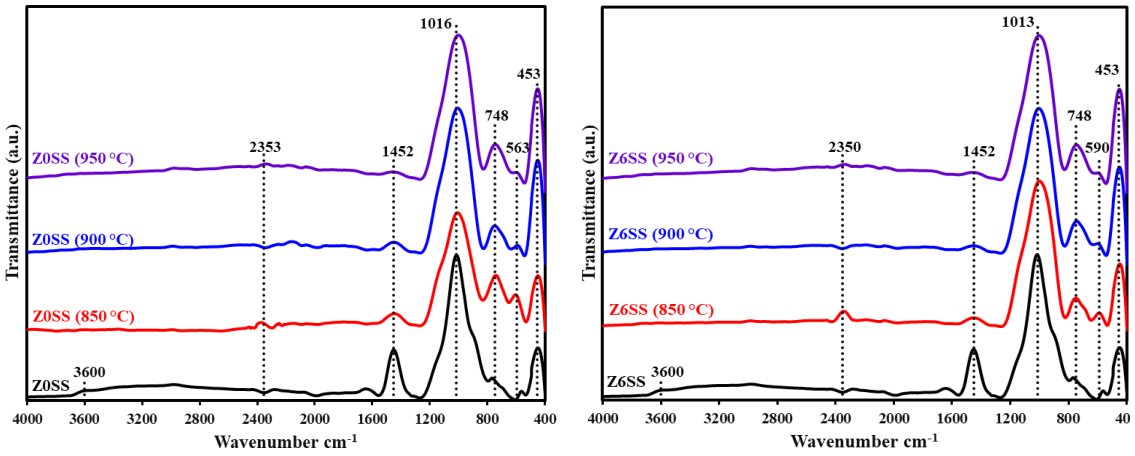

Figure 82. FTIR spectra of alkali-activated and sintered samples of a) ZS, b) Z6SS

4.7.5. SEM analysis of the alkali-activated zeolite-poor rock/sawdust mixtures

The microscopic analyses of cured alkali-activated granules (blank and with sawdust) using SEM at different magnifications reveal the formation of wickers-like aluminosilicate structure intergrowing through the thick matrix at sub-micron and nanoscale sizes (Fig. 83). The alkali-activation process modified the sawdust's initial surface characteristics (surface roughness). The inclusion of sawdust leads to the creation of longer and thinner whiskers since the alkali activation reduces the sawdust diameter giving a place for the wickers to grow [215].

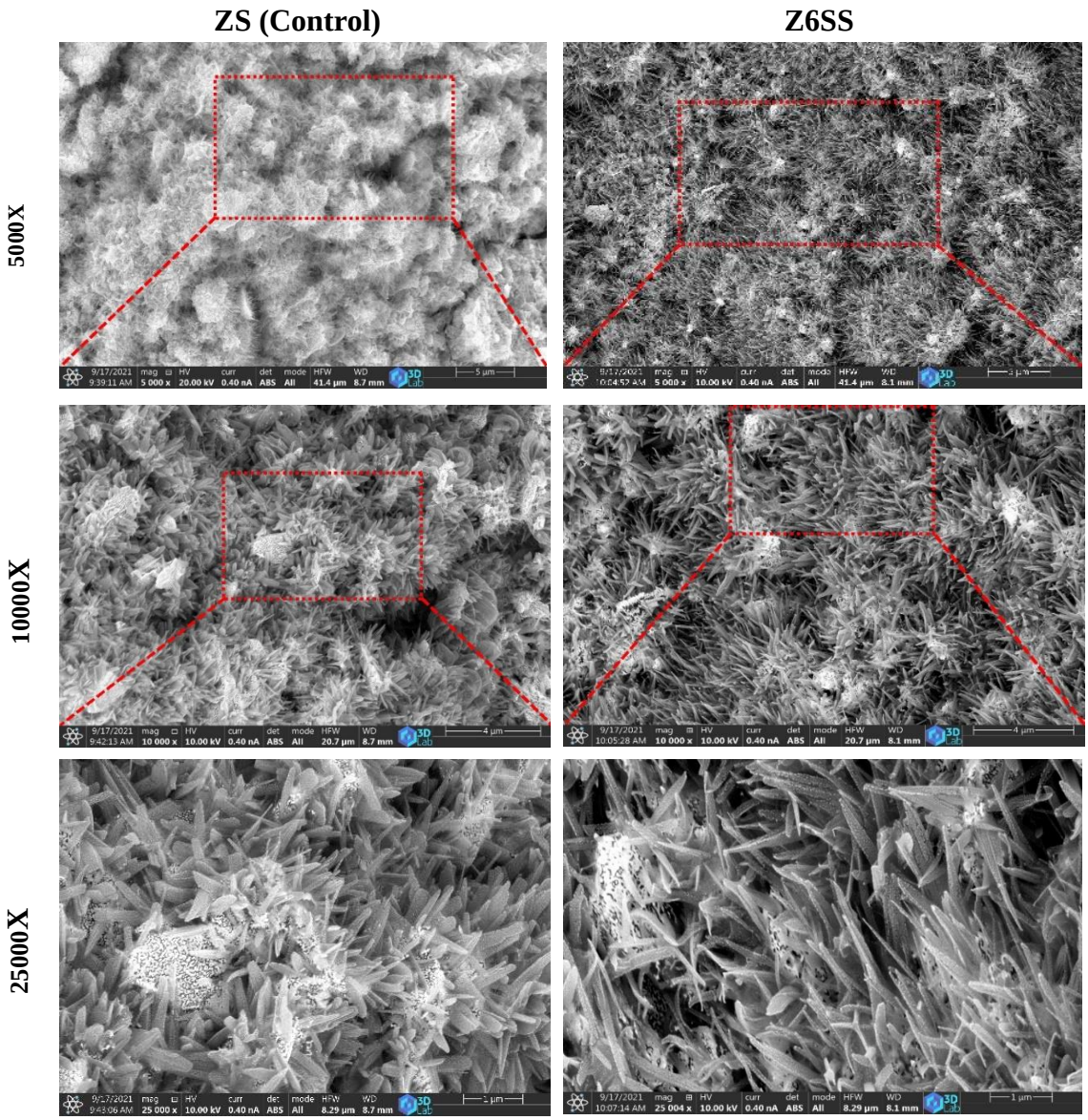

Figure 83. SEM images of the alkali-activated mixtures (ZS and Z6SS) at different magnifications

4.7.6. EDS analysis of the alkali-activated zeolite-poor rock/sawdust powders

The findings of the EDS investigation of the alkali-activated samples (ZS and Z6SS) are given in Fig. 84. According to the EDS patterns, the main components of the samples were oxygen, silicon, sodium, aluminium, and carbon, confirming the formation of aluminosilicate structure. The high amount of sodium has resulted from the alkali-activation process. The carbon content of the Z6SS sample was higher than the blank sample. This carbon has resulted from the incorporation of sawdust. Several processes occur during the chemical activation of the samples, including chemical decomposition and chemical reaction, which is critical for the sample's foaming characteristics.

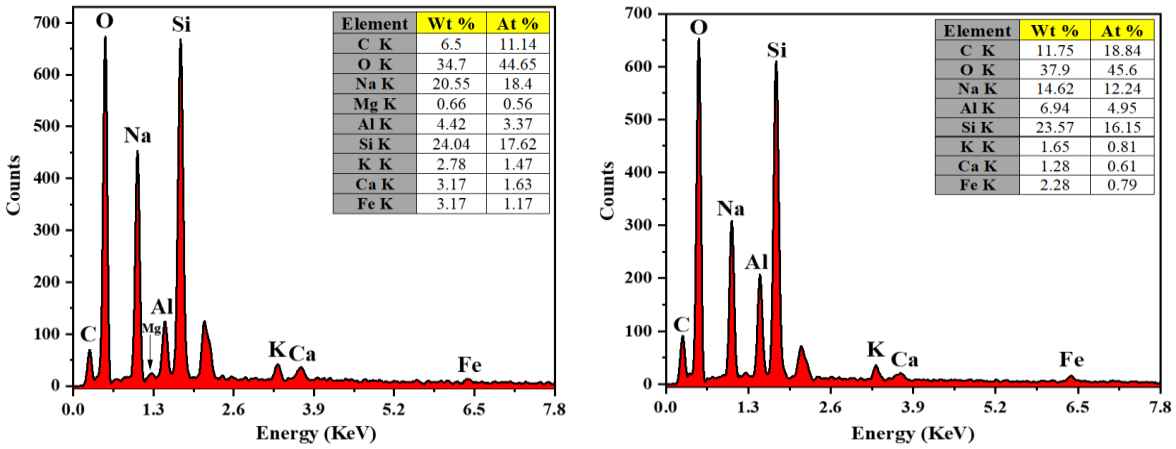

Figure 84. EDS investigation of the alkali-activated samples a) ZS, b) Z6SS

4.7.7. Heating microscope and the foaming mechanism of the alkali-activated zeolite-poor rock/sawdust samples

The heating microscope analysis was used to assess the sinterability and foaming tendencies of the alkali-activated powders within a tube furnace. The values of the height change and silhouettes taken at various stages throughout the process are determined, and the findings are displayed in Fig. 85. Moreover, the foaming mechanism is explained in Fig. 86. In the temperature range of 40–1200 °C, three distinguish foaming stages followed by shrinkage were noticed (Fig. 85). In the first stage (40–280 °C), the specimen was non-reactive, and it kept compact; a slight height shrinkage was observed due to the evaporation of the free water. The foaming process starts in the second stage at a temperature range between 300–580 °C with a maximum expansion of ≈10%; this behaviour could be ascribed to the partial decomposition of the alkali-activated zeolite-poor rock accompanied by the evaporation of crystalline water and emission of some gases resulted from the firing of the organic content in an oxygen atmosphere. The third stage starts between 580–740 °C with the highest expansion of ≈24%. The partial softening of the mixture and the increased release of CO_2 gas resulting from the sawdust decomposition in the oxygen atmosphere are responsible for this growth. Although the mixture started to soften, its viscosity remained quite high. As a consequence, the pressure of the produced gas was insufficient to produce a fully formed foam. The most intensive height expansion was 56% recorded in the third stage in the temperature range of 740–850 °C. This could be assigned to the formation of viscous materials with relatively low surface tension associated with the increased internal pressure of the gas that increases the tendency of the foaming (pores growth). Eq. 1. describes the state in which pores size enlarges [143]:

$$P_g > P_o + 2\sigma/r \qquad (1)$$

where P_g is the pore internal gas pressure, P_o is the external barrier to pore expansion, r is the radius of the pore, and σ is the surface tension.

Upon increasing the sintering temperature (950–1200 °C), the pores enlarge rapidly and move toward the surface and eventually escape from the heat-treated sample leading to the "collapse"

of the cells and hence decreasing the expansion. This occurs due to low viscosity and high vapour pressure. The speed of the pore growth can be described by Stokes law (eq. 2) [143].

$$v = \frac{2(\rho_1 - \rho_2)gr^2}{9\eta} \qquad (2)$$

where v denotes the velocity of the pore growth, ρ_1 and ρ_2 denote the densities of liquid and gas respectively at high temperature, g represents gravity, r is the radius of the pore, and η is the effective viscosity.

It is apparent that raising the sawdust percentage causes the height expansion to grow due to the larger amount of gas produced from the thermal disintegration of sawdust. These investigations reveal that the optimal sintering temperatures should be in the range of 850–950 °C with 10 °C/min heating rate since it enables the production of relatively homogenous and uniformly distributed glass-ceramic foam samples. Below the optimal temperature, the foaming is quite slow, while at higher temperatures, the fast collapse of the foams was seen (in only a few minutes).

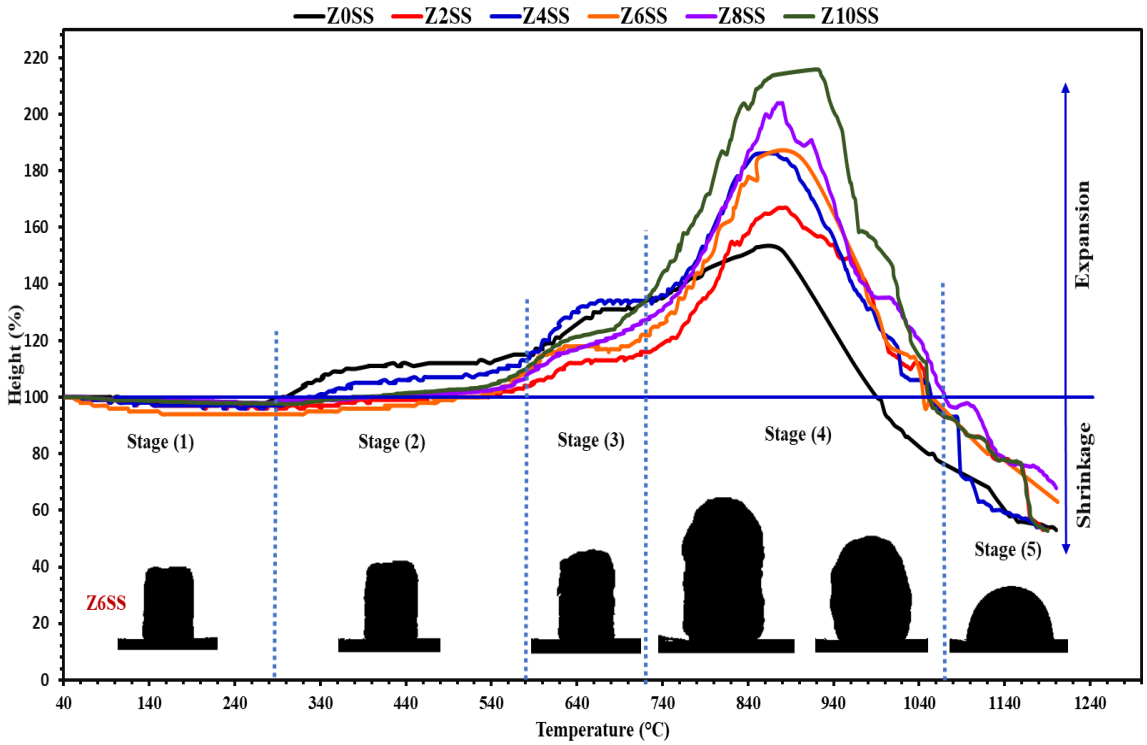

Figure 85. Heating microscope graphs of several alkali-activated zeolite-poor rock/sawdust samples heat-treated in the temperature range of 40–1200 °C at 10 °/min

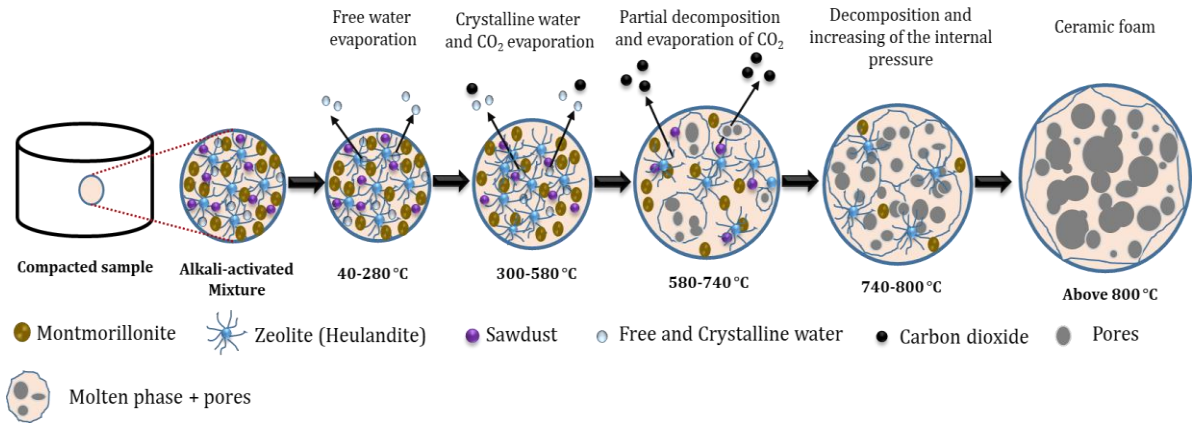

Figure 86. The foaming mechanism in different alkali-activated zeolite-poor rock/sawdust samples

4.7.8. SEM investigation of the produced alkali-activated zeolite-poor rock/sawdust foams

SEM micrographs of glass-ceramic foams made from alkali-activated zeolite-poor rocks with sawdust are shown in Fig. 87. The sample's micrograph reveals the existence of small dark holes on the cell surface, which constitute the "windows" between the linked cells. Cells were found to be linked to their neighbours in an interconnected system. Between the bigger cells lie several smaller cells which may be dissolved in bigger pores (pore coarsening) that are more likely to be favoured by a drop in the surface energy of the system, this phenomenon is observed in the preparation of the other type of foams as well (metallic foams and polymeric foams) [216]. Pore diameters grow when the firing temperature and sawdust fraction are increased due to the increase in the amount of gases produced that would increase the internal pressure. Moreover, the inclusion of sawdust changes the pore structure from a round-like to an elongated structure.

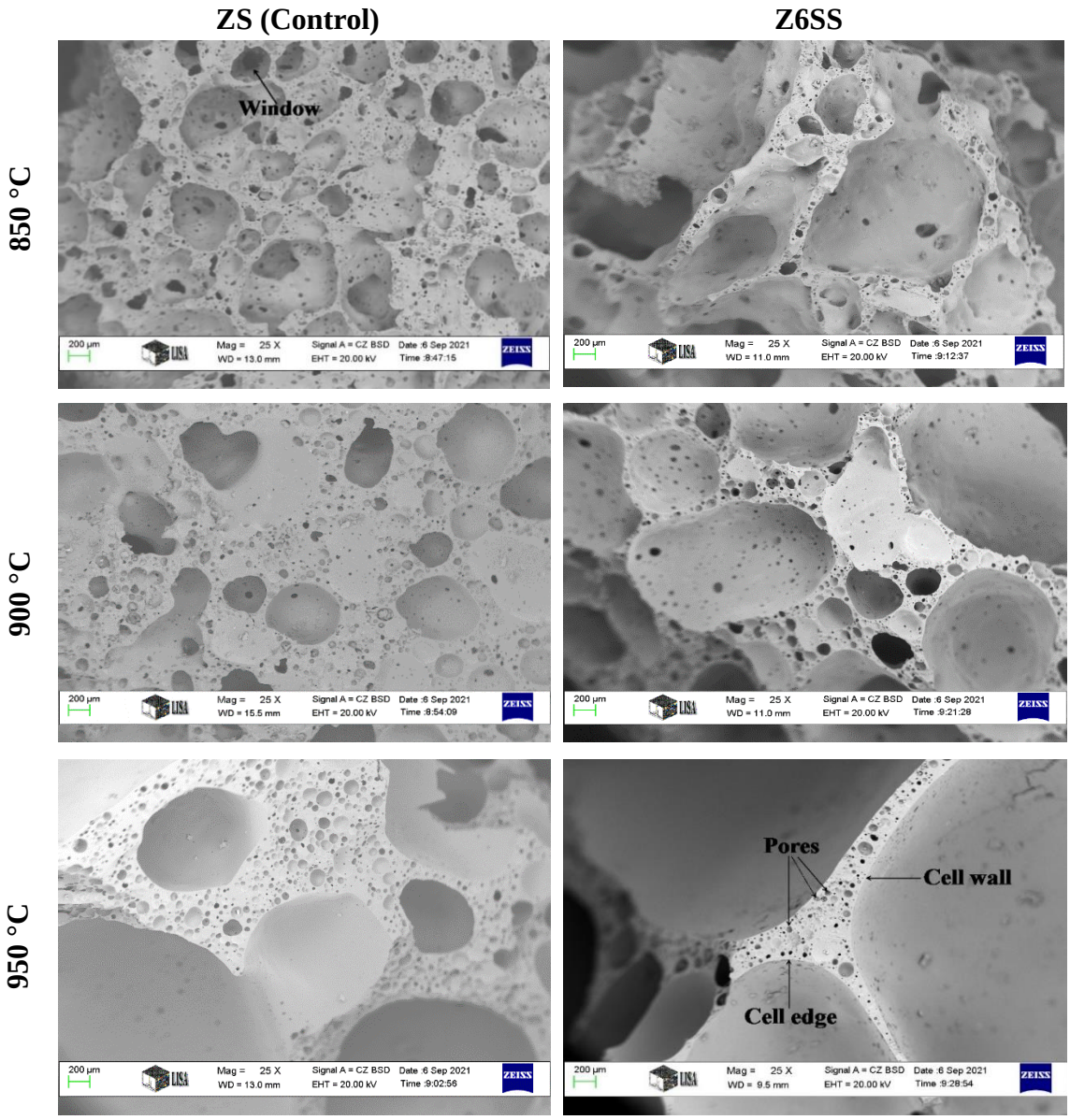

Figure 87. SEM images of ZS and Z6SS sintered samples

4.7.9. Micro-CT analysis and properties of the pore structure and morphology of zeolite-poor rock/sawdust foams

Fig. 88 shows CT microstructures of two samples (ZS and Z6SS) sintered at 850 °C. Three-dimensional CT images of each sample together with two-dimensional images of the top and two sides views are shown in Fig. 88.a. A combination of binarization and watershed segmentation is used to display the specimens' 3D photos. Due to the fact that materials of various densities absorb X-rays differently, the bright spots in Fig. 88.a indicated the solid matrix, whereas the gas in the pores was shown in various colours (blue, green, and yellow) based on the pore size and depth. In terms of mechanical aspects, pore size and wall thickness play a significant impact; particularly, smaller pore sizes and wider pore walls are preferred for increased mechanical strength, which is commonly aimed for construction materials. As seen

in Fig. 89.a, ZS had both big and tiny pores with spherical-like structures. The inclusion of 6% sawdust powder in the Z6SS sample increases the pore sizes and leads to irregular pore shape formation (maze-like structure). The porosities of the prepared glass-ceramic foams were obtained from the CT data. Porosity was found to be 66.2% for ZS and 74% for Z6SS. The porosity tests are further validated with the pycnometer test and the results showed comparable values of 67% and 75.9% for ZS and Z6SS, respectively. Following the image analysis and data processing on CT findings of two-dimensional photos, the pore size distribution of the foam samples was determined (Fig. 88.b and Fig. 89.b). Table 16 lists the statistical findings; ZS had the highest mean and median pore size distribution compared to ZS samples. As the sawdust amount increased, the pore diameter increased as well, suggesting that pore diameter and sawdust content were directly correlated. ZS samples had the narrowest range and the least standard deviation, whereas Z6SS samples had the widest. Therefore, ZS seemed to have a more homogeneous pore size distribution. It may be linked to the fact that only one type of gas was responsible for the pore formation. The Z6SS samples, on the other hand, had a very variable and uneven pore size distribution; this is in line with the distribution curve shown in Fig 89.b and the CT scan photos shown in Fig 89.a. This might be explained by the fact that the pores came from various sources involving pores formed by evaporation of water (free and crystalline), volatilization of organics matter in alkali-activated zeolite-poor rock, and pores produced by the use of blowing agent.

According to the above examination of glass-ceramic foams' microstructure. The relatively homogenous pore size distribution and lower porosity of the ZS sample led to strong compressive strength, high bulk density, and greater heat conductivity. However, the relatively non-homogenous pores distribution and high porosity could be responsible for ZS6S's lightweight and good thermal insulation efficiency, but it may also contribute to its low mechanical strength. The pore size distribution had a significant impact on the different characteristics of the produced glass-ceramic foams especially mechanical properties [217].

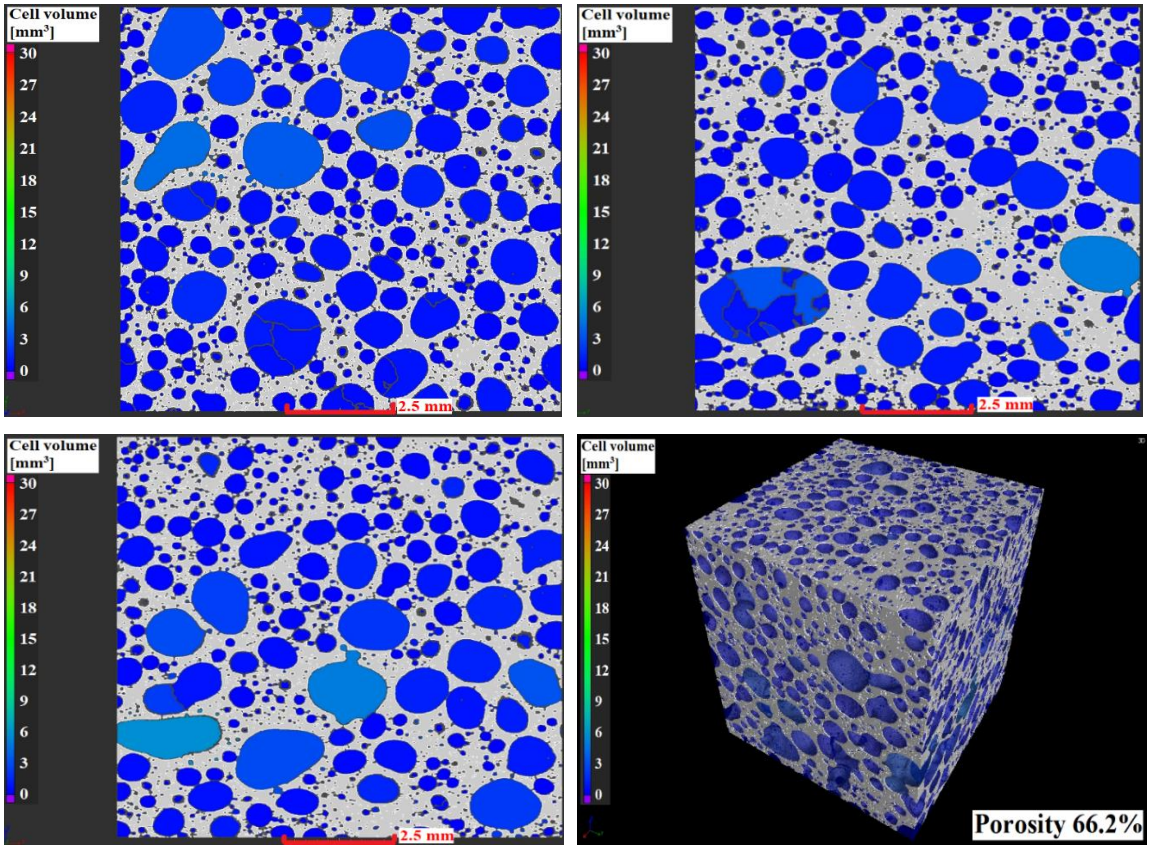

(a)

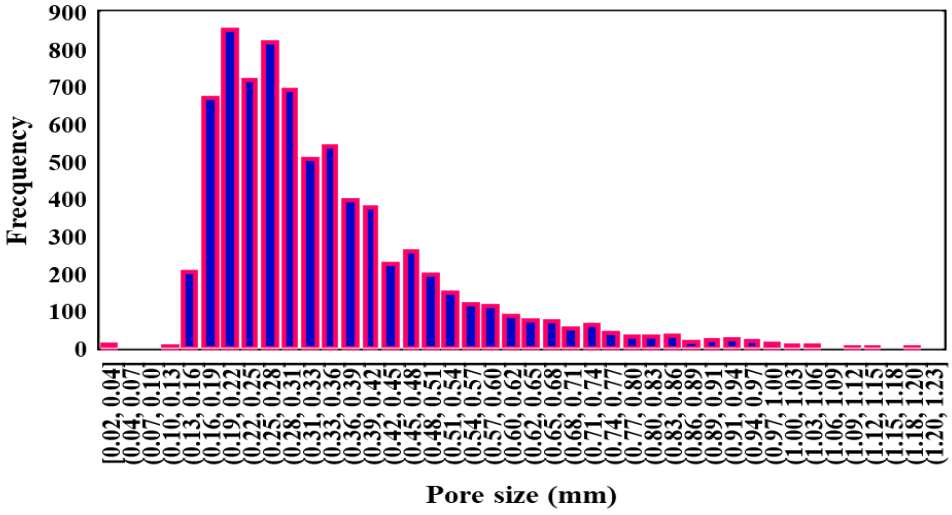

(b)

Figure 88. a) CT scan photos of the reference sample (ZS) from different sides and b) the pore size distribution of the reference sample (ZS)

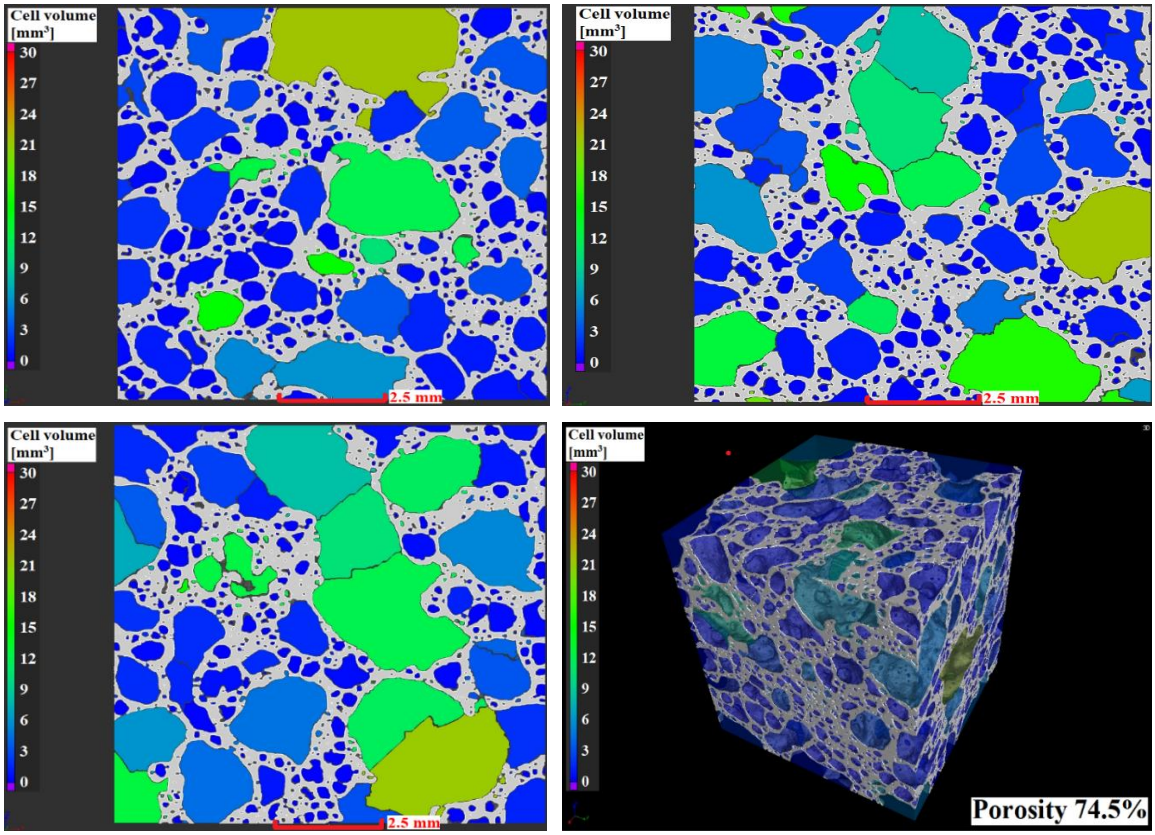

(a)

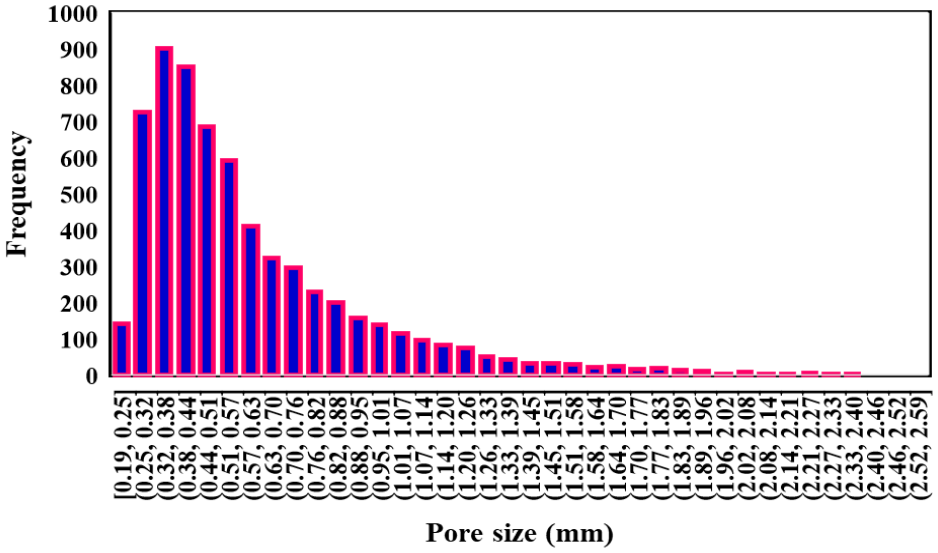

(b)

Figure 89. a) CT scan photos of the Z6SS sample from different sides and b) the pore size distribution of the Z6SS sample

Table 16. Statistical parameters of the pore size distribution data of ZS and Z6SS

Samples	Median (mm)	Mean (mm)	Minimum (mm)	Maximum (mm)	Standard deviation
ZS	0.490	0.599	0.192	3.172	0.338
Z6SS	0.304	0.397	0.015	4.661	0.345

4.7.10. Bulk density of the produced zeolite-poor rock/sawdust foams

The influence of sawdust content and sintering temperature on the bulk density of the prepared zeolite-poor rock/sawdust foams is shown in Fig. 90. All samples followed a similar pattern; their densities tend to noticeably decrease with increasing the sawdust content and the sintering temperature. The reason beyond that is upon increasing the sintering temperature, the alkali-activated samples transformed from solid to semi-liquid with relatively low viscosity, while the sawdust incorporated in the sample decomposed simultaneously, creating carbon dioxide. The rapid formation of the gas increased the internal pressure in the viscous mixture, causing it to expand; therefore, the density decreased. The burning of the sawdust contributes to the sintering; thus, at high sawdust content (20%), the increased temperature reduces the viscosity of the molten phase. At the same time, a large pressure is developed that causes the gas to escape and the foam framework to collapse due to gravity and hence increasing the density. All samples floated in water after soaking for 7 days (Fig. 91), confirming a large amount of closed porosity and low density of the samples (below 1 g/cm^3).

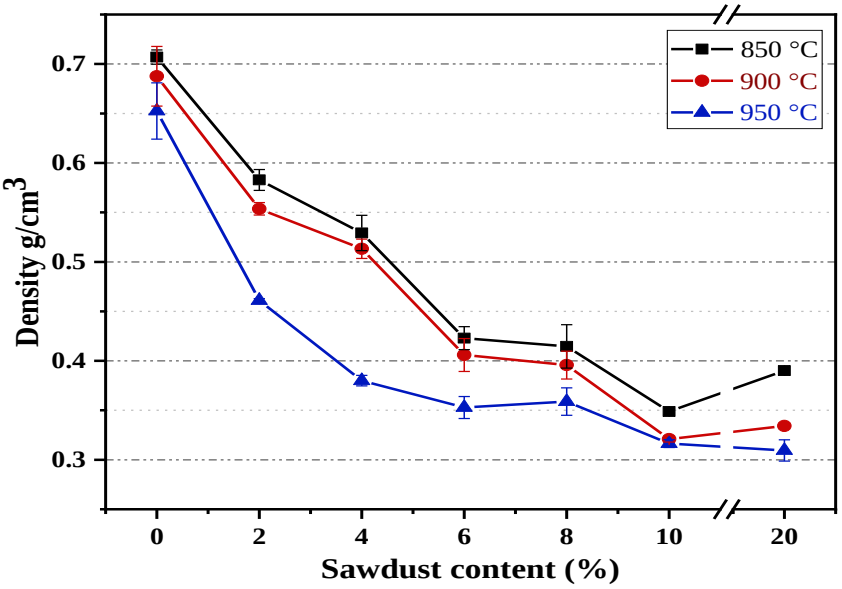

Figure 90. Bulk density of produced zeolite-poor rock/sawdust specimens of various compositions heat-treated at various temperatures

Samples without sawdust Samples with sawdust

Figure 91. Zeolite-poor rock/sawdust ceramic foams after soaking for 7 days in distilled water

4.7.11. Volume expansion of the produced zeolite-poor rock/sawdust foams

After heating, all samples demonstrated foaming capabilities with different technical properties, pore size, and morphology. The influence of sawdust content and sintering temperature on the volume expansion is shown in Fig. 92. With the sawdust increasing, the volume expansion increased, and the maximum expansion was about 300%. The discharge of gases produced by the breakdown of sawdust is the cause of this growth. However, at high sawdust content (20%), the samples start to shrink; this is due to the fact that the high amount of the gas produced increases the internal pressure until it reaches a point where the viscous material can't hold the gas. Therefore, the gas moves out, resulting in the collapse of the foams. Increasing the heat treatment temperature, on the other hand, led to an increase in the volume expansion due to the reduction in viscosity. This finding agrees perfectly with the heating microscope result.

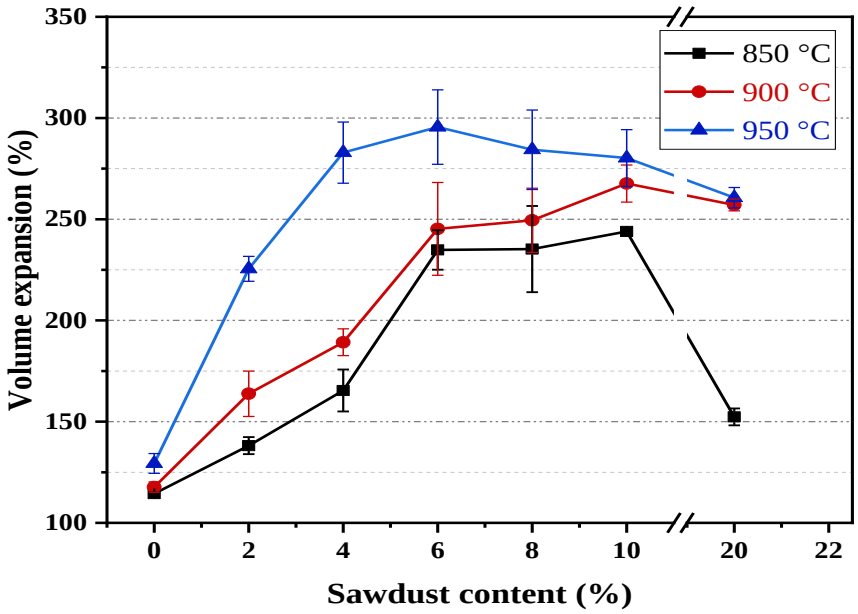

Figure 92. Volume expansion of the prepared zeolite-poor rock/sawdust with different compositions sintered at different temperatures

4.7.12. The thermal conductivity of the produced zeolite-poor rock/sawdust foams

Fig. 93 depicts the thermal conductivity of foamed ceramics as a function of sawdust concentration. It can be observed that sawdust content greatly lowers the foam density, therefore increasing the porosity and decreasing thermal conductivity. Increasing the sintering temperature lowers the thermal conductivity as well. This is due to the enhanced formability induced by the reduction in the viscosity and increase in the internal gas pressure. Moreover, the formation of amorphous carbon in the inner layer of the pores could be useful in reducing thermal conductivity by reflecting heat. Even though the high porous materials are useful for making lightweight and good thermal insulation materials, other mechanical characteristics of the foamed ceramic should be considered.

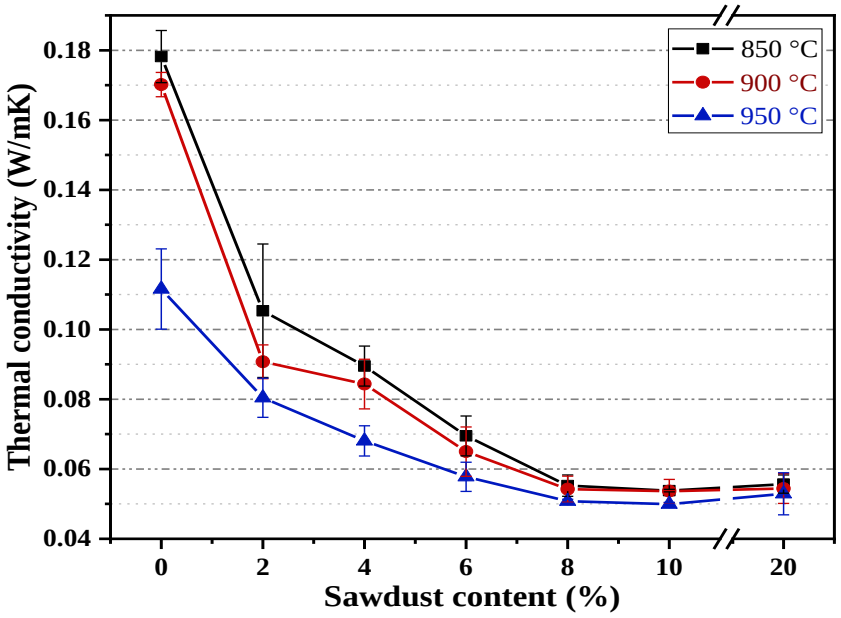

Figure 93. Thermal conductivity of the prepared zeolite-poor rock/sawdust samples with different compositions sintered at different temperatures

4.7.13. Compressive strength of the produced zeolite-poor rock/sawdust foams

The effect of sawdust dosages and sintering temperature on the compressive strength of the produced glass-ceramic foam samples is shown in Fig. 94. Generally speaking, the pore's morphology and structure, especially wall thickness and pore size, significantly impact the strength of the glass-ceramic foams generated [218]. The compressive strength decreases as the sawdust content increases. This could be assigned to the increase in porosity and reduction in wall thickness. Likewise, the increase in sintering temperature reduces the compressive strength since the higher temperature leads to the generation of larger pore sizes due to pores coarsening. Moreover, the increase in temperature converts the crystalline phases in the produced foams to an amorphous glassy phase, as confirmed by XRD (Fig. 76). However, all the samples showed compressive strength comparable to that of commercially available glass foams.

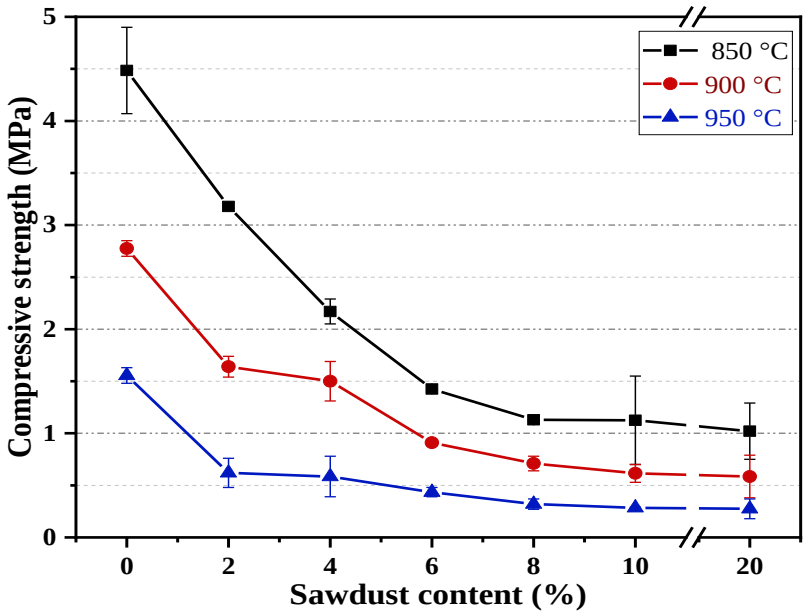

Figure 94. Compressive strength of the produced zeolite-poor rock/sawdust samples with varied compositions sintered at various temperatures

Fig. 95 shows the compressive stress-strain curves of produced glass-ceramic foams samples with different compositions (ZS and Z6SS). The examined samples showed standard stress-strain characteristics of brittle, porous materials. As the samples were subjected to the external compressive load, it revealed an elastic deformation represented by a linear relationship till it reached the maximum point (yield strength), then a rapid reduction in tension occurred, indicating the failure of upper cells, the stress was then passed to the next cells. It continued to increase until the foam was fully destroyed. The maximum stress changes between 1.5 and 4.5 MPa based on the density of the specimens. The fracture stress of the fabricated glass-ceramic foams could be described by the Gibson–Ashby equation (equation 3) [219].

$$\sigma_f = \sigma_{bend}[C(\phi\rho_{rel})^{\frac{3}{2}} + (1-\phi)\rho_{rel}] \qquad 3$$

Where σ_{bend} denotes the bending strength of the glassy phase, C is a constant, ϕ signifies the volume percentage of solids placed on the cell boundaries ρ_{rel} represents the relative density of the glass-ceramic foam. The value of the bending strength of the glassy phase and the constant (C) are consecutively provided as 0.2 and 70 MPa [220].

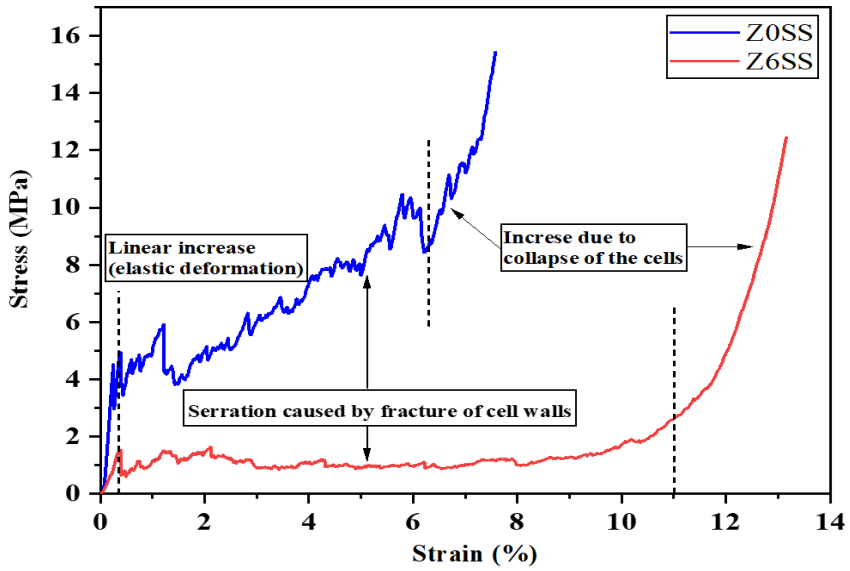

Figure 95. Compressive stress-strain curves of ZS and Z6SS foamed ceramic samples sintered at 850 °C

4.7.14. The relationships between density, compressive strength, and thermal conductivity of the produced zeolite-poor rock/sawdust foams

The correlation between the densities, the correspondence thermal conductivities, and the compressive strengths of the prepared foams are illustrated in Fig. 96. Both thermal conductivities and compressive strength exhibited a quite similar trend. In the observed region, the thermal conductivity rises continuously with the rise in density. The minimum value for the thermal conductivity was 0.04 W/mK achieved when the density was 0.32 g/cm^3. Likewise, the increase in density leads to an increase in compressive strength.

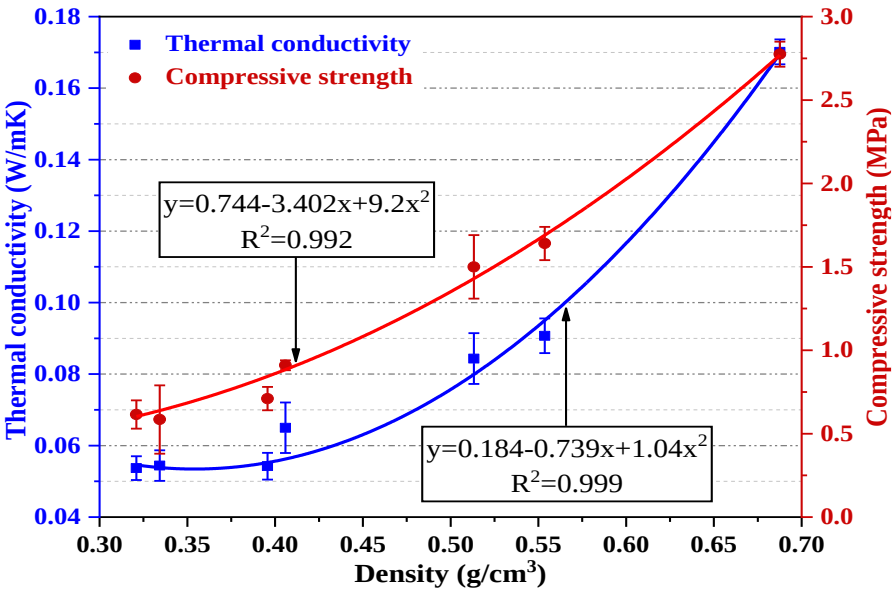

Figure 96. The relationship between density, thermal conductivity, and compressive strength of the prepared zeolite-poor rock/sawdust foams with various compositions burned at 900 °C

4.8. Discussion and conclusions

Objective listed in Chapter 1.1 and the answers:

- **To investigate the effect of chemical activation on the prepared ceramic powders.**

The effect of alkali-activation on the prepared mixtures has been systematically investigated. The SEM analysis of the alkali-activated mixtures confirms the intergrowths of whisker-like sodium aluminosilicate structure at sub-micron and nanoscale sizes (Fig. 83). This might be owing to zeolite-poor rock's porous structure, which enables better NaOH penetration, resulting in a higher reactivity.

- **To evaluate the effect of the sawdust incorporation on the foamability of the alkali-activated mixture.**

The varied mixes' alkali activation results in a notable decrease in the softening and foaming temperatures as well as an increase in the amorphous content of the generated samples. The XRD analysis carried out on alkali-activated and heat-treated samples showed that a physicochemical reaction had taken place, resulting in the creation of the two primary crystalline phases heulandite and anorthite (Fig. 81). Using a heating microscope, experimental evidence has shown that the quantity of foaming agent employed, and the sintering temperature have a substantial influence on the height expansion and foaming process. Furthermore, it was found that the optimal heat treatment conditions are 850–900 °C and 5–10 °C/min residence time (Fig. 85).

- **To evaluate the impact of sawdust incorporation on the technical properties of the developed glass-ceramic foams, such as bulk density, shrinkage, apparent porosity, water absorption, thermal conductivity, and compressive strength**.

The porosity of the foamed ceramic samples increased from 66.2% for the blank sample (ZS) to 74% for the samples containing 6% of sawdust, as confirmed in CT-scan analysis. The increase in porosity is crucial in enhancing thermal insulation. Using sawdust as a foaming agent has some extra advantages since it produces carbon in the closed pores' inner surface, contributing to better thermal insulation. Taking into account parameters like compressive strength and thermal conductivity, the ideal temperature for heat treatment was 900 °C. The achieved value of low density (0.3–0.7 g/cm^3), together with the sample's good compressive strength (0.3–4.5 MPa) and low thermal conductivity (0.04–0.17 W/mK), may be considered highly satisfying findings which can enable these materials to be a potential candidate for thermal and/or sound insulation buildings materials.

- **To compare the technical findings of the created zeolite-poor rock/sawdust samples to the results of the most recent research on glass-ceramic foams.**

According to research reported in the literature, a variety of raw materials may be used to manufacture glass-ceramic foams (Table 5). It’s worth mentioning that zeolite-poor rock and sawdust are promising foam-making components, as the produced specimens showed technical properties comparable to the commercial glass-ceramic foam having compressive strength and density of 0.6 MPa and 115 kg/m^3, respectively.

Conclusion

- **It was proved that it is possible to produce new glass-ceramic foams with low density (0.3–0.7 g/cm3), low thermal conductivity (0.04–0.17 W/mk) and good compressive strength (0.3–4.5 MPa) based on zeolite-poor rock (D <100 µm) and sawdust (D90<100 µm) using alkali activation and reactive sintering techniques. Sawdust partially substitutes zeolite-poor rock. The substitution percentages were 0–20% by wt% of zeolite-poor rock. The prepared powder mixtures were treated with 2M NaOH solutions for alkali activation, well-mixed for 5 min and then dried in the oven at 200 °C for 2 days. The alkali-activated dried powders were ground in a planetary ball mill for 15 min at 150 rpm. Using uniaxial pressing machines at a pressure of 18 MPa, the milled powders were then compacted to form cylindrical pellets. The green ceramic bodies were heat-treated at varied temperatures (850, 900, and 950 °C) for 5 min holding time, with 5 °C/min heating rate.**
- **I established that the microstructure of the alkali-activated samples could be modified by the addition of sawdust (D90<100 µm). The alkali activation of milled zeolite-poor rock + 6% sawdust using 2M of NaOH followed by drying at 200 °C for 2 days led to the formation of wickers-like aluminosilicate structure intergrowing through the thick matrix at sub-micron and nanoscale sizes (SEM images, Fig. 83).**
- **I demonstrated that the application of 8 wt% of sawdust to zeolite-poor rock (D90<100 µm) followed by the alkali activation with 2M NaOH solutions, drying at 200 C for 2 days and sintering at temperatures of 850 °C for 5 min holding time, with 5 °C/min heating rate, leads to the development of foams with the lowest thermal conductivity (0.04 W/mk) compared to the samples without sawdust (Fig. 93).**
- **I established that softening and foamability of the alkali-activated zeolite-poor rock (2M NaOH, 200 °C, 2 days) can be modified by using different foaming agents. In the case of alkali-activated zeolite-poor rock (D90<100 µm) containing sawdust (2-20 wt%) (D90<100 µm) sintered in the temperature range of 40-1200 °C, the foaming occurs in 3 steps reaching a maximum height of 216%, followed by a collapse of the foams (Fig. 85).**
- **I established that by the addition of the sawdust to zeolite-poor rock followed by alkali activation (2M NaOH, 200 °C, 2 days) and sintered at 900 °C with a heating rate of 5 °C/min and residence time of 10 min, the pore's structure can be modified, which influenced the compressive strength of the produced samples. The sample incorporated 6 wt% sawdust produced foams with irregular pore size and structure (Fig. 89) and exhibited the least compressive strength (2 MPa). The irregular pore shape and non-homogenous pore distribution are connected to the relatively high compressive strength in samples**

4.9. Result of Innovative glass-ceramic foams based on zeolite-poor rocks incorporated eggshell

4.9.1. TG/DTA of the alkali-activated zeolite-poor rock/eggshell mixtures

The TG/DTA thermal analysis of alkali-activated samples (ZS and Z4ES) at examined temperature range (40–1200 °C) is illustrated in Fig. 97.a and Fig. 97.b. Normally at a lower temperature, zeolite release the moisture adsorbed to its micropores without disrupting the aluminosilicate framework structure. The weight loss in the temperature interval of 40–177.7 °C was 6.98%, corresponding to the endothermic peak at 122.17 °C in the DTA curve. This weight loss is assigned to the removal of the free water from montmorillonite and adsorbed water from the zeolite. A second weight loss of 3.729 is observed at a temperature zone of 190–311.13 °C, which can be ascribed to the evaporation of the crystalline water in the alkali-activated sample. Finally, a weight loss of 4.19% is obtained at the temperature range of 311–810 °C and can be attributed to the burn-out of the organic content and decomposition of the aluminosilicate structure.

Fig. 97.b displays the TG/DTA measurement of the alkali-activated Z4ES sample. The TG graph indicates an overall weight loss of 21.2%, split into three segments. Initially, 11.9% weight loss is visible at temperatures varying from 40 to 148.4 °C, coinciding with the endothermic peak at 93.5 °C in the DTA graph; this is due to moisture removal. Secondly, a weight loss of 6.6% was measured at temperatures extending from 147.8 to 305.2 °C. This weight loss may be ascribed to the removal of crystalline water and the firing of organic matter. Eventually, a weight loss of 4.805% was attained between 305 °C and 725 °C, showing the continuing firing of organic content. A broad exothermic peak is visible in the temperature range of 804–1200 °C in the DTA curve. This might be ascribed to the breakdown of the sodium aluminosilicate components followed by a physicochemical reaction. It is important to note that the addition of eggshell to the alkali-activated mixture resulted in higher weight loss due to the decomposition of calcite forming CO_2 and CaO. The emission of gas resulting from eggshell disintegration is important for the foaming of the samples.

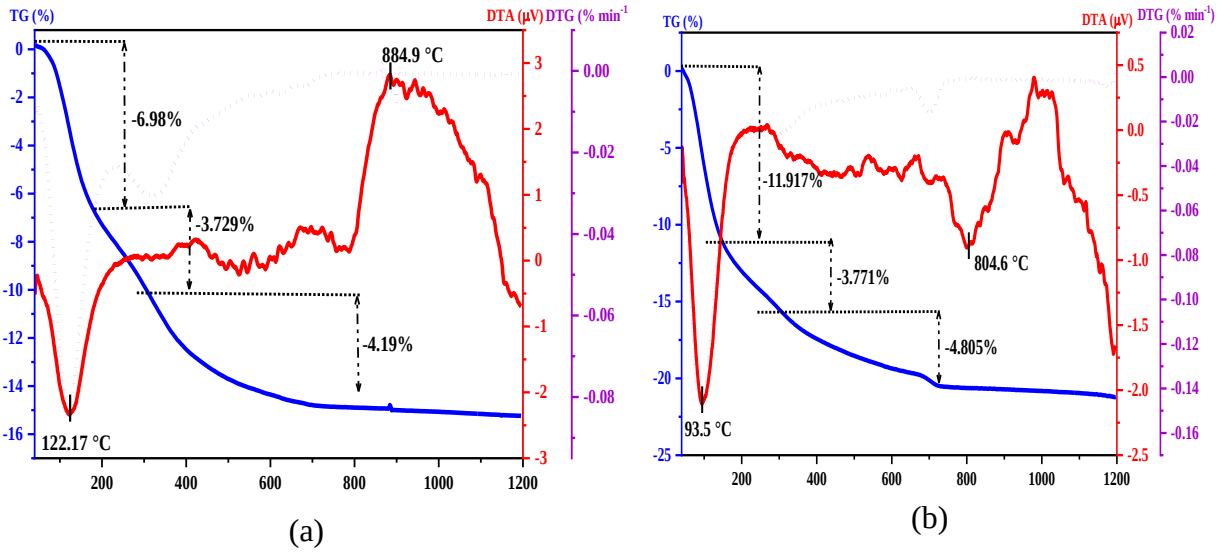

Figure 97. TG and DTA profiles of (a) ZS and (b) Z4ES

4.9.2. Dimensional properties of the sintered zeolite-poor rock/eggshell foams

Fig. 98 depicts the dimensional changes of the different zeolite-poor rock/eggshell foams burned at varying temperatures, acquired by images on a normal scale. It is worth highlighting that raising the amount of eggshell content first leads to a rise in pore size and total volume expansion, followed by shrinkage and reduced pore size. On the other hand, increasing the sintering temperature increases the pore size. This indicates the strong correlation between the pore size, amount of the foaming agent, and sintering temperature. The CaO acts as a flux reducing the melting temperature; therefore, a sparkling glassy phase is formed at high eggshell content and high sintering temperature. This is compatible with the XRD findings (Fig. 99). The reference samples (ZS) heat-treated at a temperature range of 850 °C show cracks in the surface due to insufficient molten-phase formation.

Figure 98. Photos of foamed samples with varied contents of eggshell sintered at different temperatures

4.9.3. XRD investigations of the sintered zeolite-poor rock/eggshell foams

XRD patterns of different zeolite-poor rock/eggshell foams fired at various temperatures are shown in Fig. 99. NaOH may penetrate the clinoptilolite pores more easily during the alkali-activation because of its porous nature and catalytic behaviour. This leads to the chemical interaction of cristobalite, quartz, montmorillonite, clinoptilolite, and calcite with sodium hydroxide and the formation of heulandite ($Si_{36}Al_{1.21}Na_{1.52}O_{97.84}$), PDF# 96-900-2185) as confirmed by XRD analysis. Moreover, the analysis reveals the occurrence of the amorphous phase and anorthite ($Na_{1.92}Ca_{2.08}Si_{10}A_{l6}O_{32}$, PDF# 96-100-8758) at an elevated temperature of 850 °C. Anorthite decomposes to generate a totally amorphous glassy phase at a higher temperature of 950 °C.

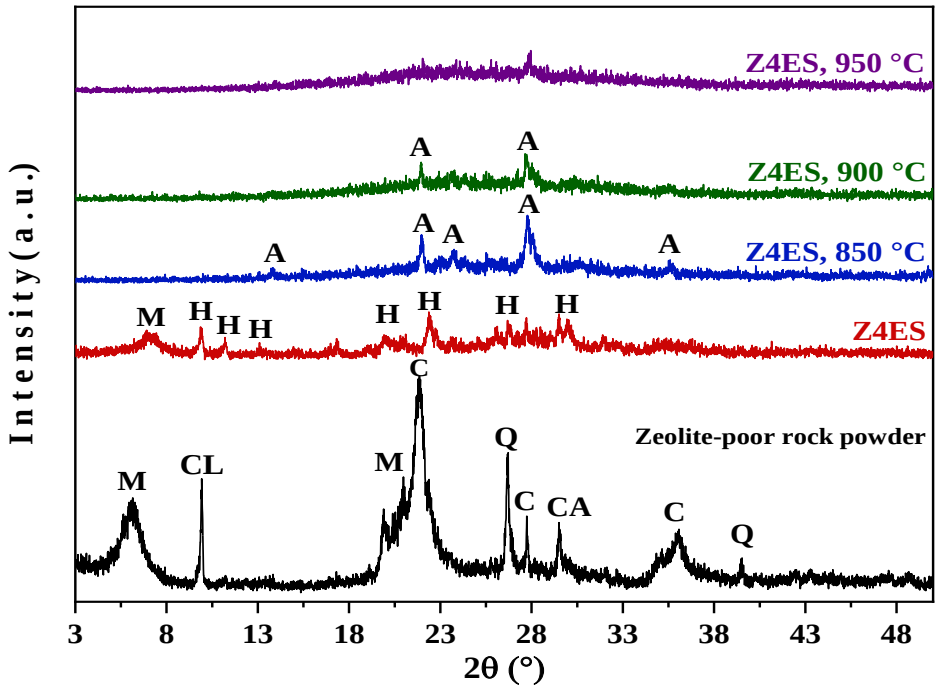

Figure 99. X-ray diffraction patterns of zeolite-poor rock, alkali-activated (Z4ES), and (Z4ES) foamed samples heat-treated at different temperatures. M= montmorillonite, CL= clinoptilolite, C= cristobalite, Q= quartz, CA= calcite, H= heulandite, A= anorthite

4.9.4. FT-IR analysis of the alkali-activated and sintered zeolite-poor rock/eggshell samples

Fig. 100 displays the FTIR spectra of alkali-activated and sintered samples (ZS and Z4ES) in infrared of a middle range (400–4000 cm^{-1}). All the samples have a significant wide asymmetric stretching vibration of the T-O-T group (T = Si, Al) that occurred at 800–1300 cm^{-1} and centred at approximately 1016 cm^{-1} in their spectra. This band is created by tetrahedral units $[SiO_4]$ and $[AlO_4]^-$ and is considered the primary band of aluminosilicate materials [77]. The absorption bands in regions around 453 cm^{-1} and 748 cm^{-1} are responsible for Si-O-Si bending vibrations and Al-O vibrations bond for aluminium in the octahedral configuration, respectively. Their appearance in the IR spectrum is owing to the aluminosilicate nature of the structure. A unique band is detected in alkali-activated materials at about 1400–1600 cm^{-1}, which is ascribed to the C-O link in carbonate ions and the O-H bond in water molecules. In the spectra of the alkali-activated samples, a soft peak at roughly 3600 cm^{-1} can be observed and indicate the OH stretching vibration of structural hydroxyl groups and water. The FTIR spectra did not change much after the heat treatment indicating the formation of aluminosilicate compound. In addition, the major bands at 1016 cm^{-1} got slightly rounder and wider in shape, which suggested a reduced degree of crystallization [214]. This outcome correlates well with the XRD data Fig. 99.

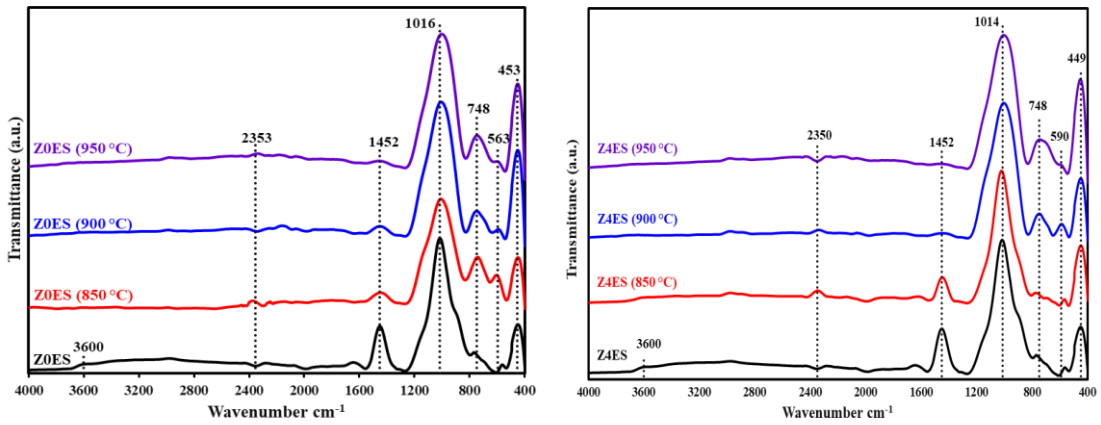

Figure 100. FTIR spectra of alkali-activated and sintered samples of a) ZS, b) Z4ES

4.9.5. SEM analysis of the alkali-activated zeolite-poor rock/eggshell samples

SEM micrographs of alkali-activated specimens (ZS and Z4ES) are displayed in Fig. 101. After the NaOH treatment of ZS samples, the constituents of zeolite-poor first decomposed, followed by a chemical reaction, resulting in the formation of heulandite in a submicron wickers-like structure. Moreover, an amorphous structure is formed, as confirmed by XRD analysis. The addition of eggshell in Z4ES sample modified the heulandite structure and led to the creation of nanofibers intergrowing from a thick matrix.

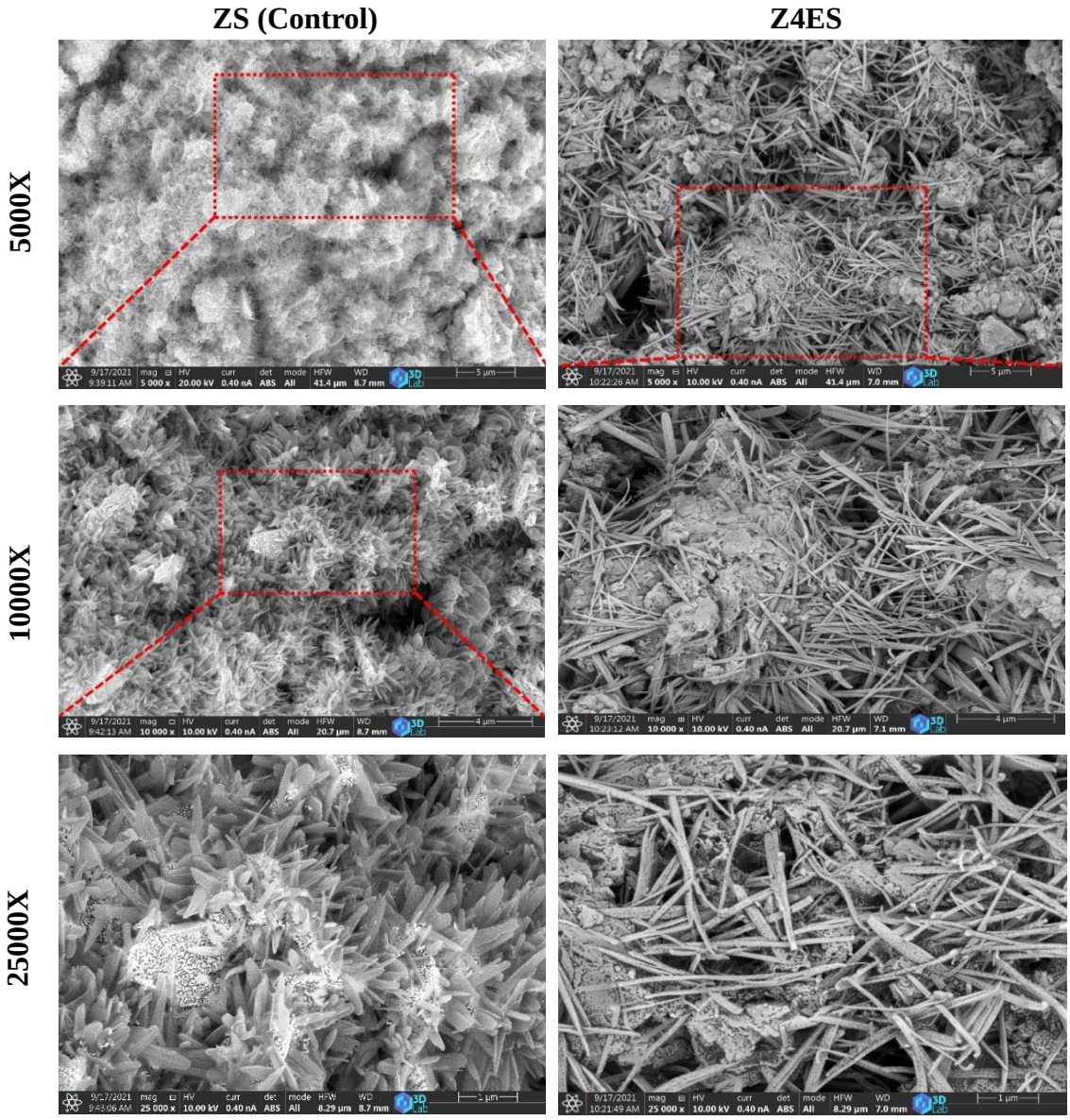

Figure 101. SEM photographs of the alkali-activated samples (ZS and Z4ES) at various magnifications

4.9.6. EDS analysis of the alkali-activated zeolite-poor rock/eggshell samples

Fig. 102 shows the EDS of the alkali-activated samples ZS and Z4ES. Based on the EDS spectra, the basic constituents of the samples were oxygen, silicon, sodium, aluminium, and carbon, indicating the creation of sodium aluminosilicate configuration. The large level of sodium has occurred from the alkali-activation step.

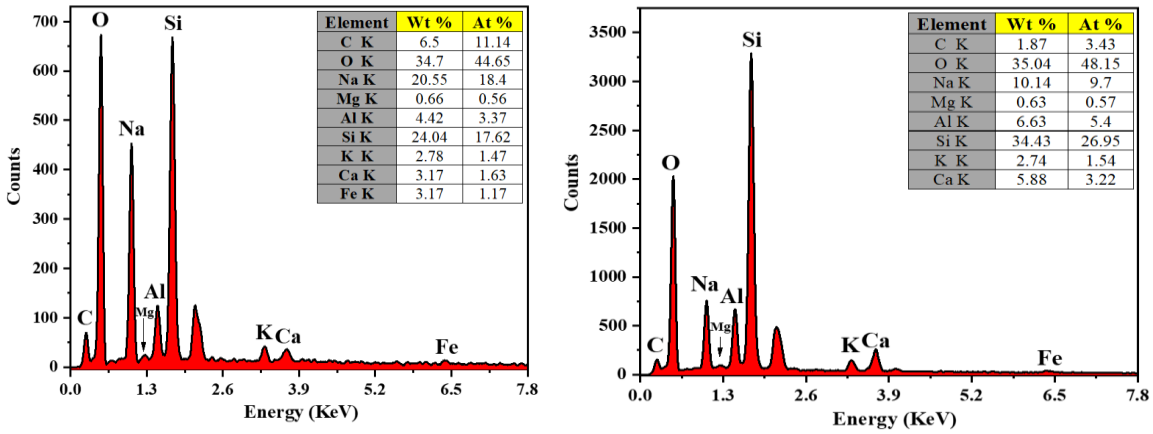

Figure 102. EDS examination of the alkali-activated samples a) ZS, b) Z4ES

4.9.7. Heating microscope and the foaming mechanism of the alkali-activated zeolite-poor rock/eggshell samples

Heating microscope studies were used to examine the heat treatment and foamability of alkali-activated zeolite-poor rock/eggshell powders in the temperature range of 40–1200 °C; the findings are presented in Fig. 103. As can be seen in Fig. 103, the foaming process is divided into four consecutive steps, which are designated from stage 1 to stage 4. In the first step, all samples showed a slight shrinkage, which increased with temperature till it reached its highest value (≈5%) at around 200 °C. This is the consequence of free water evaporation. A slight expansion appears between 220 °C and 550 °C in stage 2 for low eggshell-containing samples (ZS–Z6ES). This could be assigned to the partial decomposition of alkali-activated samples associated with the evaporation of crystalline water. In the third stage, intensive foaming has been observed in the temperature interval of 550–850 °C; this phenomenon occurs because when the mixture is heated above the softening temperature, a sealed pores structure forms, prohibiting the produced gaseous from escaping and resulting in the formation of tiny and spherical cells. As the temperature increases, the gas's internal pressure also increases, accompanied by a reduction in viscosity. As a result, the viscoelastic material expands, reaching the maximum expansion at around 850 °C. ZS exhibits a decreased "foaming" potential, which can be attributed to a lack of foaming agents. In contrast, Z4ES showed the highest foaming capability due to the optimal amount of gas produced from the foaming agent. With increasing the eggshell content above 4%, the expansion decreased because the CaO produced from the decomposition of the eggshell affects the viscosity and the gas pressure. At the end of stage 3 (above 850 °C), the big pores grow and combine with the small pores surrounding them, reducing the system's surface energy.

Finally, at stage 4, the samples begin to "collapse," which indicates that the constructed cell walls progressively melt above 1000 °C due to the increased gas pressure and reduced viscosity. The greater the eggshell content, the quicker the melting of the foams as CaO of the eggshell acts as a flux, minimizing the melting temperature.

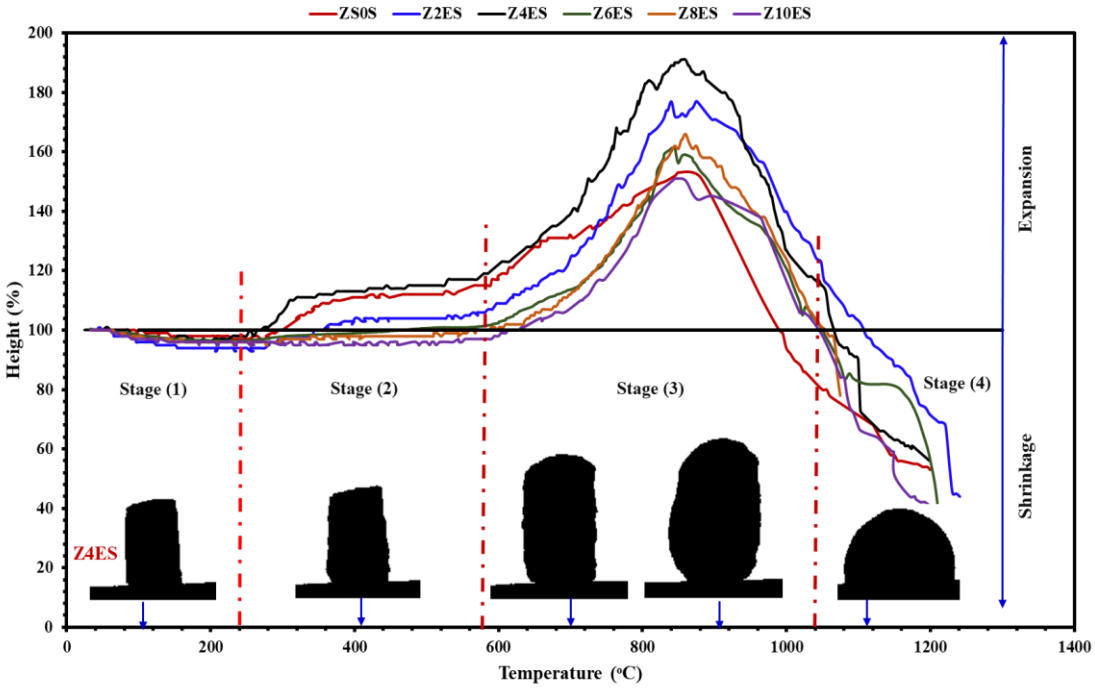

Figure 103. Heating microscope curves of different zeolite-poor rock/eggshell samples sintered in a temperature interval of (40-1200 °C) at 10 °/min

4.9.8. SEM investigation of the produced alkali-activated zeolite-poor rock/eggshell foams

Fig. 104 illustrates the microstructures of glass-ceramic foams (ZS and Z4ES) sintering at variable temperatures with a 5 °/min heating rate and 10 min residence time. As observed in these SEM micrographs, all the samples exhibit a considerable amount of porosity with non-homogeneous pore size and distribution. Demonstrated pores are approximately spherical. The wide particle size distribution of the raw powders and interconnected pores are assumed to be causative of the uneven distribution of the pores. It can be noticed that the pore morphology and size were impacted by the quantity of eggshell correspondingly. Samples without eggshell (blank) exhibit smaller and more evenly sized cells with relatively increased cellular structure uniformity. On the contrary, samples containing a high amount of eggshell demonstrate irregular microstructures with comparatively uneven and greater pore size and thicker struts. With increasing sintering temperature, the viscosity dropped. Furthermore, the amount of gas and the internal gas pressure rose during the heat treatment and led to larger pores due to the pore's coalescence. This phenomenon can be seen clearly in the samples sintered at 950 °C, where big pores are surrounded by wide cell walls with tiny, closed pores on them. The SEM findings suggest that the majority of the pores are closed pores.

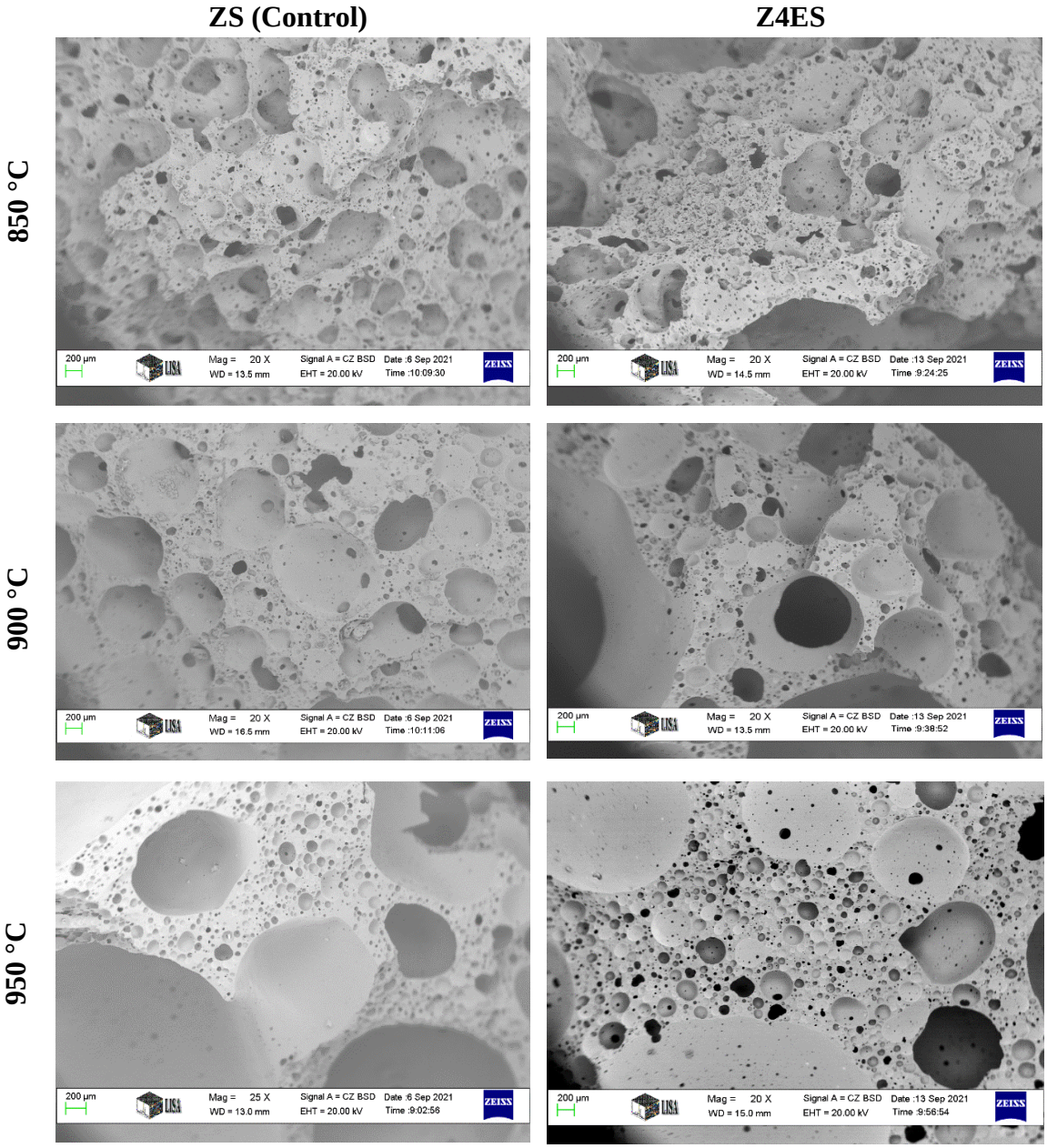

Figure 104. SEM images of the fracture surface of ZS and Z4ES samples sintered at different temperatures

4.9.9. Micro-CT analysis and properties of the pore structure and morphology of zeolite-poor rock/eggshell foams

The microstructure of the produced foams is one of the essential parameters determining the various technical properties. To evaluate the pore structure and distribution, the samples were further analyzed using CT, which allowed the creation of 3D photos (Fig. 105). As items with varied densities have variable capability in X-ray absorption, the lighter regions in Fig. 105.a and 105.c indicate the ceramic body, while other colours (blue, green, yellow, and red) depict the pores based on their width and depth. The overall porosity grew from 66.2 to 71.9% as the quantity of eggshell increased to 4%. Pore diameter ranged from 0 and 2.1 mm for ZS, but a larger pore size distribution (0–2.6 mm) was seen in samples containing 4% eggshell (Z4ES).

The porosity tests were further validated with the pycnometer test and the results showed comparable values of 67% and 72.03% for ZS and Z4ES, respectively. The increase in pore size and porosity could lead to a reduction in thermal conductivity, leading to better thermal insulation. But on the other hand, it may reduce compressive strength.

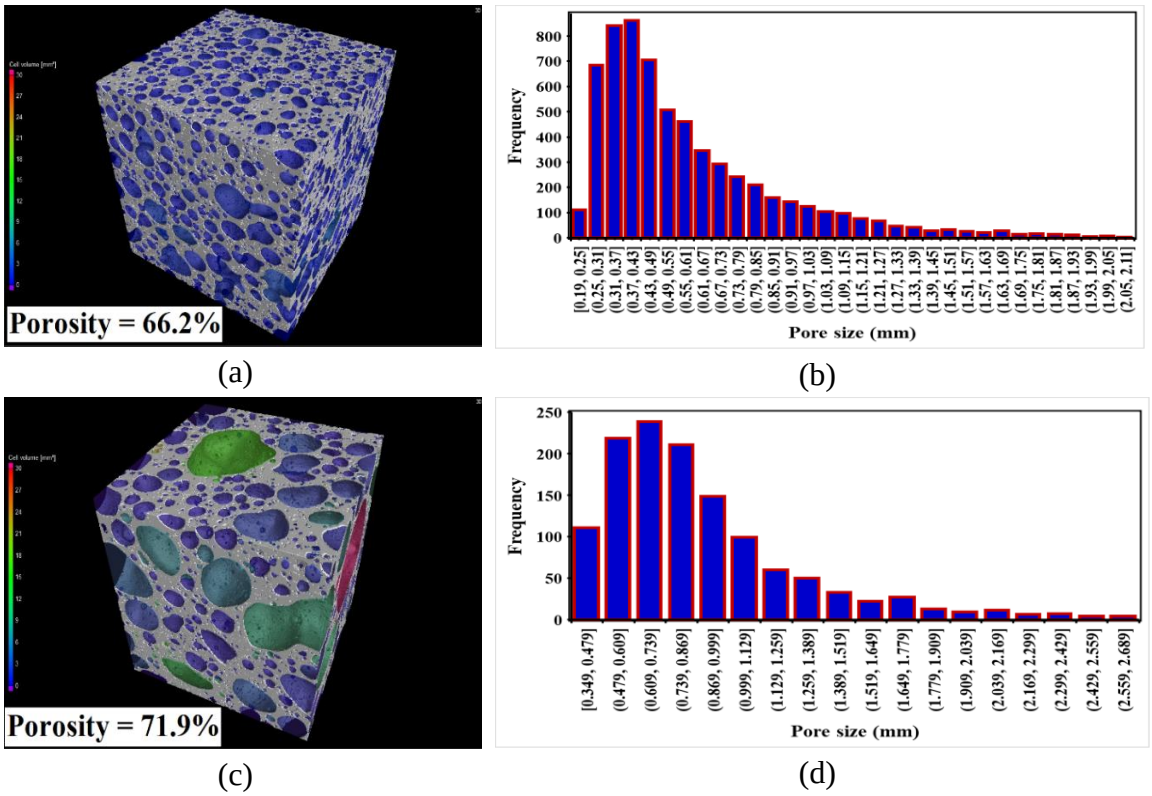

Figure 105. CT scan analysis of zeolite-poor rock/eggshell foams, a) 3D image of ZS, b) pore sizes distribution of ZS, c) 3D image of Z4ES, and d) pore sizes distribution of Z4ES

4.9.10. Bulk density of the produced zeolite-poor rock/eggshell foams

Fig. 106 depicts the influence of the pore-forming agent (eggshell) and sintering temperature on the bulk density of the foamed samples. As the eggshell content increases, the density of the specimens reduces until it reaches the minimum value (0.54 g/cm^3) when 4% of eggshell is added and sintered at 900 °C, then it starts to increase gradually with increasing the amount of eggshell till achieving the highest value of 1.07 g/cm^3 when 20% of eggshell is embedded to the mixture and heat-treated at 950 °C. The reason for this process is that upon sintering, eggshell decomposes and produces CaO and CO_2. At lower eggshell content, the gas is entrapped in the high viscous phase leading to high blowing capability. However, at high eggshell content and sintering temperature, the produced CaO affects the viscosity of the molten glass phase and hinders the foaming behaviour resulting in lower foamability. Therefore, higher densification of the samples takes place. All the foamed samples except Z20ES floated in distilled water after immersion for one week (Fig. 107), demonstrating a substantial proportion of closed porosity and density below 1 g/cm^3.

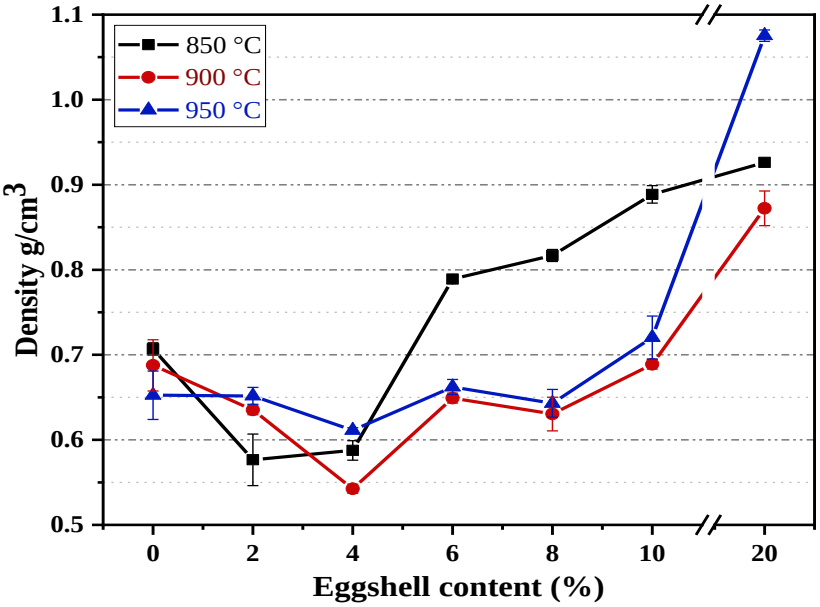

Figure 106. Bulk density of the different zeolite-poor rock/eggshell foams heat-treated at various temperatures

Samples without eggshell Samples with eggshell

Figure 107. Zeolite-poor rock/eggshell ceramic foams after immersing for a week in distilled water

4.9.11. Volume expansion of the produced zeolite-poor rock/eggshell foams

The effect of foaming agent content and sintering temperature on the volume expansion of the foamed samples is shown in Fig 108. As the quantity of foaming agent increases, the volume expansion starts to increase and reaches the maximum value with 4% addition of eggshell and sintering at 900 °C, followed by a gradual decrease with increasing the amount of the foaming agent and sintering temperature due to the limited capacity of the low viscosity liquid phase to swell under the pressure of the emitted gases. This finding agrees quite well with the heating microscope and CT scan results in Fig. 103 and Fig. 105, respectively.

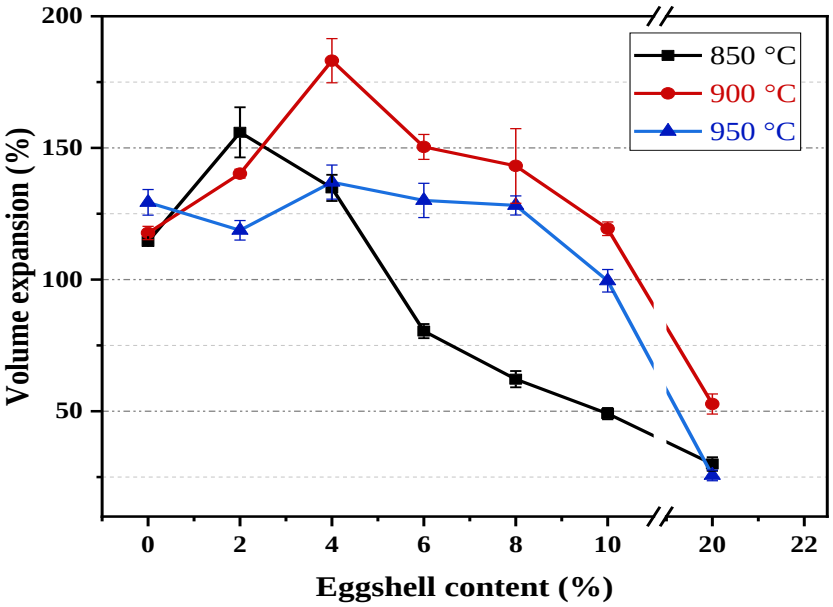

Figure 108. Volume expansion of the different zeolite-poor rock/eggshell foams heat-treated at various temperatures

4.9.12. The thermal conductivity of the produced zeolite-poor rock/eggshell foams

Fig. 109 shows the connection between the composition, thermal conductivity, and sintering temperatures of the various foamed samples. The value of thermal conductivity first decreased with increasing eggshell content and showed the minimum value (0.06 W/mK) with the addition of 8% eggshell sintered at 850 °C. Then with a further increase in eggshell content, the thermal conductivity tends to increase. The maximum measurement of the thermal conductivity was 0.3 W/mK attained from the specimen with 20% eggshell fired at 800 °C. Thermal conductivity is generally recognized to be associated with porosity as the pores are frequently occupied with gases, functioning as a barrier and lowering thermal conductivity.

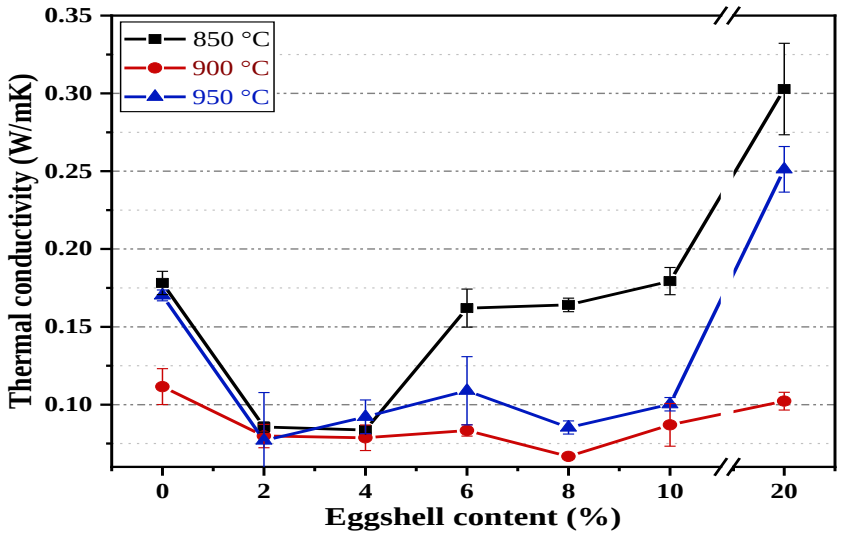

Figure 109. Thermal conductivity of the various zeolite-poor rock/eggshell foams heat-treated at various temperatures

4.9.13. Compressive strength of the produced zeolite-poor rock/eggshell foams

Fig. 110 shows the compressive strength of various samples fired at various temperatures. The compressive strength values of the produced glass-ceramic foams diminish with the rising quantity of foaming agents but then increase at the higher eggshell content. With raising the heat treatment temperature, the compressive strength tends to decrease. This could be due to the reduction in the degree of crystallization of the samples prepared at high temperature, as confirmed with XRD analysis Fig. 96. The standard deviation of the foamed samples was determined to be around 10% compared to the average compressive strength values, demonstrating uniform mechanical strengths for the different compositions of the prepared samples.

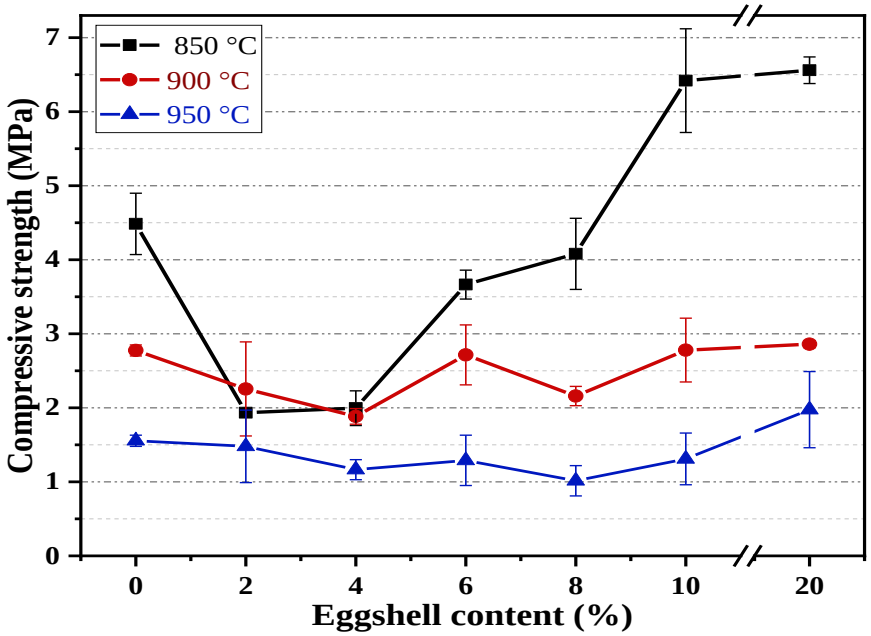

Figure 110. Compressive strength of the various zeolite-poor rock/eggshell foams heat-treated at various temperatures

4.10. Discussion and conclusions

Objective listed in Chapter 1.1 and the answers:

- **To investigate the effect of chemical activation on the prepared zeolite-poor rock/eggshell powders.**

The alkali-activation process is carried out using 2M NaOH solution; NaOH is well mixed with the previously prepared mixtures and dried for 2 days at 200 °C. The SEM analysis of the alkali-activated mixtures confirms the intergrowths of wicker-like sodium aluminosilicate structure at sub-micron and nanoscale sizes. This might be owing to zeolite-poor rock's porous structure, which enables better NaOH penetration, resulting in a higher reactivity. The alkali-activated samples possess a low-temperature melting that allows the materials to foam upon the emission of the gases. The XRD suggested the formation of heulandite and amorphous structure in the alkali-activated materials.

- **To evaluate the effect of the eggshell incorporation on the foamability of the alkali-activated mixture.**

The alkali activation in the different mixtures contributes to a remarkable lowering of both the softening and foaming temperatures and a reduction in the crystallinity of the produced samples. XRD results revealed the occurrence of physicochemical reaction with the formation of two main crystalline phases: heulandite and anorthite, after the alkali activation and thermal treatment of the mixtures. The systematic investigations using a heating microscope indicate that the amount of foaming agent used and sintering temperature significantly impact the foaming mechanism and the height expansion. Moreover, the ideal sintering temperature was determined to be in the range of 850–900 °C, while the appropriate heating rate was 10 °C/min.

- **To evaluate the impact of eggshell incorporation on the technical properties of the developed glass-ceramic foams, such as bulk density, shrinkage, apparent porosity, water absorption, thermal conductivity, and compressive strength**.

The developed samples showed density varying from 0.54 to 1.07 g/cm^3, thermal conductivity extending from 0.06 to 0.3 W/mk, and compressive strength ranging from 1.01 to 6.7 MPa, demonstrating considerable versatility of glass-ceramic foams. Glass-ceramic foams produced from zeolite-poor rock and eggshell could be an excellent energy-saving alternative to conventional glass foams in construction applications.

- **To compare the technical findings of the created zeolite-poor rock/eggshell samples to the results of the most recent research on glass-ceramic foams.**

As per the studies mentioned in the literature (Table 5), a range of raw materials could be utilized for the preparation of glass-ceramics foams, including waste glass, fly ash, coal bottom ash, red mud etc. It's worth highlighting that zeolite-poor rock (main raw material) and eggshell (foaming agent) are potential feedstock to produce glass ceramic foams since the created samples demonstrated technological features comparable to the findings in the literature with the extra benefit of cost-effectiveness.

Conclusion

- **It was proved that it is possible to produce new glass-ceramic foams with low density (0.54–1.07 g/cm^3), low thermal conductivity (0.06–0.3 W/mk) and good compressive strength (1.01–6.7 MPa) based on zeolite-poor rock (D <100 µm) and eggshell (D90<100 µm) using alkali activation and reactive sintering techniques. Eggshell partially substitute zeolite-poor rock. The substitution percentages were 0–20% by wt% of zeolite-poor rock. The prepared powder mixtures were treated with 2M NaOH solutions for alkali activation, well-mixed for 5 min and then dried in the oven at 200 °C for 2 days. The alkali-activated dried powders were ground in a planetary ball mill for 15 min at 150 rpm. Using uniaxial pressing machines at a pressure of 18 MPa, the milled powders were then compacted to form cylindrical pellets. The green ceramic bodies were heat-treated at varied temperatures (850, 900, and 950 °C) for 5 min holding time, with 5 °C/min heating rate.**
- **I established that the microstructure of the alkali-activated samples could be modified by the addition of eggshell (D90<100 µm). The alkali activation of milled zeolite-poor rock containing 4% eggshell using 2M of NaOH followed by drying at**

200 °C for 2 days leads to the decomposition of zeolite-poor rock, followed by a chemical reaction, resulting in the formation of needle-like nanofibers intergrowing from a matrix (Fig. 101). The modification of these different nanostructures (large surface area) makes it possible to produce glass-ceramic foams at a lower temperature (850–950 °C) with different properties.

- **I established that softening and foamability of the alkali-activated zeolite-poor rock (2M NaOH, 200 °C, 2 days) can be modified by using different foaming agents. In the case of alkali-activated zeolite-poor rock (D90<100 µm) containing eggshell (2-20 wt%) (D90<100 µm) sintered in the temperature range of 40-1200 °C, the foaming process takes place in two stages showing a maximum expansion in the height of 188% (Fig. 103).**
- **I established that by the addition of the eggshell to zeolite-poor rock followed by alkali activation (2M NaOH, 200 °C, 2 days) and sintered at 900 °C with a heating rate of 5 °C/min and residence time of 10 min, the pore's structure can be modified, which influenced the compressive strength of the produced samples. The samples containing 4 wt% eggshell have spherical and large pores (Fig. 105) with a moderated compressive strength (1.4 MPa)**

5. Summary

The current study is the first work to investigate the usage of zeolite-poor rock and solid waste (sawdust and eggshell) in the manufacturing of innovative ceramic bricks and glass-ceramic foams with enhanced thermal insulation properties in an attempt to address the sustainability-connected challenges. Based on the experimental findings, the following conclusions can be obtained.

- Porous bricks and glass-ceramic foams based on zeolite-poor rock and solid waste (sawdust and eggshell) have been successfully prepared and characterized. Sintering the mixtures at a temperature range of 950-1250 °C led to the formation of porous bricks, while the heat treatment of the alkali-activated mixtures in the temperature range of 850-950 °C resulted in the development of glass-ceramic foams.
- The produced samples (porous bricks and glass-ceramic foams) possess lightweight, good compressive strength and superior thermal insulation compared to the result of other works in the literature.
- The proper milling, compaction and sintering conditions have been determined. Zeolite-poor rock is a soft rock and easy to crush. It forms fine and homogenous powders when mixed with sawdust and eggshell. Upon uniaxial pressing, zeolite-poor rock mixture produces a compacted green ceramic that can be easily handled.
- The alkali activation of the samples using 2M NaOH results in the formation of whiskers-like sodium aluminum silicate in submicron and nanosize; the alkali-activated samples possess a lower softening behaviour leading to a low-temperature melting. The viscous material resulting from the heat treatment tends to expand due to the emission of the gases making the foams.
- In both cases (production of bricks and foams), the heat treatment process leads to the decomposition of the mineral phases in raw materials and the occurrence of physicochemical reaction that leads to the formation of new phases.
- Zeolite-poor rock is an easily mined and processed material, while sawdust and eggshell are available waste. They both can contribute to a safer and cleaner environment in several ways, for instance, by minimizing energy consumption and the cost related to waste management. Preparation of insulating building materials using available and relatively inexpensive raw materials could lead to economically cost-effect and environmentally-friendly building materials with superior properties.

6. Claims/New scientific results

Based on the integrated experimental research studies of porous bricks and glass-ceramic foams production from zeolite-poor rocks and solid waste (sawdust and eggshell), the following new scientific findings were derived:

6.1. Claims for the development of porous ceramic bricks

Claim 1. Preparation of innovative composite bricks based on zeolite-poor rock and solid waste (sawdust and eggshell)

It was proved that it is possible to produce innovative building bricks with low density (1.4–1.88 g/cm^3) and low thermal conductivity (0.13–0.7 W/mk) based on zeolite-poor rock (Tokaj) (D <100 μm) together with solid waste (sawdust and eggshell powder) (D90<100 μm). Sawdust and eggshell were added as a partial replacement for zeolite-poor rock in the specimens. The replacement percentages of sawdust and eggshell were 0–10 wt% and 0–20 wt%, respectively, by mass of zeolite-poor rock. The mixed powders were milled for 15 min at 150 rpm to produce homogenous mixtures. The prepared mixtures were pressed at 40-45 MPa. The produced green ceramic samples were then sintered at variable temperatures (950, 1050, 1150, and 1250 °C) for 3 h holding time and a heating rate of 60 °C/h. Bricks produced by this technique using these raw materials show no efflorescence (no salt formation on the surfaces).

Claim 2. The effect of sawdust and eggshell addition on the pores of the produced bricks.

I established that the inclusion of 8 wt% sawdust (D90 <100 μm) into zeolite-poor rock powder (D <100 μm) followed by ball milling for 15 min at 150 rpm, dry pressing at 45 MPa and sintering at a temperature range of 950-1250 °C with a residence time of 3 h and a heating rate of 60 °C/h resulted in bricks with an irregular porous structure having large numbers of open pores (Fig. A1). While the incorporation of 20 wt% eggshell powder (D90 <100 μm) into the zeolite-poor rock powder, followed by the same production process with the same conditions, led to the formation of a cellular structure with a relatively larger number of round-like closed pores (Fig. A2).

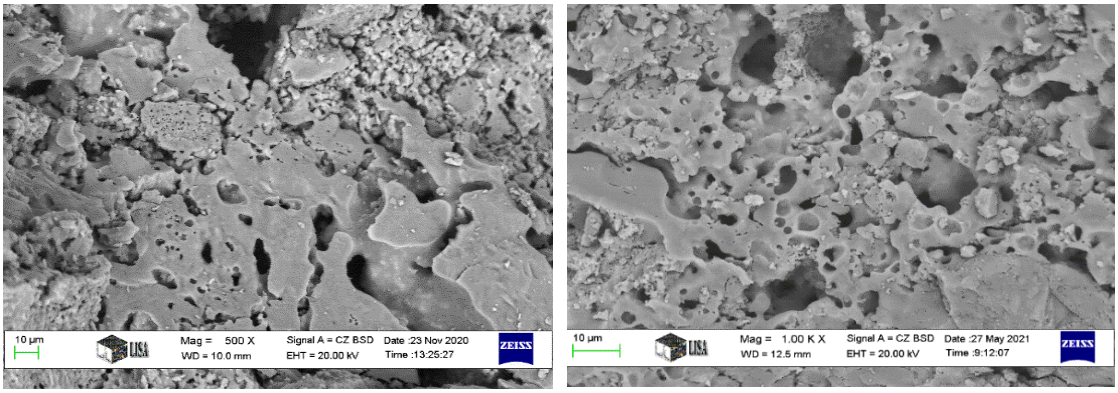

(1) (2)

Fig. A. SEM images of the fracture surface of a) zeolite-poor rock and b) zeolite-poor rock+20% eggshell sintered at 1050 °C

Claim 3. The effect of eggshell addition on the compressive strength of the produced samples

I established that with the addition of 10 wt% eggshell powder (D90<100 μm) into zeolite-poor rock powder (D<100 μm), followed by the ball milling, dry pressing at 45 MPa and sintering at a temperature range of 950-1250 °C with a residence time of 3 h and a heating rate of 60 °C/h, bricks with higher compressive strength can be obtained compared to the bricks containing the same amount of sawdust (D90 <100 μm). This could be explained by the fact that during the sintering, the eggshell decomposes and produce CaO, which acts as a flux that induces the liquid phase formation causing verification that binds the particles together and results in higher compressive strength of the produced eggshell containing bricks (Fig. B2).

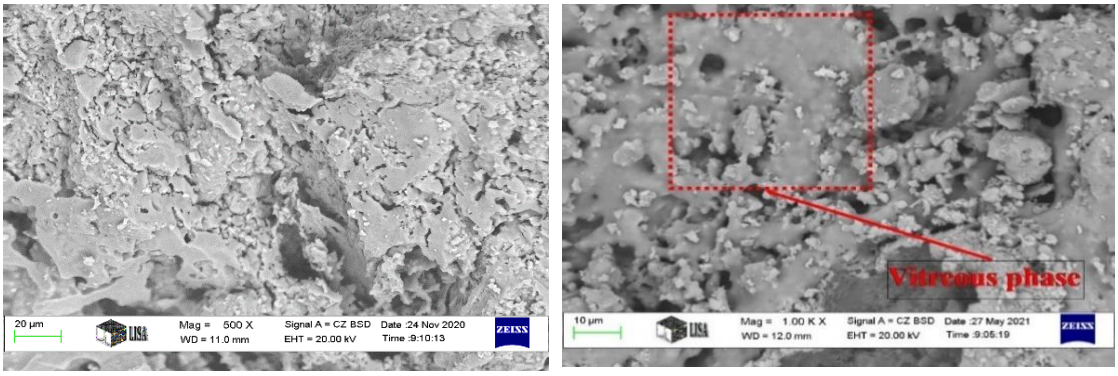

(1) (2)

Fig. B. SEM images of (a) zeolite-poor rock + 6% sawdust (b) zeolite-poor rock + 10% eggshell samples sintered at 1050 °C showing the formation of the vitreous phase

Claim 4. Formation of mullite whisker in the composite bricks containing sawdust

I established that the inclusion of 8 wt% sawdust into zeolite-poor rock (D <100 μm), followed by the ball milling for 15 min at 150 rpm, dry pressing at 45 MPa and sintering at a temperature range of 950-1250 °C with a residence time of 3 h, contributes to the firing raising the temperature. As a result, a mullite phase in a whisker-like structure has been formed at a relatively lower temperature (1150 °C), as confirmed by SEM, EDS (Fig. C) and XRD (Fig. D).

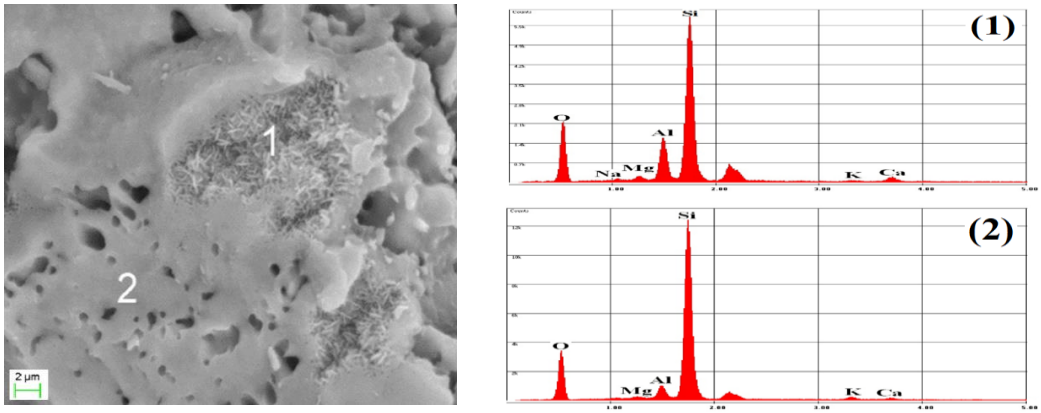

Fig. C. SEM and EDS micrograph of the fracture surface of zeolite + 8% sawdust sintered at 1150 °C

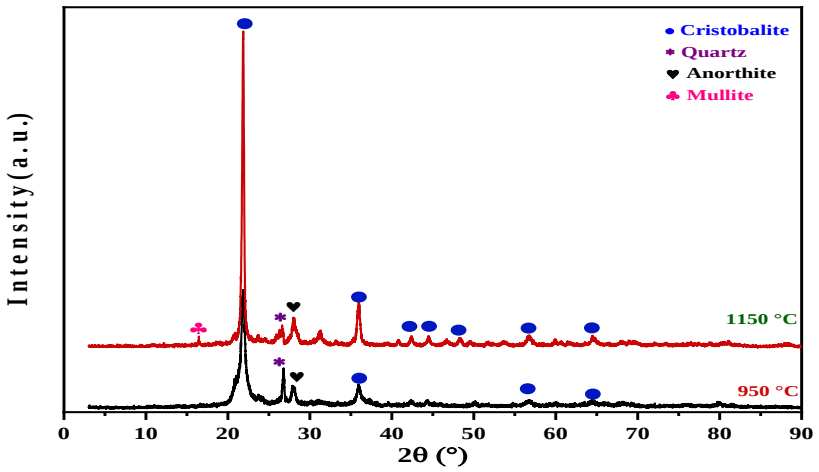

Fig. D. XRD results of zeolite-poor rock powder and fired specimens with 6% sawdust

6.2. Claims for manufacturing of glass-ceramic foams

Claim 5. Development of new glass-ceramic foams based on zeolite-poor rock and solid waste (sawdust and eggshell)

It was proved that it is possible to produce new glass-ceramic foams with low density (0.3–1.07 g/cm^3), low thermal conductivity (0.04–0.3 W/mk) and good compressive strength (0.3–6.7 MPa) based on zeolite-poor rock (D <100 μm) and (sawdust and eggshell powder) (D90<100 μm) using alkali activation and reactive sintering techniques. Sawdust and eggshell partially substitute zeolite-poor rock. The substitution percentages were 0–20% by wt% of zeolite-poor rock. The prepared powder mixtures were treated with 2M NaOH solutions for alkali activation, well-mixed for 5 min and then dried in the oven at 200 °C for 2 days. The alkali-activated dried powders were ground in a planetary ball mill for 15 min at 150 rpm. Using uniaxial pressing machines at a pressure of 18 MPa, the milled powders were then compacted to form cylindrical pellets. The green ceramic bodies were heat-treated at varied temperatures (850, 900, and 950 °C) for 5 min holding time, with 5 °C/min heating rate.

Claim 6. The alkali-activation modified the structure of the produced mixtures containing sawdust and eggshell

I established that the microstructure of the alkali-activated samples could be modified by the addition of sawdust and eggshell (D90<100 μm). The alkali activation of milled zeolite-poor rock containing 6% sawdust using 2M of NaOH followed by drying at 200 °C for 2 days led to the formation of wickers-like aluminosilicate structure intergrowing through the thick matrix at sub-micron and nanoscale sizes (SEM images, Fig. E1). While in the case of the sample containing milled zeolite-poor rock containing 4% eggshell, the alkali-activation in the same condition leads to the decomposition of zeolite-poor rock, followed by a chemical reaction, resulting in the formation of needle-like nanofibers intergrowing from a matrix (Fig. E2). The modification of these different nanostructures (large surface area) makes it possible to produce glass-ceramic foams at lower temperature (850–950 °C) with different properties.

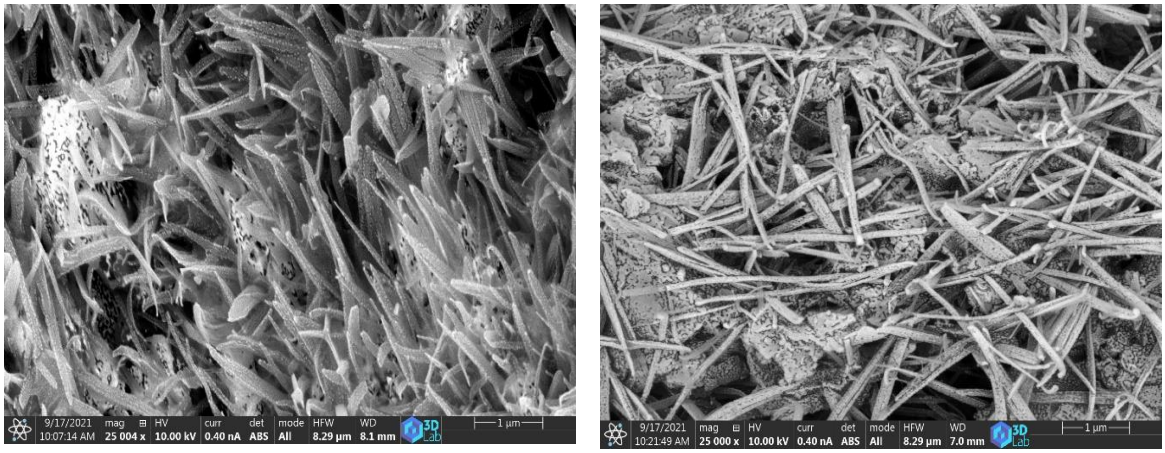

(1) (2)

Fig. E. SEM images of the alkali-activated mixtures (zeolite-poor rock + 4% sawdust and zeolite-poor rock + 4 % eggshell) at different magnifications

Claim 7. Development of zeolite-poor rock/sawdust foams with the lowest thermal conductivity.

I demonstrated that the application of 8 wt% of sawdust to zeolite-poor rock (D90<100 µm) followed by the alkali activation with 2M NaOH solutions, drying at 200 C for 2 days and sintering at temperatures of 850 °C for 5 min holding time, with 5 °C/min heating rate, leads to the development of foams with the lowest thermal conductivity (0.04 W/mk) compared to the samples without sawdust (Fig. F) and (Fig. G).

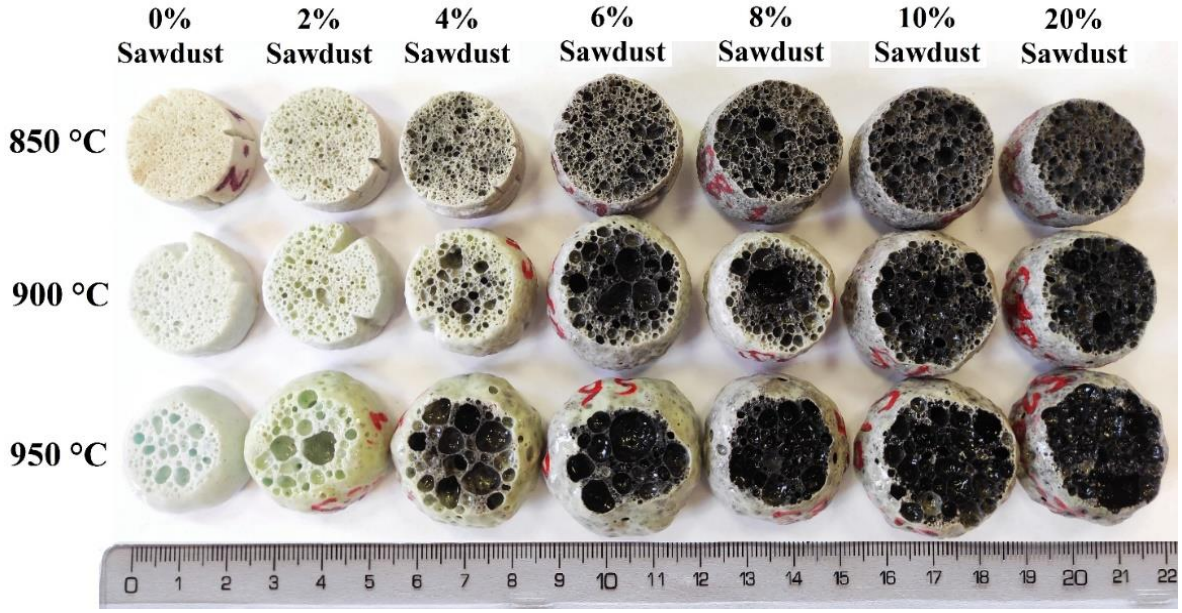

Fig. F. The produced foams with different sawdust content sintered at different temperature

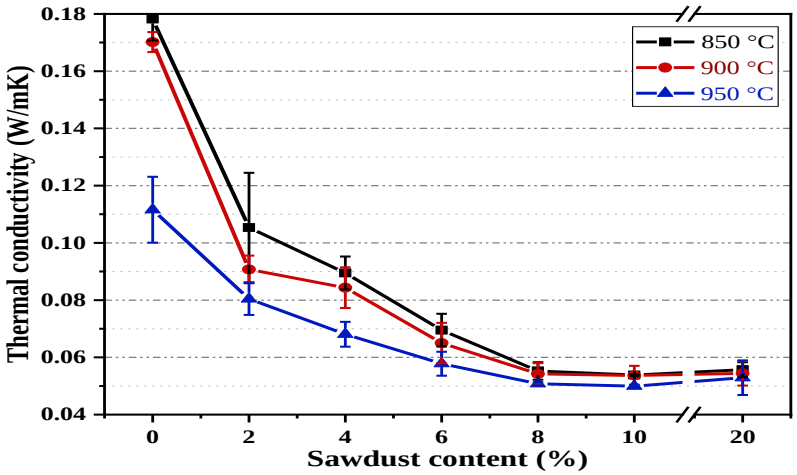

Fig. G. The correlation between thermal conductivity, and sawdust content of the samples sintered at different temperatures

Claim 8. The effect of the sawdust and eggshell incorporation on the foamability of the alkali-activated mixture.

I established that softening and foamability of the alkali-activated zeolite-poor rock (2M NaOH, 200 °C, 2 days) can be modified by using different foaming agents. In the case of alkali-activated zeolite-poor rock (D90<100 μm) containing sawdust (2-20 wt%) (D90<100 μm) sintered in the temperature range of 40-1200 °C, the foaming occurs in 3 steps reaching a maximum height of 216%, followed by a collapse of the foams (Fig. H). While in the case of alkali-activated zeolite-poor rock containing eggshell (2-20 wt%) (D90<100 μm) sintered in the temperature range of 40-1200 °C, the foaming process takes place in two stages showing a maximum expansion in the height of 188% (Fig. I). This change is due to the different behaviour of the decomposition of the foaming agents. During the sintering, the sawdust decomposition takes place in a temperature interval of 230–650 °C, while the eggshell decomposition occurs in the temperature range of 620–927 °C, producing gas that contributes to the foaming of the samples.

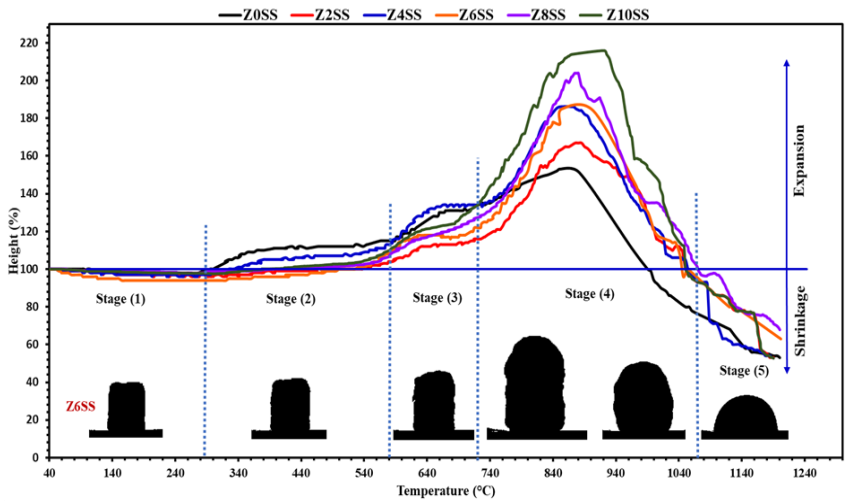

Fig. H. Heating microscope graphs of zeolite-containing sawdust samples heat-treated in the temperature range (40–1200 °C) at 10 °/min.

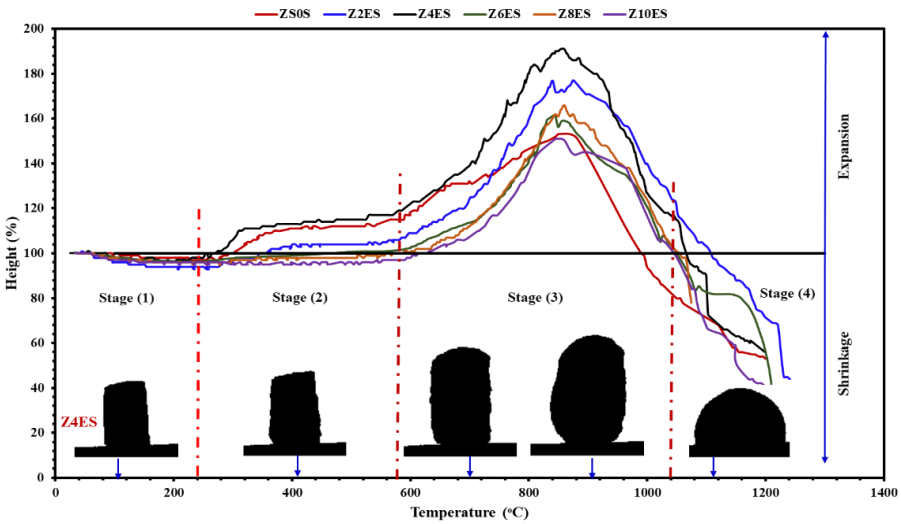

Fig. I. Heating microscope curves of different zeolite-poor rock/eggshell samples sintered in a temperature interval of (40-1200 °C) at 10°/min

Claim 9. The effect of the sawdust and eggshell addition on the pore structure and compressive strength of the produced foams.

I established that by the addition of the sawdust and eggshell to alkali-activated zeolite-poor rock (2M NaOH, 200 °C, 2 days) sintered at 900 °C, the pore's structure can be modified, which influenced the compressive strength of the produced samples. The produced alkali-activated zeolite-poor rock foams sintered at 900 °C with a heating rate of 5 °C/min and residence time of 10 min possess spherical and small pore sizes with higher compressive strength (6.7 MPa) (Fig. J1), while the alkali-activated samples containing 4 wt% eggshell sintered at 900 °C with a heating rate of 5 °C/min and residence time of 10 min produce foams having spherical and large pores (Fig. J2) with a moderated compressive strength (1.4 MPa) However, the alkali-activated sample incorporated 6 wt% sawdust sintered at 900 °C with a heating rate of 5 °C/min and residence time of 10 min produced foams with irregular pore size and structure (Fig. J3) and exhibit the least compressive strength (2 MPa). The spherical shape of the pores and relatively better distribution are connected to the relatively high compressive strength in samples (reference and sample containing 4 wt% eggshell).

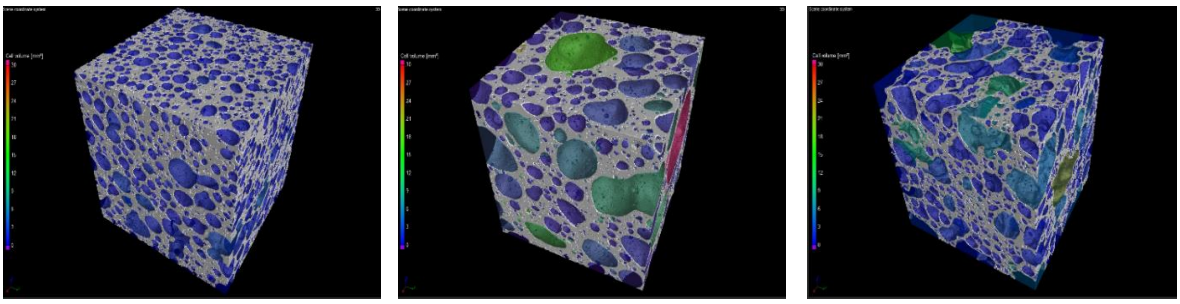

(1) (2) (3)

Fig. J. 3D image of 1) ZS, 2) Z4ES and 3) Z6SS

Publications

Construction and Building Materials 297 (2021) 123715

Contents lists available at ScienceDirect

Construction and Building Materials

journal homepage: www.elsevier.com/locate/conbuildmat

Environmentally-friendly ceramic bricks made from zeolite-poor rock and sawdust

Jamal Eldin F.M. Ibrahim *, Mohammed Tihtih, László A. Gömze

Institute of Ceramics and Polymer Engineering, University of Miskolc, H-3515 Miskolc-Egyetemváros, Hungary

Journal of Building Engineering 45 (2022) 103491

Contents lists available at ScienceDirect

Journal of Building Engineering

journal homepage: www.elsevier.com/locate/jobe

Preparation of innovative eco-efficient composite bricks based on zeolite-poor rock and Hen's eggshell

Jamal Eldin F.M. Ibrahim [a,*], Olga B. Kotova [b], Shiyong Sun [c], Emese Kurovics [a,d], Mohammed Tihtih [a], László A. Gömze [a,d]

[a] *Institute of Ceramic and Polymer Engineering, University of Miskolc, H-3515, Miskolc-Egyetemváros, Hungary*
[b] *Institute of Geology, Komi Science Center, Ural Branch of the Russian Academy of Sciences, Russian Federation*
[c] *School of Environment and Resource, Key Laboratory of Solid Waste Treatment and Resource Recycle of Ministry of Education, Southwest University of Science and Technology, Mianyang, Sichuan, China*
[d] *IGREX Engineering Service Ltd, H-3459, Igrici, Hungary*

Journal of Building Engineering 59 (2022) 105160

Contents lists available at ScienceDirect

Journal of Building Engineering

journal homepage: www.elsevier.com/locate/jobe

Innovative glass-ceramic foams prepared by alkali activation and reactive sintering of clay containing zeolite (zeolite-poor rock) and sawdust for thermal insulation

Jamal Eldin F.M. Ibrahim *, Mohammed Tihtih, Emese Kurovics, László A. Gömze [1], István Kocserha

Institute of Ceramics and Polymer Engineering, University of Miskolc, H-3515, Miskolc, Egyetemváros, Hungary

Ceramics International 48 (2022) 25905–25917

Contents lists available at ScienceDirect

Ceramics International

journal homepage: www.elsevier.com/locate/ceramint

Preparation, characterization, and physicomechanical properties of glass-ceramic foams based on alkali-activation and sintering of zeolite-poor rock and eggshell

Jamal Eldin F.M. Ibrahim [a,*], László A. Gömze [a,1], Daniel Koncz-Horvath [b], Ádám Filep [b], István Kocserha [a]

[a] Institute of Ceramics and Polymer Engineering, University of Miskolc, H-3515, Miskolc-Egyetemváros, Hungary
[b] Institute of Metallurgy, Metal Forming and Nanotechnology, University of Miskolc, H-3515, Miskolc-Egyetemváros, Hungary

Articles related to the dissertation:

1. **Jamal Eldin FM Ibrahim**, Mohammed Tihtih, Emese Kurovics, László A. Gömze and István Kocserha. " Innovative glass-ceramic foams prepared by alkali activation and reactive sintering of zeolite-poor rock and sawdust for thermal insulation." *Journal of Building Engineering* (2022): ***IF (7.144) D1***
2. **Jamal Eldin FM Ibrahim**, László A. Gömze, Daniel Koncz-Horvath, Ádám Filep, and István Kocserha. "Preparation, characterization, and physicomechanical properties of glass-ceramic foams based on alkali-activation and sintering of zeolite-poor rock and eggshell." *Ceramics International* 48 (2022): 25905. ***IF (5.532) Q1***
3. **Jamal Eldin FM Ibrahim**, Mohammed Tihtih, and László A. Gömze. "Environmentally-friendly ceramic bricks made from zeolite-poor rock and sawdust." *Construction and Building Materials* 297 (2021): 123715. ***IF (6.14) D1***
4. **Jamal Eldin FM Ibrahim**, Olga B. Kotova, Shiyong Sun, Emese Kurovics, Mohammed Tihtih, and László A. Gömze. "Preparation of innovative eco-efficient composite bricks based on zeolite-poor rock and Hen's eggshell." *Journal of Building Engineering* 45 (2022): 103491. ***IF (7.144) D1***
5. **Jamal Eldin FM Ibrahim**, Emese Kurovics, Mohammed Tihtih, and László A. Gömze. "Ceramic bricks with enhanced thermal insulation produced from natural zeolite." *Pollack Periodica* 16, no. 3 (2021): 101-107. ***IF (0.87) Q3***
6. **Jamal Eldin FM Ibrahim**, Mohammed Tihtih, Emese Kurovics, Ethem İlhan Şahin László A. Gömze and István Kocserha. " Glass-ceramic foams produced from zeolite-poor rock (Tokaj)." *Pollack Periodica* 16, no. 3 (2021): 101-107. ***IF (0.87) Q3***
7. **Jamal Eldin FM Ibrahim**, Emese Kurovics, Mohammed Tihtih, and László A. Gömze and István Kocserha. "Synthesis and characterization of alkali-activated zeolite-poor rocks." In Journal of Physics: Conference Series, vol. 2315, no. 1, p. 012020. IOP Publishing, 2022.

Other publications:

1. **Jamal Eldin FM Ibrahim**, Kurovics, M. Tihtih, P. Somdee, A. G. Gerezgiher, K. Nuilek, E. E. Khine, and M. Sassi. "Preparation and Investigation of Alumina-Zeolite Composite Materials." In *Journal of Physics: Conference Series*, vol. 1527, no. 1, p. 012029. IOP Publishing, 2020. ***IF (0.55) Q3***
2. **Jamal Eldin FM Ibrahim**, and L. A. Gömze. "Investigation of the Rheological Properties of Complex Zeolite-Alumina Mixtures." In *Journal of Physics: Conference Series*, vol. 1527, no. 1, p. 012009. IOP Publishing, 2020. ***IF (0.55) Q3***
3. **Jamal Eldin FM Ibrahim**, Afanasy S. Apkarian, Mohammed Tihtih, Sergei N. Kulkov, and László A. Gömze. "In-situ carbonization of natural zeolite-alumina composite materials incorporated sawdust." *Epitoanyag-Journal of Silicate Based & Composite Materials* 73, no. 4 (2021). ***IF (1.079)***
4. **Jamal Eldin FM Ibrahim**, Dmitry A. Shushkov, Emese Kurovics, Mohammed Tihtih, Olga B. Kotova, Péter Pala, and László A. Gömze. "Effect of composition and sintering temperature on thermal properties of zeolite-alumina composite materials." *Epitoanyag-Journal of Silicate Based & Composite Materials* 72, no. 4 (2020). ***IF (1.079)***
5. **Jamal Eldin FM Ibrahim**, Ayhan Mergen, Umut Parlak, Emese Kurovics, Mohammed Tihtih, and László A. Gömze. "Synthesis and characterization of iron-doped $GdMnO_3$ multiferroic ceramics." *Építöanyag* (Online) 1 (2021): 24-27. ***IF (1.079)***
6. **Jamal Eldin FM Ibrahim**, Ayhen Mergen, Umut Parlak, and Emese Kurovics. "The Influence of Cr doping on the Structural and Magnetic Properties of $HoMnO_3$ Multiferroic Ceramics." In *IOP Conference Series: Materials Science and Engineering*, vol. 613, no. 1, p. 012009. IOP Publishing, 2019. ***IF (0.51)***
7. **Jamal Eldin FM Ibrahim**, Ayhan Mergen, Ethem İlhan SAHİN, and Haythem S Basheer. "The effect of europium doping on the structural and magnetic properties of $GdMnO_3$ multiferroic ceramics." *Advanced Ceramics Progress* 3, no. 4 (2017): 1-5.
8. Mohammed Tihtih, **Jamal Eldin FM Ibrahim**, Mohamed A. Basyooni, Emese Kurovics, Walid Belaid and István Kocserha. " Role of A-site (Sr), B-site Y, and A, B sites (Sr, Y) substitution in lead-free $BaTiO_3$ ceramic compounds: Structural, optical, microstructure, mechanical, and thermal conductivity properties." *Ceramics International* (2022). ***IF (5.532) Q1***
9. Mohammed Tihtih, **Jamal Eldin FM Ibrahim**, Mohamed A. Basyooni, Walid Belaid, László A. Gömze, and István Kocserha. "Structural, optical, and electronic properties of barium titanate: experiment characterisation and first-principles study." *Materials Technology* (2022): 1-11. ***IF (3.846) Q2***
10. Mohammed Tihtih, **Jamal Eldin FM Ibrahim**, Emese Kurovics, and László A. Gömze. "Synthesis of $Ba_{1-x}SrxTiO_3$ (x= 0–0.3) ceramic powders via sol-gel method: structural, microstructure, thermal conductivity, and compressive strength properties." *Crystal Research and Technology* 57, no. 1 (2022): 2100106. ***IF (1.639) Q2***
11. Mohammed Tihtih, **Jamal Eldin FM Ibrahim**, Emese Kurovics, and László A. Gömze. "Study of the structure, microstructure and temperature dependent thermal

conductivity properties of $SrTiO_3$: via Y^{3+} substitution." In *Journal of Nano Research*, vol. 69, pp. 33-42. Trans Tech Publications Ltd, 2021. ***IF (3.06) Q3***

12. Dmitry A. Shushkov, Olga B. Kotova, **Jamal Eldin FM Ibrahim**, Maria Harja, László A. Gömze, Tatyana N. Shchemelinina, and Grigoriy V. Ignatiev. "Analcime-bearing rocks as advanced sorbents." *Epitoanyag-Journal of Silicate Based & Composite Materials* 72, no. 5 (2020). ***IF (1.079)***
13. Afanasy S. Apkarian, László A. Gömze, **Jamal Eldin FM Ibrahim**, and Sergei N. Kulkov. "Sintering of silica-alumina granular materials and its catalytic properties." *Epitoanyag-Journal of Silicate Based & Composite Materials* 73, no. 4 (2021). ***IF (1.079)***
14. Emese Kurovics, Aleksey S. Kulkov, **Jamal Eldin FM Ibrahim**, AD Kashin, Péter Pala, Veronika Nagy, Sergei N. Kulkov, and László A. Gömze. "Mechanical properties of mullite reinforced ceramics composite produced from kaolin and corn starch." *Epitoanyag-Journal of Silicate Based & Composite Materials* 73, no. 4 (2021). ***IF (1.079)***
15. Mohammed Tihtih, Aleksei V. Ponaryadov, **Jamal Eldin FM Ibrahim**, Emese Kurovics, Elena L. Kotova, and László A. Gömze. "Effect of temperature on the structural properties of barium titanate nanopowders synthesis via sol-gel process." *Epitoanyag-Journal of Silicate Based & Composite Materials* 72, no. 5 (2020). ***IF (1.079)***
16. Emese Kurovics, Olga B. Kotova, **Jamal Eldin FM Ibrahim**, Mohammed Tihtih, Shiyong Sun, Péter Pala, and László A. Gomze. "Characterization of phase transformation and thermal behavior of Sedlecky Kaolin." *Építöanyag* (Online) 4 (2020): 144-147. ***IF (1.079)***
17. Emese Kurovics, **Jamal Eldin FM Ibrahim**, Mohammed Tihtih, Bella Udvardi, Kanokon Nuilek, & László A. Gömze. (2020, April). Examination of mullite ceramic specimens made by conventional casting method from kaolin and sawdust. In *Journal of Physics: Conference Series* (Vol. 1527, No. 1, p. 012034). IOP Publishing. ***IF (0.55) Q3***
18. Emese Kurovics, **Jamal Eldin FM Ibrahim**, and László A. Gömze. "Influence of compaction times and pressures on rheological properties of kaolin and sawdust powder mixtures." In *Journal of Physics: Conference Series*, vol. 1527, no. 1, p. 012002. IOP Publishing, 2020. ***IF (0.55) Q3***
19. Mohammed Tihtih, **Jamal Eldin FM Ibrahim**, Emese Kurovics, and Mohamed Abdelfattah. "Study on the effect of Bi dopant on the structural and optical properties of $BaTiO_3$ nanoceramics synthesized via sol-gel method." In *Journal of Physics: Conference Series*, vol. 1527, no. 1, p. 012043. IOP Publishing, 2020. ***IF (0.55) Q3***
20. Emese Kurovics, László A. Gömze, **Jamal Eldin FM Ibrahim**, and Ludmila N. Gömze. "Effect of composition and heat treatment on porosity and microstructures of technical ceramics made from kaolin and IG-017 additive." In *IOP Conference Series: Materials Science and Engineering*, vol. 613, no. 1, p. 012025. IOP Publishing, 2019. ***IF (0.51) Q3***

21. Mohammed Tihtih, Karoum Limame, Yahya Ababou, Salaheddine Sayouri, and **Jamal Eldin FM Ibrahim**. "Sol-gel synthesis and structural characterization of Fe doped barium titanate nanoceramics." *Építöanyag* (Online) 6 (2019): 190-193. ***IF (1.079)***
22. Tatyana N. Shchemelinina, László A. Gömze, Olga B. Kotova, **Jamal Eldin FM Ibrahim**, Dmitry A. Shushkov, Maria Harja, Grigoriy V. Ignatiev, and Elena M. Anchugova. "Clay-and zeolite-based biogeosorbents: modelling and properties." *Építöanyag* (Online) 4 (2019): 131-137.

Proceeding papers.

1. **Jamal Eldin FM Ibrahim**, L. A. Gömze. new zeolite-alumina composite materials-development and investigation, preparation of ceramic materials proceedings of the xiiith international conference, Jahodná, 25–27th June 2019. ISBN: 978-80-553-3314-4.
2. **Jamal Eldin FM Ibrahim**, E. Kurovics, and L. A. Gömze. "Synthesis, characterization and rheological properties of alumina-zeolite mixtures." Multi Science-XXXIII. Micro CAD International Multidisciplinary Scientific Conference, Hungary, http://dx. doi. org/10.26649/musci, 2019

Conference presentations

1. **Jamal Eldin FM Ibrahim**, A. Mergen, **Oral presentation**, "The Influence of Cr doping on the Structural and Magnetic Properties of $HoMnO_3$ Multiferroic Ceramics". The 5th International Conference on Competitive Materials and Technology Processes, Miskolc, Hungary. October 8 th –12 th, 2018.
2. **Jamal Eldin FM Ibrahim**, A. Mergen, **Poster presentation**, "Structural and Magnetic Properties of iron-doped GdMnO3 Multiferroic Ceramics". The 5th International Conference on Competitive Materials and Technology Processes, Miskolc, Hungary. October 8 th – 12 th, 2018.
3. **Jamal Eldin FM Ibrahim**, L.A. Gömze, **Poster presentation**, "The Influence of compacting times and pressures on rheological properties of zeolite-alumina ceramic powder mixtures", Annual European Rheology Conference 2019 (AERC 2019) Portoroz/Slovenia, April 8 th – 11 th, 2019.
4. **Jamal Eldin FM Ibrahim**, L.A. Gömze, **Oral presentation**, Synthesis, characterization and rheological properties of alumina-zeolite mixtures. 1st Science Unlimited Conference - Eötvös Symposium, Miskolc, Hungary. May 23 th – 24 th, 2019.
5. **Jamal Eldin FM Ibrahim**, L.A. Gömze, **Oral presentation,** "New Zeolite-Alumina Composite Materials – Development and Investigation" XIIIth International Conference in Preparation of Ceramic Materials, Jahodná, Slovakia, 25th – 27th June 2019.
6. **Jamal Eldin FM Ibrahim**, L.A. Gömze, **Oral presentation,** "Preparation and Investigation of Alumina-Zeolite- Composite Materials" The 1st European Conference on Silicon and Silica Based Materials, Miskolc, Hungary, 7th – 11th October 2019.
7. **Jamal Eldin FM Ibrahim**, L.A. Gömze, **Short oral presentation,** "Investigation of the Rheological Properties of Complex Zeolite-Alumina Mixtures" 4th International

Conference on Rheology and Modeling of Materials, Miskolc, Hungary, 7th – 11th October 2019.

8. **Jamal Eldin FM Ibrahim**, L.A. Gömze, **Oral presentation, "**Eco-friendly ceramic specimens with enhanced thermal insulation properties produced from Zeolite-poor rock**"** The 16th Miklós Iványi International PhD and DLA Symposium, University of Pécs, 26 th – 27 th Oct 2020, Pécs, Hungary.
9. **Jamal Eldin FM Ibrahim**, L.A. Gömze, **Poster presentation,** "Effect of composition and sintering temperature on the thermal conductivity of zeolite-sawdust composite bricks" 1st International e-Conference on Chemicals & Materials for Emergent technologies (CheMET-2020), center for advance materials, Qatar university, 15 th – 17 th Nov 2020.
10. **Jamal Eldin FM Ibrahim**, L.A. Gömze, **Oral presentation,** "Thermal and mechanical properties of Zeolite-Alumina composite materials" Materials Science Day of PhD students, University of Pannonia, 16 th Nov 2020, Veszprem Hungary.
11. **Jamal Eldin FM Ibrahim**, L.A. Gömze, **Oral presentation,** "The influence of composition and sintering temperature on thermal properties of zeolite alumina composite materials", 9th Interdisciplinary Doctoral Conference (IDK2020), University of Pécs, 27th – 28th Nov 2020 Pécs, Hungary.
12. **Jamal Eldin FM Ibrahim**, L.A. Gömze, **Oral presentation,** "Preparation of composite materials based on natural zeolite containing different minerals and their characteristics", «Modern Problems of Theoretical, Experimental and Applied Mineralogy «(Yushkin Readings - 2020), Syktyvkar, Komi Republic, Russia, 7th – 10th Dec 2020.
13. **Jamal Eldin FM Ibrahim**, L.A. Gömze, **Oral presentation,** "In-situ synthesis and characterization of mullite-based ceramic composite", MAEC 1st International Mathematic, Architecture and Engineering Conference, Jakarta, Indonesia, February 26 th – 28 th, 2021.
14. **Jamal Eldin FM Ibrahim**, L.A. Gömze, **Oral presentation,** "Eco-friendly ceramic specimens with enhanced thermal insulation properties produced from natural zeolite and sawdust", MAEC 2nd International Mathematic, Architecture and Engineering Conference, Roma, Italy, June 5 th – 6 th, 2021.
15. **Jamal Eldin FM Ibrahim**, L.A. Gömze, **Oral presentation,** "Environmentally-friendly ceramic specimens with improved thermal insulation characteristics produced from natural zeolite and eggshell", ic-cmtp6: The 6th International Conference on Competitive Materials and Technology Processes, Miskolc-Lillafüred, Hungary, October 4 th – 8 th, 2021.
16. **Jamal Eldin FM Ibrahim**, L.A. Gömze, **Oral presentation,** "In-situ synthesis, characterization and properties of silica reinforced nano-structured mullite ceramic composites", Ec-Siliconf2: The 2nd European Conference on Silicon and Silica Based Materials, Miskolc-Lillafüred, Hungary, October 4 th – 8 th, 2021.

References

[1] A. M. Omer, "Energy use and environmental impacts: A general review," in *Advances in Energy Research*, vol. 17, no. 5, Nova Science Publishers, Inc., 2014, pp. 1–38.

[2] Holdren et al., "Energy, the environment and health," *New York United Nations Dev. Program.*, 2018.

[3] P. A. Owusu and S. Asumadu-Sarkodie, "A review of renewable energy sources, sustainability issues and climate change mitigation," *Cogent Engineering*, vol. 3, no. 1. Cogent OA, p. 1167990, Dec. 2016, doi: 10.1080/23311916.2016.1167990.

[4] M. A. Rosen, "Energy sustainability: A pragmatic approach and illustrations," *Sustainability*, vol. 1, no. 1, pp. 55–80, 2009, doi: 10.3390/su1010055.

[5] P. Farnood Ahmadi, A. Ardeshir, A. M. Ramezanianpour, and H. Bayat, "Characteristics of heat insulating clay bricks made from zeolite, waste steel slag and expanded perlite," *Ceram. Int.*, vol. 44, no. 7, pp. 7588–7598, May 2018, doi: 10.1016/j.ceramint. 2018. 01.175.

[6] X. Cao, X. Dai, and J. Liu, "Building energy-consumption status worldwide and the state-of-the-art technologies for zero-energy buildings during the past decade," *Energy Build.*, vol. 128, pp. 198–213, Sep. 2016, doi: 10.1016/j.enbuild.2016.06.089.

[7] Bosseboeuf et al., "Energy Efficiency Trends and Policies in the Household and Tertiary Sectors," no. June, p. 97, 2015.

[8] et al Pacheco-Torgal, Fernando, "Handbook of Alkali-Activated Cements, Mortars and Concretes - 1st Edition," *Elsevier*, 2014. .

[9] J. E. F. M. Ibrahim, E. Kurovics, M. Tihtih, and L. A. Gömze, "Ceramic bricks with enhanced thermal insulation produced from natural zeolite," *Pollack Period.*, vol. 16, no. 3, pp. 101–107, 2021, doi: 10.1556/606.2021.00341.

[10] Johansson et al., Thomas B., "Global Energy Assessment Toward a Sustainable Future." pp. 1203–1306, 2012.

[11] H. M. Taleb, "Using passive cooling strategies to improve thermal performance and reduce energy consumption of residential buildings in U.A.E. buildings," *Front. Archit. Res.*, vol. 3, no. 2, pp. 154–165, Jun. 2014, doi: 10.1016/j.foar.2014.01.002.

[12] E. Clements-Croome, Derek, "Intelligent Buildings: An Introduction - 1st Edition - Derek Clements," 2013.

[13] A. Reilly and O. Kinnane, "The impact of thermal mass on building energy consumption," *Appl. Energy*, vol. 198, pp. 108–121, Jul. 2017, doi: 10.1016/j.apenergy. 2017.04.024.

[14] EN 832:1998 - Thermal performance of buildings - Calculation of energy use for heating - Residential, 1998. .

[15] G. Görhan and O. Şimşek, "Porous clay bricks manufactured with rice husks," *Constr. Build. Mater.*, vol. 40, pp. 390–396, Mar. 2013, doi:10.1016/j.conbuildmat. 2012. 09.110.

[16] D. Eliche-Quesada *et al.*, "The use of different forms of waste in the manufacture of ceramic bricks," *Appl. Clay Sci.*, vol. 52, no. 3, pp. 270–276, 2011, doi: 10.1016/j.clay. 2011.03.003.

[17] M. Sutcu and S. Akkurt, "The use of recycled paper processing residues in making porous brick with reduced thermal conductivity," *Ceram. Int.*, vol. 35, no. 7, pp. 2625–2631, Sep. 2009, doi: 10.1016/j.ceramint.2009.02.027.

[18] L. C. S. Herek, C. E. Hori, M. H. M. Reis, N. D. Mora, C. R. G. Tavares, and R. Bergamasco, "Characterization of ceramic bricks incorporated with textile laundry sludge," *Ceram. Int.*, vol. 38, no. 2, pp. 951–959, Mar. 2012, doi: 10.1016/j.ceramint. 2011.08.015.

[19] M. De Simone and G. Fajilla, “Occupant behavior: a new factor in energy performance of buildings. Methods for its detection in houses and in offices.,” *J. World Archit.*, vol. 2, no. 2, pp. 1–8, 2019, doi: 10.26689/jwa.v2i2.544.
[20] M. J. Munir, S. M. S. Kazmi, O. Gencel, M. R. Ahmad, and B. Chen, “Synergistic effect of rice husk, glass and marble sludges on the engineering characteristics of eco-friendly bricks,” *J. Build. Eng.*, vol. 42, no. March, p. 102484, 2021, doi: 10.1016/j.jobe. 2021. 102484.
[21] O. David and H. Hubel, “Waste production must peak this century,” pp. 5–7.
[22] A. Ukwatta, A. Mohajerani, N. Eshtiaghi, and S. Setunge, “Variation in physical and mechanical properties of fired-clay bricks incorporating ETP biosolids,” *J. Clean. Prod.*, vol. 119, pp. 76–85, 2016, doi: 10.1016/j.jclepro.2016.01.094.
[23] O. Gencel, M. Sutcu, E. Erdogmus, V. Koc, V. V. Cay, and M. S. Gok, “Properties of bricks with waste ferrochromium slag and zeolite,” *J. Clean. Prod.*, vol. 59, pp. 111–119, 2013, doi: 10.1016/j.jclepro.2013.06.055.
[24] P. Muñoz, V. Letelier, D. Zamora, and M. P. Morales, “Feasibility of using paper pulp residues into fired clay bricks,” *J. Clean. Prod.*, vol. 262, 2020, doi: 10.1016/ j.jclepro. 2020.121464.
[25] V. G. Karayannis, “Development of extruded and fired bricks with steel industry byproduct towards circular economy,” *J. Build. Eng.*, vol. 7, pp. 382–387, 2016, doi: 10.1016/j.jobe.2016.08.003.
[26] M. J. Munir, S. M. S. Kazmi, Y. F. Wu, A. Hanif, and M. U. A. Khan, “Thermally efficient fired clay bricks incorporating waste marble sludge: An industrial-scale study,” *J. Clean. Prod.*, vol. 174, pp. 1122–1135, 2018, doi: 10.1016/j.jclepro.2017.11.060.
[27] J. J. Reinosa, A. C. Silva, F. Rubio-Marcos, S. R. H. Mello-Castanho, J. S. Moya, and J. F. Fernandez, “High chemical stability of stoneware tiles containing waste metals,” *J. Eur. Ceram. Soc.*, vol. 30, no. 14, pp. 2997–3004, 2010, doi: 10.1016/j.jeurceramsoc. 2010.02.017.
[28] A. A. Shakir and A. Ahmed Mohammed, “Manufacturing of Bricks in the Past, in the Present and in the Future: A state of the Art Review,” *Int. J. Adv. Appl. Sci.*, vol. 2, no. 3, 2013, doi: 10.11591/ijaas.v2i3.1751.
[29] V. Mymrin *et al.*, “Red ceramics from composites of hazardous sludge with foundry sand, glass waste and acid neutralization salts,” *J. Environ. Chem. Eng.*, vol. 4, no. 1, pp. 753–761, 2016, doi: 10.1016/j.jece.2015.07.015.
[30] L. Wiemes, U. Pawlowsky, and V. Mymrin, “Incorporation of industrial wastes as raw materials in brick’s formulation,” *J. Clean. Prod.*, vol. 142, pp. 69–77, 2017, doi: 10.1016/j.jclepro.2016.06.174.
[31] M. Sutcu, E. Erdogmus, O. Gencel, A. Gholampour, E. Atan, and T. Ozbakkaloglu, “Recycling of bottom ash and fly ash wastes in eco-friendly clay brick production,” *J. Clean. Prod.*, vol. 233, pp. 753–764, 2019, doi: 10.1016/j.jclepro.2019.06.017.
[32] R. Taurino, D. Ferretti, L. Cattani, F. Bozzoli, and F. Bondioli, “Lightweight clay bricks manufactured by using locally available wine industry waste,” *J. Build. Eng.*, vol. 26, no. October 2018, p. 100892, 2019, doi: 10.1016/j.jobe.2019.100892.
[33] A. Martinez-Amariz, L. P. Muñoz, F. Posso, and D. Bellon, “Compressive evaluation of mansory bricks produced with industrial byproduct aggregates,” *Int. J. Appl. Ceram. Technol.*, vol. 17, no. 6, pp. 2681–2689, 2020, doi: 10.1111/ijac.13601.
[34] R. Ahmadi, B. Souri, and M. Ebrahimi, “Evaluation of wheat straw to insulate fired clay hollow bricks as a construction material,” *J. Clean. Prod.*, vol. 254, p. 120043, 2020, doi: 10.1016/j.jclepro.2020.120043.

[35] M. H. Riaz, A. Khitab, and S. Ahmed, “Evaluation of sustainable clay bricks incorporating Brick Kiln Dust,” *J. Build. Eng.*, vol. 24, no. February, p. 100725, 2019, doi: 10.1016/j.jobe.2019.02.017.
[36] K. Alshuhail, A. Aldawoud, J. Syarif, and I. A. Abdoun, “Enhancing the performance of compressed soil bricks with natural additives: Wood chips and date palm fibers,” *Constr. Build. Mater.*, vol. 295, p. 123611, 2021, doi: 10.1016/j.conbuildmat. 2021. 123611.
[37] E. Annunziata, M. Frey, and F. Rizzi, “Towards nearly zero-energy buildings: The state-of-art of national regulations in Europe,” *Energy*, vol. 57, pp. 125–133, 2013, doi: 10.1016/j.energy.2012.11.049.
[38] A. Kosonen and A. Keskisaari, “Zero-energy log house – Future concept for an energy efficient building in the Nordic conditions,” *Energy Build.*, vol. 228, p. 110449, 2020, doi: 10.1016/j.enbuild.2020.110449.
[39] M. Roser, “Future population growth,” *Our world data*, 2013.
[40] J. E. F. M. Ibrahim, O. B. Kotova, S. Sun, E. Kurovics, M. Tihtih, and L. A. Gömze, “Preparation of innovative eco-efficient composite bricks based on zeolite-poor rock and Hen’s eggshell,” *J. Build. Eng.*, vol. 45, 2022, doi: 10.1016/j.jobe.2021.103491.
[41] D. Kalló, J. Papp, and J. Valyon, “Adsorption and catalytic properties of sedimentary clinoptilolite and mordenite from the Tokaj Hills, Hungary,” *Zeolites*, vol. 2, no. 1, pp. 13–16, Jan. 1982, doi: 10.1016/S0144-2449(82)80034-1.
[42] L. K. Kazantseva, T. S. Yusupov, T. Z. Lygina, L. G. Shumskaya, and D. S. Tsyplakov, “Foam glass from mechanoactivated zeolite-poor rock,” *Glas. Ceram. (English Transl. Steklo i Keramika)*, vol. 70, no. 9–10, pp. 360–364, Jan. 2014, doi: 10.1007/s10717-014-9580-7.
[43] G. Marcari, G. Fabbrocino, and P. B. Lourenço, “Investigation on compressive behaviour of tuff masonry panels,” 2010.
[44] R. H. Price, *Analysis of the rock mechanics properties of volcanic tuff units from Yucca Mountain, Nevada Test Site, No. SAND-82-1315*. 1983.
[45] L. Pérez-Lombard, J. Ortiz, and C. Pout, “A review on buildings energy consumption information,” *Energy Build.*, vol. 40, no. 3, pp. 394–398, 2008, doi: 10.1016/j.enbuild. 2007.03.007.
[46] L. Aditya *et al.*, “A review on insulation materials for energy conservation in buildings,” *Renew. Sustain. Energy Rev.*, vol. 73, no. February, pp. 1352–1365, 2017, doi: 10.1016/j.rser.2017.02.034.
[47] A. M. Papadopoulos, “State of the art in thermal insulation materials and aims for future developments,” *Energy Build.*, vol. 37, no. 1, pp. 77–86, 2005, doi: 10.1016/j.enbuild. 2004.05.006.
[48] D. Bozsaky, “The historical development of thermal insulation materials,” *Period. Polytech. Archit.*, vol. 41, no. 2, p. 49, 2010, doi: 10.3311/pp.ar.2010-2.02.
[49] S. Beaino, P. El Hage, R. Sonnier, S. Seif, and R. El Hage, “Novel Foaming-Agent Free Insulating Geopolymer Based on Industrial Fly Ash and Rice Husk,” *Molecules*, vol. 27, no. 2, pp. 1–19, 2022, doi: 10.3390/molecules27020531.
[50] Y. Tanaka, *Principles of ion exchange membrane electrodialysis for saline water desalination*. 2012.
[51] P. A. Jacobs, Edith M. Flanigen, J. C. Jansen, *Introduction to zeolite science and practice*. 2001.
[52] C. Feng, K. C. Khulbe, T. Matsuura, R. Farnood, and A. F. Ismail, “Recent progress in zeolite/zeotype membranes,” *J. Membr. Sci. Res.*, vol. 1, no. 2, pp. 49–72, 2015, doi: 10.22079/jmsr.2015.13530.

[53] A. S. Ülkü and M. Mobedi, “Adsorption in Energy Storage,” *Energy Storage Syst.*, pp. 487–507, 1989, doi: 10.1007/978-94-009-2350-8_21.
[54] A. Mastinu *et al.*, “Zeolite clinoptilolite: Therapeutic virtues of an ancient mineral,” *Molecules*, vol. 24, no. 8, 2019, doi: 10.3390/molecules24081517.
[55] R. Xu, W. Pang, J. Yu, Q. Huo, and J. Chen, *Chemistry of Zeolites and Related Porous Materials: Synthesis and Structure*. 2010.
[56] L. A. Price, C. J. Ridley, C. L. Bull, S. A. Wells, and A. Sartbaeva, “Determining the structure of zeolite frameworks at high pressures,” *CrystEngComm*, vol. 23, no. 33, pp. 5615–5623, 2021, doi: 10.1039/d1ce00142f.
[57] S. Kulprathipanja, “Zeolites in Industrial Separation and Catalysis,” *Zeolites Ind. Sep. Catal.*, 2010, doi: 10.1002/9783527629565.
[58] P. Auerbach, S., Carrado, K., Dutta, Handbook of Zeolite Science and Technology. CRC press, 2003.
[59] P. Sudarsanam, E. Peeters, E. V. Makshina, V. I. Parvulescu, and B. F. Sels, “Advances in porous and nanoscale catalysts for viable biomass conversion,” *Chem. Soc. Rev.*, vol. 48, no. 8, pp. 2366–2421, 2019, doi: 10.1039/c8cs00452h.
[60] T. Wajima, “Synthesis of zeolitic material with high cation exchange capacity from paper sludge ash using edta,” *Appl. Sci.*, vol. 11, no. 23, 2021, doi: 10.3390/app112311231.
[61] X. Ren *et al.*, “Synthesis of zeolites from coal fly ash for the removal of harmful gaseous pollutants: A review,” *Aerosol Air Qual. Res.*, vol. 20, no. 5, pp. 1127–1144, 2020, doi: 10.4209/aaqr.2019.12.0651.
[62] Y. T. Tran, J. Lee, P. Kumar, K. H. Kim, and S. S. Lee, “Natural zeolite and its application in concrete composite production,” *Compos. Part B Eng.*, vol. 165, no. July 2018, pp. 354–364, 2019, doi: 10.1016/j.compositesb.2018.12.084.
[63] S. Al-Jubouri, “Synthesis and characterization of hierarchically porous zeolite composites for enhancing mass transfer,” *PQDT - UK Irel.*, 2016.
[64] S. Kulprathipanja, *Zeolites in Industrial Separation and Catalysis*. 2010.
[65] K. Ramesh and D. D. Reddy, “Zeolites and Their Potential Uses in Agriculture,” *Adv. Agron.*, vol. 113, pp. 219–241, 2011, doi: 10.1016/B978-0-12-386473-4.00004-X.
[66] J. G. G. Mendoza, *Synthesis and applications of low silica zeolites from Bolivian Clay and Diatomaceous Earth*. 2017.
[67] K. Sozana, N. Kamarudin, H. Hamdan, and H. Mat, “Methane Adsorption Characteristic Dependency on Zeolite Structures and Properties ∗,” *Synthesis (Stuttg).*, no. December, pp. 29–30, 2003,. Available: http://citeseerx.ist.psu.edu/viewdoc/download?doi=10.1.1.599.3622&rep=rep1&type=pdf.
[68] A. C. McLean and C. D. Gribble, *Minerals and rocks*. 2018.
[69] G. A. Dykes, R. Coorey, J. T. Ravensdale, and A. Sarjit, *Phosphates*. 2018.
[70] Fahri Esenli, S. Kadir, and B. E. Şans, “Geochemistry of the Zeolite-rich Miocene Pyroclastic Rocks from the Gördes, Demirci and Şaphane Regions, West Anatolia, Turkey,” *Geochemistry Int.*, vol. 57, no. 11, pp. 1158–1172, 2019, doi: 10.1134/S001670291911003X.
[71] Y. Li, L. Li, and J. Yu, “Applications of Zeolites in Sustainable Chemistry,” *Chem*, vol. 3, no. 6. Elsevier Inc, pp. 928–949, Dec. 2017, doi: 10.1016/j.chempr.2017.10.009.
[72] F. Akhtar, L. Andersson, S. Ogunwumi, N. Hedin, and L. Bergström, “Structuring adsorbents and catalysts by processing of porous powders,” *J. Eur. Ceram. Soc.*, vol. 34, no. 7, pp. 1643–1666, Jul. 2014, doi: 10.1016/j.jeurceramsoc.2014.01.008.
[73] O. B. Kotova *et al.*, “Composite materials based on zeolite-montmorillonite rocks and aluminosilicate wastes,” *Epa. - J. Silic. Based Compos. Mater.*, vol. 71, no. 4, pp. 125–130, 2019, doi: 10.14382/epitoanyag-jsbcm.2019.22.

[74] W. Parham, “Natural zeolites: Some potential agricultural applications for developing countries,” *Nat. Resour. Forum*, vol. 13, no. 2, pp. 107–115, 1989, doi: 10.1111/j.1477-8947.1989.tb00324.x.
[75] J. E. F. M. Ibrahim, E. Kurovics, M. Tihtih, and L. A. Gömze, “Ceramic bricks with enhanced thermal insulation produced from natural zeolite,” *Pollack Period.*, 2021, doi: 10.1556/606.2021.00341.
[76] L. K. Kazantseva and S. V. Rashchenko, “Optimization of porous heat-insulating ceramics manufacturing from zeolitic rocks,” *Ceram. Int.*, vol. 42, no. 16, pp. 19250–19256, 2016, doi: 10.1016/j.ceramint.2016.09.091.
[77] Z. Tišler, K. Hrachovcová, E. Svobodová, J. Šafář, and L. Pelíšková, “Acid and thermal treatment of alkali-activated zeolite foams,” *Minerals*, vol. 9, no. 12, 2019, doi: 10.3390/min9120719.
[78] V. K. B. Raja *et al.*, “Geopolymer green technology,” *Mater. Today Proc.*, vol. 46, no. February, pp. 1003–1007, 2021, doi: 10.1016/j.matpr.2021.01.138.
[79] et al. Southard, R. J., *Silica, crystalline Encyclopedia of Toxicology*. 2014.
[80] W. A. Dollase, *Solid state chemistry and its applications by A. R. West* , vol. 41, no. 6. 1985.
[81] H. M. Moura and M. M. Unterlass, “Biogenic metal oxides,” *Biomimetics*, vol. 5, no. 2, pp. 1–39, 2020, doi: 10.3390/BIOMIMETICS5020029.
[82] F. Uddin, “Montmorillonite: An Introduction to Properties and Utilization-C,” *Curr. Top. Util. Clay Ind. Med. Appl.*, pp. 4–23, 2018.
[83] J. Tanijaya and D. Hardjito, “Experimental study on the use of natural zeolites as partial replacement for cement in concrete,” *EASEC-11 - Elev. East Asia-Pacific Conf. Struct. Eng. Constr.*, pp. 1–5, 2008.
[84] Z. Zhang, Y. C. Wong, A. Arulrajah, and S. Horpibulsuk, “A review of studies on bricks using alternative materials and approaches,” *Construction and Building Materials*, vol. 188. Elsevier Ltd, pp. 1101–1118, Nov. 2018, doi: 10.1016/j.conbuildmat.2018.08.152.
[85] N. F. Nazira Ab Karim, N. Nabilah Sarbini, N. H. Abdul Shukor Lim, I. Syahrizal Ibrahim, E. Aminuddin, and A. Rosseira Abu Talib, “Thermal Insulation Properties of Organic and Inorganic Material in Clay Brick - A Review,” *IOP Conf. Ser. Earth Environ. Sci.*, vol. 268, no. 1, pp. 0–6, 2019, doi: 10.1088/1755-1315/268/1/012082.
[86] A. N. Adazabra, G. Viruthagiri, and P. Kannan, “Influence of spent shea waste addition on the technological properties of fired clay bricks,” *J. Build. Eng.*, vol. 11, no. April, pp. 166–177, 2017, doi: 10.1016/j.jobe.2017.04.006.
[87] G. Cultrone, I. Aurrekoetxea, C. Casado, and A. Arizzi, “Sawdust recycling in the production of lightweight bricks: How the amount of additive and the firing temperature influence the physical properties of the bricks,” *Constr. Build. Mater.*, vol. 235, p. 117436, 2020, doi: 10.1016/j.conbuildmat.2019.117436.
[88] K. P. Rotich, “Carbonization and Briquetting of Sawdust for Use in Domestic Cookers,” 1998.
[89] J. S. Srndovic, *Interactions between Wood Polymers in Wood Cell Walls and Cellulose/Hemicellulose Biocomposites*, vol. Doctor of. 2011.
[90] J. Yang, Y. C. Ching, and C. H. Chuah, “Applications of lignocellulosic fibers and lignin in bioplastics: A review,” *Polymers (Basel).*, vol. 11, no. 5, pp. 1–26, 2019, doi: 10.3390/polym11050751.
[91] R. Iqbal *et al.*, “Potential agricultural and environmental benefits of mulches a review,” *Bull. Natl. Res. Cent.*, vol. 44, no. 1, 2020, doi: 10.1186/s42269-020-00290-3.
[92] O. Awogbemi, F. Inambao, and E. I. Onuh, “Modification and characterization of chicken eggshell for possible catalytic applications,” *Heliyon*, vol. 6, no. 10, p. e05283, 2020, doi: 10.1016/j.heliyon.2020.e05283.

[93] B. H. Ngayakamo, A. Bello, and A. P. Onwualu, “Development of eco-friendly fired clay bricks incorporated with granite and eggshell wastes,” *Environ. Challenges*, vol. 1, no. November, p. 100006, 2020, doi: 10.1016/j.envc.2020.100006.
[94] H. Z. L. Oukal, “Adsorption of Curcumin and Silver-Nanoparticles by Using Eggshell Powder,” 2019.
[95] S. Owuamanam and D. Cree, “Progress of bio-calcium carbonate waste eggshell and seashell fillers in polymer composites: A review,” *J. Compos. Sci.*, vol. 4, no. 2, 2020, doi: 10.3390/jcs4020070.
[96] I. Abdulrahman *et al.*, “From Garbage to Biomaterials: An overview on eggshell based hydroxyapatite,” *J. Mater.*, vol. 2014, pp. 1–6, 2014, doi: 10.1155/2014/802467.
[97] N. Tangboriboon, S. Moonsri, A. Netthip, and A. Sirivat, “Innovation of embedding eggshell to enhance physical-mechanical-thermal properties in fired clay bricks via extrusion process,” in *MATEC Web of Conferences*, Oct. 2016, vol. 78, p. 01003, doi: 10.1051/matecconf/20167801003.
[98] N. Dalkılıç and A. Nabikoğlu, “Traditional manufacturing of clay brick used in the historical buildings of Diyarbakir (Turkey),” *Front. Archit. Res.*, vol. 6, no. 3, pp. 346–359, 2017, doi: 10.1016/j.foar.2017.06.003.
[99] A. Mohajerani *et al.*, “A proposal for recycling theworld’s unused stockpiles of treated wastewater sludge (biosolids) in fired-clay bricks,” *Buildings*, vol. 9, no. 1, 2019, doi: 10.3390/buildings9010014.
[100] Ö. Sağiroğlu and A. Ö. Yavuz, “Use of Unglazed Brick in Monumental Architecture as an Ornamental Element,” vol. 5, no. 2, pp. 1–11, 2017.
[101] J. N. Falana, R. Attalla, and A. F. Gelany, “The technology of Mud-bricks from the sacred architecture in ancient Egypt to the green house revolution (Case study of Luxor City, Egypt),” *Int. J. Adv. Sci. Technol.*, vol. 29, no. 4 Special Issue, pp. 1264–1277, 2020.
[102] G. Ripepi, “Mudbricks and Modular Architecture at Tell es-Sultan from the Neolithic to the Bronze Age,” *Digging Up Jericho*, no. May 2020, pp. 215–230, 2020, doi: 10.2307/j.ctvwh8bss.16.
[103] P. N. Sayyed, S. Singh, N. Lakha, S. Bageshwar, and A. Mandlik, “Manufacturing of sand bricks using mahurzari village lake sand,” vol. 4, no. 4, pp. 523–526, 2021, doi: 10.15680/IJMRSET.2021.0404005.
[104] Ö. A. Özkaya and H. Böke, “Properties of Roman bricks and mortars used in Serapis temple in the city of Pergamon,” *Mater. Charact.*, vol. 60, no. 9, pp. 995–1000, 2009, doi: 10.1016/j.matchar.2009.04.003.
[105] I. Poll, “Recycling of roman bricks from Romula,” no. January 2021.
[106] P. W. Campbell JWP, *Backstein - eine Architekturgeschichte*. Munich, 2003.
[107] E. Solgi, H. Gitinavard, and R. Tavakkoli-Moghaddam, “Sustainable high-tech brick production with energy-Oriented consumption: An integrated possibilistic approach based on criteria interdependencies,” *Sustain.*, vol. 14, no. 1, 2022, doi: 10.3390/su14010202.
[108] F. Moedinger, “Advances in the utilization of waste materials and alternative sources of energy in clay brick making A South Tyrolean case study investigating environmental and financial impacts,” no. December, p. 287, 2010.
[109] N. K. Foley, “Environmental characteristics of clays and clay mineral deposits. USGS Informational Handout.,” *U. S. Geol. Surv.*, no. September, pp. 1–2, 1999.
[110] R. E. Izzaty, B. Astuti, and N. Cholimah, *Basic construction materials*. 1967.
[111] M. S. Mamlouk and J. P. Zaniewski, *Materials for civil and construction engineers*. 2011.

[112] G. C. J. Lynch, “Bricks: properties and classifications,” *Struct. Surv.*, vol. 12, no. 4, pp. 15–20, 1994, doi: 10.1108/02630809410066447.
[113] M. N. Rahaman, *Ceramic processing and sintering*. 2003.
[114] L. A. Gömze and E. Kurovics, “Influence of compacting times and pressures on rheological properties of alumina and quartz ceramic powder mixtures,” *J. Phys. Conf. Ser.*, vol. 1045, no. 1, pp. 0–8, 2018, doi: 10.1088/1742-6596/1045/1/012011.
[115] G. D. Taylor, *Materials in construction: principles, practice and performance*. 2002.
[116] M. S. Tite and Y. Maniatis, “Examination of ancient pottery using the scanning electron microscope,” *Nature*, vol. 257, no. 5522, pp. 122–123, Sep. 1975, doi: 10.1038/257122a0.
[117] A. Eil, J. Li, P. Baral, and E. Saikawa, “Dirty Stacks, High Stakes,” *Dirty Stacks, High Stakes*, 2020, doi: 10.1596/33727.
[118] S. Jain, “Development of unfired bricks using industrial waste,” no. December, p. 73, 2016, doi: 10.13140/RG.2.2.23905.51047.
[119] Z. Tian, “Fired clay bricks : effects of porosity,” 2018.
[120] I. Demir, “Effect of organic residues addition on the technological properties of clay bricks,” *Waste Manag.*, vol. 28, no. 3, pp. 622–627, 2008, doi: 10.1016/j.wasman.2007.03.019.
[121] A. Yaras, M. Sutcu, E. Erdogmus, and O. Gencel, “Recycling and immobilization of zinc extraction residue in clay-based brick manufacturing,” *J. Build. Eng.*, vol. 41, no. March, 2021, doi: 10.1016/j.jobe.2021.102421.
[122] N. Phonphuak, S. Kanyakam, and P. Chindaprasirt, “Utilization of waste glass to enhance physical-mechanical properties of fired clay brick,” *J. Clean. Prod.*, vol. 112, pp. 3057–3062, 2016, doi: 10.1016/j.jclepro.2015.10.084.
[123] K. J. Krakowiak, P. B. Lourenço, and F. J. Ulm, “Multitechnique investigation of extruded clay brick microstructure,” *J. Am. Ceram. Soc.*, vol. 94, no. 9, pp. 3012–3022, 2011, doi: 10.1111/j.1551-2916.2011.04484.x.
[124] A. Yaras, “Combined effects of paper mill sludge and carbonation sludge on characteristics of fired clay bricks,” *Constr. Build. Mater.*, vol. 249, p. 118722, 2020, doi: 10.1016/j.conbuildmat.2020.118722.
[125] J. B. Wachtman, W. R. Cannon, and M. J. Matthewson, mechanical properties of ceramics, John Wiley & Sons, 2009.
[126] Z. Chen, W. Chen, C. Mai, J. Shi, Y. Xie, and H. Hu, “Experimental study on the compressive behaviors of brick masonry strengthened with modified oyster shell ash mortar,” *Buildings*, vol. 11, no. 7, 2021, doi: 10.3390/buildings11070266.
[127] H. Alabduljabbar, O. Benjeddou, C. Soussi, M. A. Khadimallah, and R. Alyousef, “Effects of incorporating wood sawdust on the firing program and the physical and mechanical properties of fired clay bricks,” *J. Build. Eng.*, vol. 35, no. December 2020, p. 102106, 2021, doi: 10.1016/j.jobe.2020.102106.
[128] B. Ngayakamo, A. M. Aboubakar, C. G. Komadja, A. Bello, and A. P. Onwualu, “Eco-friendly use of eggshell powder as a bio-filler and flux material to enhance technological properties of fired clay bricks,” *Metall. Mater. Eng.*, vol. 27, no. 3, pp. 371–383, 2021, doi: 10.30544/628.
[129] G. S. dos Reis *et al.*, “Fabrication, microstructure, and properties of fired clay bricks using construction and demolition waste sludge as the main additive,” *J. Clean. Prod.*, vol. 258, 2020, doi: 10.1016/j.jclepro.2020.120733.
[130] C. W. Tang, “Properties of fired bricks incorporating TFT-LCD waste glass powder with reservoir sediments,” *Sustain.*, vol. 10, no. 7, 2018, doi: 10.3390/su10072503.

[131] G. Goel and A. S. Kalamdhad, “An investigation on use of paper mill sludge in brick manufacturing,” *Constr. Build. Mater.*, vol. 148, pp. 334–343, 2017, doi: 10.1016/j.conbuildmat.2017.05.087.
[132] J. Man, W. Gao, S. Yan, G. Liu, and H. Hao, “Preparation of porous brick from diatomite and sugar filter mud at lower temperature,” *Constr. Build. Mater.*, vol. 156, pp. 1035–1042, 2017, doi: 10.1016/j.conbuildmat.2017.09.021.
[133] K. L. Lin, J. C. Chang, J. L. Shie, H. J. Chen, and C. M. Ma, “Characteristics of porous ceramics produced from waste diatomite and water purification sludge,” *Environ. Eng. Sci.*, vol. 29, no. 6, pp. 436–446, 2012, doi: 10.1089/ees.2010.0340.
[134] E. Escalera, G. Garcia, R. Terán, R. Tegman, M. L. Antti, and M. Odén, “The production of porous brick material from diatomaceous earth and Brazil nut shell ash,” *Constr. Build. Mater.*, vol. 98, pp. 257–264, 2015, doi: 10.1016/j.conbuildmat.2015.08.003.
[135] H. He *et al.*, “Preparation and mechanism of the sintered bricks produced from Yellow River silt and red mud,” *J. Hazard. Mater.*, vol. 203–204, pp. 53–61, 2012, doi: 10.1016/j.jhazmat.2011.11.095.
[136] C. Yang, C. Cui, J. Qin, and X. Cui, “Characteristics of the fired bricks with low-silicon iron tailings,” *Constr. Build. Mater.*, vol. 70, pp. 36–42, 2014, doi: 10.1016/j.conbuildmat.2014.07.075.
[137] W. Zhou *et al.*, “Mechanism analysis of pore structure and crystalline phase of thermal insulation bricks with high municipal sewage sludge content,” *Constr. Build. Mater.*, vol. 263, p. 120021, 2020, doi: 10.1016/j.conbuildmat.2020.120021.
[138] I. Kocserha, A. Hamza, and R. Géber, “The effects of red mud on clay compounds,” *IOP Conf. Ser. Mater. Sci. Eng.*, vol. 426, no. 1, 2018, doi: 10.1088/1757-899X/426/1/012026.
[139] S. Ahmad *et al.*, “Sustainable use of marble waste in industrial production of fired clay bricks and its employment for treatment of flue gases,” *ACS Omega*, vol. 6, no. 35, pp. 22559–22569, 2021, doi: 10.1021/acsomega.1c02279.
[140] G. Goel and A. S. Kalamdhad, “A practical proposal for utilisation of water hyacinth: Recycling in fired bricks,” *J. Clean. Prod.*, vol. 190, pp. 261–271, 2018, doi: 10.1016/j.jclepro.2018.04.179.
[141] U. Javed, R. A. Khushnood, S. A. Memon, F. E. Jalal, and M. S. Zafar, “Sustainable incorporation of lime-bentonite clay composite for production of ecofriendly bricks,” *J. Clean. Prod.*, vol. 263, p. 121469, 2020, doi: 10.1016/j.jclepro.2020.121469.
[142] F. Yang *et al.*, “Synergistic effects of amorphous porous materials and anhydrous Na_2CO_3 on the performance of bricks with high municipal sewage sludge content,” *J. Clean. Prod.*, vol. 280, p. 124338, 2021, doi: 10.1016/j.jclepro.2020.124338.
[143] Z. Chen, H. Wang, R. Ji, L. Liu, C. Cheeseman, and X. Wang, “Reuse of mineral wool waste and recycled glass in ceramic foams,” *Ceram. Int.*, vol. 45, no. 12, pp. 15057–15064, 2019, doi: 10.1016/j.ceramint.2019.04.242.
[144] H. R. Fernandes, D. U. Tulyaganov, and J. M. F. Ferreira, “Preparation and characterization of foams from sheet glass and fly ash using carbonates as foaming agents,” *Ceram. Int.*, vol. 35, no. 1, pp. 229–235, 2009, doi: 10.1016/j.ceramint. 2007.10.019.
[145] L. Kern, “Process of manufacturing porous silica,” 1898839, 1933.
[146] B. K. Demidovich, “Production and Application of glass foam (in Russian),” *Ed. Nauk. i. Tekhnika, Minsk*, vol. 164, 1972.
[147] F. B. Long (Saint Gobain, “Glass product and method of manu- facturing sponge-like glass,” US Patent 1,945,052, 1934.
[148] W.O. Lytle. Pittsburgh plate glass, “Porous material manufacture,” US 2215223, 1940.

[149] W. O. Lytle. Pittsburgh plate glass, “Manufacture of Vesicular Glass,” US patent 2,354,807, 1944.
[150] H. R. Black, (Corning, USA), 2,272,930, 1942.
[151] I. Peyches, “Apparatus for the manufacture of multicellular glass,” US Patent 2,658,096, 1953.
[152] W. D. FORD, “(Pittsburgh Corning),” US Paten 2,691,248, 1954.
[153] A. Karamanov, E. M. A. Hamzawy, E. Karamanova, N. B. Jordanov, and H. Darwish, “Sintered glass-ceramics and foams by metallurgical slag with addition of CaF2,” *Ceram. Int.*, vol. 46, no. 5, pp. 6507–6516, 2020, doi: 10.1016/j.ceramint.2019.11.132.
[154] S. Smiljanić, U. Hribar, M. Spreitzer, and J. König, “Influence of additives on the crystallization and thermal conductivity of container glass cullet for foamed glass preparation,” *Ceram. Int.*, 2021, doi: 10.1016/j.ceramint.2021.08.183.
[155] R. R. Petersen, J. König, N. Iversen, M. B. Østergaard, and Y. Yue, “The foaming mechanism of glass foams prepared from the mixture of Mn3O4, carbon and CRT panel glass,” *Ceram. Int.*, vol. 47, no. 2, pp. 2839–2847, 2021, doi: 10.1016/ j.ceramint. 2020.09.138.
[156] U. Hribar, M. Spreitzer, and J. König, “Applicability of water glass for the transfer of the glass-foaming process from controlled to air atmosphere,” *J. Clean. Prod.*, vol. 282, 2021, doi: 10.1016/j.jclepro.2020.125428.
[157] V. I. Vereshagin and S. N. Sokolova, “Granulated foam glass-ceramic material from zeolitic rocks,” *Constr. Build. Mater.*, vol. 22, no. 5, pp. 999–1003, 2008, doi: 10.1016/ j.conbuildmat.2007.01.016.
[158] M. Assefi, S. Maroufi, I. Mansuri, and V. Sahajwalla, “High strength glass foams recycled from LCD waste screens for insulation application,” *J. Clean. Prod.*, vol. 280, 2021, doi: 10.1016/j.jclepro.2020.124311.
[159] S. Abdollahi and B. E. Yekta, “Prediction of foaming temperature of glass in the presence of various oxidizers via thermodynamics route,” *Ceram. Int.*, vol. 46, no. 16, pp. 25626–25632, 2020, doi: 10.1016/j.ceramint.2020.07.037.
[160] A. Hoppe and A. R. Boccaccini, *Bioactive glass foams for tissue engineering applications*. Woodhead Publishing Limited, 2014.
[161] A. C. Bento, E. T. Kubaski, T. Sequinel, S. A. Pianaro, J. A. Varela, and S. M. Tebcherani, “Glass foam of macroporosity using glass waste and sodium hydroxide as the foaming agent,” *Ceram. Int.*, vol. 39, no. 3, pp. 2423–2430, 2013, doi: 10.1016/ j.ceramint.2012.09.002.
[162] M. T. Souza, B. G. O. Maia, L. B. Teixeira, K. G. de Oliveira, A. H. B. Teixeira, and A. P. Novaes de Oliveira, “Glass foams produced from glass bottles and eggshell wastes,” *Process Saf. Environ. Prot.*, vol. 111, pp. 60–64, 2017, doi: 10.1016/j.psep.2017.06.011.
[163] C. Zhang *et al.*, “Preparation and properties of foam ceramic from nickel slag and waste glass powder,” *Ceram. Int.*, vol. 46, no. 15, pp. 23623–23628, 2020, doi: 10.1016/ j.ceramint.2020.06.134.
[164] M. Sassi and A. Simon, “Waste-to-reuse foam glasses produced from soda-lime-silicate glass, cathode ray tube glass, and aluminium dross,” *Inorganics*, vol. 10, no. 1, 2022, doi: 10.3390/inorganics10010001.
[165] M. B. Østergaard, *Preparation and characteristics of glass foam*. 2019.
[166] G. Scarinci, G. Brusatin, and E. Bernardo, “Glass foams,” *Cell. Ceram. Struct. Manuf. Prop. Appl.*, pp. 158–176, 2006, doi: 10.1002/3527606696.ch2g.
[167] M. Sedlaˇ, “Preparation and characterization of glass-ceramic foam from clay-rich waste diatomaceous earth,” 2022.

[168] Y. Gong, R. Dongol, C. Yatongchai, A. W. Wren, S. K. Sundaram, and N. P. Mellott, "Recycling of waste amber glass and porcine bone into fast sintered and high strength glass foams," *J. Clean. Prod.*, vol. 112, pp. 4534–4539, 2016, doi: 10.1016/j.jclepro.2015.09.052.
[169] Y. A. Spiridonov and L. A. Orlova, "Problems of foam glass production," *Glas. Ceram. (English Transl. Steklo i Keramika)*, vol. 60, no. 9–10, pp. 313–314, 2003, doi: 10.1023/B:GLAC.0000008234.79970.2c.
[170] M. Tramontin Souza *et al.*, "Sustainable glass foams produced with stone waste as a pore-forming agent: Assessing the role of heating rate in foamability and glass foams recyclability," *J. Clean. Prod.*, vol. 338, no. January, p. 130596, 2022, doi: 10.1016/j.jclepro.2022.130596.
[171] M. K. Choudhary, B. Purnode, A. M. Lankhorst, and A. F. J. A. Habraken, "Radiative heat transfer in processing of glass-forming melts," *Int. J. Appl. Glas. Sci.*, vol. 9, no. 2, pp. 218–234, 2018, doi: 10.1111/ijag.12286.
[172] B. K. Larkin and S. W. Churchill, "Heat transfer by radiation through porous insulations," *AIChE J.*, vol. 5, no. 4, pp. 467–474, 1959, doi: 10.1002/aic.690050413.
[173] J. R. G. Evans and P. G. Collishaw, "An assessment of expressions for the apparent thermal conductivity of cellular materials," *J. Mater. Sci.*, vol. 29, pp. 2261–2273, 1994.
[174] S. N. Salama, S. M. Salman, and S. Gharib, "Thermal conductivity of some silicate glasses and their respective crystalline products," vol. 93, 1987.
[175] D. S. Smith *et al.*, "Thermal conductivity of porous materials," *J. Mater. Res.*, vol. 28, no. 17, pp. 2260–2272, 2013, doi: 10.1557/jmr.2013.179.
[176] J. Li *et al.*, "Utilization of coal fly ash from a Chinese power plant for manufacturing highly insulating foam glass: Implications of physical, mechanical properties and environmental features," *Constr. Build. Mater.*, vol. 175, pp. 64–76, 2018, doi: 10.1016/j.conbuildmat.2018.04.158.
[177] T. Liu *et al.*, "Phase evolution, pore morphology and microstructure of glass ceramic foams derived from tailings wastes," *Ceram. Int.*, vol. 44, no. 12, pp. 14393–14400, 2018, doi: 10.1016/j.ceramint.2018.05.049.
[178] J. Zhang, B. Liu, S. Zhao, H. Shen, J. Liu, and S. Zhang, "Preparation and characterization of glass ceramic foams based on municipal solid waste incineration ashes using secondary aluminum ash as foaming agent," *Constr. Build. Mater.*, vol. 262, p. 120781, 2020, doi: 10.1016/j.conbuildmat.2020.120781.
[179] X. Ge, M. Zhou, H. Wang, L. Chen, X. Li, and X. Chen, "Effects of flux components on the properties and pore structure of ceramic foams produced from coal bottom ash," *Ceram. Int.*, vol. 45, no. 9, pp. 12528–12534, 2019, doi: 10.1016/j.ceramint.2019.03.190.
[180] H. Wang, Z. Chen, L. Liu, R. Ji, and X. Wang, "Synthesis of a foam ceramic based on ceramic tile polishing waste using SiC as foaming agent," *Ceram. Int.*, vol. 44, no. 9, pp. 10078–10086, 2018, doi: 10.1016/j.ceramint.2018.02.211.
[181] L. B. Teixeira, V. K. Fernandes, B. G. O. Maia, S. Arcaro, and A. P. N. de Oliveira, "Vitrocrystalline foams produced from glass and oyster shell wastes," *Ceram. Int.*, vol. 43, no. 9, pp. 6730–6737, 2017, doi: 10.1016/j.ceramint.2017.02.078.
[182] J. König, R. R. Petersen, and Y. Yue, "Fabrication of highly insulating foam glass made from CRT panel glass," *Ceram. Int.*, vol. 41, no. 8, pp. 9793–9800, 2015, doi: 10.1016/j.ceramint.2015.04.051.
[183] H. Cengizler, M. Koç, and O. Şan, "Production of ceramic glass foam of low thermal conductivity by a simple method entirely from fly ash," *Ceram. Int.*, vol. 47, no. 20, pp. 28460–28470, 2021, doi: 10.1016/j.ceramint.2021.06.265.

[184] S. Volland, “Influence of the mechanical activation of raw mixes on the properties of foam glass from sand sludge,” *Constr. Build. Mater.*, vol. 125, pp. 119–126, 2016, doi: 10.1016/j.conbuildmat.2016.07.116.
[185] Y. Guo *et al.*, “Novel glass ceramic foams materials based on polishing porcelain waste using the carbon ash waste as foaming agent,” *Constr. Build. Mater.*, vol. 125, pp. 1093–1100, 2016, doi: 10.1016/j.conbuildmat.2016.08.134.
[186] M. Zhu, R. Ji, Z. Li, H. Wang, L. L. Liu, and Z. Zhang, “Preparation of glass ceramic foams for thermal insulation applications from coal fly ash and waste glass,” *Constr. Build. Mater.*, vol. 112, pp. 398–405, 2016, doi: 10.1016/j.conbuildmat.2016.02.183.
[187] C. Xi *et al.*, “Preparation of glass-ceramic foams using extracted titanium tailing and glass waste as raw materials,” *Constr. Build. Mater.*, vol. 190, pp. 896–909, 2018, doi: 10.1016/j.conbuildmat.2018.09.170.
[188] Q. Zhang *et al.*, “Preparation of high strength glass ceramic foams from waste cathode ray tube and germanium tailings,” *Constr. Build. Mater.*, vol. 111, pp. 105–110, 2016, doi: 10.1016/j.conbuildmat.2016.01.036.
[189] R. Ji *et al.*, “Utilization of mineral wool waste and waste glass for synthesis of foam glass at low temperature,” *Constr. Build. Mater.*, vol. 215, pp. 623–632, 2019, doi: 10.1016/j.conbuildmat.2019.04.226.
[190] D. I. Saparuddin, M. H. M. Zaid, S. H. Ab Aziz, and K. A. Matori, “Reuse of eggshell waste and recycled glass in the fabrication porous glass-ceramics,” *Appl. Sci.*, vol. 10, no. 16, 2020, doi: 10.3390/APP10165404.
[191] E. T. Brunauer, Stephen, Paul Hugh Emmett, “Adsorption of gases in multimolecular layers,” *J. Am. Chem. Soc.*, vol. 60, no. 2, pp. 309–319, 1938, doi: 10.1016/j.fuel.2016.10.086.
[192] ASTM C20, “Standard test methods for apparent porosity, water absorption, apparent specific gravity, and bulk density of burned refractory brick and shapes by boiling water 1 This international standard was developed in accordance with internationally recognized pri,” *ASTM Int.*, no. Reapproved 2015, pp. 20–22, 2017, doi: 10.1520/C0020-00R10.
[193] A. C326, “Standard test method for drying and firing shrinkages of ceramic whiteware clays.” 1997.
[194] H. Zhao, J. H. Kwak, Z. Conrad Zhang, H. M. Brown, B. W. Arey, and J. E. Holladay, “Studying cellulose fiber structure by SEM, XRD, NMR and acid hydrolysis,” *Carbohydr. Polym.*, vol. 68, no. 2, pp. 235–241, Mar. 2007, doi: 10.1016/j.carbpol.2006.12.013.
[195] P. Lu and Y. Lo Hsieh, “Preparation and properties of cellulose nanocrystals: Rods, spheres, and network,” *Carbohydr. Polym.*, vol. 82, no. 2, pp. 329–336, Sep. 2010, doi: 10.1016/j.carbpol.2010.04.073.
[196] T. I. Shaheen and H. E. Emam, “Sono-chemical synthesis of cellulose nanocrystals from wood sawdust using Acid hydrolysis,” *Int. J. Biol. Macromol.*, vol. 107, pp. 1599–1606, Feb. 2018, doi: 10.1016/j.ijbiomac.2017.10.028.
[197] C. Zanelato, A. Pires, S. da Silva, and A. Galdino, “Development of biphasic bone cement obtained from chicken eggshell,” *J. Mater. Res. Technol.*, vol. 9, no. 4, pp. 7297–7304, 2020, doi: 10.1016/j.jmrt.2020.05.053.
[198] M. Foldvari, *Handbook of thermogravimetric system of minerals and its use in geological practice*, vol. 213. 2011.
[199] D. Simón, N. Quaranta, S. Gass, R. Procaccini, and A. Cristóbal, “Ceramic bricks containing Ni ions from contaminated biomass used as an adsorbent,” *Sustain. Environ. Res.*, vol. 30, no. 1, p. 26, Dec. 2020, doi: 10.1186/s42834-020-00067-3.

[200] M. Kristl, S. Jurak, M. Brus, V. Sem, and J. Kristl, “Evaluation of calcium carbonate in eggshell using thermal analysis,” *J. Therm. Anal. Calorim.*, vol. 138, no. 4, pp. 2751–2758, 2019, doi: 10.1007/s10973-019-08678-8.
[201] A. C20-00, “Standard test methods for apparent porosity, water absorption, apparent specific gravity, and bulk density of burned refractory brick and shapes.”
[202] F. Kristály, “The effect of vegetal pore-forming additives on the composition, microstructure and physical properties of clay bricks,” University of Miskolc, 2013.
[203] E. Anastasiou, K. O. Lorentz, G. J. Stein, and P. D. Mitchell, “Prehistoric schistosomiasis parasite found in the Middle East,” *Lancet Infect. Dis.*, vol. 14, no. 7, pp. 553–554, 2014, doi: 10.1016/S1473-3099(14)70794-7.
[204] M. S. El-Mahllawy, “Characteristics of acid resisting bricks made from quarry residues and waste steel slag,” *Constr. Build. Mater.*, vol. 22, no. 8, pp. 1887–1896, Aug. 2008, doi: 10.1016/j.conbuildmat.2007.04.007.
[205] D. Eliche-Quesada *et al.*, “The use of different forms of waste in the manufacture of ceramic bricks,” *Appl. Clay Sci.*, vol. 52, no. 3, pp. 270–276, May 2011, doi: 10.1016/j.clay.2011.03.003.
[206] J.-E. F. M. Ibrahim *et al.*, “Effect of composition and sintering temperature on thermal properties of zeolite-alumina composite materials,” *Epa. - J. Silic. Based Compos. Mater.*, vol. 72, no. 4, pp. 131–134, 2020, doi: 10.14382/epitoanyag-jsbcm.2020.21.
[207] M. Yang, J. Li, Y. Man, Z. Peng, X. Zhang, and X. Luo, “A novel hollow alumina sphere-based ceramic bonded by in situ mullite whisker framework,” *Mater. Des.*, vol. 186, p. 108334, 2020, doi: 10.1016/j.matdes.2019.108334.
[208] X. Xu *et al.*, “Preparation and thermal shock resistance of corundum-mullite composite ceramics from andalusite,” *Ceram. Int.*, vol. 43, no. 2, pp. 1762–1767, 2017, doi: 10.1016/j.ceramint.2016.10.116.
[209] Y. Liu, X. Li, G. Wei, P. Chen, and B. Zhu, “Effect of in-situ formation of columnar mullite and pore structure refinement on high temperature properties of corundum casatbles,” *Ceram. Int.*, vol. 46, no. 15, pp. 24204–24212, 2020, doi: 10.1016/j.ceramint.2020.06.200.
[210] X. Chen *et al.*, “Mullite whisker network reinforced ceramic with high strength and lightweight,” *J. Alloys Compd.*, vol. 700, pp. 37–42, 2017, doi: 10.1016/j.jallcom.2017.01.075.
[211] A. C67-12, “standard test methods for sampling and testing brick and structural clay tile,” *ASTM International, West Conshohocken, PA, USA*, 2009. .
[212] M. H. Riaz, A. Khitab, S. Ahmad, W. Anwar, and M. T. Arshad, “Use of ceramic waste powder for manufacturing durable and eco-friendly bricks,” *Asian J. Civ. Eng.*, vol. 21, no. 2, pp. 243–252, 2020, doi: 10.1007/s42107-019-00205-2.
[213] M. Sutcu, H. Alptekin, E. Erdogmus, Y. Er, and O. Gencel, “Characteristics of fired clay bricks with waste marble powder addition as building materials,” *Constr. Build. Mater.*, vol. 82, pp. 1–8, 2015, doi: 10.1016/j.conbuildmat.2015.02.055.
[214] O. Biel, P. Rożek, P. Florek, W. Mozgawa, and M. Król, “Alkaline activation of kaolin group minerals,” *Crystals*, vol. 10, no. 4, 2020, doi: 10.3390/cryst10040268.
[215] H. Jaya, M. F. Omar, H. Md Akil, Z. A. Ahmad, and N. N. Zulkepli, “Effect of alkaline treatment on sawdust reinforced high density polyethylene composite under wide strain rate,” *Mater. Sci. Forum*, vol. 840, pp. 103–107, 2016, doi:10.4028/www.scientific. net/MSF.840.103.
[216] F. Méar, P. Yot, R. Viennois, and M. Ribes, “Mechanical behaviour and thermal and electrical properties of foam glass,” *Ceram. Int.*, vol. 33, no. 4, pp. 543–550, 2007, doi: 10.1016/j.ceramint.2005.11.002.

[217] T. Liu *et al.*, “The utilization of electrical insulators waste and red mud for fabrication of partially vitrified ceramic materials with high porosity and high strength,” *J. Clean. Prod.*, vol. 223, pp. 790–800, 2019, doi: 10.1016/j.jclepro.2019.03.162.
[218] Y. Guo *et al.*, “Novel glass ceramic foams materials based on red mud,” *Ceram. Int.*, vol. 40, no. 5, pp. 6677–6683, 2014, doi: 10.1016/j.ceramint.2013.11.128.
[219] R. S. Lakes, “Cellular solids,” *Journal of Biomechanics*, vol. 22, no. 4. p. 397, 1989, doi: 10.1016/0021-9290(89)90056-0.
[220] Y. Attila, M. Güden, and A. Taşdemirci, “Foam glass processing using a polishing glass powder residue,” *Ceram. Int.*, vol. 39, no. 5, pp. 5869–5877, 2013, doi: 10.1016/j.ceramint.2012.12.104.